University of Alberta
Department of Civil and
Environmental Engineering

Structural Engineering Report No. 213

THERMAL ICE LOADS ON STRUCTURES

by

AZITA AZARNEJAD

and

TERRY M. HRUDEY

November 1996

Structural Engineering Report No. 213

THERMAL ICE LOADS ON STRUCTURES

by

A. Azarnejad

and

T.M. Hrudey

Department of Civil and Environmental Engineering

University of Alberta

Edmonton, Alberta

November, 1996

ABSTRACT

Structures that are in contact with naturally occurring ice covers can be subjected to considerable forces due to thermal expansion of the ice. These forces are especially important for structures like low head dams, spillways, water intakes, gates, water reservoirs, and bridge piers. Although the importance of thermal ice loads has been recognized for over a century, due to lack of a three dimensional model, various factors that affect the thermal ice pressure are not considered in analytical studies. Such factors include the bending behavior of the ice sheet coupled with the elastic foundation effect of the underlying water, the geometry of the reservoir, shore-line features, the flexibility of the resisting structure, and cracking activity in the ice. The objective of this study was to develop an improved analytical capability for predicting ice forces.

A numerical model is developed that allows the prediction of the three dimensional stress field in an ice sheet due to temperature changes, as a function of time, under a variety of conditions. The model relies on two separate computer programs for the thermal and mechanical aspects of the problem. The thermal program uses the finite difference method to calculate the temperature distribution through the thickness of the ice cover, under a variety of meteorological input conditions. The mechanical part of the analysis is conducted using the finite element method. Relevant features of the finite element model include variable temperatures and properties through the thickness, an elastic foundation representation of the underlying water, nonlinear constitutive behavior

of the ice, temperature dependent mechanical properties, flexibility of the resisting structure, and boundary conditions representing a variety of shoreline types.

The predictions of both models are verified by comparison with analytical and other numerical solutions, published data on laboratory experiments, and field measurements conducted by the Canadian Electricity Association. The models are then used to investigate the factors that affect the thermal ice pressure. These factors include meteorological conditions, ice thickness, temperature history, different shore types, flexibility of resisting structure, and tensile cracking.

ACKNOWLEDGMENT

This report is a reprint of a thesis by the same title, written by the first author under the supervision of the second author.

Financial support for the project was provided by the Natural Sciences and Engineering Research Council (NSERC) to Dr. T.M. Hrudey under Research Grant No. 4450. Financial support to the first author was provided by the University of Alberta through the R. (Larry) Gerard Memorial Graduate Scholarship in Ice Engineering and the J. Gordin Kaplin Graduate Student Award.

The cooperation of the Canadian Electricity Association and Fleet Technology Limited in sharing their field data is appreciated and acknowledged.

Table of Contents

Chapter **Page**

Chapter **Page**

List of Tables

List of Figures

List of Symbols

a	a constant in the equations.
a_a	transmittance of the atmosphere.
a_{11}, a_{22}, a_{12}	elements of matrix [A].
a_{33}, a_{44}, a_{55}	elements of matrix [A].
[A]	the matrix that relates the stress to viscous strain rate.
b	a constant in the equations.
B	Bowen's ratio.
[B]	strain-displacement matrix.
B_c	constant for calculating the intermediate value in the Crank-Nicolson method.
c	a constant in the equations.
C	cloud cover.
c_o	a constant in differential equation.
$\{c_1\}$	a constant in differential equation.
Cp	specific heat.
D	the number of the day in a year.
$[D_1]$	stress-strain matrix.
$[\overline{D}]$	visco-elastic stress-strain matrix.
DOSM	the difference between the standard time and mean solar time.
e_a	vapor pressure of the air.
e_s	saturation vapor pressure at the ice surface.
ET	equation of time.
E_1	modulus of elasticity (stiffness) of the elastic element in the Maxwell unit.
E_2	modulus of elasticity (stiffness) of the elastic element in the Kelvin-Voigt unit.
$\{f\}$	right hand side vector.

f_t	tensile strength.
$f(u_w)$	wind function.
$\{F\}$	mechanical load vector.
F_w	force due to the effect of elastic foundation.
$\{\overline{F}\}$	body force.
$\{F_\theta\}$	load vector corresponding to total thermal strain.
G	shear modulus.
h	thickness of the ice cover.
h_s	the local hour angle of the sun.
H	coefficient of heat transfer.
i	denotes a grid point in finite difference analysis.
I	denotes the increment (time step) number.
[I]	identity matrix.
I_0	the solar constant.
$I+\beta$	denotes the intermediate value calculated using β.
$I+\beta_1$	denotes the intermediate value calculated using β_1.
$I+\beta_2$	denotes the intermediate value calculated using β_2.
J	denotes the iteration number in a time step.
k	thermal conductivity.
K	coefficient of absorption.
[K]	combined stiffness matrix.
K_1, K_2	shear correction factors.
L_f	specific heat of fusion.
L_s	the specific heat of sublimation.
m	exponent of stress for the viscous element in the Kelvin-Voigt unit.
m_a	the optical air mass.
m_0	the optical air mass at sea level.
n	exponent of stress for the viscous element in the Maxwell unit.
n_r	refractive index.

N	number of nodes in finite difference analysis.
$[N]$	shape function matrix.
$\{N_z\}$	nodal shape functions for vertical displacements.
$[P]$	the matrix that relates σ' to ε_d or σ'' to $\dot{\varepsilon}_d$.
$\bar{q}$	weighted time average heat flux.
q_b	heat flux due to emitted long-wave radiation from the surface.
q_c	solar radiation under a cloudy sky.
q_{cl}	solar radiation under clear sky.
q_e	heat flux due to evaporation and condensation.
q_l	heat flux due to long-wave radiation from the atmosphere.
q_{la}	radiation emitted from the atmosphere under clear sky.
q_{lc}	radiation from the atmosphere under a cloudy sky.
q_{li}	the part of radiation from the atmosphere that is absorbed by the ice cover.
$q_{l\,sky}$	heat flux due to long-wave radiation received on a horizontal plane.
q_r	heat flux due to radiation.
q_s	heat flux due to short-wave solar radiation.
q_{sz}	heat flux due to short-wave solar radiation at distance z from the surface.
q_t	heat flux due to temperature difference between the air and the atmosphere.
$\{q\}$	nodal displacements.
r	radius.
r_i	the ratio between the reflected radiation and incident radiation for the ice.
R	the universal gas constant.
$[R]$	the change in creep (viscous + delayed elastic) strain increment with respect to stress.
R_h	relative humidity.
s	energy source.
S_w	stiffness of the elastic foundation.
t	time coordinate.
T	absolute temperature.

$\{\bar{T}\}$	surface traction.
T_a	absolute temperature of the atmosphere.
u	vertical displacement.
$\dot{u}$	vertical displacement rate.
$\{u\}$	displacement vector.
u_w	wind speed.
v	non-dimensional velocity.
$\{v\}_{ik}$	nodal coordinate set .
x	global coordinate axis in the horizontal plane.
$\{x\}$	global coordinate set.
$\{x'\}$	local coordinate set in each Gauss point.
y	global coordinate axis in the horizontal plane.
z	global coordinate axis in vertical direction.
Z	altitude.
α	coefficient of thermal expansion.
α_s	the altitude of the sun.
α_1	$\frac{\pi}{2} - \alpha_s$.
β, β_1, β_2	constants for calculating the intermediate values within a time step.
β_i	the angle between the absorbed light in the ice and the vertical.
δ	declination of the sun.
$\{\delta u\}$	virtual displacement.
$\{\delta\varepsilon\}$	virtual strain.
$[\Delta D_1]$	change in stress-strain matrix due to change in temperature.
Δz	distance between grid points in finite difference analysis.
Δt	time step.
ε, $\{\varepsilon\}$	total strain (one and three dimensional).
$\dot{\varepsilon}$	total strain rate.
$\ddot{\varepsilon}$	second derivative of total strain with respect to time.

ε_a	emissivity of the atmosphere.
ε_d, $\{\varepsilon_d\}$	delayed elastic strain (one and three dimensional).
$\dot{\varepsilon}_d$, $\{\dot{\varepsilon}_d\}$	delayed elastic strain rate (one and three dimensional).
ε_e, $\{\varepsilon_e\}$	instantaneous elastic strain (one and three dimensional).
$\dot{\varepsilon}_e$	instantaneous elastic strain rate.
ε_r	emissivity.
ε_s	emissivity of the surface.
ε_v, $\{\varepsilon_v\}$	viscous strain (one and three dimensional).
$\dot{\varepsilon}_v$, $\{\dot{\varepsilon}_v\}$	viscous strain rate (one and three dimensional).
ε_θ, $\{\varepsilon_\theta\}$	thermal strain (one and three dimensional).
ϕ	latitude.
$\{\phi\}$	residual stress.
$\{\bar{\phi}\}$	residual stress after manipulations.
Φ	scalar potential function used for calculating the viscous strain rate from the effective stress.
γ	psycrometric constant.
η	curvilinear coordinate axis in the middle plane of each element.
η_1	fluidity parameter of the viscous element in the Maxwell unit.
η_2	fluidity parameter of the viscous element in the Kelvin-Voigt unit.
λ_c	error limit in convergence criteria.
μ_1	viscosity of the viscous element in the Maxwell unit.
ν	Poisson's ratio.
θ	temperature.
$\dot{\theta}$	temperature rate.
$\bar{\theta}$	weighted time average temperature.
θ_a	air temperature.
θ_{am}	amplitude of temperature variation.
θ_i	initial temperature.

ρ	density.
ρ_w	density of water.
σ, $\{\sigma\}$	stress (one and three dimensional).
$\dot{\sigma}$	stress rate.
$\ddot{\sigma}$	second derivative of stress with respect to time.
σ', $\{\sigma'\}$	stress in the elastic element of the Kelvin-Voigt unit (one and three dimensional).
σ'', $\{\sigma''\}$	stress in the viscous element of the Kelvin-Voigt unit (one and three dimensional).
σ''_{eff}	the effective value of σ''.
σ_r	the Stefan-Boltzman constant.
τ	the effective stress.
ξ	curvilinear coordinate axis in the middle plane of each element.
ξ_m	ratio of the molecular weights of water and dry air.
ζ	curvilinear coordinate axis in the thickness direction.

1 - INTRODUCTION

Many civil engineering structures in cold regions must be designed to resist loads due to interaction with ice. Normally the dominant mechanisms giving rise to these loads are wind and current driving forces. However, under certain conditions, thermal ice loads can be equally important. The thermal ice load acting on a structure is defined to be the static pressure arising from the thermal expansion of a solid ice sheet which is in contact with the structure. When the ice initially forms, its temperature is at the freezing point. As the ice sheet grows in thickness, the temperature at the bottom surface remains at the freezing point but the temperature at the top surface can vary due to heat exchange between the ice and the surrounding atmosphere. The temperature variation causes volume changes but under relatively steady state conditions any stresses in the ice sheet will relax to zero due to creep. However, a subsequent rapid rise in temperature will cause expansion, which if prevented by a structure, will cause thermal stresses to be developed (Fig. 1.1). Ultimately these will dissipate due to creep, but before this can happen, very significant loads may be generated. In some cases the ice force may even control the design of the structure.

1.1 - Background

The significance of thermal ice loads has been recognized for over a century. Attention was drawn to the problem by various failures. One of the earliest failures in Canada was the Rice Lake Railway Bridge (Dumble, 1891). As stated by Dumble,

> "The truss bridge was very strong, with eighty feet spans resting on stout timber piers filled with stone. The whole structure was of the strongest and most substantial character of its kind, and yet this bridge was wrecked in a few minutes, in the early part of December, by an ice shove, and when the ice was comparatively

thin. The pile work south of the island was inclined like a pack of cards to nearly an angle of forty-five degrees."

The railway was abandoned and the million dollars spent on its construction was lost. Other examples of failures were noted in the discussion of Dumble's paper.

A much more recent example is shown in Fig. 1.2. This involved a water intake on the Tilley B reservoir in Southern Alberta. Prior to failure, the 2.0 m wide concrete box was oriented vertically. It was pushed into the inclined position shown in Fig. 1.2, by an ice sheet about 0.9 m thick. The ice load was subsequently estimated to have exceeded 300-400 kN/m (Gerard, 1989).

Additional data on thermal ice loads is summarized in Table 1.1. The various loads shown were obtained by field measurements. The data in Table 1.1 gives some indication of the uncertainty that exists with regard to thermal ice loads. With loads as high as 320 kN/m, it also gives some sense of their relevance. It should be noted that the data listed in Table 1.1 were obtained by a variety of measurement techniques and could vary significantly in terms of their accuracy.

A category of structure for which thermal ice loads are particularly important, is that of low to medium head dams. The significance of the ice load in the design of dams is illustrated in Fig. 1.3 (Gerard, 1989) where the overturning moment due to hydrostatic pressure from the reservoir is compared to the overturning moment due to ice thrusts of different magnitudes. It can be seen that for a low head dam with a height of ten metres, the overturning moment due to the ice force can be larger than the overturning moment due to hydrostatic pressure. Thermal ice loads are also important in the design of spillways, water intakes, and bridge piers.

The measured ice thrusts listed in Table 1.1 cover a wide range. This is due in part to the fact that the ice thicknesses range from 0.16 m to 1.10 m. However for a single thickness, for example around 0.4 m, quite different values of ice thrust are listed. This can be explained by the fact that the ice pressure depends on many parameters. Some, like those related to meteorological conditions (e.g. air temperature, solar radiation, snow cover, etc.), affect the temperature distribution through the ice sheet. Factors of a mechanical nature, such as the restraint against movement provided by the shore and

cracking of the ice, affect the stress distribution. Because the actual ice load that occurs in a particular situation depends on many such factors it is difficult to assign a single load that is suitable for all situations.

In the Dam Safety Guidelines for existing dams prepared by the Canadian Dam Safety Association (1995) the following recommendations are given for the ice pressure:

> "The thermal ice loads used in the design reviews are usually assumed to be 146 kN/m (10 kips/ft) for concrete dams, 73 kN/m (5 kips/ft) for steel gates, and 29 kN/m (2 kips/ft) for timber stop logs. Ice load shall be considered to act at 300 mm (1 foot) below the water level.
>
> If site specific characteristics and operating information warrant, different values of static ice loads may be used in the assessment and, in addition, dynamic ice loads may also be considered."

Comparing the values in the first paragraph of the CDSA recommendations with the ice forces listed in Table 1.1, it appears that the former could be unconservative in some cases.

Criteria for the design of gates under ice conditions in Northern Europe are given in DIN 19704 (Lewin, 1995), where different empirical rules apply to inland and estuarial conditions. For inland conditions, the triangular hydrostatic distribution of water pressure at a depth of 1 m is replaced with a uniform pressure of 0.02, and 0.03 MPa, where the ice thickness is below and above 0.3 m, respectively. In estuarial conditions, different values are suggested for skin plates and main girders. In the design of skin plates the following loads are suggested over the hydrostatic load within 0.5 m above and below water level:

-A uniform pressure of 0.1 MPa, when severe ice formation is present and ice movement occurs.

-In conditions of moderate ice formation, a uniform pressure of 0.03 MPa should be used.

For main girders, additional loads of 350 and 100 kN/m are suggested for severe and moderate ice conditions respectively.

A uniform pressure of 0.03 MPa over a height of one metre, will give a line load of 30 kN/m. According to Table 1.1 the measured line load on the gate in Paugan Dam,

which is considered an inland condition was about 82 kN/m during the 1991-1992 winter. In estuarial conditions where the ice movements are possible, much higher stresses and loads may develop.

Gerard (1989) reviewed measured ice thrusts and design guides and concluded that most values suggested in the design guides were unconservative. Then, using the measured data, an upper bound of 500 kN/m with a probability of exceedence of about 1% was suggested for wide structures where failure would not be catastrophic. For the design of dams, where failure would be catastrophic, higher values for ice loads were recommended. Gerard noted that the resulting recommended ice load could be very high in some situations.

Two conclusions can be drawn from the wide range of measured and recommended ice loads. First, the problem of thermal ice loads on structures is still not fully understood. Second, each site must be treated individually. The design load for a particular structure should be estimated according to the meteorological data and conditions of the reservoir and the structure.

Efforts directed at predicting the ice pressure that would develop under different conditions began more than 100 years ago. Dumble (1891) performed experiments on the movements of a floating ice sheet due to temperature changes. But due to lack of information on the stress-strain relationship for ice, it was not possible to determine the ice stresses. The earliest approach was based on the crushing strength of the ice which resulted in very high load predictions. One of the early investigations on the stress-strain relationship for ice was in 1922 (Royen, 1922). Since then, many investigators in cold regions have tried different approaches to estimate the thermal ice pressure. Many laboratory tests were performed and many field measurements were conducted. Some investigators obtained empirical relationships and some used analytical or numerical calculations to predict the thermal ice load. Some of these methods are discussed in Chapter 2. Despite these investigations, the problem of thermal ice pressure is not at all close to being solved. There is a lack of a three-dimensional model for ice covers. Due to non-uniform temperature variations through the thickness, ice covers can have both bending and membrane deformations and because of creep, the bending and membrane

stresses are coupled. In some studies the stresses due to temperature changes in different layers of the ice covers are studied and the effect of the interactions between the layers and inplane restraint is ignored. In some cases only the inplane behavior is considered and a single temperature change is considered through the whole thickness. There has not been a model which could consider bending and membrane behavior simultaneously.

1.2 - Objective and Organization of the Thesis

The objective of this study was to develop an improved analytical capability for predicting thermally induced ice forces, and to use that modeling capability to investigate and assess the importance of the various factors that affect the thermal pressure. To achieve these objectives, two separate computer programs were developed. One deals with the thermal aspect of the problem and the other with the mechanical aspects. The thermal program uses a finite difference scheme to predict the temperature distribution through the thickness of the ice sheet. The output from this program is the temperature profile as a function of time. This serves as a part of the input for the mechanical or stress analysis program. It uses the finite element method to predict the three-dimensional distribution of stress in the ice cover. A layered shell element is used, which allows nonlinear temperature distributions through the thickness, temperature dependent material properties, and both bending and membrane behavior of the ice cover.

The thesis contains seven chapters. Chapter 1 provides a brief introduction. Previous investigations on the subject of thermal ice loads are discussed in Chapter 2.

Chapter 3 deals with the thermal analysis. First the governing differential equation is introduced and the various heat transfer mechanisms considered in this study are described. Then the finite difference formulation and some features of the program are explained. The chapter concludes with the results of verification studies in which predictions of the program are compared with available analytical or other numerical solutions.

In Chapter 4, the finite element formulation is presented. Following a description of the element used, the constitutive law is explained. Then some features of the program are described and the overall formulation together with the solution algorithm are presented. At the end of the chapter, verification studies involving simple test cases are presented.

Chapter 5 consists of the comparisons between the predictions of the present models with laboratory and field measurements. First the issue of the material properties of ice is discussed. Then the stresses predicted by the present model using different mechanical properties are compared to those presented in published laboratory tests for different ice types. In the last part of the chapter, the predictions of both the thermal and mechanical models are compared with published field measurements.

In Chapter 6 results are presented from a number of studies that were performed to investigate the importance of different factors that affect the temperature and stress distribution in an ice cover. The first group of tests were performed with the thermal analysis program. The parameters studied include: the ice type and material properties, wind speed, relative humidity, cloud cover, time of the year, snow cover, thickness of the ice cover, duration of temperature increase, and the magnitude of the temperature increase. The second series of tests deal with factors of a mechanical nature that affect the stress distribution. These include: the number of layers through the thickness, the total thickness, the duration of the temperature increase, the initial temperature, the rate and magnitude of the temperature increase, the underlying water, the geometry of the reservoir, the boundary conditions, the inclination of the shore, stiffness of the resisting structure, isolated structure, and tensile cracking. The chapter ends with a list of the important conclusions reached from the various tests.

The last chapter of the thesis, Chapter 7, consists of a summary, the overall conclusions reached in this project, and recommendations for further studies.

Place	Winter	Thickness (m)	Ice load (kN/m)	Reference
Tainter gate of the Hastings Dam on Mississipi River	1932-33	0.46	51	Hill (after Michel, 1978)
Joachims Dam, Ontario	1951-52		102	Wilmot, 1952
Eleven mile Canon , Colorado	1947-48 1948-49 1949-50		235 206 294	Monfore, 1954
Antero, Colorado	1950-51	0.3	53	Monfore, 1954
Shadow Mountains, Colorado	1950-51	0.4	85	Monfore, 1954
Evergreen, Colorado	1950-51		138	Monfore, 1954
Taryall Reservoir, Colorado	1950-51	0.4	253	Monfore, 1954
Ges Reservoir, Dnieper River	1954-55		123	Korzhavin (after Michel, 1978)
Taisetsu Reservoir, Hokkaido, Japan	1977	0.4	56	Yamaoka et al., 1988
Taipingchi, China	1974	0.78	324	Xu Bomeng, 1986
Erlonghu, China	1977	0.82	226	Xu Bomeng, 1986
Shanghewan,China	1975	0.72	167	Xu Bomeng, 1986
Yinhe, China	1978	1.10	235	Xu Bomeng, 1986
Taiyangsheng, China	1979	1.02	128	Xu Bomeng, 1986
Yadian, China	1980	0.26	39	Xu Bomeng, 1986
Shengli, China	1981	0.84	216	Xu Bomeng, 1986
Hangali, China	1985	0.80	245	Xu Bomeng, 1986
Arnprior Dam, Ontario	1992-93	0.46	156	Comfort et al., 1994
Paugan Dam, Quebec reservoir spillway pier spillway gate reservoir spillway pier spillway gate	 1991-92 1991-92 1991-92 1992-93 1992-93 1992-93	 0.28 0.16 	 115 288 82 52 122 22	Comfort et al., 1993 Comfort et al., 1994

Table 1.1 - Measured ice thrusts.

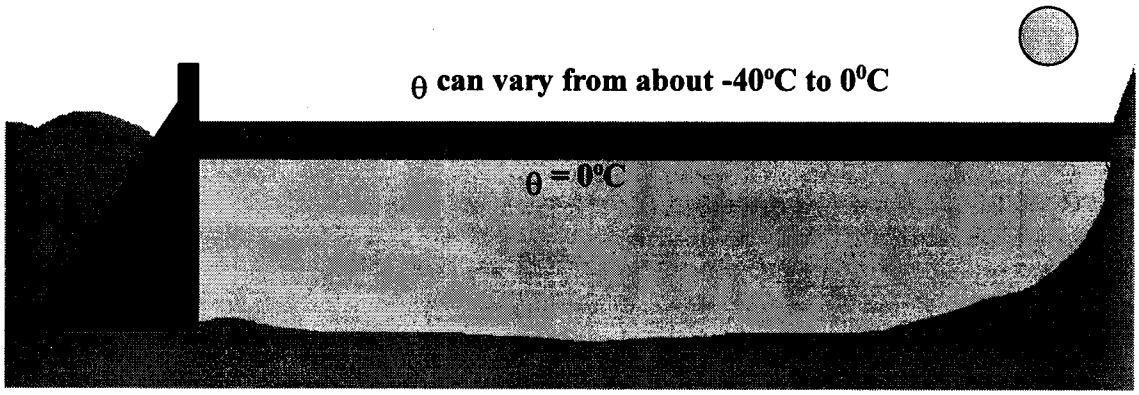

Figure 1.1 - Thermal ice load on a structure.

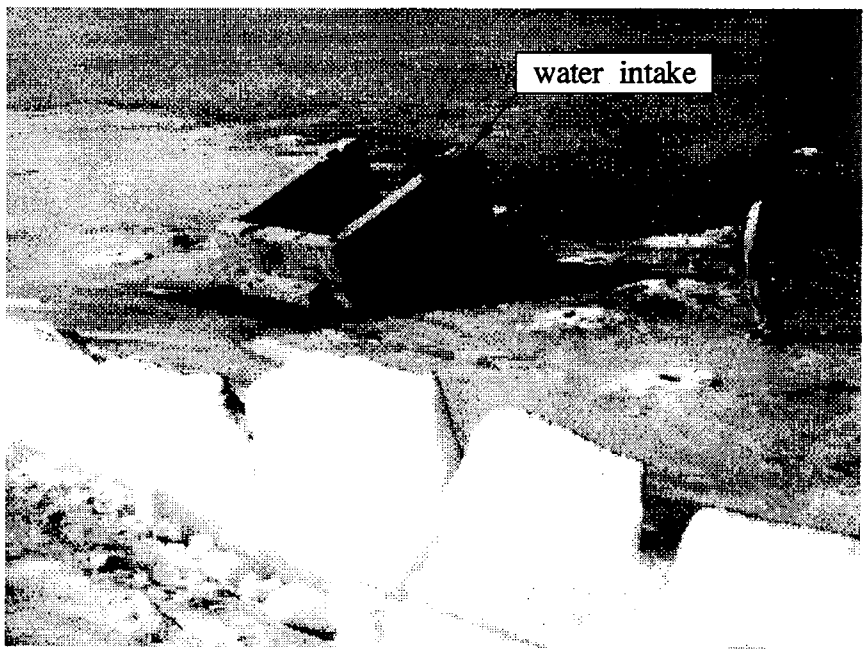

Figure 1.2 - Water intake on the Tilley B Reservoir in southern Alberta, pushed to inclined position by ice cover.

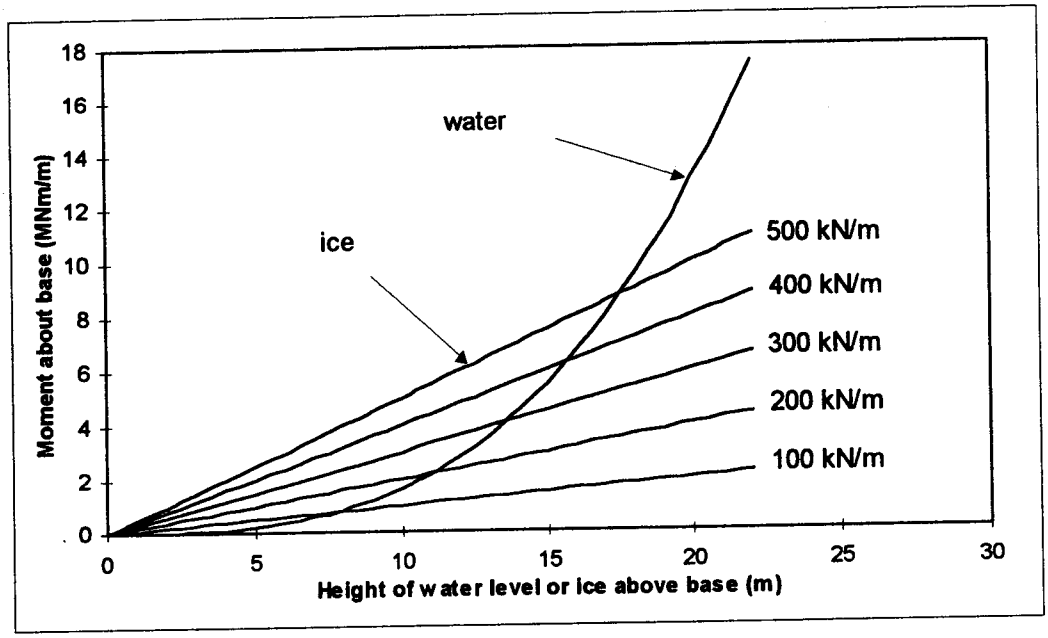

Figure 1.3 - Overturning moment due to a water column and ice thrusts of different magnitudes (reproduced from Gerard, 1989).

2 - LITERATURE REVIEW

In this chapter a brief review of the evolution of research related to thermal ice pressure is presented. Investigations related to ice behavior but not directly concerned with the problem of thermal pressure are not included in this chapter although some of this work is used elsewhere in this study. Reference is made to literature reviews conducted previously by Drouin and Michel (1971), Bergdahl (1978), and Kjelgard and Carstens (1980). In order to facilitate the comparison of various works, numerical values for all physical quantities are converted to S.I. units.

Investigation of thermal ice pressure began about a century ago. In 1891 Dumble reported the results of his experiments on the movements of a floating ice sheet due to temperature changes (Dumble, 1891). But due to lack of information on the stress-strain relationship for ice, it was not possible to determine the ice stresses. The earliest approach was based on the crushing strength of ice, which was estimated to be about 2.76 MPa. Assuming that this crushing stress was realized in the upper part of the ice sheet and that no pressure was exerted from the lower region, the thrust for an 0.45 m ice sheet would amount to 620 kN/m. For example, in the case of the Gouin Dam (1917) in Quebec, allowance was made for a thrust of 730 kN/m (Drouin & Michel, 1971). Figure 1.3 shows that for a small dam with 10 m height the over-turning moment due to this thrust can be 3 times the over-turning moment due to water pressure. Taking such a large force into account can compromise the profitability of a hydroelectric project.

2.1 - Royen (1922)

In 1922 Royen from Sweden proposed a general uniaxial stress-strain relationship for ice on the basis of experiments with wax and lake ice (Royen, 1922). It was given by

$$\varepsilon = \frac{c\sigma t^{1/3}}{1+|\theta|} \tag{2.1.1}$$

where

ε = compressive strain

σ = stress (kg/cm^2)

t = duration of load (hours)

θ = ice temperature (C^o)

c = a factor determined experimentally, whose value lies between 60×10^{-5} and 90×10^{-5} .

This equation was used to calculate thermal ice pressure. The strain rate due to free expansion of the ice sheet can be written as:

$$\frac{d\varepsilon}{dt} = \alpha\frac{d\theta}{dt} \tag{2.1.2}$$

where α is the coefficient of thermal expansion. Assuming that the expansion of the ice sheet is completely restrained, Royen differentiated (2.1.1) with respect to time and equated the result with (2.1.2). That gives:

$$\sigma = \frac{3\alpha}{c}(1+\theta)t^{2/3}\frac{d\theta}{dt} \tag{2.1.3}$$

In this differentiation, σ and θ are considered to be constant despite the fact that in reality they both vary with time. Royen justified this approximation on the basis of agreement with experimental results. Royen assumed a linear variation of temperature with time and differentiated (2.1.3) with respect to time in order to find the time of maximum stress. Finally the maximum thrust in tonnes per metre (for $\alpha=5.5\times10^{-5}$ $C^{o\,-1}$) was expressed by:

$$p_{max} = 0.09d(\theta_i + 1)\sqrt[3]{\dot{\theta}(\theta_i+1)^2} \tag{2.1.4}$$

where

d = ice thickness (cm)

θ_i = average initial temperature of the ice (C^o, absolute value)

$\dot{\theta}$ = constant rate of average temperature increase

Royen assumed a minimum temperature of -40°C for Sweden with the average minimum temperature of -12°C in the ice sheet. He suggested rates of temperature

increase of 0.12, 0.07, and 0.033 C°/hr. For a maximum thickness of 1 metre the values of maximum pressure were 338, 281 and 221 kN/m. Allowing for some decrease in stress due to plastic deformation, Royen suggested a value of 294 kN/m for a completely restrained ice cover.

Later research showed that for several reasons, Royen's theory could not be applied with confidence. The calculations were based on a constitutive law that was not able to represent the behavior of ice adequately. Heat transfer in the ice sheet was not considered and therefore the maximum force predicted was proportional to ice thickness. A uniaxial theory was used for a problem involving biaxial restraint.

2.2 - Brown and Clarke (1932)

In 1932, Brown and Clarke performed a number of tests on ice cubes in order to obtain an estimate of the thermal pressure to be used in the design of the dams for the hydro-electric power development at Island Falls on the Churchill River in Saskatchewan (Brown and Clarke, 1932). In these experiments 0.0762 m ice cubes were subjected to a temperature rise while one of the dimensions was kept constant between the two platens of a manual press. Each test was divided into time intervals. During each time interval the temperature rate was almost constant. They reported two tests in which they had observed linear rise in pressure due to linear temperature rise. On the basis of these two tests they drew a curve for the rate of increase of stress as a function of the rate of increase of temperature (Fig. 2.1). They argued that the effect of lateral restraint would offset the effect of heat transfer and temperature gradient in the ice cover, so the total pressure could be conservatively obtained by using the air temperature increase rate and total thickness of the ice cover. An ice pressure of 146 kN/m was used in the design of the dams at Island Falls.

Brown and Clarke's contribution did not provide an acceptable solution for the problem of thermal ice pressure. Their test apparatus was not accurate enough to capture the true ice behavior and their results were not consistent with what is now well known

about ice creep. The results of only two tests were used to obtain the curve and the initial temperature was not considered. Brown and Clarke's argument, that the effect of lateral restraint would offset the effect of heat transfer, is questionable.

2.3 - Rose (1947)

In 1947 Rose suggested a method for determining thermal ice pressures (Rose, 1947) which was based on:

1) The experimental data of Brown and Clarke.
2) Using heat transfer theory to obtain the temperature gradient in an ice cover.
3) An evaluation of the effect of the lateral restraint according to the theory of elasticity.

Rose's main contribution consisted of introducing a thermal analysis for calculating the temperature distribution in the ice sheet. He assumed that the surface temperature was equal to the air temperature and the initial air temperature was -40°C.

Finite difference integration was used to find the rate of the temperature increase at different levels in the ice cover. Rates of air temperature increase of 2.78, 5.56, and 8.34°C/hr were considered . Then using the curve drawn by Brown and Clarke (Fig. 2.1) the pressure at different levels was obtained. Rose made an extension of this curve on the basis of other tests on continuous yielding of ice under sustained loads. The total force per unit length was obtained by summation of stresses at different levels. Rose was the first to consider the effect of solar radiation penetrating an ice sheet. In these calculations a latitude of 40 degrees, and the time of vernal equinox was assumed.

Finally the effect of lateral restraint was estimated on the basis of the behavior of an elastic slab. The pressures were multiplied by a factor equal to $1/(1-\nu)$, where ν is Poisson's ratio. Assuming $\nu=0.365$, a factor of 1.575 was obtained. The results were presented in the form of a family of curves for ice thrust as a function of ice thickness (Fig. 2.2).

Although Rose improved on the representation of the thermal aspects of the problem, his force predictions were not satisfactory because they were based on Brown and Clarke's curves which did not give a reliable description of the stresses developing during thermal expansion. Also, using elastic theory when considering the effect of lateral restraint is not consistent with the creep of ice which occurs without volume change. In spite of these deficiencies, Rose's values were widely accepted and continue to be used by engineers (see for example USBR, 1977 and Smith, 1985).

2.4 - Monfore's Tests (1946 - 1954)

Experimental investigations of ice pressure were conducted by the United States Bureau of Reclamation, USBR, from 1946 to 1951. These investigations included field studies at several reservoirs located in the mountains of Colorado and laboratory studies performed in the engineering laboratories of the USBR in Denver, Colorado. The results of these studies were given by Monfore in a number of reports (see for example Monfore, 1951) and a summary of results was presented by Monfore at an ASCE symposium (Monfore, 1954).

Monfore's laboratory tests were conducted in the same way as Brown and Clarke's, but better equipment used was. The specimens were 0.102 m long by 0.102 m diameter cylinders taken from 0.45 m thick field ice. The cylindrical axes of the specimens were in the same direction as the horizontal plane of the ice sheet. Before each test the sample was kept for some time at one of several temperatures (-34.4, -28.9, -23.3, -17.8, -12.2, and -6.7°C). During the tests, while the temperature was increasing, the load on the specimen was adjusted to maintain zero strain in the ice.

Monfore observed that for all the tests, the curve of pressure versus time was fairly linear at the start, then bent over reaching a maximum and finally decreased. Although qualitatively the stress-time curves were similar, the maximum pressure and the time to reach the maximum pressure were quite different for tests made under the same conditions. The average deviation in the maximum pressure was 6% for duplicate tests on

the same specimen and 25% for different specimens. Monfore studied the crystal orientation in a few samples and did find some marked differences. Even so, it was not used as an independent parameter in his studies.

Monfore calculated the average maximum stress and the average time to reach the maximum stress for a number of tests performed at the initial temperature of -23.3°C with a temperature rate of 2.8°C/h. These values were used to normalize the results of the tests performed at different initial temperatures and temperature rates. The average dimensionless stress-time curve is shown in Fig. 2.3. On the basis of this average curve, the stress-time curves were determined for different initial temperatures and different rates of temperature increase.

The results of the experiments were summarized in two diagrams (Fig. 2.4) showing the maximum pressure as functions of the rate of change of ice temperature for different initial temperatures. The method for calculating ice pressure was as follows. First for each level in the ice, values for the initial temperature and the temperature increase rate were chosen. Then from the figures, the maximum pressure was read and the available time was checked. Then the average pressure was multiplied by the ice thickness to obtain the total thrust per unit length.

Monfore gave three examples where the calculated values were compared with field measurements. The pressure gages used for field measurements were installed at three different levels in the ice sheet and the total thrust was obtained by multiplying the average measured stress by thickness. Ice temperatures were also measured at different depths in the ice sheet. In the three examples, Monfore used the temperature measurements to calculate the ice pressure and then compared the results with measured values. In these cases the calculated thrusts were 88, 190, and 153 kN/m whereas the measured thrusts were 88, 175, and 212 kN/m respectively.

The highest seasonal thrusts measured during the field investigations for three winters ranged from 204 to 292 kN/m. In general, high pressures occurred during relatively warm weather following periods of cold weather. The effect of shore type was generally as expected. The highest thrust at a reservoir with flat shores was 85 kN/m and for a reservoir with moderately steep shores was 137 kN/m. The highest values happened in

reservoirs with rocky and steep walls. The highest pressure usually occurred at the top of the ice sheet except for a case when there were open cracks during the day and the maximum pressure was recorded by the middle gage.

Monfore's experiments and measurements were a step forward in understanding the behavior of ice subjected to thermal load. The calculations however, had some weaknesses including neglecting the crystal type, not considering the lateral restraint, not considering the time lag between the maximum pressure at different levels, and using the average pressure for obtaining the total thrust. Monfore used measured temperatures in the calculations and did not make any attempt to calculate the temperature distribution in the ice sheet.

2.5 - Lofquist (1954)

An investigation was undertaken by the Swedish State Power Board to solve the problem of thermal ice pressure. Lofquist reported the results of one of the experiments at an ASCE symposium in 1954 (Lofquist, 1954). In this experiment an ice cover was grown in a cylindrical concrete container with insulated walls and an internal diameter of 0.5 m. The ice was formed in the same way as occurs in nature; by cooling at the top surface. When the ice reached a maximum thickness of about 0.6 m, the ice surface was exposed to an approximately exponential temperature increase from -30°C to 0°C over a period of 25 hours. The stress profiles obtained in this experiment are shown in Fig. 2.5. It can be seen that the position of the maximum stress moves down through the thickness as time increases. It was also observed that the pressure in different gages increased with time, reached a maximum and then decreased. The maximum thrust per unit length in this experiment was 196 kN/m which was recorded at about 14 hours after the start of the temperature increase.

Lofquist remarked that the measured ice pressure was reduced by the fact that container itself deformed due to both thermal expansion and the thrust exerted by ice. Also some cracks were observed in the uppermost part of the ice cover that might have

reduced the pressure. It was estimated that the thrust would be 25% higher for the case of complete restraint. Lofquist noted that the thermal pressure increased with thickness up to the order of 0.5 m with only a marginal increase for thicker ice sheets. Lofquist's experiment was the first biaxial test on ice and provided understanding of the behavior of ice when partially restrained in two directions and subjected to a temperature increase. However, Lofquist did not analyze the data in such a way that it could be used for predicting ice pressures.

2.6 - Assur (1959)

In 1959 Assur suggested a rheological model which was later used by others (Assur, 1959). The constitutive equation was the solution of the differential equation for a model with a Maxwell and Kelvin unit in series under constant load. The solution for strain is:

$$\varepsilon = \frac{\sigma}{E_1} + \frac{\sigma}{ms}[\eta_2 t_0 (1 - e^{-\frac{t}{t_0}}) + \eta_1 t] \tag{2.6.1}$$

where

$t_0 = 1/E_2\eta_2$ = relaxation time for elastic lag

$m = 2(1+\nu)$ for uniaxial case (m=3 for viscous flow)

$m = 2/\nu$ for biaxial case (m=4 for viscous flow)

$$s = \exp(\frac{Q_c}{RT}) \frac{\frac{\tau}{\tau_0}}{\sinh(\frac{\tau}{\tau_0})} \tag{2.6.2}$$

and

Q_c = activation energy for creep

R = the universal gas constant

T = the absolute temperature

$\tau = \sigma/m$

$\tau_0 = cT$

heat transfer in the ice sheet is not considered, and since the standard is based on Royen's rheological model it has the same short-comings.

2.8 - Lindgren (1968)

Lindgren performed uniaxial and biaxial laboratory experiments on ice samples to determine the rheological properties of ice (Lindgren, 1970). Results were used to calculate the thermal ice pressure for a prescribed air temperature variation.

The largest recorded air temperature rise in Arjeplog, which occurred during the winter of 1963 (-34°C to +2°C) was used in calculating the temperature distribution in a 0.6 m thick ice cover for the three cases of 0.0, 0.05, and 0.4 m snow cover. The thermal resistance of the surface was included. The calculations showed the great effect that snow cover has on the temperature distribution in an ice cover.

Lindgren used a linear visco-elastic model similar to that suggested by Assur (equation 2.7.1) to calculate the stress in the ice. The strain solution obtained is:

$$\varepsilon = \frac{\sigma}{E_1} + \frac{\sigma}{E_2}[1 - \exp(-E_2\eta_2 t)] + \sigma\eta_1 t \qquad (2.8.1)$$

Lindgren mentions that

" ...several studies have shown that" the equation (2.8.1) "...does not give a complete picture of the deformation characteristics of ice. Ice is therefore not linearly visco-elastic."

To account for that, Lindgren investigated the dependence of the viscosity on the stress and time, although in the differential equation the assumption was that the parameters were constant.

The results of the experimental tests were used to evaluate the parameters in the rheological equation. In the uniaxial tests, 0.07×0.07×0.2 m prisms were subjected to constant load. The deformation-time plots for some of the tests are shown in Fig. 2.6. Lindgren gave the following values based on the uniaxial experiments:

$E_1 = 66000(1\text{-}0.012\theta)$ kg/cm^2

$E_2 = 70000$ kg/cm^2

$\eta_2 = 1.1\times10^8$ kg·s/cm^2

$$\eta_1 = 18.5\sigma^{-1}(0.2\text{-}0.08\theta)(t/3600)^{0.5}\times10^8 \text{ kg/cm}^2 \qquad (2.8.2)$$

In the biaxial tests a steel ring with inner diameter 0.8 m was placed around a circular ice plate of about 0.07 m thickness. The space between was filled with water which was then frozen. The ice plate and steel ring were subjected to a rising temperature and the ice pressure was obtained from the strain in the steel ring. The results of one of these tests are shown in Fig. 2.7. From the biaxial tests the same values for E_1, E_2, and η_2 were obtained assuming a Poisson's ratio value of 0.36. A new equation was given for η_1 on the assumption that Poisson's ratio was 0.5 for viscous flow (to model incompressiblity):

$$\eta_1 = 31\sigma^{-1}(0.3\text{-}0.07\theta)(t/3600)^{0.25}\times10^8 \text{ kg/cm}^2. \qquad (2.8.3)$$

On the basis of these values the stress-time diagram for different starting temperatures and different rates of temperature increase was determined. The method for calculating ice thrust was to divide the ice sheet into layers and calculate the pressure at different times depending on the temperature changes in the layers in question. The sum of ice pressure in the various layers gave the total ice thrust. For the three cases selected, the ice pressure was calculated to be 451, 118, and 49 kN/m respectively.

Lindgren did not consider different types of ice crystals. The type of ice in the experiments and the method of ice formation were not identified. Lindgren started with a uniaxial model with constant parameters and constant stress, then used it for a biaxial case with temperature changes, where the stress and parameters were no longer constant. Although an attempt was made to fit the model with test data, getting a good agreement was unlikely, since the method was not consistent with the assumptions. Lindgren offered the following rather interesting comment:

"Calculations of the values of the maximum pressure are somewhat unreliable. With this in mind, rough estimates can be used to assess maximum ice pressure."

2.9 - Drouin and Michel (1971)

Drouin and Michel contributed significantly to the study of thermal ice pressure (Drouin & Michel, 1971). In their report they first reviewed previous research on thermal ice pressure and then studied the thermal aspect of the problem. They reviewed the thermal ice properties and conducted a statistical study of the air temperature records for Quebec City to get an estimate of the initial temperature, spread, duration and shape of temperature rises.

Concluding that the temperature versus time curve generally has a sinusoidal shape, they solved the differential equation for thermal diffusion in ice, using a sinusoidal increase in surface temperature. The effect of snow cover was accounted for by increasing the thickness of ice by an amount that would result in the same temperature distribution as for ice with a snow cover. For an ice thickness of more than 0.4 m the temperature distribution was approximated by the Fourier solution for a semi-infinite space. The effect of the thermal boundary layer and solar radiation were not considered. It was argued that these two effects would offset each other.

The most valuable parts of their work were the uniaxial and biaxial tests. Tests were performed on three different kinds of ice: snow-ice, columnar ice with optical axis vertical (S1), and columnar ice with optical axis horizontal (S2). In the uniaxial tests, the cylindrical specimens with 0.0254 m diameter and 0.0762 m height were subjected to constant strain rates at different temperatures. The strain rates ranged from 1.8×10^{-8} to 1.8×10^{-7} s^{-1} and the temperatures from -3.2°C to -28.3°C. These strain rates are in the range of those encountered in nature when an ice sheet undergoes thermal expansion. There are few tests cited in the literature for strain rates lower than 5×10^{-7} s^{-1} because these low strain rates require a long test duration and also because the slightest instantaneous temperature variation of the ambient medium will affect the test results. In the case of S2 ice it was concluded that the samples were too small compared to the grain size, so only two tests with larger specimens were reported ($h = 0.1016$ m and $d = 0.0508$ m). The results of a typical test for each kind of ice are shown in Figs. 2.8 to 2.10. It can be seen that in the case of snow-ice and S2 ice the stress reaches a maximum

and remains almost constant while for S1 ice there is a marked decrease in stress after the maximum stress is reached. This rapid decrease is attributed to sudden lateral deformation of these ice samples.

The following rheological model for the uniaxial case was suggested:

$$\frac{d\sigma}{dt} = \dot{\varepsilon}E_a - 2b\beta E_a[(\frac{n_0}{\beta} + \dot{\varepsilon}t) - \frac{\sigma(t)}{E_a}](\frac{\sigma(t)}{2p})^m \qquad (2.9.1)$$

where

σ = stress

$\dot{\varepsilon}$ = strain rate

t = time

E_a = apparent elastic modulus

n_0 = initial number of dislocations

β = rate of multiplication of dislocations

b = length of Berger's vector

p = a function of temperature

m = a constant

As stated by Drouin and Michel, this rheological model is somewhere between the conventional models consisting of Maxwell and Kelvin elements on one hand, and models based entirely on theories of molecular mechanisms on the other. The results of uniaxial tests were used to find the parameters for the rheological model. In order to get a match with the test results, the effect of rigidity of the assembly was considered in the calculations and stress-time curves for ice plus testing machine were calculated. Then by assuming infinite rigidity for the assembly the theoretical curves for ice alone were calculated. The following values were determined from the experiments:

$E_a = 4.52\exp(2060/T)$ kg/cm^2 (snow-ice)

T = absolute temperature K°

$E_a = c\,\dot{\varepsilon}^{0.079}\exp(1335/T)$ kg/cm^2 (S1 ice)

$c = 344\dot{\varepsilon}$ ($\dot{\varepsilon}$ in s^{-1})

m = 4 (snow-ice)

m = 3.7 (S1 ice)

$n_0 = 10^9/cm^2$ (snow-ice)

$n_0 = 5\times10^5/cm^2$ (S1 ice)

$\beta = 10^9/cm^2$

$p = 367\exp(-0.04\theta) = 18\times10^{-3}\exp(2710/T)$

θ = temperature in C°

b = 4.523 A°

The theoretical rheological model for ice alone was used to calculate the stress-time curves for ice subjected to increasing temperature. In these calculations the variation of the coefficient of thermal expansion with temperature was considered. Stress-time curves for different initial temperatures and different rates of temperature increase were drawn. Both linear and sinusoidal temperature variations were considered. In these curves the pressures for temperatures below -30°C were calculated although all the tests were performed above this temperature.

The results of the studies for the uniaxial case were summarized in curves that showed the thermal pressure as a function of ice thickness and duration of temperature increase for different initial temperatures (Fig. 2.11). These curves were calculated for a sinusoidal temperature increase and thicknesses more than 0.4 m. To obtain these curves the ice cover was divided into layers and the rate of temperature change was calculated in each layer. The rheological model was then used to calculate the stress for the strain rate corresponding to each temperature rate.

The biaxial tests were similar to those performed by Lindgren. The ice samples were circular discs 0.05 m in height and 0.15 to 0.30 m in diameter. They were placed in an invar ring which had a very low coefficient of thermal expansion. During the tests the ice temperature was increased from an initial value to 0°C with a constant rate and the thermal pressure was obtained from the measured strain in the ring. Five tests were performed on snow-ice, eight tests on S1 ice, and eight tests on S2 ice. The maximum pressure that would develop in the uniaxial test under the same temperature conditions was calculated. Then the ratio between the maximum measured biaxial pressure and the maximum calculated uniaxial pressure was found. Figure 2.12 shows the stress-time curves corresponding to these cases. For snow-ice, the ratios were from 1.51 to 1.81. The ratios

for S1 ice were in the range 1.0 to 1.97. For S2 ice, due to a lack of results for uniaxial case, the maximum uniaxial pressure for S1 ice was used. The values of these ratios were between 0.83 and 1.16. The apparent Poisson's ratio, ν, was calculated assuming that these ratios were equal to $1/(1-\nu)$.

Drouin and Michel considered the effect of cracks by assuming a certain crack width per length. The amount of temperature increase was then decreased, so that the reduction in thermal deformation would equal the deformation due to the crack opening.

The experiments performed by Drouin and Michel are very valuable in defining a constitutive model and material properties for different kinds of ice at low strain rates. , However, their calculations for predicting the thermal ice pressure, have some weaknesses. The curves for uniaxial stress are based on a thermal analysis for a semi-infinite space with the assumption that the ice surface temperature is equal to the air temperature. Calculations by Bergdahl (1978) and observations by Comfort and Abdelnour, (1993) show that in many cases the ice surface temperature is quite different from the air temperature. Considering the ice sheet as a semi-infinite space might be a good assumption for thick ice plates, but some of the thermal events happen in early winter when the ice sheet is thin, and more accurate thermal analysis is needed for these cases. Solar radiation also has a major effect on ice temperature and cannot be neglected.

The effect of biaxial restraint is poorly handled. Figure 2.12 shows that the maximum pressure in the uniaxial and biaxial cases do not happen at the same time and the ratio between the stresses was not constant during the tests. The ratio $1/(1-\nu)$ is valid for an elastic material, but its use cannot be justified when creep is considered. Defining Poisson's ratio on this basis and using it for predicting the thermal pressure under biaxial restraint is questionable .

2.10 - Jumppanen (1973)

In 1973 Jumpannen used a two dimensional constitutive equation to calculate ice pressure (Jumppanen, 1973). This equation is

$$\varepsilon = J_0 I + \int_0^t [J_1(t-\tau,\theta) I(\dot{\sigma}_x + \dot{\sigma}_y) + J_2(t-\tau,\theta)\dot{S}]d\tau \qquad (2.10.1)$$

where ε and S are strain and stress matrices.

$$\varepsilon = \begin{bmatrix} \varepsilon_x & \frac{1}{2}\gamma \\ \frac{1}{2}\gamma & \varepsilon_y \end{bmatrix} \quad \text{and} \quad S = \begin{bmatrix} \sigma_x & \tau \\ \tau & \sigma_y \end{bmatrix} \qquad (2.10.2)$$

The parameters J_0, J_1, and J_2 are creep functions, I is the identity matrix, τ is a time variable on the interval [0,t], and a superposed dot denotes the derivative with respect to time. Jumppanen stated that a comparison between equation 2.10.1 and the elasticity equation

$$\varepsilon = \frac{\nu}{E} I(\sigma_x + \sigma_y) + \frac{1}{2G} S \qquad (2.10.3)$$

led to the interpretation of J_1 as the time variation of the elasticity modulus ν/E, and correspondingly for J_2 as the time variation of the modulus 1/2G. Equation (2.10.1) was studied for two special cases.

a - One dimensional case, $\sigma_x = \sigma$, $\sigma_y = \tau = 0$

If the first term is omitted, equation (2.10.1) for this case can be written as

$$\varepsilon_x = \int_0^t (J_1 + J_2)\dot{\sigma}d\tau = \int_0^t J(t-\tau,\theta)\dot{\sigma}(\tau)d\tau \qquad (2.10.4)$$

where

$J = J_1 + J_2$.

b - Biaxial hydrostatic, $\sigma_x = \sigma_y = \sigma$, $\tau = 0$

In this case the strains are

$$\varepsilon_x = \varepsilon_y = \int_0^t (2J_1 + J_2)\dot{\sigma}d\tau = [1 - \nu(\theta)]\int_0^t J(t-\tau,\theta)\dot{\sigma}(\tau)d\tau \qquad (2.10.5)$$

The results of 50 creep tests performed in the cold laboratory of the Civil Engineering Department at the Helsinki University of Technology were used to define the creep function J. Two types of fresh water ice were used: columnar grained ice made from tap water, and columnar grained ice taken from the ice cover on the Saima Channel.

The samples were cylinders 0.15 m in height and 0.09 m in diameter. They were tested at -2, -5, -12, and -25°C. The stress levels were 0.29, 0.69, and 1.18 MPa. For experiments at 0.29 and 0.69 MPa, the creep function showed weak nonlinearity and strong nonlinearity at 1.18 MPa. Only the linear case was considered for stresses under 0.69 MPa and the expression for J which gave the best agreement with test results was found to be:

$$J(t,\bar{\theta}) = a(\bar{\theta}) + b(\bar{\theta})t^n \qquad (2.10.6)$$

where

$$a(\bar{\theta}) = (1.17 + 0.36\bar{\theta}) \times 10^{-5} \quad (cm^2/kg) \qquad (2.10.7)$$

$$b(\bar{\theta}) = (24.5 + 0.05\bar{\theta}) \times 10^{-5} \quad (cm^2/kg) \text{ (tap water ice)} \qquad (2.10.8)$$

$$b(\bar{\theta}) = (12 + 0.25\bar{\theta}) \times 10^{-5} \quad (cm^2/kg) \text{ (Saima Channel ice)} \qquad (2.10.9)$$

$n = 0.3$

$\theta_0 = -25°C$, $\bar{\theta} = \theta - \theta_0$, $-25°C \le \theta \le 0°C$

These values were used to calculate the ice pressure for some simple ice pressure problems including a cylindrical water reservoir, a rectangular water reservoir, and a long channel trough. In these calculations Poisson's ratio was taken to be:

$$\nu(\bar{\theta}) = 0.3 + 0.004\bar{\theta} \qquad (2.10.10)$$

The ice pressure at a depth 0.08 m for the Saima Channel was also calculated and compared with the measured stresses.The difference between the measured and calculated stresses was less than 20%. The temperature distribution in the ice cover was not considered and the calculations are valid only for stresses under 0.69 MPa.

2.11 - Metge (1976)

In a Ph.D. thesis submitted to Queen's University, Metge studied the thermal cracks on Lake Ontario near Kingston (Metge, 1976). The field investigation during the winters of 1970, 71, and 72 included ice condition monitoring, ice thickness measurements, temperature gradient measurements, solar radiation and wind velocity recording, recording

of pressure ridge movement, time lapse photography of pressure ridges, seismic recording of ice cracking, and observation of thermal cracks.

The cracks were separated into three different groups and the observations of these cracks were as follows.

1 - Dry cracks

These are the most common cracks that form during cooling periods. These cracks do not usually fill with water because the cracks do not result in complete separation of the ice on either side. Figure 2.13 shows a typical section of a dry crack. The crack is straight down to about two thirds of the ice thickness and is met there by one or two shear cracks, usually at about 45 degrees to vertical. Dry cracks act like a set of bellows, absorbing some of the contraction and expansion of the ice without causing stresses. The width of dry cracks in the Kingston observations ranged from 1 to 20 mm. An estimate of the average crack width was 5 mm. The spacing of the cracks was estimated to be 25 metres.

2 - Narrow wet cracks

With further contraction of the ice cover the sides of a dry crack can separate allowing water to rise in the crack. When the water freezes, seals the crack. Metge indicated that each cooling period opened the crack, which was weak in tension and a layer of ice was added (Fig. 2.14). The thickness of the new ice bridge was large enough to withstand the compression caused by a subsequent warming period. Metge mentioned that in the Kingston area such cracks were extremely rare and numbered only two or three across the wide region studied.

3 - Wide cracks

Metge described that as the amount of contraction increased, the ice had to separate from the land and the total contraction was then absorbed along one or two cracks which usually formed near tensile stress raisers such as between two headlands. It was stated that the overall contraction of the ice sheet was concentrated at these cracks and some had been observed that were more than 200 mm wide. The large volume of water in these cracks could not freeze completely during the night and as a result, by morning a typical wide crack took the shape shown in Fig. 2.15. During the next day, if the ice temperature

rose, the thin bridge of ice across the crack was put in compression and suddenly failed. The closure of these cracks produced a loud noise and a violent impact. Metge indicated that when the crack closed the sides of the crack became out of alignment. One side lifted up while the other side sank under it. This caused the crack to act like an obstacle against snow and this was the initiation a of pressure ridge formation. Metge's observations showed that pressure ridges were usually preceded by wide cracks.

According to Metge's observations, dry cracks are the most important type of crack which should be considered in a thermal analysis, because they are the most common cracks and are active during the thermal events. The narrow wet cracks are very rare and wide cracks appear only at special locations. The impact due to closure of the wide cracks might exert a large force on a structures, but this cannot be considered in a thermal analysis and requires separate study.

2.12 - Bergdahl (1978)

In 1978 Bergdahl submitted a doctoral dissertation on thermal ice pressure to Charmers Institute of Technology in Sweden (Bergdahl, 1977; Bergdahl, 1978, and Bergdahl & Wernersson, 1977). A numerical model was proposed that calculated thermal ice pressure in ice covers. The thermal analysis was done by an implicit finite difference method which took into account solar radiation, latent heat transfer, and heat transferred by conduction and convection. Input included: air temperature, wind speed, cloudiness, air vapor pressure, location of the site and time of the year.

Bergdahl assumed that the ice cover was completely restrained and adopted the following rheological equation for calculating the ice pressure.

$$\alpha \frac{d\theta}{dt} = \frac{d\varepsilon}{dt} = \frac{1}{E}\frac{d\sigma}{dt} + KD\sigma^{n} \qquad (2.12.1)$$

This is the differential equation for a model composed of a linear spring and a non-linear dashpot where

$$E = (1-0.012\theta)6100 \text{ MPa} \qquad (2.12.2)$$

$D = D_0 \exp(-Q_s/RT)$ (2.12.3)

$D_0 = (9.13 \pm 0.57) \times 10^{-4}$ m^2/s

Q_s = the activation energy for self diffusion = 59.8 kJ/mol

R = the universal gas constant = 8.31 J/(mol·K°)

T = the absolute temperature

The values for K and n were chosen based on the experiments by Drouin and Michel (1971) on ice monocrystals loaded parallel to the basal plane. The values used were

$K = 4.40 \times 10^{-16}$ $(m^{-2} Pa^{-n})$ and

$n = 3.651$.

The calculated temperature profile was used to determine the thermal ice pressure for each layer separately. The differential equation (2.12.2) was written in difference form and solved using a special iterative procedure. The pressures were then integrated over the depth of the ice to obtain the total pressure. In order to consider the cracking of ice in tension, the ice pressure was allowed to reach a negative minimum value (the tensile stress had a negative sign), after which the stresses were set to zero. When the temperature started to rise again, the cracks were assumed to be healed completely.

Bergdahl made some comparisons between the calculated ice pressure from the proposed model and ice pressures calculated by other authors or obtained from the experiments. Figure 2.16 shows a comparison between Bergdahl's proposed model and other models. Monfore's corrected curve is obtained by assuming Poisson's ratio equal to 0.36. Figure 2.17 shows the comparison with measured pressures. Bergdahl stated that:

> "The proposed model seems to give an upper bound for the thermal pressure in the plate experiments. In a thick ice cover such high pressure levels could be reached more often, but in a vast ice cover there ought to be factors that limit the pressures."

Bergdahl also made a comparison between different methods for calculating the ice pressure and obtained the maximum ice pressure in two hypothetical conditions. The thickness of the ice cover was 0.45 m and 0.9 m in these cases. The initial air temperature was set to -30°C and made to rise 2.8°C/h to 0°C. No solar energy was absorbed. The proposed model was calculated assuming a clear sky and vapor pressure equal to 80% of

the saturation vapor pressure of the air. Table 2.1 shows the calculated pressures. Bergdahl's equation gives higher values than other methods. Bergdahl concluded that:

"It might be reasonable to reduce values of the highest pressures because in vast covers the conditions may be less favorable for high pressures".

Bergdahl and Wernersson calculated the thermal ice pressure for five Swedish lakes (Bergdahl and Wernersson, 1977). They did statistical studies and gave the expected pressures for return periods of 100, 500, and 1000 years. Results are shown in Table 2.2.

The thermal analysis conducted by Bergdahl included most of the parameters that have an effect on the temperature distribution in an ice cover. However the pressure analysis had some weaknesses. Bergdahl actually performed a uniaxial analysis. He used the method of Drouin and Michel based on estimating the biaxial stress from the stress obtained in uniaxial calculations. As mentioned before, this cannot be considered a proper biaxial analysis. The forces calculated by Bergdahl are very high and this might be due to the choice of the material properties. For example, the value selected for E seems very high considering the low strain rates that occur in thermal events.

2.13 - Cox (1984)

Field measurements of ice pressure were performed by Cox on a small urban lake during February and March 1983, using a newly designed biaxial ice-stress sensor. The objectives of the field program were to obtain field experience in deploying the sensor and some preliminary measurements of thermal ice pressures. In 1984 Cox presented the results of this field measurement program together with the calculation of thermal ice pressure, based on the measured ice temperatures (Cox, 1984). Although the ice sheet was relatively warm and temperature changes were small, stresses up to0.3 MPa were recorded. The peak stresses were about 0.21 MPa in compression and 0.31 MPa in tension in one direction and about 0.14 MPa in compression and 0.24 MPa in tension in the other direction.

Ice pressures were first calculated using Bergdahl's rheological model, with the measured temperature history at the depth of the sensing portion of the gauge. The model was modified to allow tensile stress to accumulate in the ice cover during cooling periods without any ice cracking. It was observed that Bergdahl's model over predicted compressive and tensile stresses in the ice.

Cox concluded that this over-prediction was due to Bergdahl's values for E, K, and D. As stated by Cox, for the low strain rates typical of thermal expansion, the effective modulus of ice was expected to be lower than 6000 MPa. Also above -10°C, a plot of $\ln(\varepsilon)$ versus 1/T was strongly non-linear and the creep activation energy, Q_c, was not constant. Therefore, the product, KD, in Bergdahl's model needed to be re-evaluated for ice thermal expansion problems. Cox suggested that a modulus of 4000 MPa might be more appropriate and defined a new function A(T) to account for the temperature dependence of the creep rate:

$$\dot{\varepsilon} = \frac{\dot{\sigma}}{E} + A(T)\left(\frac{\sigma}{\sigma^*}\right)^n \qquad (2.13.1)$$

where

σ^* = a unit stress

$$A(T) = \frac{\dot{\varepsilon}}{(\sigma_{max} / \sigma^*)^n}$$ in a constant strain-rate test, or

$$A(T) = \frac{\dot{\varepsilon}_{min}}{(\sigma / \sigma^*)^n}$$ in a constant load test.

The values of σ_{max} from the curves presented by Drouin and Michel for a strain rate of 2×10^{-8} s^{-1} were used to obtain A(T), and ln[A(T)] was plotted against ln(T). In order to obtain a linear fit it was assumed that the 0°C tests were performed at -1°C. By adjusting the data the following relationship was obtained:

$$A(T) = B\left(\frac{T}{T^*}\right)^m \qquad (2.13.2)$$

where

T^* = a unit temperature

$B = 2.46\times10^{-29}$ s^{-1}

m = 1.92

Cox compared the pressures predicted by the suggested model with the measured stresses and the stresses calculated by Bergdahl. The pressures predicted by Cox were in good agreement with the measured stresses. Bergdahl's values were high in both compression and tension. Cox made the calculations using the measured temperature at a single depth and did not analyze the whole ice cover. Biaxial restraint was not considered in the analysis.

2.14 - Sanderson (1984)

At the seventh I.A.H.R. International Symposium on Ice, in 1984, Sanderson presented a paper on thermal ice forces against isolated structures (Sanderson, 1984). It was noted that depending on the boundary conditions two distinct types of thermal force might develop. In reservoirs and rivers, where the ice is confined in a limited space thermal stresses develop which may lead to loads of 200 to 600 kN/m across a structure. In the seas where the ice is free to expand, thermal ice velocities occur. In the case of an offshore isolated structure, as the ice expands it moves past the structure, and forces can be calculated by solving the indentation problem. These forces typically amount to 2000 kN/m for a wide structure.

After a review of the previous methods for calculating the pressure in the case of restricted expansion, a method was suggested for determining the velocity in free expansion conditions. It was noted that thin ice covers would expand directly in response to any temperature change while a thick ice cover would consist of two coupled layers, one active and one passive, which expand at a slower net rate. For an ice cover many times thicker than the active surface layer, the following steps were suggested for calculating the strain rate: 1) calculate the thermal stress in the active layer with the assumption of total restraint, 2) distribute the stress over the total thickness, 3) calculate gross strain rate due to the distributed stress.

In a part of this paper the propagation of thermal waves in ice covers was studied. According to Sanderson, in many conditions, the temperature distribution in ice cover is dominated by surface temperature changes and can be obtained by heat conduction analysis with negligible convection. It was noted that any periodic surface temperature history could be represented by a Fourier series of sinusoidal terms and each temperature wave became attenuated with depth according to:

$$\exp[-y(\omega/2a_d)^{1/2}] \qquad (2.14.1)$$

where

a_d = thermal diffusivity of ice

ω = angular frequency

y = depth

Assuming $a_d = 1.15\times10^{-6}$ m^2/s for pure ice, the depth y_0, at which the temperature wave is attenuated to 1/e of its surface amplitude could be calculated for different ω.

$$y_0 = (2k/\omega)^{1/2} \qquad (2.14.2)$$

This was called the "skin depth", which is tabulated in Table 2.3.

Sanderson also calculated the wave frequency which caused the maximum rate of temperature change, $d\theta/dt$, at a given depth.

$$\omega = 8k/y^2 \qquad (2.14.3)$$

The dominant period which gives the maximum rate of change of temperature at a particular depth is shown in Table 2.4. As stated by Sanderson:

> "The important temperature cycles of period one day or less dominate only at depths less than 0.36 m".

This means that for thin ice sheets daily temperature changes should be considered for calculating the maximum pressure and for thicker ice sheets longer periods should be taken into account. It also means that for thin ice covers the whole thickness is affected by the daily temperature changes and the total force will increase rapidly with increasing thickness. But for thick ice covers only the upper part will be active and the total force will not change very much with increasing thickness, unless the period of temperature change is more than one day.

2.15 - Bomeng (1986)

Xu Bomeng from the People's Republic of China suggested the following equation for ice pressure which was obtained using data from several reservoirs in the northeast of China (Bomeng, 1986).

$$p = KK_sC_h(3-t_a)^{1/2}(\Delta\theta_a)^{1/3}(t^{0.26}-0.6)/(-\theta_a^{3/4}) \qquad (2.15.1)$$

where

p = average pressure of ice sheet, kg/cm^2

K_s = factor for snow cover (for no snow K_s=1.0).

C_h = conversion factor related to thickness of ice cover, as shown in Table 2.5.

θ_a = initial air temperature at 8 a.m. (C^o), usually not higher than -10°C

$\Delta\theta_a$ = increment in air temperature (C^o) from 8 a.m. to 2 p.m., or from 8 a.m. of the first day to 2 p.m. of the second day or third day for sustained temperature increases; the highest air temperature should not , however exceed 0°C.

t = duration of sustained temperature increase (h), corresponding to $\Delta\theta_a$.

t = 6 hours for daily changes.

t=30 hours for successive days of air temperature increase (two days).

K = coefficient to account for overall effects of other factors.

In order to simplify the calculations, some of the parameters in equation 2.15.1 were determined based on the data of field observation. It was argued that for thin ice sheets the maximum pressure could be reached in a single day but for ice sheets thicker than 0.5 m longer duration of temperature increase , up to two or three days should be taken into account. Therefore, for ice of less than 0.5 m thickness the duration was taken to be six hours. For thicker ice sheets, the duration was 30 hours. From observations, initial air temperature and temperature rise were taken -15°C and 15°C respectively. Finally, assuming no snow on the surface of the ice sheet, the ice pressure predicted by equation 2.15.1 would depend on the thickness of the ice sheet.

$$P = 13.73hKC_hm_t \qquad (2.15.2)$$

where

P = ice thrust (tonnes/m)

m_t = time factor of temperature rise (1.0 or 1.82)

The magnitude of K is affected primarily by the surface area of the reservoir and the conditions of the restraint against expansion, and lies between 3.5 and 5.0. In Fig. 2.18 ice thrust according to equation 2.15.2 is plotted versus thickness for different values of K. The maximum thrusts measured at nine reservoirs are also marked in this figure.

Equation 2.15.1 includes most of the important factors that affect the thermal pressure, but since it is based on data fitting, it cannot be used freely for other places. It is not possible to judge equation 2.15.2 on the basis of the Fig. 2.18. The measured thrusts cover a wide range and it is difficult to express them as a function of thickness.

2.16 - Yamaoka, Fujita, and Hasegawa (1988)

At the ninth I.A.H.R. International Symposium on Ice in 1988, Yamaoka, Fujita and Hasegawa from Japan presented the results of measured and calculated thermal ice thrusts at the Taisetsu Dam. The thickness of ice cover was about 0.4 m at the time of the measurements. The site where the measurements were done was almost free from snow. A summary of the results is presented in Table 2.6. It was observed that no thermal pressure was recorded below a depth of 0.175 m. Therefore the effective ice thickness was considered as 0.175 m.

The coordinate system in Fig. 2.19 was used in the calculation of the thermal stress under three different boundary conditions.

Case (1):

$$\sigma_1(z) = f(\alpha\theta) \qquad (2.16.1)$$

$\delta = 0$ at $x = \pm 1$

$M = 0$ at $z = \pm a/2$

where

α = the coefficient of thermal expansion

θ = ice temperature

δ = horizontal displacement

M = in-plane displacement by thermal bending

Case(2):

$$\sigma_2(z) = \sigma_1(z) + \frac{1}{a}\int_{-a/2}^{a/2}\sigma_1 dz \qquad (2.16.2)$$

δ = free at $x = \pm 1$

$M = 0$ at $z = \pm a/2$

Case(3):

$$\sigma_3(z) = \sigma_1(z) + \frac{1}{a}\int_{-a/2}^{a/2}\sigma_1 dz + \frac{12z}{a^3}\int_{-a/2}^{a/2}\sigma_1 z dz \qquad (2.16.3)$$

δ = free at $x = \pm 1$

M = free at $z = \pm a/2$

For the constitutive relationship a rheological model consisting of a Maxwell unit and a Kelvin unit in series was used. The rheological equation for this model is:

$$\frac{d^2\varepsilon}{dt^2} + \frac{E_v d\varepsilon}{\eta_v dt} = \frac{1}{E_m}\frac{d^2\sigma}{dt^2} + \left(\frac{1}{\eta_v} + \frac{1}{\eta_m} + \frac{E_v}{\eta_v E_m}\right)\frac{d\sigma}{dt} + \frac{E_v}{\eta_v \eta_m}\sigma \qquad (2.16.4)$$

where E and η are rheological coefficients. These coefficients were estimated by curve fitting Lindgren's experimental data. The values obtained are:

$E_m = 8584$ MPa

$\eta_m = 6.60\times10^7$ MPa.s

$E_v = 5347$ MPa

$\eta_v = 6.43\times10^6$ MPa.s .

The temperature distribution in the ice cover was calculated using the thermal diffusion equation,

$$\frac{\partial\theta}{\partial t} = a_d \frac{\partial^2\theta}{\partial z^2} \qquad (2.16.5)$$

where

a_d = the thermal diffusivity of ice = 1.15×10^{-2} cm^2/s

The boundary conditions used in conjunction with equation 2.16.5 were

$\theta(a/2,t) = A\cos\omega(t+4\times3600)+B$

$\theta(-a/2,t) = 0$

$\theta(z,0) = 0$

$\omega = 2\pi/(24\times3600)$ 1/s

$A = -5°C$

$B = -12°C$

$a = 0.5$ m

The maximum values calculated for σ_1, σ_2, and σ_3 at 0.08 m depth were about 0.44, 0.25, and 0.04 MPa, respectively. The calculations predicted maximum pressures at the ice surface whereas the measurements showed the highest pressures at 0.085 m. It was argued that this difference was due to thermal cracks at the ice surface.

The method suggested by Yamaoka et al. has the advantage that it considers the bending and expansion of the ice cover, when the ice sheet is not completely restrained and is free to rotate or expand. The bending stress (the third term in equation 2.16.3), however, is obtained according to elastic theory even though it is not consistent with the behavior of ice. The effects of lateral deformation, underlying water, and change in ice properties with respect to temperature are not considered in the calculations.

2.17 - Xian-Zhi (1988)

At the ninth I.H.A.R. International Symposium on Ice in 1988, Xian-Zhi from China presented measured ice pressures from several reservoirs in China along with some observations regarding the thermal ice pressure. The maximum ice pressures observed in the reservoirs are given in Table 2.7.

The measured temperatures showed that the effect of periodic change of surface temperature gradually weakened with increasing depth and there was negligible effect below a depth of 0.6-0.7 m. It was observed that the destructive action of the ice cover on the revetments occurred mainly in either early or late winter. Xian-Zhi explained that in early winter, the ice cover was thin and its temperature changed rapidly. Therefore if

the integrity of the revetment was poor (such as loose-stone laid revetments) it could easily be pushed by the ice body. In late winter the ice cover reached its maximum thickness and when the temperature increased the total ice pressure was large. Xian-Zhi cited the case of the Baiquan Reservoir where, on March 31, 1974 a large area of the revetment slid 0.18 m upwards. The ice thickness was 1.2 m at the time.

The measured pressures showed that when other conditions remained the same, a higher rate of temperature increase caused a higher ice pressure. It was also found that for the same temperature increase rate, a lower initial temperature resulted in greater ice pressure. This might be due to the fact that the value of modulus of elasticity is higher at lower temperatures. Observations indicated that at a depth of 0.1-0.3 m, the ice pressure was a maximum, and it was zero on the surface and at the bottom of the ice cover.

2.18 - Tunik (1988)

In 1988, Tunik from Finland presented a paper about the design ice forces on offshore installations (Tunik, 1988). In a part of this paper an equation was suggested for calculating static forces due to the thermal expansion of ice covers. It was assumed that the pressure varied linearly from a maximum value, p_t, at the ice surface to zero at a depth h_t. Thus the maximum force could be expressed as:

$$F_t = 0.5 p_t B h_t \qquad (2.18.1)$$

where B is the width of the structure. The maximum thermal pressure was obtained from Peschansky's equation (Peschansky, 1971), which was written in a simplified form as:

$$P_t = K(0.0089\text{-}0.0204\ s/t)(\Delta t+1)^2(\tau_0)^{1/3} \qquad (2.18.2)$$

where

s = salinity (parts/thousand)

t = ice surface temperature at the end of the temperature change period (in C^o with positive sign).

τ_0 = period of time during which temperature had changed in hours; equation 2.18 is applicable for τ_0 from several hours to 2-3 days.

K = 1 for saline ice when temperature increases and for fresh water ice

K = -1 for saline ice when temperature decreases (saline ice expands when temperature decreases).

The depth of thermally stressed ice, h_t, was obtained from Sanderson's "skin depth" (the depth at which temperature is attenuated to 1/e of its surface magnitude; Sanderson, 1984), with some modifications (Figure 2.20). It was estimated using the formula:

$$h_t = 0.14\ln 0.6(\tau_0+4) \qquad (2.18.3)$$

It was assumed that the skin depth is the depth at which the stress is zero, but according to Sanderson at this depth the temperature is about half of its surface magnitude, and it is not zero.

2.19 - Ivchenko (1990)

At the I.A.H.R. International Symposium on Ice in 1990, Ivchenko from the USSR presented an analytical method for calculating thermal ice pressure (Ivchenko, 1990). The procedure was based on a rheological model consisting of a Maxwell unit in series with a Kelvin-Voigt unit. It was assumed the ice cover is divided into a number horizontal layers, the stress in each layer is independent from the stress in other layers, the layers are completely restrained in the horizontal direction, and the temperature change is uniform within a layer.

The equation for the rheological model is given in the form:

$$\dot{d}_+ = \frac{1}{9\ell}\dot{S}_1\delta + \frac{\dot{S}S^{m-1}m}{2\mu_M} + \frac{S^n}{2\eta_M} + \frac{S^k}{2\eta_k} - \frac{\mu_k}{2\eta_k^2}\exp[-\frac{\mu_k}{\eta_k}(t-t_0)]\int_{t_0}^{t} S^k \exp(\frac{\mu_k}{\eta_k}t)dt \,. \qquad (2.19.1)$$

The symbols in equation 2.19.1 are not defined in the paper, except for d which is mentioned to be the "complete relative strain". Assuming that S denotes the stress, it seem that the first term is for elastic deformation, the second to fourth terms for viscous deformation and the last term for the delayed elastic deformation. Then it is assumed that the state of stress is uniform at each point so that

$$\sigma_i = \sigma_j = \sigma\,, \qquad \sigma_k = 0\,, \qquad (2.19.2)$$

$$d_{-i} = d_{-j} = d_{-} = \alpha(\theta - \theta_0)(1 - \nu_1) - \frac{\sigma}{\mu_m}(\nu_1 - \nu_2) \qquad (2.19.3)$$

where

α = coefficient of thermal expansion

θ = temperature of the layer under consideration

θ_0 = initial temperature

σ = normal stress

ν_1 = coefficient of viscous diametrical restraint

ν_2 = coefficient of the elastic diametrical restraint.

Assuming that the rheological model consists of linear elements and the strain in the Kelvin unit is equal to zero the final differential equation for the stress is given by:

$$\ddot{\sigma}\left[\frac{1}{6\mu_m} + \frac{2}{27\ell} + \frac{\nu_1 - \nu_2}{\mu_m}\right] + \dot{\sigma}\left[\frac{\mu_k}{6\mu_m\eta_k} + \frac{1}{6\eta_m} + \frac{1}{6\eta_k} + \frac{2\mu_k}{27\ell\eta_k} + \frac{\mu_k(\nu_1 - \nu_2)}{\mu_m\eta_k}\right] +$$

$$\sigma\frac{\mu_k}{6\eta_m\eta_k} = -\alpha(1+\nu)(\ddot{\theta} + \dot{\theta}\frac{\mu_k}{\eta_k}). \qquad (2.19.4)$$

Equation (2.19.4) is a function of stress only, and can be solved for a given temperature function. The thermal line load is obtained by integrating 2.19.4 over the thickness of the ice cover. A comparison was made between the predicted stresses and the stresses measured in an outdoor basin with diameter of 1.8 m and at Lake Baikal. There was good agreement between the measured and predicted stresses.

Since the symbols are not defined, it is difficult to assess equation 2.19.4. The material properties used in obtaining the solution are important but are not mentioned in the paper.

2.20 - Li, Zhang, and Shen (1991)

In a paper presented at the 10th International Conference on Offshore Mechanics and Arctic engineering in 1991, Li et al. described the results of an experimental study on thermal ice pressure (Li, Zhang, and Shen, 1991). The tests were performed in a

controlled cold-room, where an ice cover was grown inside a cylindrical tank. The process attempted to simulate ice growth in natural conditions. The ice type grown in the tank was columnar S2 ice.

In the experiments, the ice cover was subjected to a linear increase in air temperature. The temperature and stress distributions in the ice were studied for different initial values of air temperature and different rates and duration of temperature increase. The durations of temperature increase varied from 12 to 15 hours, the initial temperatures were -5, -10, and -20°C, and the temperature increase rates were less than 1°C/h.

It was concluded from the tests that there was a transition depth in the ice cover. Above this transition depth the ice temperature was controlled by the air temperature and a large thermal pressure was produced. Below this depth the temperature changes and the pressure were very small and could be neglected. The transition depth was reported to be 0.3 m according to the tests. An empirical relationship was suggested for the ice temperature above the transition depth, as a function of air temperature, and transition depth. It was observed that the ice pressure increased with decreasing initial temperature, increasing the temperature rate, and increasing the duration.

The thickness of the ice cover were not reported, and the effects of the thickness on the temperatures and stresses was not studied. It seems that the tests were performed only on thick ice sheets where the effect of the bottom boundary could be neglected. In the thin ice sheets the bottom boundary affects both the temperatures and stresses.

The effect of the duration of temperature increase on the transition depth was not considered, and the transition depth was reported as a constant value. The durations of temperature increase in the tests were less that 15 hours which corresponds to a daily temperature increase. With this duration the active zone as far as temperature change is concerned is usually down to a depth of 0.3 m to 0.4 m. Normal weather fluctuations can give longer periods of temperature increase, for example 20 to 30 hours. In this case the temperature change and the thermal stresses might occur to a larger depth. Therefore the transition depth is not constant and depends on the duration of temperature increase.

2.21 - Comfort, Abdelnour, and Gong (1993-94)

In order to improve the understanding of ice loads on hydro-electric structures, a series of field measurements and large scale tests were sponsored by Canadian Electricity Association (CEA). The tests were conducted on their behalf by Fleet Technology Ltd. Field data were collected at Hydro Quebec's Paugan dam on the Gatineau River at Low, Quebec and Ontario Hydro's dam at Arnprior, Ontario, during the winters of 1991-92 to 1993-94. The large scale tests were conducted at a 120 m by 60 m outdoor basin at the National Research Council (NRC) in Ottawa. The objective in all these tests was to measure both thermal loads and loads due to water level changes. The data collected included temperature and stress histories, ice and snow cover thickness, and meteorological data. The results were reported in three phases. Only those for the first two phases (Comfort and Abdelnour, 1993; Comfort, Abdelnour, and Gong, 1994), which correspond to the winters of 1991-92 and 1992-93 were used in this study to assess the numerical model, as the report for 1993-94 winter was not available. The details of the measurements are described in Chapter 5, and only the general results will be discussed here.

Arnprior Dam - winter 1992-93

At the Arnprior dam the temperatures and the stresses were measured at a location close to the vertical concrete face of the dam. In early winter the ice was continuously broken by the water level changes. The loads in January were very low (less than 10 kN/m), because the ice cover was not well bonded to the dam. When the ice cover became thicker, a crack that absorbed the rotations of the ice cover due to water level fluctuations, formed 10 m from the dam. Subsequently the ice sheet became well bonded to the dam. The highest loads measured during the whole program occurred at the Arnprior Dam in February. The peak line load was 156 kN/m which was due to the combination of temperature increase and water level changes.

Paugan Dam - winter 1991-92 and 1992-93

During the 1991-92 winter the temperatures and the stresses were measured at four locations: near the gates and piers of the spillway, 30 m from the gates, near the vertical

face of the dam and nearby rock face, and 30 m away from the vertical face of the dam. During the 1992-93 winter the stresses were measured near the gates and piers and 30 m away from them. The daily water level changes at the Paugan Dam were relatively small (less than 5 cm). The loads at the locations away from the structures were mainly thermally induced, but in the vicinity of the structures the loads were affected by the water level changes. The loads and the stresses measured during the 1992-93 winter were much less than those recorded during the 1991-92 winter. The measured stresses during the 1991-92 winter were considered less reliable by Comfort et al. because the thermal events happened shortly after the installation of the stress sensors and were affected by freeze-in stresses. In the winter of 1992-93 the highest line loads over the full width of the pier and gate were 122 kN/m and 22 kN/m, respectively. Away from the gates and piers the maximum line load was 52 kN/m. In early winter, when relatively large loads occurred, the loads on the pier were typically two to five times higher than those on the gate. Later, the difference reduced and in February the loads on the gate and the pier were similar. This was attributed to the higher temperatures which caused more stress redistribution by creep. The average line load over the total width of the pier and gate was also calculated and compared to the line load at far field. The far field line loads tracked the average line load with a difference of about 10% in magnitude. It was concluded that the load "seen" by dam was similar to that produced in the reservoir ice sheet away from the dam.

Comfort et al. categorized the thermal events into two groups: "early season", and "late season". In the early season events the ice is thin and cold and there is little snow cover. During these events the ice surface temperature changes greatly and rapidly, while the temperature change inside the ice sheet is relatively small. Therefore this type of event produces high stresses in the upper parts of the ice sheet. In the late season events the ice is thicker and warmer, and there is usually more snow cover on the ice sheet. The temperature change happens at a smaller rate over almost the full thickness of the ice cover. The late season events produce more load per-unit temperature rise.

In order to predict the ice load on the Paugan Dam gates and piers, a two dimensional plane stress finite element analysis was carried out. The analysis was performed by Selvadurai and Associates Inc. (1992), and submitted to Fleet Technology Ltd. The

constitutive law was a two dimensional generalization of the rheological model suggested by Bergdahl (1978). The mechanical properties suggested by Bergdahl were also used in the stress analysis. In the cooling periods when the stresses exceeded the tensile strength of the ice (0.5 MPa), it was assumed that the ice cracked and the cracks refroze due to the influx of water. An additional pressure due to refreezing was applied by considering prescribed displacements. A part of the ice cover in front of the gates and spillways was modeled in the finite element mesh. In order to consider the flexibility of the gates, the gate structure was modeled as a beam of variable but finite flexibility. The stiffness of the beam was included in the global stiffness matrix.

The finite element model which was based on a two dimensional element could not capture the three dimensional behavior including the bending of the ice cover. Only an average temperature was used for the whole thickness of the ice sheet and the temperature variation through the thickness of the ice cover was not considered. The assumption that all the cracks refreeze is not valid. Most of the cracks in an ice sheet are dry and open or close with temperature changes. Comfort et al. also discussed a number of anomalies in the results of the numerical analysis. It was stated that the model predicted significant tensile stresses in the cooling periods whereas the measured stresses were mainly compressive. Also the model predicted higher stresses on a flexible gate than a rigid one.

NRC Basin Test - winter 1992-93

In the first part of the program the water level was kept constant in the basin and the stresses due to temperature changes were recorded. In the second part of the program, which started on January 25, the stresses due to water level changes were studied. The thermal events were grouped into early season and late season events. The highest line load was 51 kN/m which occurred in late December during an early season event. The data collected in the second part were also affected by the temperature changes. It was stated that the component of the load which corresponded to the water level changes increased with the rate of change and total displacement.

The data collected by Fleet Technology Ltd. is a valuable set of data that provides useful information about the different mechanisms that affect the ice load on hydraulic structures.

2.22 - Noponen and Maattanen (1994)

At the I.A.H.R. 12th International Symposium on Ice, Noponen and Maattanen presented a paper on thermal ice loads against isolated structures (Noponen and Maattanen, 1994). An isolated structure is a structure in the interior of the ice cover, which is surrounded by the ice. This term is usually used for offshore structures. The main part of this paper concerned the calculation of the ice velocity due to temperature changes. A summary of this part is discussed here.

It was assumed that the ice surface temperature increases linearly with time until it reaches 0°C and remains constant at that level. The equation of thermal diffusion was then solved analytically using a Fourier series approach. Knowing the temperature distribution through the thickness, two methods were suggested for calculating the global strain rate. In the first method, which was called the elastic model, the global strain rate was obtained as a weighted average strain rate of the cross-section of the ice cover. In the second method, which was called the creeping model, the effect of elastic and viscous deformation was also considered in calculating the global strain rate. The suggested equation was based on a rheological model consisting of a linear spring in series with a non-linear dashpot. The global strain rate was given as the sum of the strain rate due to temperature changes, the elastic strain rate, and the viscous strain rate. The ice cover was divided into ten layers and it was assumed that the sum of the stresses in the cross section was equal to zero. The differential equation was solved by the finite difference method. Then the uniaxial velocity was obtained as the product of the global strain rate and length of the ice cover.

It was stated that the velocity was also affected by the biaxial restraint and boundary conditions. In order to consider those effects a "boundary condition coefficient" was introduced. The two dimensional ice velocity was given as the product of the boundary condition coefficient and the one dimensional velocity. The boundary condition coefficient was obtained from an elastic finite element analysis for different boundary conditions and

different aspect ratios of the ice field (Fig. 2.21). It was assumed that the ice field is free to expand towards the water.

Although there was an effort to consider the three dimensional behavior of the ice cover, this was poorly handled. With the assumption of free expansion on one boundary, the geometry of the ice cover and the boundary conditions on the rest of the boundary have a significant effect on the stresses. The creep of ice and the underlying water also have significant effects which cannot be ignored. Since the stresses also affect the strain rates all of these factors should be considered simultaneously. The effect of boundary conditions and biaxial restraint cannot be introduced simply with a coefficient from elastic analysis.

2.23 - Summary and Conclusion

This review of previous research shows that interest and concern regarding thermal ice pressures has existed in many northern countries for a long time. Numerous investigators in cold regions have tried a variety of methods to estimate ice pressures. These methods have been based on laboratory tests, field measurements, empirical relationships, and analytical or numerical calculations. Most methods for determining ice pressure consist of the following steps.

1) Assume a temperature rate: In early investigations the temperature variation through the thickness of the ice cover was neglected and only a single temperature rate was considered in the analysis. In some studies the measured temperature profiles were used. Subsequent investigators performed a thermal analysis and calculated the temperature profile in the ice cover.
2) Divide the ice sheet into a number of layers.
3) Assume a complete restraint and obtain the strain rate from product of the coefficient of thermal expansion and the temperature rate.
4) Adopt a constitutive model for ice: In early studies empirical stress-strain relationships based on curves obtained from lab experiments were used. Later,

uniaxial rheological models consisting of a Maxwell unit or Maxwell and Kelvin-Voigt units were adopted by most investigators. The rheological models were calibrated using experimental data.

5) Obtain the stress at each layer: Using the constitutive model the stress in each layer was obtained from the strain rate.
6) Calculate the force per unit length: The force per unit length was calculated by integrating the stresses through the thickness.
7) Estimate the stress under biaxial restraint: The stress under biaxial restraint was estimated using the elastic theory and Poisson's ratio or by comparing the biaxial and uniaxial test results.

The development of methods for determining thermal ice pressures have occurred concurrently with the development of better constitutive models for ice. Most of the past research, however is based on uniaxial constitutive laws and there are a number of factors which are not considered in the previous studies. The most important factor is the three dimensional behavior of the ice cover. The temperature distribution through the thickness of the ice cover is non-uniform. In the conditions of total restraint where the interaction between the layers can be neglected, the stress in each layer is affected by the temperature changes of that layer and the biaxial restraint in the horizontal plane. Due to three dimensional creep of ice, the ratio between the stresses in uniaxial and biaxial constraint, is not constant and cannot be obtained from the elastic theory using Poisson's ratio. The stresses are also affected by the tensile cracking during the cooling periods.

When an ice cover is free to expand along one shore, the lower layers, which undergo smaller temperature changes, resist the expansion of the upper layers. Therefore the interaction between the layers should also be considered in the analysis. In this case the underlying water, the boundary conditions (the shore type or flexible structure), and geometry of the reservoir can all have a significant effect on the stresses. Due to the nonlinear behavior the effect of the bending and membrane stresses are coupled and cannot be considered separately. Due to free expansion, the lower layers undergo tensile stresses and tensile cracking affects both the stresses and the resultant forces.

The past research has been exclusively concerned with wide structures and fully constrained ice sheets. Investigations dealing with free expansion have focused on offshore structures and sea ice. This case can be dealt with as an indentation problem where an indentor moves towards the ice sheet with a prescribed velocity. There have been no investigations on thermal expansion in reservoirs where the ice cover is free to expand on a part of the boundary. While the free expansion might reduce the load on a wide structure, it may increase the load on an isolated structure like a water intake. In this case the load on the isolated structure might be higher than the load on a wide structure but not as high as the load exerted on an offshore structure. Factors such as the effect of the underlying water, bending of the ice cover, geometry of the reservoir, flexibility of the resisting structure and shore-line features are also not considered in the past research. Even in the case of fully constrained ice sheets, the effect of biaxial restraint and tensile cracking is either not considered or poorly handled. Although the development of three dimensional constitutive models has made it possible to use the finite element method to analyze the ice sheets, there is only one case in the literature where the finite element method was used to obtain thermal ice pressures. In that case, however, a plane stress element with a single temperature rate was used and the temperature distribution through the thickness and bending deformation were not considered.

The purpose of this study was to develop an improved analytical capability for predicting the ice forces; a model that could consider all of the above mentioned factors and could be used for both fully constrained and free expansion conditions. Such a model makes it possible to study and assess the importance of the different factors that affect the stresses in an ice sheet.

		Line load (kN/m)	
Method	Origin	h=0.45 m	h=0.9 m
Rose (1947)	Drouin (1970)	47	86
Monfore (1954)	Drouin (1970)	222	232
SN 76-59 (1959)	Drouin (1970)	128	255
Drouin & Michel (1971) - S1 ice	Kjeldgaard (1977)	330	390
Drouin & Michel (1971) - Snow-ice	Kjeldgaard (1977)	220	270
SN 76-66, wind speed = 0 m/s	Kjeldgaard (1977)	30	60
SN 76-66, wind speed = 5 m/s	Kjeldgaard (1977)	310	440
SN 76-66, wind speed = 20 m/s	Kjeldgaard (1977)	410	580
Bergdahl, wind speed = 0 m/s	Bergdahl (1978)	459	752
Bergdahl, wind speed = 5 m/s	Bergdahl (1978)	502	830
Bergdahl, wind speed = 20 m/s	Bergdahl (1978)	531	829

Table 2.1. - Ice pressure for ice covers of two thicknesses for the hypothetical conditions stated in the text. A comparison between different methods (reproduced from Bergdahl, 1978).

		Return Period (years)		
Lake		100	500	1000
Torn träsk	(64.3°N 19.5°E)	507	550	569
Stora Bygdträsket	(68.3°N 20.5°E)	453	532	568
Runn	(60.6°N 15.6°E)	410	475	500
Glan	(58.6°N 16.0°E)	419	507	543
Vidöstern	(57.1°N 14.0°E)	330	380	400

Table 2.2. - Expected thermal ice load in kN/m for some return periods of annual maxima (reproduced from Bergdahl, 1978).

Period	ω (rad/s)	Skin depth (m)
1 hour	1.7×10^{-3}	0.04
2 hours	8.7×10^{-4}	0.05
6 hours	2.9×10^{-4}	0.09
12 hours	1.5×10^{-4}	0.13
24 hours	7.3×10^{-5}	0.18
7 days	1.0×10^{-5}	0.47
14 days	5.2×10^{-6}	0.67
30 days	2.4×10^{-6}	0.97
1 year	2.0×10^{-7}	3.40

Table 2.3 - Depth of penetration of surface temperature waves through an ice cover. The "skin depth" (depth at which the wave is attenuated to 1/e of its surface amplitude) is shown as a function of wave period and frequency ω (reproduced from Sanderson, 1984).

Depth (m)	Dominant period
0.1	1.9 hours
0.2	7.6 hours
0.3	17 hours
0.4	30 hours
0.5	2 days
1.0	8 days
2.0	30 days

Table 2.4 - Period of surface temperature wave which at a particular depth gives rise to maximum rate of change of temperature. All waves are assumed to have the same amplitude (reproduced from Sanderson, 1984).

Ice thickness (m)	C_h
0.4	0.391
0.6	0.311
0.8	0.274
1.0	0.252
1.2	0.237

Table 2.5 - Values of C_h at equation 2.15.1 (Xu Bomeng, 1986).

	Temperature (C°)			Measured stress (MPa)			Stress over .175m	
Date (1977)	at 6:00	at 14:00	rate (C°/h)	at 0.035 m	at 0.085 m	at 0.125 m	average (MPa)	total (kN/m)
Feb. 14	-15.5	-9.5	4.7	0.45	0.46	0.14	0.30	52.7
Feb. 15	-16.5	-9.0	5.9	0.45	0.47	0.16	0.28	49.5
Feb. 16	-15.0	-8.5	6.2	0.36	0.39	0.14	0.25	43.1
Feb. 17	-16.5	-9.5	6.8	0.0	0.53	0.21	0.32	56.3

Table 2.6 - Daily ice temperature and pressure at Taisetsu dam reservoir.

			Ice Pressure		
Name of reservoir	Date	Thickness of ice (m)	Mean (MPa)	Max (MPa)	Total (kN/m)
Sifengshan	Nov. 30, 1963	0.36	0.177	0.245	
Taipingchi	Feb. 15, 1974		0.455	0.785	219.7
Yinhi	Mar. 17, 1978			0.206	226.6
Yadian	Feb. 9, 1980		0.138		35.3
Yuejin	Nov. 28, 1980	0.38		0.177	
Shengli	Dec. 2, 1982	0.36	0.196	0.392	141.3
Erado	Jan. 16, 1986			0.319	269.4

Table 2.7 - Major ice pressure events that have been recorded in China.

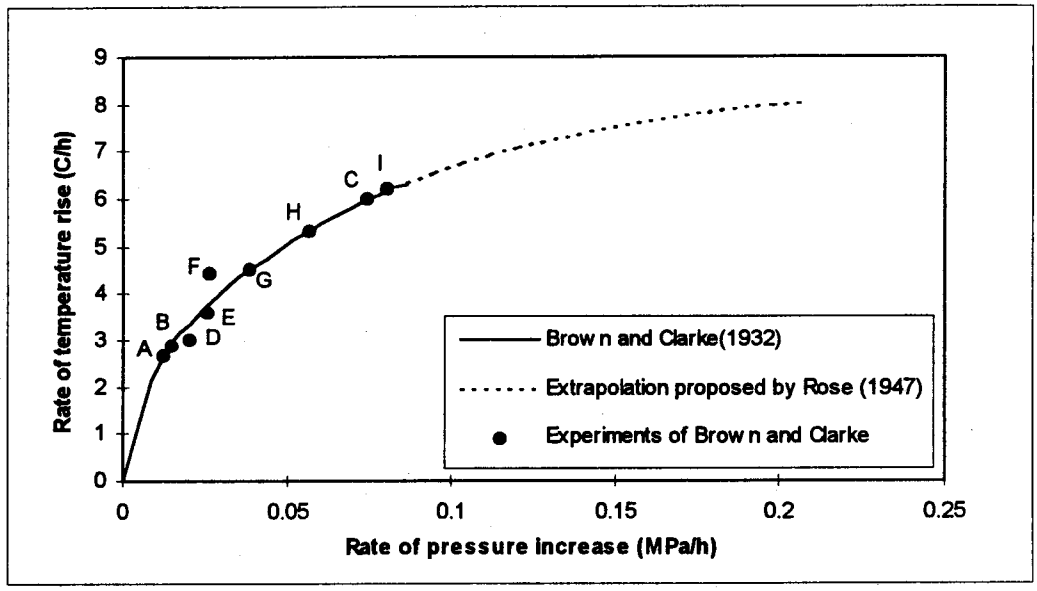

Figure 2.1 - Rate of pressure increase versus rate of temperature rise (reproduced from Bergdahl, 1978).

Filled circles: A-C original points, D-I from shorter parts of the same two experiments.

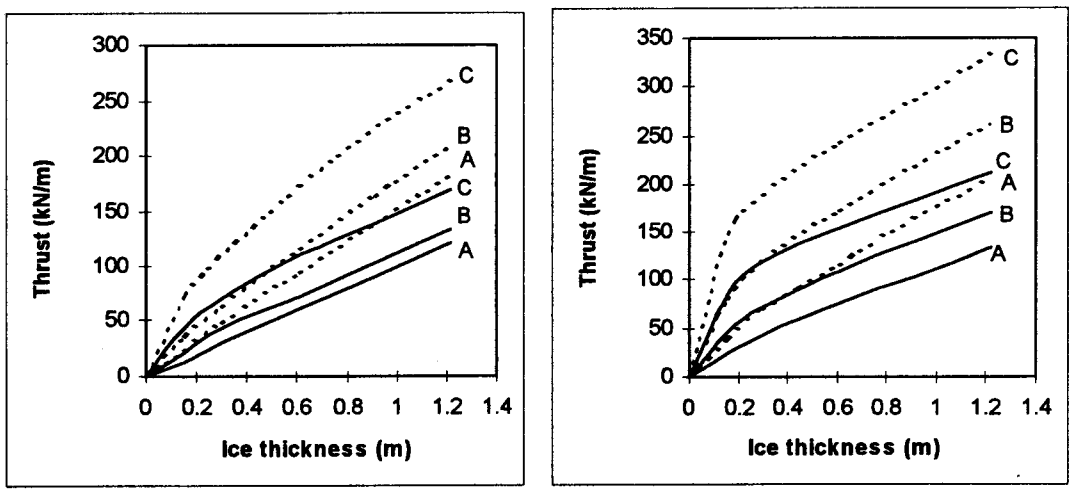

a) Solar energy neglected. b) solar energy considered

Figure 2.2 - Ice thrust in relation to ice thickness, air temperature rise, and restraint. Curves A, B, and C are for air temperature rises of 2.78, 5.56, and 8.33°C/h respectively. Solid lines are for no lateral restraint, and dotted lines are for complete lateral restraint with ν=0.36 (reproduced from Rose, 1947).

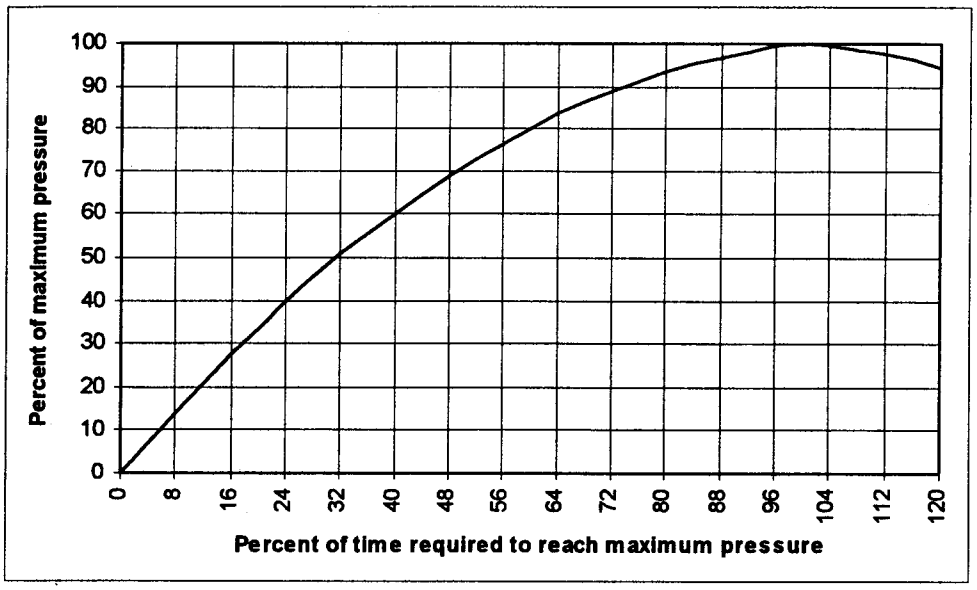

Figure 2.3 - Average pressure-time curve on a percentage basis (reproduced from Monfore, 1954).

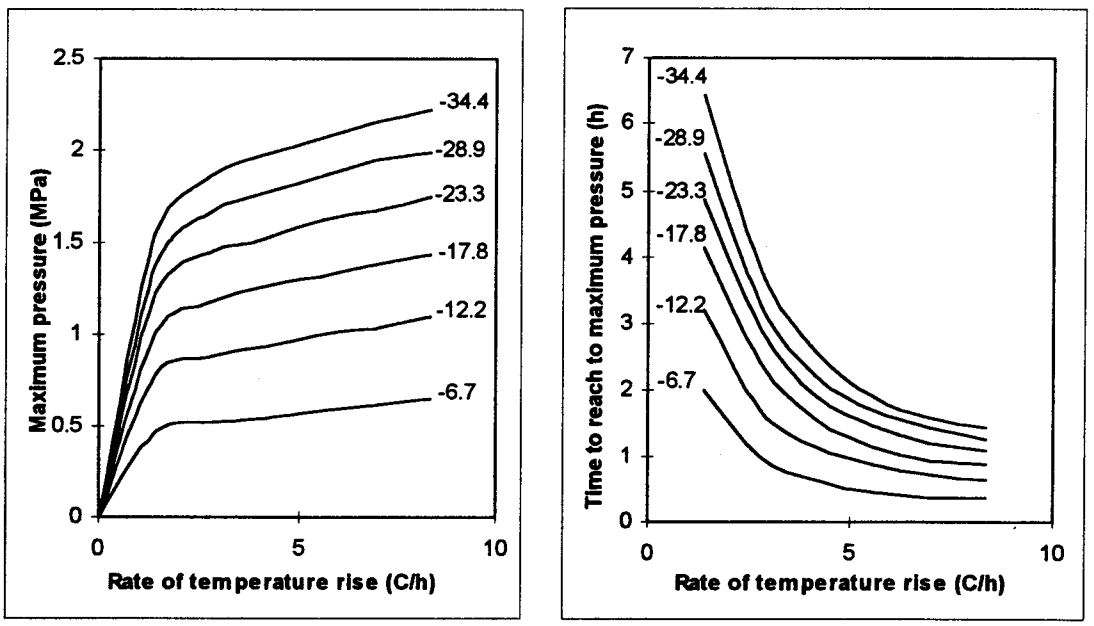

a)Maximum ice pressure. b)Time to reach to maximum pressure.

Figure 2.4 - Maximum ice pressure and time to reach it. Numbers show the initial temperature in C^{o} (reproduced from Monfore, 1954).

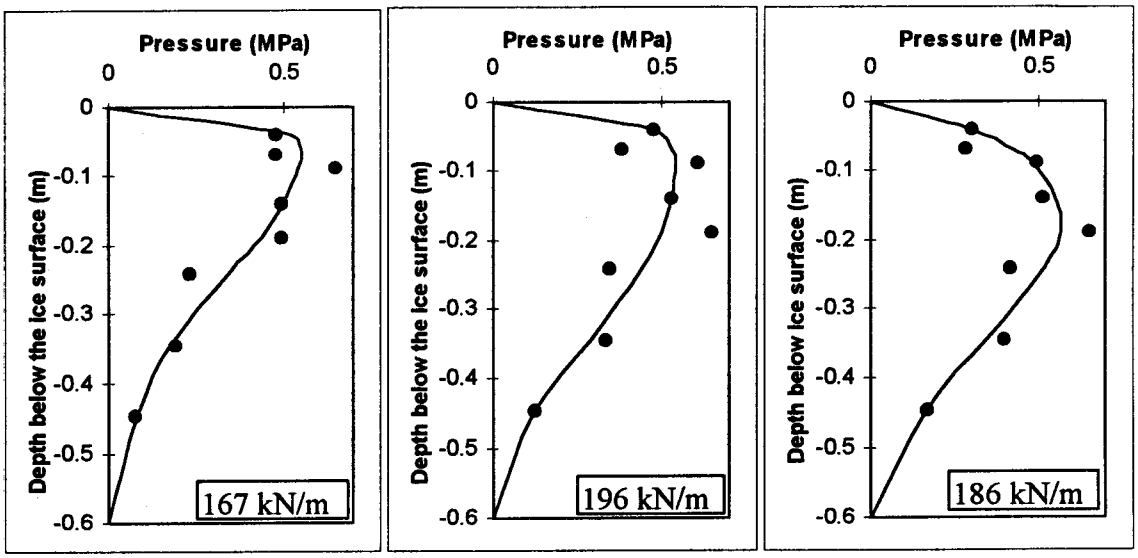

a) After 10 hours b) after 14 hours c) After 17 hours.

Figure 2.5 - Pressure distribution in a cross section of ice (reproduced from Lofquist, 1954).

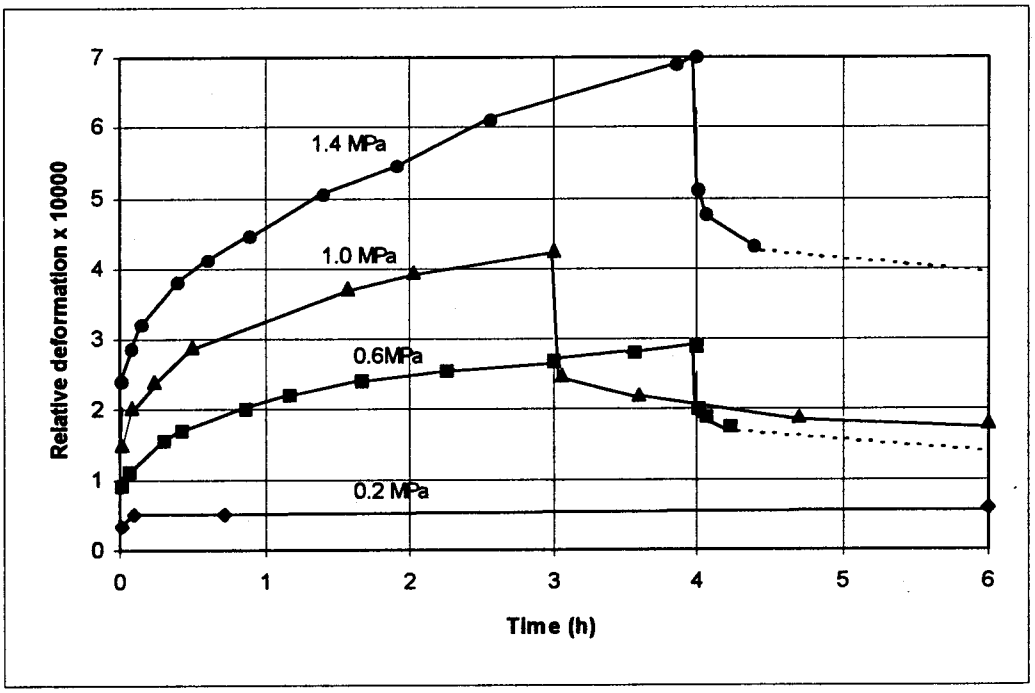

Figure 2.6 - Deformation as a function of time for different stress levels. Specimens unloaded after 3 or 4 hours (reproduced from Lindgren, 1968).

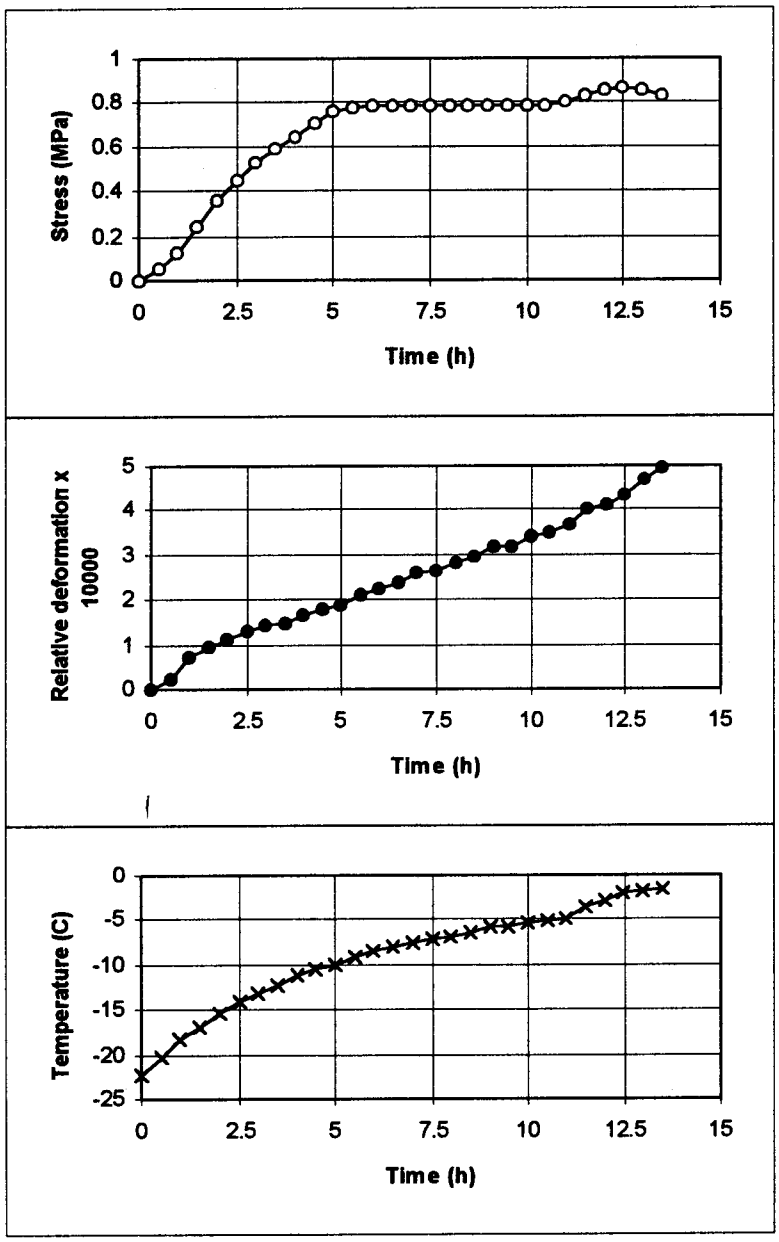

Figure 2.7 - Biaxial thermal pressure test. Ice temperature, the relative deformation between the ice plate and the steel ring, and ice pressure as a function of time (reproduced from Lindgren, 1968).

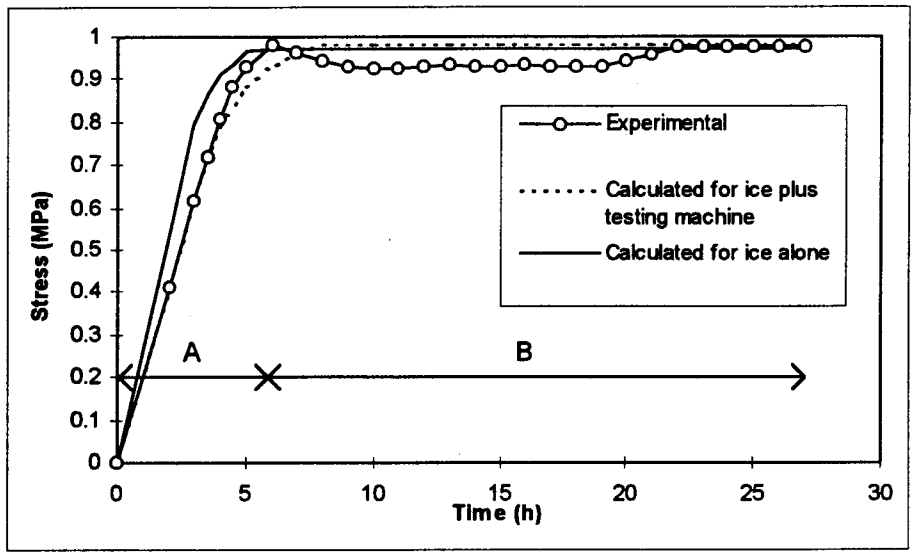

Figure 2.8 - Stress versus time, for snow-ice, at θ = -8.9°C (reproduced from Drouin and Michel, 1971). The calculated values for ice alone are calculated for $\dot{\varepsilon}_2$= constant.

A: $\dot{\varepsilon}_1 = 6.52\times10^{-8}$ sec^{-1} B: $\dot{\varepsilon}_2 = 9.37\times10^{-8}$ sec^{-1}

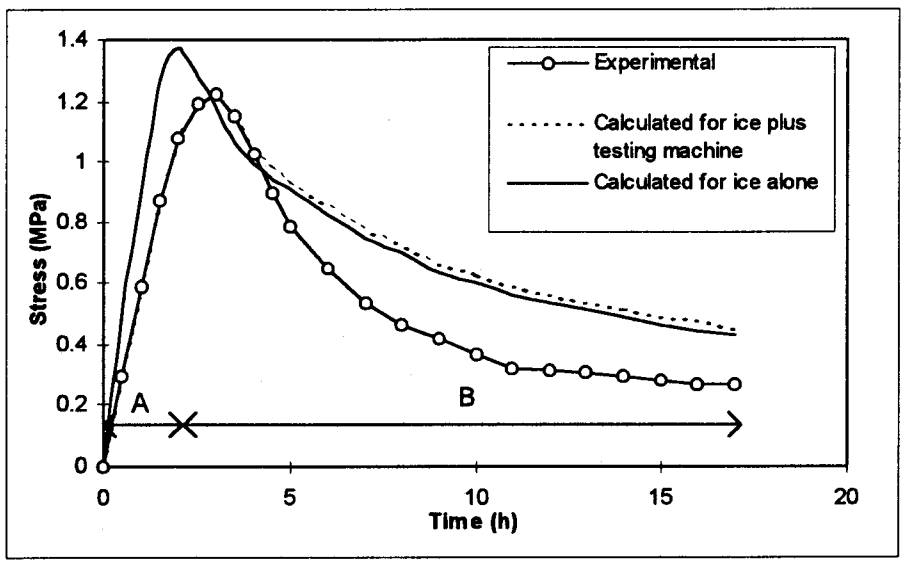

Figure 2.9 - Stress versus time, for columnar ice with optical axis vertical (S1), at θ=-4.3°C (reproduced from Drouin and Michel, 1971). The theoretical values for ice alone are calculated for $\dot{\varepsilon}_2$= constant.

A: $\dot{\varepsilon}_1 = 1.1\times10^{-7}$sec^{-1} B: $\dot{\varepsilon}_2 = 1.84\times10^{-7}$sec^{-1}

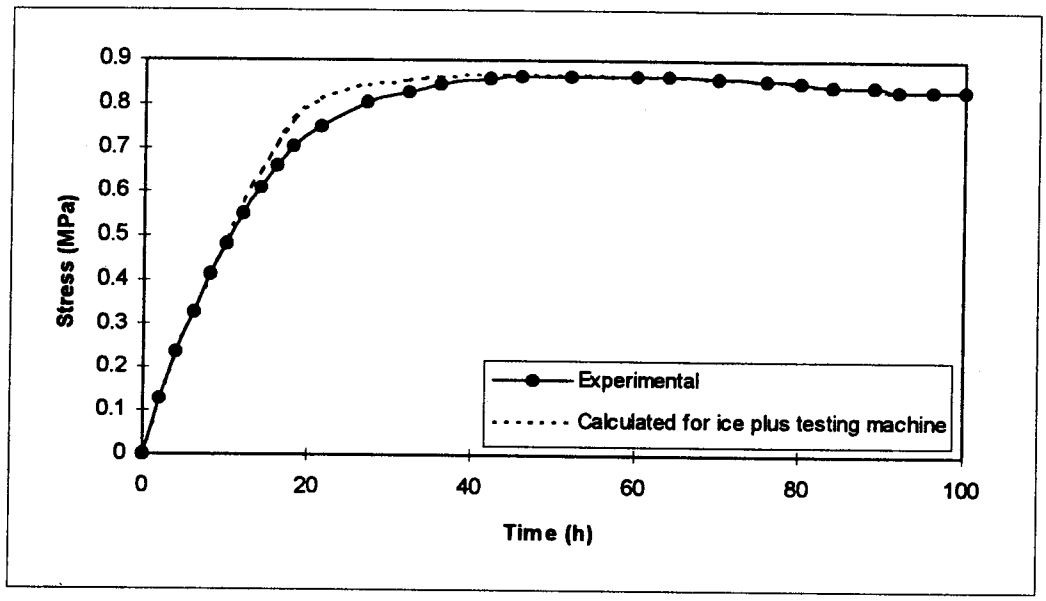

Figure 2.10 - Stress versus time for nucleated columnar ice (S2), at θ = -20.6°C (reproduced from Drouin and Michel, 1971). Up to 20 hours: strain rate = 5.2×10^{-8} sec^{-1}. After 20 hours: strain rate = $6.9\times10^{-8}sec^{-1}$

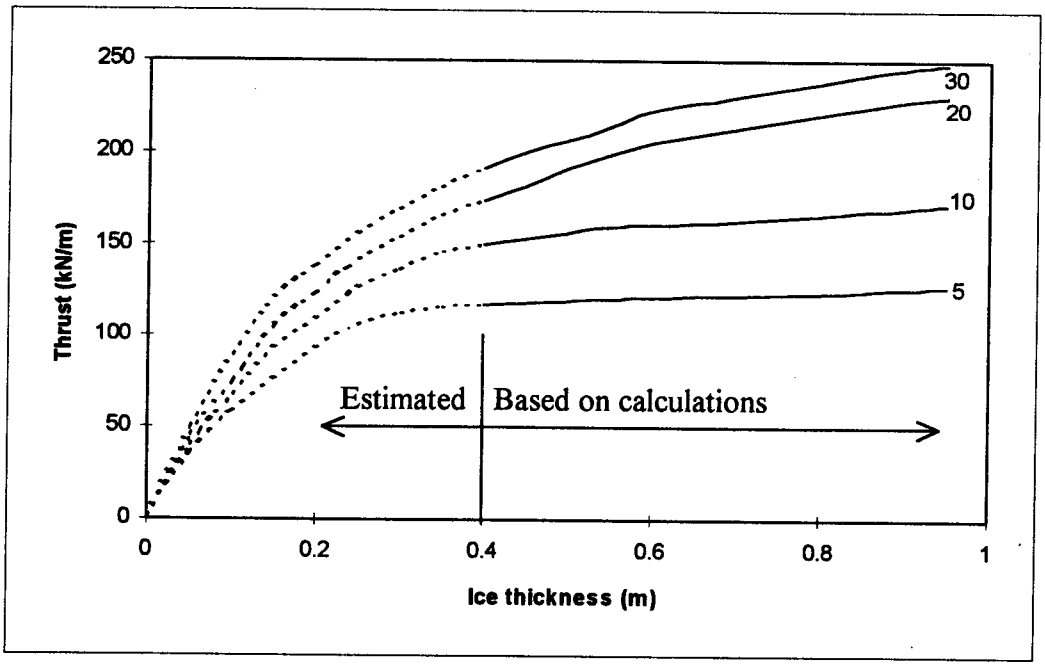

Figure 2.11 - Thermal thrust exerted by an ice sheet restrained in one direction (snow-ice). Temperature varies as a sine function from -20°C to 0°C. Numbers in the figure show the duration of temperature increase in hours. Calculations were done only for the solid parts of the curves (reproduced from Drouin and Michel, 1971).

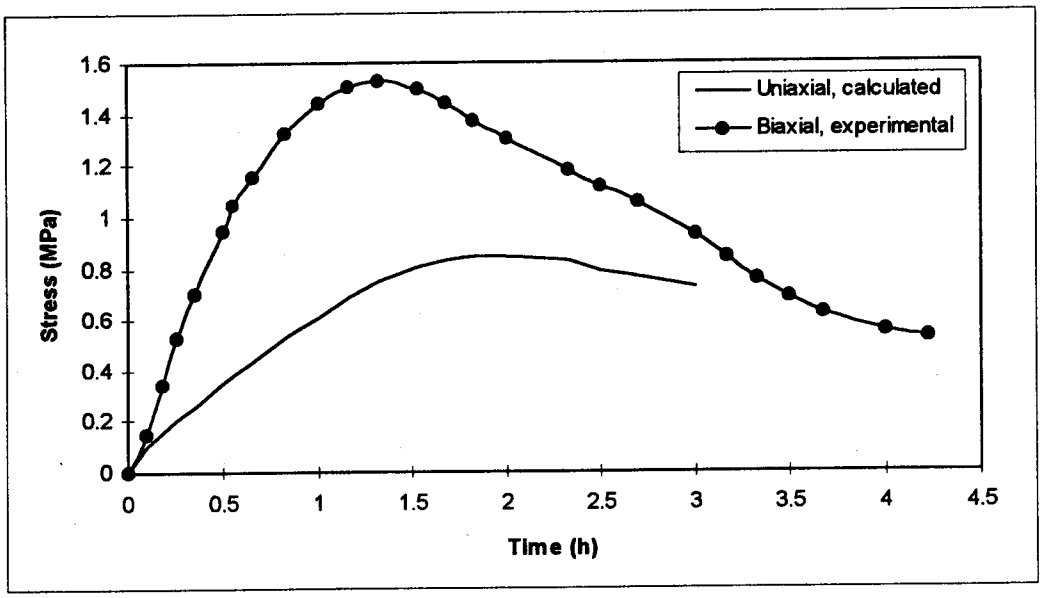

Figure 2.12 - Relation between experimentally measured stress for biaxial condition and calculated equivalent uniaxial condition, for $\dot{\theta} \approx 8.6°C/h$ (reproduced from Drouin and Michel, 1971).

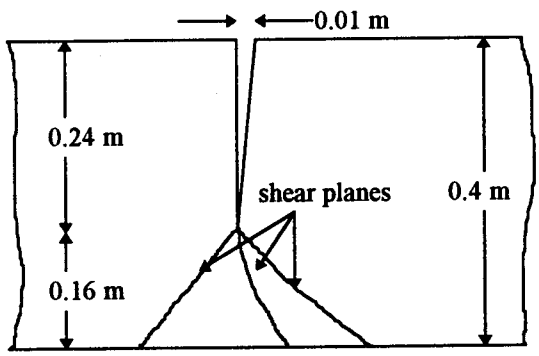

Figure 2.13 - Typical dry crack (reproduced from Metge, 1976).

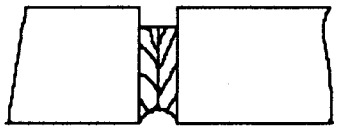

First night, first wet crack has refrozen.

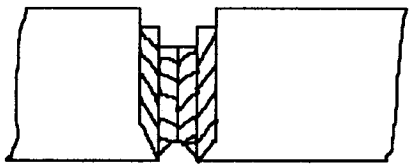

Second night, second crack has formed and refrozen, but ice sheet has grown in thickness and water reaches only 9/10 of new thickness.

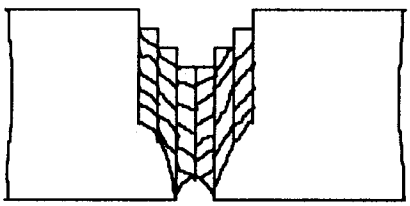

Third night, process is repeated.

Figure 2.14 - Formation of a staircase crack (reproduced from Metge, 1976).

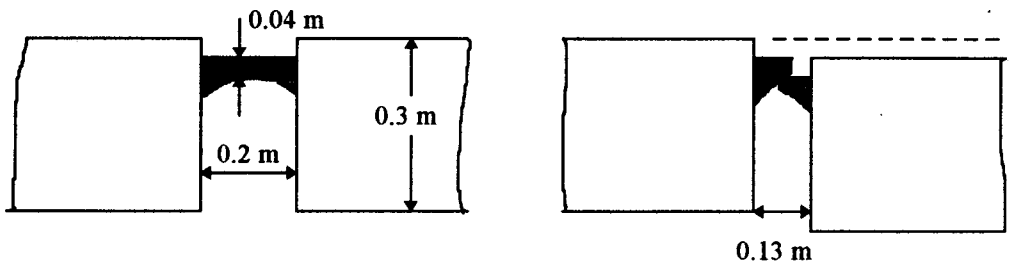

Figure 2.15 - A wide crack before and after breaking (reproduced from Metge, 1976).

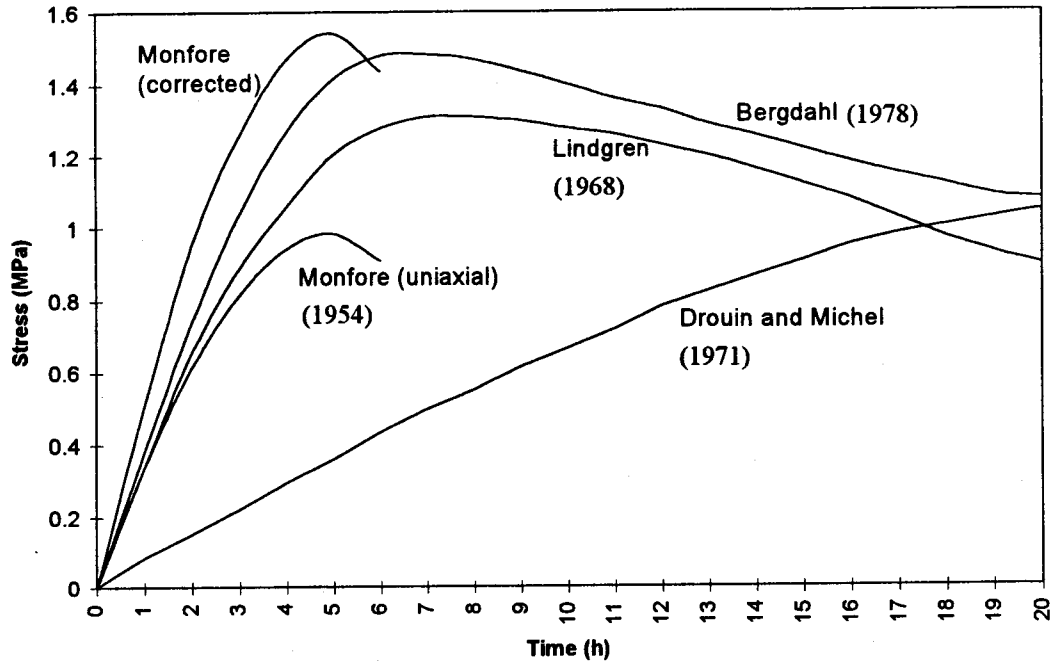

Figure 2.16 - Stress as a function of time for constant rate of temperature change (1°C/h), and initial temperature of -20°C (reproduced from Bergdahl ,1978).

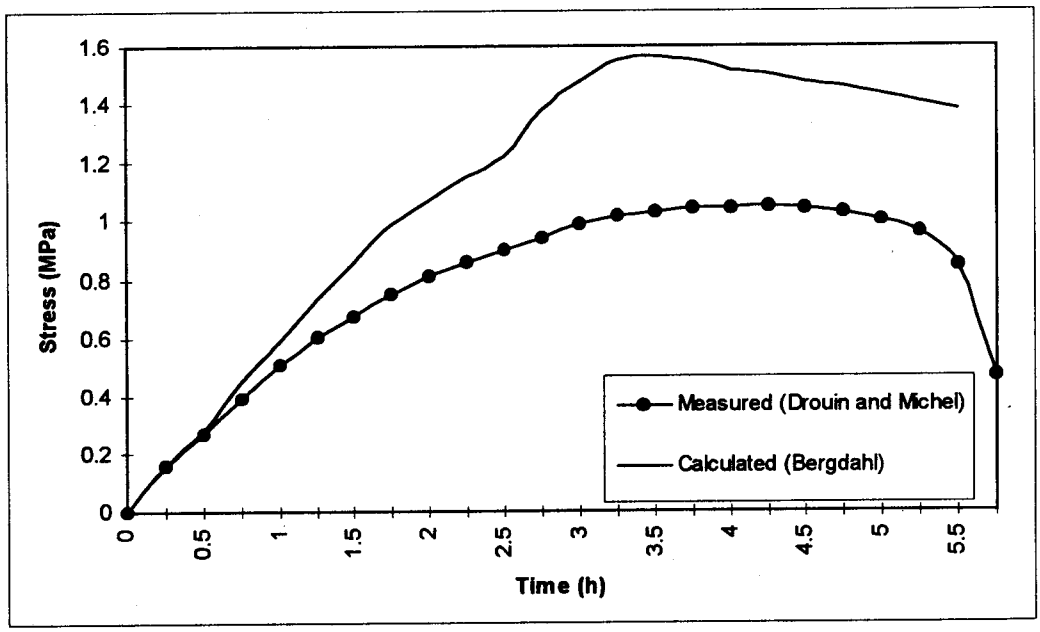

Figure 2.17 - Comparison between measured and calculated ice pressures (reproduced from Bergdahl, 1978).

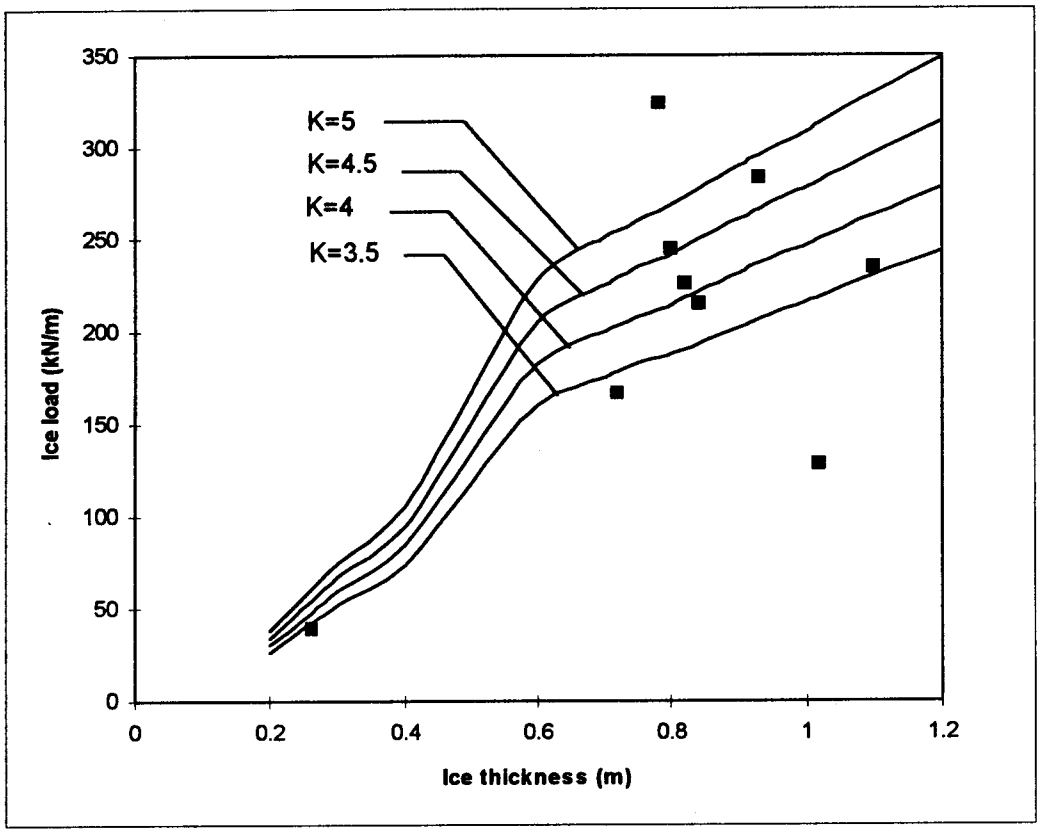

Figure 2.18 - Measured and calculated ice loads as a function of ice thickness (reproduced from Bomeng, 1986).

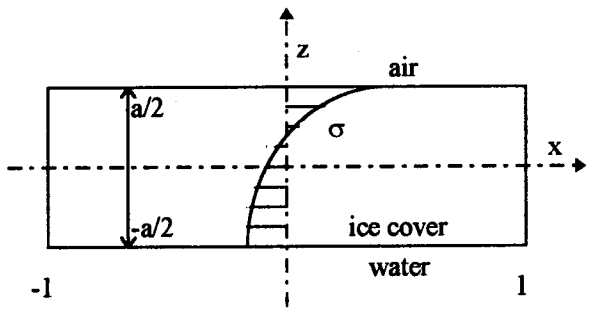

Figure 2.19 - Definition of co-ordinate system for Equations 2.16.1 to 2.16.3 (reproduced from Yamaoka et al., 1988)

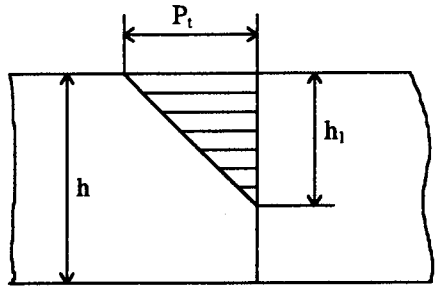

Figure 2.20 - Design schematic for Equation 2.18.1 (reproduced from Tunik, 1988).

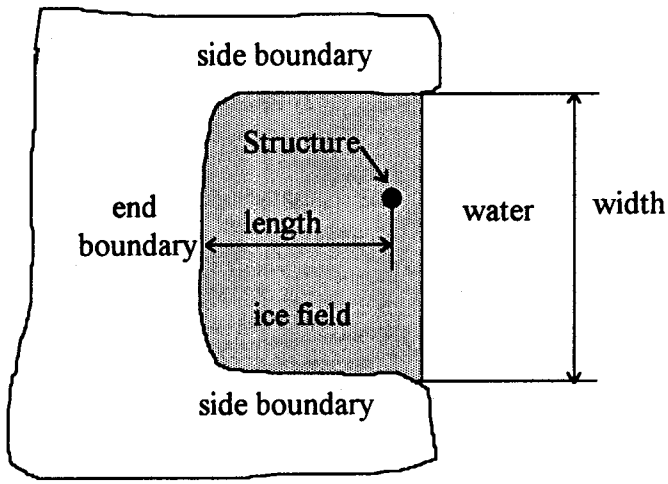

Figure 2.21 - Geometry and definition of the ice field (reproduced from Noponen and Maattanen, 1994).

3 - THERMAL ANALYSIS

To estimate the ice pressure due to thermal expansion, temperature variations within the ice cover need to be calculated. In this study, the thermal analysis required is performed using the finite difference method. A computer program was developed which calculates the temperature profile in the ice cover at different instants in time. The output of this program was used as an input for the stress analysis program. In this chapter a brief review of the theory and formulation of the thermal analysis is presented.

The study of energy balance in ice and snow covers has been of interest for many years and numerous methods and theoretical and empirical equations have been suggested. The work of Bergdahl (1978) serves as the basis for the formulation of the thermal analysis in the present study. However other procedures and formulations are discussed for comparison.

3.1 - Governing Differential Equation

Temperature changes in an ice cover depend on various factors such as climatological factors, ice thickness, ice properties, and snow cover. Also, local effects like currents, or the presence of structures or a power house can influence temperatures in the ice. Since the stress analysis is three dimensional, it is also possible to use the results from a three-dimensional thermal analysis. However, the thermal analysis is simplified considerably if it can be assumed the temperature distribution is the same at every point in the ice sheet. Observations show that in early winter when most thermal events happen the thickness of an ice cover and the temperature distribution through the thickness are usually uniform throughout a reservoir (Comfort & Abdelnour, 1993; Comfort et al., 1994). In late winter when the ice sheet becomes thicker, snow accumulation and snow-ice formation might cause changes in thickness and different temperature profiles in the ice sheet. Even in that

case the temperature variation which causes the thermal pressure occurs in the upper layers and does not vary very much with regard to horizontal position. Meteorological data such as air temperature, wind speed, humidity, cloud cover, and solar radiation, which are used as input for a thermal analysis usually do not vary significantly throughout a lake or a reservoir and are typically measured at one station. From a practical point of view there is often only one set of data available for analysis. Furthermore, it is probable that in most cases the results of a one-dimensional analysis would not be much different from those for a three-dimensional analysis. Considering all of these factors, it was decided to do the thermal analysis only in the vertical direction and it is assumed that the vertical temperature distribution is the same everywhere in the ice sheet. This assumption is acceptable in most cases. In special situations, for example where a reservoir is very large, it is still possible to do separate one-dimensional analyses for individual regions.

Heat transfer occurs within an ice sheet because of temperature gradients, and heat flows from regions of high temperature to regions of low temperature. The governing differential equation for the temperature distribution through the thickness of an ice cover is the equation of thermal diffusion which is given by (Patankar, 1980)

$$\rho Cp\frac{\partial\theta}{\partial t}=\frac{\partial}{\partial z}(k\frac{\partial\theta}{\partial z})+s \qquad (3.1.1)$$

where

z = vertical space coordinate

t = time coordinate

θ = temperature

k = thermal conductivity

ρ = density

Cp = specific heat

s = energy source per unit volume and unit time at (z,t).

If the thermal conductivity is constant with respect to z, equation 3.1.1 takes the form

$$\rho Cp\frac{\partial\theta}{\partial t}=k\frac{\partial^2\theta}{\partial z^2}+s \qquad (3.1.2)$$

To properly formulate the boundary value problem, 3.1.2 must be supplemented by appropriate boundary conditions.

3.2 - Components of Heat Exchange

In northern climates during the fall and winter, the heat accumulated by lakes and reservoirs during the spring and summer is lost through the water surface. If the temperature drops sufficiently, an ice cover forms. During this process the temperature distribution in an ice cover is affected by the amount of heat exchange between the ice and surrounding environment. Heat exchange is controlled by various mechanisms that depend on climatological factors. The mechanisms that are considered in this study are:

1) Latent heat transfer due to evaporation and condensation; denoted as q_e
2) Sensible heat transfer due to temperature difference between the air and the surface (q_t).
3) Emitted long-wave radiation from the surface (q_b).
4) Long-wave radiation from the atmosphere (q_l).
5) Short-wave solar radiation (q_s).

Snow or rain fall both have an effect on the temperature distribution in an ice cover. Snow fall will form a snow layer on top of the ice cover. It acts as insulation and should be considered in the thermal analysis. Periods of warm and cold weather might result in melting and freezing of snow that increases the thickness of ice from the top surface. If the weather is warm, rain fall might form a layer of water on the top surface. This can increase the temperature of the complete ice sheet to 0°C and prevent any further increase or decrease of temperature in the ice cover. Considering all of these effects during the period of analysis requires significant changes in the finite difference grid (like changing the thickness of the top snow or ice layer). Since these effects were not considered, the model developed here is valid only for periods during which there is no precipitation.

At the bottom surface, the temperature remains nominally at 0°C. However, the thickness of the ice cover might increase due to ice growth at the bottom. This can be

considered in the thermal analysis but it is not possible to use the results directly in a stress analysis because the thickness is assumed constant in the finite element analysis.

3.2.1 - Latent and Sensible Heat Transfer

Latent heat transfer occurs due to evaporation and condensation on the ice surface, and sensible heat transfer is the heat exchange due to a temperature difference between the air and the ice surface. The heat flux due to evaporation can be calculated with different methods such as the water budget method, the energy budget method, the empirical method, the mass transfer method, and a combination method (see for example Paily et al., 1974). Among these different methods, the mass transfer method is the most feasible method for this study. In this method it is assumed that the evaporation is a function of wind speed and the difference between the vapor pressures of the atmosphere and the ice surface.

When the ice or water surface is in contact with air, the molecules with the highest velocities will escape from the surface into the space above. The latent heat is the energy per unit mass needed to overcome the molecular attraction. These escaped molecules will form a layer of vapor above the surface. The number of molecules leaving the surface per unit area and unit time will depend on the saturation vapor pressure in this layer. Usually the air above this layer contains some water vapor at a certain partial pressure. If the vapor pressure in the air is less than the saturation vapor pressure corresponding to the surface temperature, a moisture deficit is produced that causes the number of molecules leaving the surface to be much larger than the number of molecules returning to the surface. Therefore the amount of heat exchange due to evaporation is proportional to the difference between the saturation vapor pressure in the layer near the surface and the vapor pressure in the air above it.

Pailey et al.(1974) reviewed 63 evaporation formulas and found that only two have been developed for sub-freezing air temperatures, and only one of these is applicable to field conditions. This was the Russian winter equation presented by Rimsha and Donchenko (1958). This was also used by Bergdahl for thermal analysis. The equation is

$$q_e = f(u_w)(e_a - e_s) \tag{3.2.1}$$

where

e_a = the vapor pressure of the air 2m above the surface

e_s = saturation vapor pressure at the ice surface

$f(u_w)$ = wind function

The saturation vapor pressure is approximated by a linear function,

$$e_s = a(1 + b\theta) \qquad (-32^\circ C \le \theta \le 0^\circ C) \tag{3.2.2}$$

where

$a = 610$ Pa

$b = (32^\circ C)^{-1} = 0.031^\circ C^{-1}$

θ = the ice surface temperature in C°

The wind function is given by:

$$f(u_w) = \rho_w L_s a[1 + bu_w + c(\theta - \theta_a)] \tag{3.2.3}$$

where

$a = 2.42\times10^{-11}$ m/(s.Pa)

$b = 0.49$ s/m

$c = 4.36\times10^{-2}$ $(C^\circ)^{-1}$

ρ_w = the density of water = 1000 kg/m^3

u_w = the wind speed at 2m above the surface

θ = the surface temperature (C°)

θ_a = the air temperature

L_s = the specific heat of sublimation (condensation and fusion) = 2.82×10^6 J/kg

After substituting the constants the equation takes the form:

$$q_e = [0.0682 + 0.0334u_w + 0.003(\theta - \theta_a)](e_a - e_s) \tag{3.2.4}$$

The evaporation heat flux obtained from these equations is not very precise and the error might exceed 25% (Cui, 1996). However, the heat flux due to evaporation is in the range of -30 to 20 W/m^2, which is considered small compared to other heat fluxes. The heat components due to the long-wave and short-wave radiation can be in the range of 200-500 W/m^2.

The energy conducted away from the surface due to the temperature difference between an ice cover and the air above it, can be evaluated using the method proposed by Bowen (1926). Bowen suggested that the heat exchange due to conduction by air is a fixed ratio of that by evaporation. Thus

$$q_t = Bq_e \tag{3.2.5}$$

The constant of proportionality, B, is known as Bowen's ratio and is given by:

$$B = \frac{\gamma(\theta_a - \theta)}{e_a - e_s} \tag{3.2.6}$$

where

$\gamma = 61$ Pa/C° is a constant.

The total convective heat transfer, q_c, due to latent and sensible heat transfer can be written as:

$$q_c = q_e + q_t = f(u_w)[(e_a - e_s) + \gamma(\theta_a - \theta)] \tag{3.2.7}$$

Some authors have used a coefficient of heat transfer, H, for calculating the latent and sensible heat transfer. For example Loset (1992) suggested:

$$q_t = H(\theta_a - \theta) \tag{3.2.8}$$

$$q_e = \frac{H(e_a - e_s)}{\gamma} \tag{3.2.9}$$

where e_s is the saturation vapor pressure for the ice surface temperature. It can be calculated from the Clausius-Clapyron equation:

$$e_s = 0.611\exp[\frac{\xi_m L_s}{R}(\frac{1}{273.15} - \frac{1}{T_{sur}})] \tag{3.2.10}$$

where

L_s = latent heat transfer due to sublimation

ξ_m = ratio of the molecular weights of water and dry air = 0.622

R = the universal gas constant = 8314 (m^3.Pa/kg.mol.K°)

The water vapor pressure of the air is given by:

$$e_a = 0.611R_h \exp[\frac{\xi_m L_s}{R}(\frac{1}{273.15} - \frac{1}{T_\infty})] \tag{3.2.11}$$

where R_h is the relative humidity of the air in fraction of unity. The heat transfer coefficient, H, can be calculated to fit the measured data.

3.2.2 - Long-wave Radiation

Radiation heat transfer is the transfer of heat by electromagnetic radiation. First the thermal energy of a source is converted into energy of electromagnetic radiation waves. These waves travel through the intervening space until they strike another object. When electromagnetic waves fall on a body, part is absorbed by the body and the rest is reflected back into space. The fraction of the energy that is absorbed is called the absorptivity of the body. A body that absorbs all the radiant energy and reflects none is called a black body. A black body also emits radiation depending on its temperature. The heat transferred by radiation from a black body can be calculated from the Stefan-Boltzman law,

$$q_r = \sigma_r T^4 \qquad (3.2.12)$$

where

q_r = heat flux in W/m^2,

σ_r = the Stefan-Boltzman constant = 5.6697×10^{-8} $W/(m^2.{}^oK^4)$,

T = the absolute temperature.

The ratio of the emissive power of a surface to that of a black body is called the emissivity, ε_r, and is 1.0 for a black body. Kirchhoff's law states that at a specified temperature the emissivity and absorptivity of a given surface are the same. For a body that is not a black body, the emitted heat is reduced by ε_r, or

$$q_r = \varepsilon_r \sigma_r T^4 . \qquad (3.2.13)$$

A substance that has an emissivity less than one is called a gray body. Ice and the surrounding atmosphere could both be considered as gray bodies that emit and absorb radiation. The wave-length of the emitted radiation is in the range of 5000 to 100000 nm (Ashton, 1986). This is considered long-wave compared to the radiation that is received directly from the sun, which has a wave-length below 4000 nm. The heat flux

corresponding to emitted long-wave radiation from an ice surface can be calculated from 3.2.13.

$$q_b = \varepsilon_s \sigma_r T^4 \qquad (3.2.14)$$

where ε_s is the emissivity of the surface which can be set to 0.97 for snow and ice (Bergdahl, 1978), and q_b is the emitted radiation from the ice surface.

The gases and particles in the atmosphere including water vapor, ozone, carbon dioxide, and oxygen also emit radiation which can be absorbed by an ice cover. The intensity of long-wave radiation reaching the ice surface depends particularly on the content of water vapor in the atmosphere. The problem in calculating the atmospheric radiation is establishing a value for the emittance of the atmosphere and the effect of clouds.

Paily et al. (1974) studied the different relations suggested for the emissivity of the sky. Some of these relations are a function of vapor pressure of the air and some depend on air temperature only. Since the water content of the air is important in absorbing and emitting long-wave radiation and can not be defined as a function of temperature only, the formulas based on vapor pressure are preferable. The two main equations of this type are due to Angstrom (1915) and Brunt (1932) and are given respectively by:

$$\varepsilon_a = a - b \exp(-ce_a) \qquad (3.2.15)$$

and

$$\varepsilon_a = a + b\sqrt{e_a} \quad . \qquad (3.2.16)$$

The coefficients a, b, and c are constants for which many different values are suggested based on measurements at various locations. Tables 3.1 and 3.2 give the suggested values for these coefficients. The coefficients are generally obtained by a regression analysis for a specific location. A decision about the selection of the proper coefficients can be made on the basis of the location and the coefficient of correlation. In this study, the Angstrom equation(3.2.15), with the values suggested by him are used to calculate the emissivity of the air. These values are:

a = 0.806

b = 0.236

$c = 1.15\times10^{-3}\ Pa^{-1}$.

The radiation emitted by the atmosphere can be expressed as:

$$q_{la} = \varepsilon_a \sigma_r T_a^4 \tag{3.2.17}$$

where

T_a = the absolute temperature of the atmosphere.

Usually the ambient temperature is used to calculate the heat emitted by the atmosphere, and that is the approach used in the model. However, the temperature and moisture may not be the same at different layers of atmosphere. Observations show that the ratio between the long-wave radiation received on a horizontal plane and the value calculated using the air temperature can be from about 0.6 under a clear sky to about 0.96 for completely overcast skies (Parmelee and Aubele, 1952). In order to include these effects the heat flux can be adjusted using the equation suggested by Brunt (Parmelee and Aubele, 1952), which is given by:

$$q_{l\,sky} = q_{la}(0.55 + 5.68\times10^{-3}\sqrt{e_a}) \tag{3.2.18}$$

The part of the long-wave radiation which is absorbed by an ice cover is:

$$q_{li} = \varepsilon_s q_{la} \tag{3.2.19}$$

When clouds are present in the sky, the water and ice particles emit additional radiation. Therefore, the atmospheric radiation is larger under the cloudy sky. Empirical equations have been proposed to estimate the radiation under a cloudy sky. These involve the product of the radiation for a clear sky by a function that depends on the cloud cover. The relation suggested by Bergdahl and Ashton (1986) is:

$$q_{lc} = q_{la}(1 + aC^2) \tag{3.2.20}$$

where

$a = 0.0027$

C = the cloud cover in eighths.

Finally the net radiation flux will be equal to:

$$q_l = q_{li} - q_b = \varepsilon_s \varepsilon_a \sigma_r (1 + aC^2) T_a^4 - \varepsilon_s \sigma_r T^4 \tag{3.2.21}$$

3.2.3 - Short-wave Solar Radiation

Radiation from the sun that reaches the earth has wave lengths in the range 300 to 4000 nm. When passing through the atmosphere, part of the radiation is scattered and diffused or absorbed by the gases and particles in the air. As a result of these processes, the solar radiation reaching the ground has two components, direct solar radiation and diffuse sky radiation. The sum of these components is called insolation and can be measured or calculated from empirical equations. According to Bergdahl (1978), each of the components could be assumed constant and the flux through a horizontal surface from a clear sky can be approximated as:

$$q_{cl} = a \sin\alpha_s + b \qquad (3.2.21)$$

where

a = direct solar radiation calculated on an area normal to the sun rays = 900 W/m^2

b = diffused sky radiation = 100 W/m^2

α_s = the altitude of the sun.

The solar altitude, α_s, is the angle in a vertical plane between the sun's rays and the horizontal. It can be approximated by:

$$\alpha_s = \sin^{-1}(\sin\phi \sin\delta + \cos\phi \cos\delta \cosh_s) \qquad (3.2.22)$$

where

ϕ = the latitude

δ = the declination of the sun

h_s = the local hour angle of the sun.

When the sun is below the horizon ($\sin\alpha_s<0$), the short wave radiation is set to zero.

The declination of the sun, δ, is the angular distance of the sun, north or south of the celestial equator. It has a seasonal variation but can be considered constant for a given day. The declination can be expressed as:

$$\delta = 23.45 \times \frac{\pi}{180} \cos[\frac{2\pi}{365}(172 - D)] \qquad (3.2.23)$$

where D is the day of the year (1 to 365).

The local hour angle of the sun is the angle measured westward around earth's axis from the upper meridian of the observation point to the meridian of the sun (Paily et al., 1974). When the sun is at the local meridian (local noon), h_s is equal to zero. The true solar time is measured in the same way but from the lower meridian of the observation point. Therefore there is a 12 hour difference between the local and the true solar time (Fig. 3.1). Due to irregular angular motion of the earth around the sun, there is a difference between the true solar time and the mean solar time. This is called the equation of time, ET, which varies between 0 and ±16 minutes over a year. The equation of time can be calculated from the following relation given by Woolf (1968).

$$ET = -60(0.123570\sin d' - 0.004289\cos d' + 0.153809\sin 2d' + 0.060783\cos 2d') \quad (3.2.24)$$

where

$$d' = \frac{2\pi}{365.242}(D-1) \qquad \text{(in radians)} \quad (3.2.25)$$

D is the number of the day and ET is in minutes of time.

When using standard time in a location it should be noted that the standard time is equal to the mean solar time for the standard meridian of the time zone. The difference between the standard time and mean solar time is called DOSM (Paily et al., 1974).

$$DOSM = (\frac{\pm 4}{60})(\text{distance between the meridian of the observation and the standard meridian of the time zone, in degrees}) \quad (3.2.26)$$

In 3.2.26 the plus sign applies to the east longitude and the minus sign applies to the west longitude.

In summary h_s is related to standard time by:

$$h_s \text{ (radians)} = \frac{\pi}{12}[\text{standard time (hours) - DOSM + ET} \pm 12 \text{ hours}] \quad (3.2.27)$$

The plus sign is for the mornings and minus sign is for the afternoons.

There are other empirical equations for calculating the insolation. For example Ashton (1986) suggested the following formula:

$$q_{cl} = I_0 \sin\alpha_s \; a_a^{\,m_a} \quad (3.2.28)$$

where

$I_0 \sin \alpha_s$ = intensity of solar radiation on a horizontal plane above the atmosphere

I_0 = the solar constant, which is the intensity of solar radiation at the mean annual distance (a value of 1380 W/m^2 is suggested by Ashton)

a_a = transmittance of the atmosphere

m_a = optical air mass.

The atmospheric transmittance is a measure of the content of the absorbing and scattering constituents in the atmosphere. The optical air mass is a measure of the length of the path that rays have to penetrate before reaching the ground. It is approximately $(\sin \alpha_s)^{-1}$ which is the ratio of path length to the vertical height of the atmosphere. McCulloch (1958) suggested the following relationship for the optical air mass and the transmittance of the atmosphere (Ashton, 1986).

$$a_a^{\,m_a} = 0.99 - 0.17 m_a \tag{3.2.29}$$

According to Klein (1948), the optical air mass at sea level, m_0, can be calculated from the solar altitude, α_s (Ashton, 1986).

$$m_0 = [\sin \alpha_s + 0.15(\alpha_s + 3.885)^{-1.253}]^{-1} \tag{3.2.30}$$

Above sea level, m_0 could be corrected by the ratio of the air pressures.

$$m_a = m_0 \frac{p_{air}}{p_{0\,air}} \tag{3.2.31}$$

The pressure ratio could be obtained from the altitude, Z (Ashton, 1986).

$$\frac{p_{air}}{p_{0\,air}} = \left(\frac{288 - 0.0065Z}{288}\right)^{5.256} \tag{3.2.32}$$

When clouds are present in the sky, there is a further reduction in the amount of solar radiation. Several empirical formulas have been suggested for including the effect of clouds. In most of these relations the cloud cover is presented as the fraction of the sky covered by clouds. Considerable deviation occurs among the predictions of the proposed formulas. Problems in estimating the cloud cover also causes errors. Bergdahl (1978) used the following equation to consider the effect of clouds.

$$q_c = q_{cl}\left[0.35 + 0.65\left(1 - \frac{C}{8}\right)\right] \tag{3.2.33}$$

where

q_{cl} = radiation from a clear sky

C = cloud cover in eighths.

Some of the incident light is reflected from the ice surface. The ratio between the reflected radiation and the incident radiation for the ice can be calculated from the Fresnel formula (Ashton, 1986):

$$r_i = 0.5\{\frac{[\sin(\alpha_1 - \beta_i)]^2}{[\sin(\alpha_1 + \beta_i)]^2} + \frac{[\tan(\alpha_1 - \beta_i)]^2}{[\tan(\alpha_1 + \beta_i)]^2}\} \tag{3.2.34}$$

where

$\alpha_1 = \pi/2 - \alpha_s$

α_s = altitude of the sun (see Fig. 3.2).

Angles α_1 and β_i are related to the refractive index, n_r, through:

$$n_r = \frac{\sin\alpha_1}{\sin\beta_i} \tag{3.2.35}$$

The refractive index for ice is 1.33 (Bergdahl, 1978). Table (3.3), which is reproduced from Ashton(1986) gives the values of r calculated with the Fresnel equation and the values measured or suggested by other authors. The coefficient of reflection suggested by Bergdahl for ice and snow-ice are given in Table 3.4.

The reflection coefficient for diffuse light is more uncertain since the angles of incidence cover all directions and the intensive distribution is not known. Bergdahl sets this value equal to 0.02, while Ashton suggests 0.10. It is assumed that approximately 50% of the energy flux lies between 350-700 nm, 25% between 700-1200 nm, and 25% between 1200-4000 nm. Finally the radiation flux entering the surface will be equal to:

$$q_s = [a(1 - r_i)\sin\alpha_s + 0.98b][0.35 + 0.65(1 - \frac{C}{8})] \tag{3.2.36}$$

Short wave radiation is different from other heat fluxes since it is absorbed not only in the upper surface of the ice but throughout the thickness of the ice cover. The radiation flux at distance z from the upper surface can be obtained from the exponential law (Bergdahl, 1978).

$$q_{sz} = q_s \exp(-Kz) \tag{3.2.37}$$

where

q_s = net flux of radiation entering the surface at z=0

K = coefficient of absorption

The absorption coefficient for ice is strongly wave-length dependent. The absorption coefficients for different materials and different wave lengths are given in Table 3.5. The high values of K for long wave-lengths suggest that for these wave-lengths, absorption occurs in a thin surface layer.

3.3 - Finite Difference Formulation

The equation of thermal diffusion (3.1.1), can be solved by different methods. The analytical solution for this equation is limited to certain boundary conditions. The flexibility of numerical methods and their ability to deal with different boundary conditions makes their use highly desirable. The finite difference method and finite element method can both be used for solving this equation. The finite element method is most desirable for two or three-dimensional analysis particularly when the thermal analysis is required for a subsequent stress analysis, since the same mesh can be used for both. For one-dimensional analysis the formulation is easier with the finite difference method. In this study, since the thermal analysis needs to be done only in the vertical direction, and the stress analysis required is three dimensional, it was most convenient to solve the equation of diffusion using the finite difference method.

In numerical analysis by the finite difference method, the continuous space is replaced by a finite number of grid points and the time is divided into a finite number of time steps. The distance between the grid points (in this case, Δz), and the length of time step (Δt), are used to approximate the derivatives in space and time. The temperature at the grid points in space and time are the unknowns.

The equation of thermal diffusion (3.1.1), requires approximation for the second derivative in space and the first derivative in time. A forward finite divided difference formula can be used to approximate the first derivative in time.

$$(\frac{\partial\theta}{\partial t})_z^t = \frac{\theta(z,t+\Delta t)-\theta(z,t)}{\Delta t} \tag{3.3.1}$$

The second derivative in space can be approximated using a generalized form of the Crank-Nicolson implicit method:

$$(\frac{\partial^2\theta}{\partial z^2})_z^t = (1-B_c)\frac{\theta(z-\Delta z,t)-2\theta(z,t)+\theta(z+\Delta z,t)}{\Delta z^2} +$$

$$B_c\frac{\theta(z-\Delta z,t+\Delta t)-2\theta(z,t+\Delta t)+\theta(z+\Delta z,t+\Delta t)}{\Delta z^2} \tag{3.3.2}$$

The Crank-Nicolson method is often used for thermal analysis and it is unconditionally stable. In the usual Crank-Nicolson method, B_c is equal to 0.5, but the value 0.6 is suggested by Bergdahl in order to overcome the instabilities introduced by the boundary conditions at the upper surface. When the equation 3.3.2 together with the boundary conditions is written for all of the nodes the result is a set of n linear algebraic equations with n unknowns. However, the system is tridiagonal and the extremely efficient solution algorithms that are available for tridiagonal systems can be employed.

When the body is composed of different materials and heat fluxes other than conduction are present, it is easier to use the control volume method for deriving the finite difference equations. Each grid point is surrounded by a control volume (in this case a control layer), for which the equation of heat balance can be written. The discretization of the ice cover for the finite difference analysis is shown in Figure 3.3. Solid lines show the grid points where the temperatures are calculated. Each grid point is surrounded by a control layer. The boundaries of the control layers are shown with dashed lines.

Conservation of heat can be used to develop a heat balance for a control layer surrounding an internal node, i.

(rate of heat accumulation) = (rate of heat in) - (rate of heat out) (3.3.3)

The rate of heat accumulation is

$$\frac{\Delta\theta_i}{\Delta t}(Cp_{i-1}\rho_{i-1}\frac{\Delta z_{i-1}}{2}+Cp_i\rho_i\frac{\Delta z_i}{2}) \tag{3.3.4}$$

where

$$\Delta\theta_i = \theta(z,t+\Delta t)-\theta(z,t) \tag{3.3.5}$$

The total heat flux entering the layer is the sum of the conductive heat flux and the short-wave radiation heat flux.

$$\bar{q}_{i-\frac{1}{2}} = \frac{k_{i-1}}{\Delta z_{i-1}}(\bar{\theta}_{i-1} - \bar{\theta}_i) + \bar{q}_{s\,i-\frac{1}{2}} \tag{3.3.6}$$

Bars denote the weighted time average:

$$\bar{\theta}_i = (1 - B_c)\theta(z_i, t) + B_c\theta(z_i, t + \Delta t) \tag{3.3.7}$$

$$\bar{q}_{s\,i-\frac{1}{2}} = (1 - B_c)q^t_{s\,i-\frac{1}{2}} + B_c q^{t+\Delta t}_{s\,i-\frac{1}{2}} \tag{3.3.8}$$

The heat flux exiting the layer is also the sum of conductive and short-wave radiation heat fluxes.

$$\bar{q}_{i+\frac{1}{2}} = \frac{k_i}{\Delta z_i}(\bar{\theta}_i - \bar{\theta}_{i+1}) + \bar{q}_{s\,i+\frac{1}{2}} \tag{3.3.9}$$

Substituting 3.3.4, 3.3.6, and 3.3.9 into 3.3.3 gives:

$$\frac{\Delta\theta_i}{\Delta t}(Cp_{i-1}\rho_{i-1}\frac{\Delta z_{i-1}}{2} + Cp_i\rho_i\frac{\Delta z_i}{2}) = \bar{q}_{i-\frac{1}{2}} - \bar{q}_{i+\frac{1}{2}}$$

$$= \frac{k_{i-1}}{\Delta z_{i-1}}(\bar{\theta}_{i-1} - \bar{\theta}_i) - \frac{k_i}{\Delta z_i}(\bar{\theta}_i - \bar{\theta}_{i+1}) + \bar{q}_{s\,i-\frac{1}{2}} - \bar{q}_{s\,i+\frac{1}{2}} \tag{3.3.10}$$

The short wave radiation flux entering and exiting the control layer is obtained from:

$$\bar{q}_{s\,i-\frac{1}{2}} = \bar{q}_s \exp[-K_{i-1}(z_i - \frac{\Delta z_{i-1}}{2})] \tag{3.3.11}$$

$$\bar{q}_{s\,i+\frac{1}{2}} = \bar{q}_s \exp[-K_i(z_i + \frac{\Delta z_i}{2})] \tag{3.3.12}$$

This formulation facilitates dealing with layers of different thickness and different material properties, for example layers of snow and ice.

At the upper interface the difference formulation can be written for the control layer bounded by z_1 and $z_1+\Delta z_1/2$.

$$\frac{\Delta\theta_{1.25}}{\Delta t}Cp_1\rho_1\frac{\Delta z_1}{2} = \bar{q}_1 - \bar{q}_{1.5} \tag{3.3.13}$$

Approximating $\Delta\theta_{1.25}$ by $\Delta\theta_1$ gives

$$\frac{\Delta\theta_1}{\Delta t} Cp_1\rho_1 \frac{\Delta z_1}{2} = \frac{2k_1}{\Delta z_1}(\bar{\theta}_1 - \bar{\theta}_2) + \bar{q}_c + \bar{q}_l + \bar{q}_b + \bar{q}_s - \bar{q}_{s\,1+\frac{1}{2}} \tag{3.3.14}$$

where the bars denote weighted time average and

$$q_c = f(u_w)[e_a - e_s + \gamma(\theta_a - \theta)] \tag{3.3.15}$$

$$f(u_w) = \rho L_s a[1 + bu_w + c(\theta - \theta_a)] \tag{3.3.16}$$

$$q_b = \varepsilon_s \sigma_r T_1^4 \tag{3.3.17}$$

$$q_l = \varepsilon_s \varepsilon_a \sigma_r T_a^4 \tag{3.3.18}$$

$$q_s = [(1 - r_i)a\sin\alpha_s + 0.98b][0.35 + 0.65(1 - \frac{C}{8})] \tag{3.3.19}$$

$$q_{s\,1+\frac{1}{2}} = q_s \exp(-K\frac{\Delta z_1}{2}) \tag{3.3.20}$$

As may be seen from the above equations, some of the heat fluxes are non-linear functions of surface temperatures. There are two ways to deal with this problem. One is to perform an iterative process and the other is to use a linear approximation of the above functions. The second approach is applied in this study. For example $f(u_w)$ is calculated from the temperature at the previous time step and q_b is approximated with a linear function as:

$$q_b = \varepsilon_s \sigma_r (273.15^4 + 4 \times 273.15\theta_1) \tag{3.3.23}$$

At the ice-water interface the boundary condition θ=0°C can be used. It is also possible to estimate the ice cover growth from the heat conducted away from the boundary. The following equation can be used to obtain the ice growth Δz_n.

$$\Delta z_N \frac{\rho_{N-1} L_f}{\Delta t} = \frac{k_{N-1}}{\Delta z_{N-1}} \bar{\theta}_{N-1} + \bar{q}_{s\,N-\frac{1}{2}} - \bar{q}_{sN} \tag{3.3.24}$$

where

N = number of grid points

L_f = specific heat of fusion

The calculated ice growth, Δz_N, can be added to the coordinate of the last grid point, $z_{N,}$, so that the thickness of the last layer would increase with time. This method over estimates the ice growth, because a part of the heat conducted away from the last layer

will decrease the temperature of the water below the ice cover. It might also cause numerical problems in some cases. It should be noted that in the stress analysis the thickness of the ice cover will remain constant. Therefore, in order to use the results of this analysis, some assumptions and approximations should be made. For example it is possible to study the ice growth in the thermal analysis and then use an average thickness for the stress analysis.

3.4 - Computer Program

A computer program for the thermal analysis was developed based on the finite difference formulation described in section 3.3. The features of the program are summarized as follows:

- Different materials can be considered in the ice cover. The materials can be selected from those for which the properties are defined in the program, or the properties can be given in the input data. The materials defined in the program and their properties are shown in Table 3.6.
- Grid points can be selected at different intervals.
- Changes in air temperature can be given in one of the following ways:
  1) A sine function for which the initial temperature, period, and amplitude are specified.
  2) Cosine function with specified initial temperature, period, and amplitude.
  3) A set of (t,θ) pairs from which the temperature at the required time steps is calculated by a linear interpolation.
- The following boundary condition types can be considered:
  1) The boundary temperatures are prescribed at the top and bottom surfaces.
  2) The surface temperature is prescribed and the bottom temperature is equal to 0°C.
  3) A coefficient of heat transfer, H, is introduced where the heat flux at the upper surface is given by:

$$q = H(\theta_a - \theta_{ice}) \qquad (3.4.1)$$

At the bottom surface the temperature is equal to 0°C.

4) A general case where the heat fluxes are calculated by the program from the given data including air temperature, relative humidity, cloudiness of the sky, wind speed, location of the site, and date and hour when the problem starts. Short-wave solar radiation can be excluded simply by putting the date equal to zero. At the bottom surface the temperature is equal to 0°C.
5) General case as in 4, but the wind speed, or short-wave solar radiation flux, or both are read from prepared input files.

- Ice growth can be calculated and added to the thickness of the last layer.

3.5 -Verification of the Thermal Model

In this section the results of the present program are compared to analytical and numerical solutions from other authors. A wide variety of problems are considered which cover the different aspects of the thermal analysis. The purpose of these numerical experiments was to verify the thermal model.

3.5.1 - Sinusoidally Varying Surface Temperature

If the material properties of the ice cover are assumed to be constant, and there are no heat sources, the governing differential equation (3.1.1) becomes:

$$\frac{\partial \theta}{\partial t} = \frac{k}{\rho Cp}\frac{\partial^2 \theta}{\partial z^2} \tag{3.5.1}$$

Assuming that the surface temperature varies as a sine function, the boundary conditions are:

$$\theta(0,t) = \theta_{av} + \theta_{am} \sin\frac{2\pi}{T_\theta} t \tag{3.5.2}$$

$$\theta(h,t) = 0^\circ C \tag{3.5.3}$$

where

θ_{av} = the average temperature during cyclic temperature variations at the surface of the ice sheet.

θ_{am} = the amplitude of the cycle

T_θ = period

h = ice thickness

The solution for the steady state problem satisfying the boundary conditions (3.5.2 and 3.5.3)

is given by Drouin and Michel (1971) as

$$\theta(z,t) = \theta_{av}(1-\frac{z}{h}) + \theta_{am} B_\lambda \sqrt{E_{\lambda z}^{\ 2} + F_{\lambda z}^{\ 2}} \sin(\frac{2\pi t}{T_\theta} - \psi) \tag{3.5.4}$$

where

$$B_\lambda = \frac{1}{1 + e^{-2\lambda h} \dfrac{\cosh\lambda h \sin^2\lambda h - \sinh\lambda h \cos^2\lambda h}{\cosh\lambda h \sin^2\lambda h + \sinh\lambda h \cos^2\lambda h}} \tag{3.5.5}$$

$$\lambda = \sqrt{\frac{\pi\rho Cp}{kT}} \tag{3.5.6}$$

$$E_{\lambda z} = (e^{-\lambda z} + C_1 e^{\lambda z})\cos\lambda z + C_2 \cosh\lambda z \sin\lambda z \tag{3.5.7}$$

$$F_{\lambda z} = (e^{-\lambda z} - C_1 e^{\lambda z})\sin\lambda z + C_2 \sinh\lambda z \cos\lambda z \tag{3.5.8}$$

$$C_1 = \frac{e^{-2\lambda h}(\cosh\lambda h \sin^2\lambda h - \sinh\lambda h \cos^2\lambda h)}{\cosh\lambda h \sin^2\lambda h + \sinh\lambda h \cos^2\lambda h} \tag{3.5.9}$$

$$C_2 = \frac{-2e^{-\lambda h}\sin\lambda h \cos\lambda h}{\cosh\lambda h \sin^2\lambda h + \sinh\lambda h \cos^2\lambda h} \tag{3.5.10}$$

$$\psi = \tan^{-1}(\frac{F_{\lambda z}}{E_{\lambda z}}) \tag{3.5.11}$$

In Fig. 3.4 the temperature distribution obtained from (3.5.4) is compared to the temperature distribution from the present program. The ice cover has the material properties of the columnar ice given in Table 3.6. Other data are as follows:

h = 0.4m

θ_{am} = 30°C

θ_{av} = -30°C

T_θ = 24 hours

time of comparison = 48 hours

Δt = 200 s

Δz = 0.02 m

In Table 3.7, the temperature at z = 0.2 m obtained from the present program for different time steps, Δt, and different layer thickness, Δz, are compared to the analytical solution. It can be seen that even for large time steps and small number of layers, the error is small (≈2%).

3.5.2 - Coefficient of Heat Transfer

In some cases it might be possible to define a coefficient of heat transfer using previous field data. If measured data are available this coefficient can be obtained by trial and error so that it gives the correct surface temperature when only the air temperature data is used in the analysis. It accounts for the boundary layer between the ice cover and the air and approximates the thermal fluxes due to convection and long-wave radiation.

$$q_m = H(\theta_a - \theta) \qquad (3.5.12)$$

In equation 3.5.12 H is the coefficient of heat transfer. When this coefficient is defined, the only data needed in the calculations would be the air temperature. This approach is based on the assumptions that:

1. The heat flux due to long-wave radiation is a linear function of the difference between the air and the ice surface temperature. Acording to Cue (1996) this assumption is valid for temperature differences up to about 14°C.
2. The convective heat flux is a linear function of the difference between the air and the ice surface temperature. This assumption is valid for temperature differences up to about 7°C (Cue, 1996).

3. The evaporation heat component is negligible. The heat flux due to evaporation is usually less than 10% of the radiation heat fluxes and can be considered when calibrating the coefficient.

Figure 3.5 shows the comparison between the results of this program and those obtained numerically by Bergdahl (1978) for a problem in which the coefficient of heat transfer is used. The coefficient of heat transfer used is 33.3 W/m^2. The air temperature varies as a half a cosine wave from -30°C to 0°C in five hours and the ice thickness is 0.4m. The figure shows the temperature profiles obtained after three and five hours.

3.5.3 - Complete Case without Solar Radiation

In Fig. 3.6 the temperature profiles predicted by Bergdahl (1978) and by the present program are compared for a complete case including latent and sensible heat transfer and long wave radiation without short-wave solar radiation. The initial air temperature is -30°C and rises as a single cosine half wave to 0°C in five hours. The ice thickness is 0.4m. The wind speed is constant (u_w=2 m/s), the sky is clear (C=0), and the vapor pressure is 80% of the saturation vapor pressure of the air.

The overall agreement is good and the slight difference which is not more than 0.4°C is probably due to minor differences in how the heat fluxes are calculated.

3.5.4 - Short-wave Solar radiation

Short-wave solar radiation differs from other heat fluxes in that it can be absorbed through the thickness of the ice cover. In order to check the accuracy of the numerical model in dealing with this issue, a case is studied where the heat flux at the upper surface is due only to short-wave radiation. The numerical results are compared to the analytical solution.

Considering the absorbed short-wave radiation as a heat source, the governing differential equation for this case is

$$\rho Cp\frac{\partial\theta}{\partial t} = k\frac{\partial^2\theta}{\partial z^2} + s(z,t) \quad , \tag{3.5.13}$$

where

$$s(z,t) = q_s K e^{-Kz} \quad . \tag{3.5.14}$$

The boundary conditions are:

$$\frac{\partial\theta}{\partial z} = 0 \quad \text{at } z=h \tag{3.5.15}$$

$$\theta = 0 \quad \text{at} \quad z = 0 \tag{3.5.16}$$

The initial condition is:

$$\theta = -\theta_0(1-\frac{z}{h}) \quad \text{at } t=0 \tag{3.5.17}$$

The analytical solution for this problem is (Hrudey, 1992):

$$\theta(z,t) = \sum_{n=1}^{\infty}\{\frac{d_n}{a\lambda_n^2}[1-\exp(-a_d\lambda_n^2 t)] - \frac{2\theta_0}{(\lambda_n h)^2}\exp(-a_d\lambda_n^2 t)\}\cos\lambda_n z \tag{3.5.18}$$

where

$$a_d = \frac{k}{\rho Cp} \tag{3.5.19}$$

$$\lambda_n = \frac{(2n-1)\pi}{2h} \tag{3.5.20}$$

$$d_n = \frac{q_s}{\rho Cph}\{\frac{2[1 \pm e^{-Kh}(\frac{\lambda_n}{K})]}{1+(\frac{\lambda_n}{K})^2}\} \qquad \text{+ for odd n and -for even n} \tag{3.5.21}$$

In non-dimensional form the solution becomes:

$$\frac{\theta}{\theta_0} = \sum_{n=1}^{\infty}\frac{1}{\Lambda_n^2}\{\delta_n[1-\exp(-\Lambda_n^2\iota)] - \frac{2}{\Lambda_n^2}\exp(-\Lambda_n^2\iota)\}\cos\Lambda_n\zeta \tag{3.5.22}$$

where

$$\zeta = \frac{z}{h} \tag{3.5.23}$$

$$\iota = \frac{a_d t}{h^2} \tag{3.5.24}$$

$$\Lambda_n = \frac{(2n-1)\pi}{2} \tag{3.5.25}$$

$$\delta_n = \gamma \frac{2[1 \pm e^{-\kappa}(\frac{\Lambda_n}{\kappa})]}{1+(\frac{\Lambda_n}{\kappa})^2} \tag{3.5.26}$$

The solution depends on two parameters in addition to the time constant ι. These are

$$\gamma = \frac{q_s h}{\theta_0 k} \tag{3.5.27}$$

$$\kappa = Kh \tag{3.5.28}$$

In Fig. 3.7 the non-dimensional solution from the present program is compared to the results of the analytical solution. The short-wave radiation is taken constant and the coefficient of absorption is the same for all wave-lengths. There is an excellent agreement.

3.6- Summary and Conclusion

In this chapter the issues regarding the thermal analysis were described. The governing differential equation was introduced, different mechanisms of heat transfer and their formulations were explained, the finite difference formulation was presented, some features of the computer program were described and finally the results obtained from the thermal analysis program were compared to the available analytical and other numerical solutions. The comparisons were made for different aspects of the program and different mechanisms of heat transfer including conduction, convection, long and short-wave radiation, and heat transferred using a coefficient of heat transfer. The agreement was good in all cases. These verifications show that the present program can be used to estimate the temperatures in an ice cover in various meteorological conditions. Further comparisons with field measurements are performed in Chapter 5.

Investigator	a	b	c (1/mb)	Remarks
Angstrom (Sweden)	0.806	0.236	0.115	
Kimball (Virginia)	0.800	0.326	0.154	
Eckel (Austria)	0.710	0.240	0.163	
Anderson (Oklahoma)	1.107	0.405	0.022	
Linke's Meteorol Taschenbuch	0.790	0.174	0.041	
Bolz-Falchenberg (Baltic Sea Coast)	0.820	0.250	0.218	e_a and T_a measured at 16m above ground at 150m from seashore. valid for $1.3<e_a<27$ mb.
Raman (India)	0.790	0.273	0.112	
TVA (Paradise data)	0.999	0.605	0.124	Monthly average values based on daily average data; includes the effect of clouds.

Table 3.1 - Coefficients a, b, and c in Angstrom formula $\varepsilon_a = a - b\exp(-c\,e_a)$ (reproduced from Pailey et al. , 1974).

Δt = 200 s			Δz = 0.02 m		
Δz (m)	Solution (C°)	Error (%)	Δt (s)	Solution (C°)	Error (%)
0.020	-23.910	.16	200	-23.910	.16
0.025	-23.899	.20	300	-23.904	.19
0.033	-23.876	.30	600	-23.883	.28
0.040	-23.852	.40	900	-23.863	.36
0.050	-23.808	.59	1800	-23.801	.61
0.067	-23.715	.98	3600	-23.676	1.14
0.100	-23.456	2.01	7200	-23.417	2.22

Table 3.7 - Temperatures at mid-depth of the ice cover (analytical solution = 23.949°C).

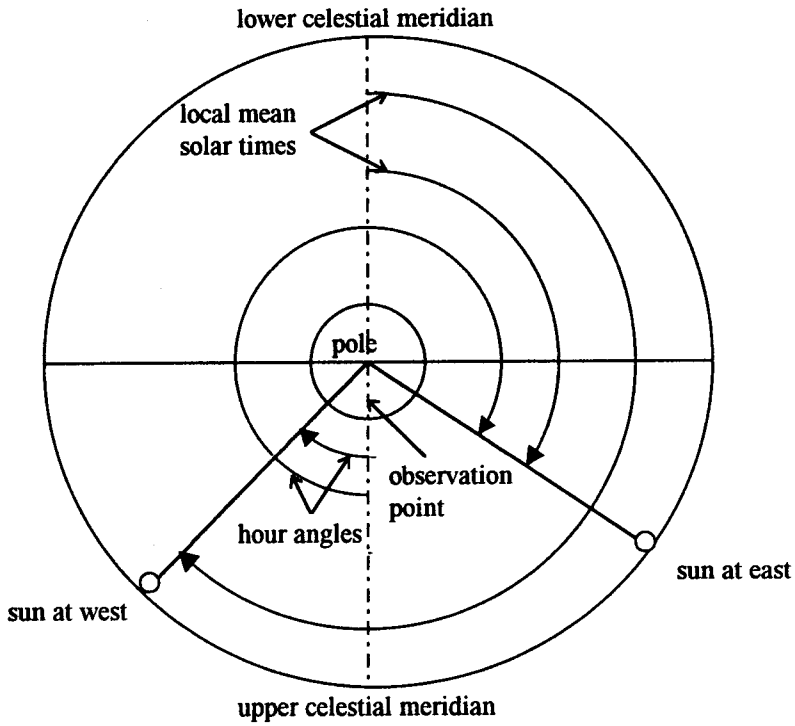

Figure 3.1 - Time diagram for solar radiation (reproduced from Paily et al., 1974).

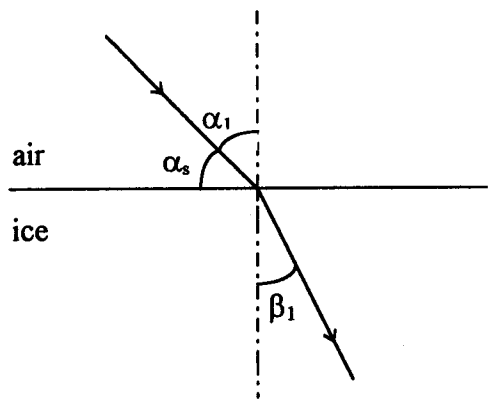

Figure 3.2 - Definition of angles in Equation 3.2.34.

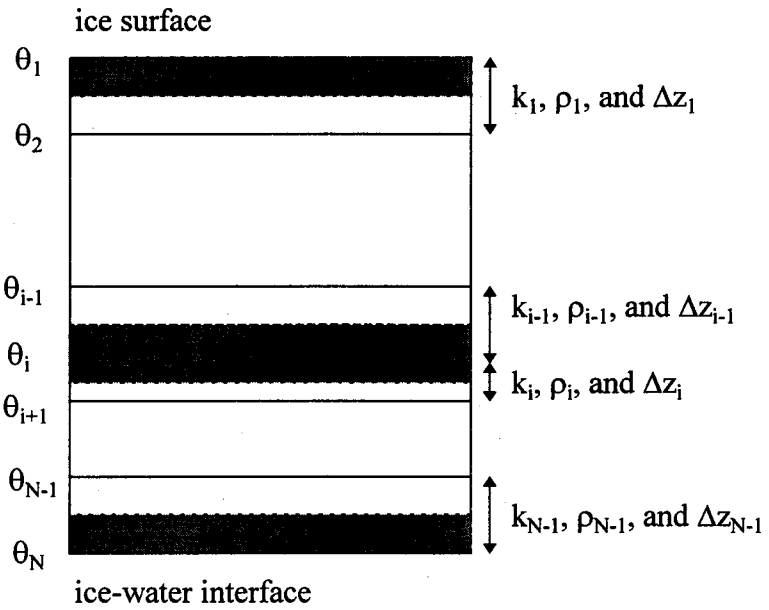

Figure 3.3 - Discretization of the ice cover for finite difference analysis.

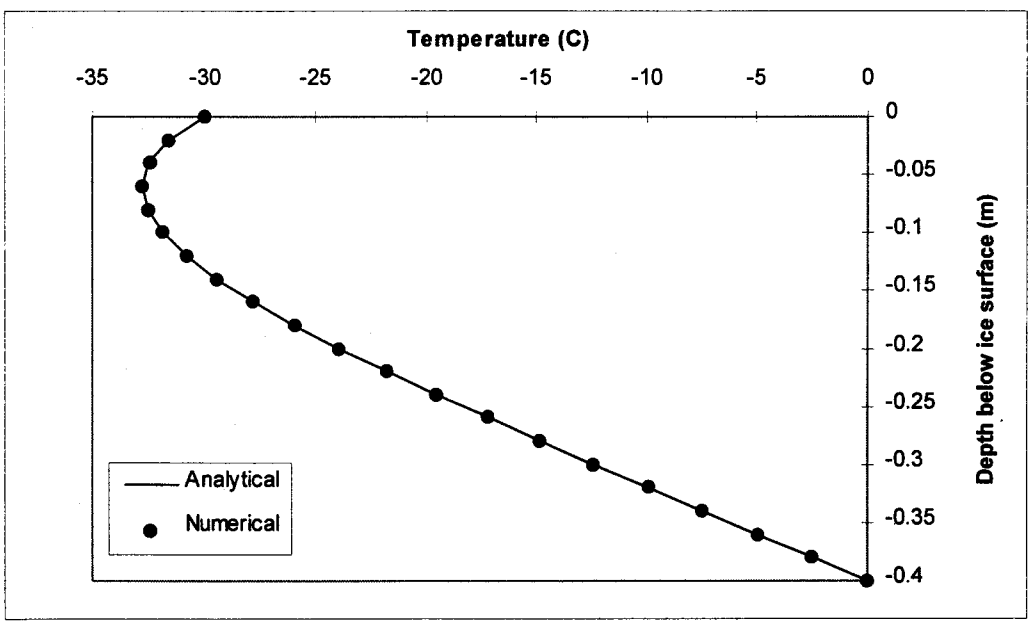

Figure 3.4 - Temperature distribution through the thickness of an ice cover due to sinusoidally varying surface temperature.

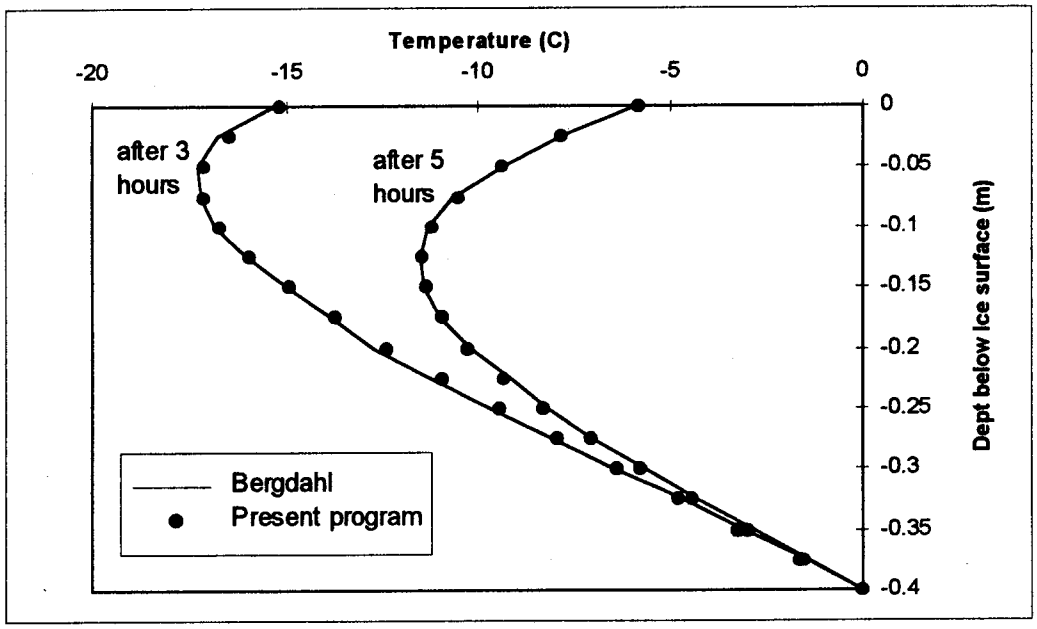

Figure 3.5 - Temperature distribution through the thickness of the ice cover when the coefficient of heat transfer is used.

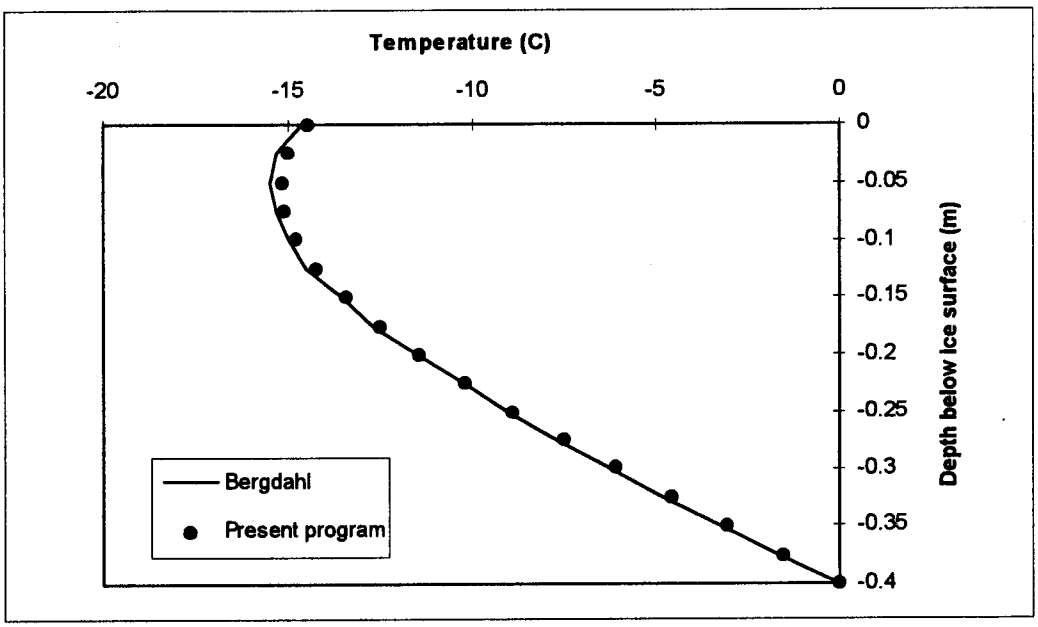

Figure 3.6 - Temperature distribution through the thickness of the ice cover for the complete case without short-wave solar radiation.

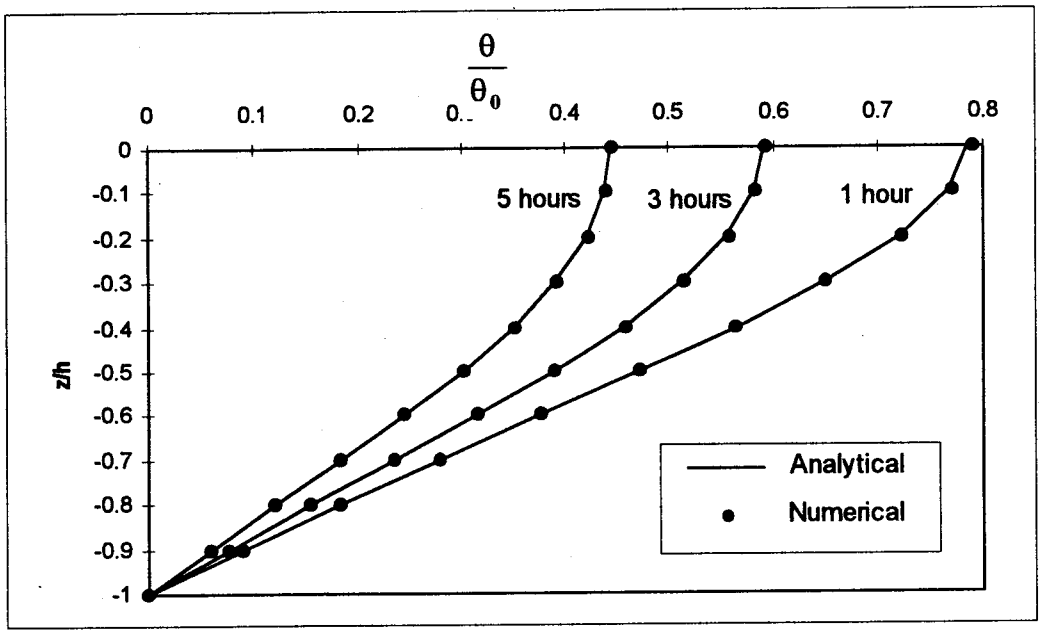

Figure 3.7 - Non-dimensional temperature distribution through the thickness of the ice cover with short-wave solar radiation only.

4 - FINITE ELEMENT FORMULATION

If the temperature distribution in an ice cover is known as a function of time, calculations can then be done to estimate the thermal stress distribution . In this study, a computer program was developed which uses the finite element method. In this chapter the overall formulation of the finite element procedure and the different features of the computer program are described. The finite element used is introduced first, and then the constitutive law and some of the important features of the computer program are explained. This is followed by a description of the solution algorithm and a flowchart of the program. Finally, some numerical tests are described which were performed to verify the model. In these tests the results of the finite element program are compared to available analytical and numerical solutions.

4.1 - Finite Element Used

The finite element program uses a quadratic degenerate shell element. A shell element is used for two reasons. The membrane behavior must be present since that is the dominant mechanism. Bending is included because the nonlinear material behavior couples the membrane and bending effects. The element is referred to as a degenerate element because the formulation begins with a three dimensional element that is subsequently reduced to a shell element by invoking assumptions. Firstly it is assumed that normals to the mid-surface remain practically straight after deformation. Secondly, the stress component normal to mid-surface is constrained to be zero in the constitutive equations.

In a degenerate shell element the nodes are located on the mid-surface and the element geometry is defined by the global coordinates of pairs of points on the top and bottom surface. The mid-surface nodes are midway between these points so that

$$x_{ik}^{mid} = 0.5(x_{ik}^{top} + x_{ik}^{bot}). \qquad (4.1.1)$$

Five degrees of freedom are defined at each node corresponding to the three displacements and the two rotations of the normal at node. The definition of independent rotational and displacement degrees of freedom permits transverse shear deformation to be taken into account, since the rotations are not constrained to be equal to the slope of the mid-surface. The finite element formulation of this element is described in detail in Hinton & Owen (1984) and only the main points are explained here.

In the formulation of the degenerate shell element four different coordinate systems are used:

1. Global coordinate set - x_i

This is a Cartesian coordinate system that is used to define the geometry of the ice cover. Nodal coordinates and displacements as well as the global stiffness matrix and applied force vector are referred to this system. In this study the x and y axes are taken in the plane of the ice cover and the z axes is perpendicular to the ice cover and pointing upwards.

2. Nodal coordinate set $\{v\}_{ik}$

A nodal coordinate system is defined at each nodal point, with the origin at the mid-surface. The vector $\{v\}_{3k}$ extends from the bottom to the top surface at node k so that

$$\{v\}_{3k} = \{x\}_k^{top} - \{x\}_k^{bot} \qquad (4.1.2)$$

where

$$\{x\}_k = [x\ y\ z]_k .$$

The vector $\{v\}_{1k}$ is perpendicular to $\{v\}_{3k}$ and parallel to the global xz plane so that

$$v_{1k}^x = v_{3k}^z \quad , \quad v_{1k}^y = 0.0 \quad , \quad v_{1k}^z = -v_{3k}^x . \qquad (4.1.3)$$

The vector $\{v\}_{2k}$ is perpendicular to the plane defined by $\{v\}_{1k}$ and $\{v\}_{3k}$. The vector $\{v\}_{3k}$ defines the direction of the 'normal' at node k, which is not necessarily perpendicular to the mid -surface at k. The rotations β_{1k} and β_{2k} are defined as the rotations of the normal at node k, about axes in the directions of $\{v\}_{2k}$ and $\{v\}_{1k}$ respectively.

3. Curvilinear coordinate system

A curvilinear coordinate system is defined in which, ξ and η are curvilinear coordinates in the middle surface of the element and ζ is a linear coordinate in the thickness direction. The coordinates are normalized so that ξ, η, and ζ vary between -1 and 1 on the respective faces of the element.

4. Local coordinate system

A local Cartesian coordinate system is defined at each sampling point where stresses and strains are calculated. The direction x_3' is taken perpendicular to the surface of constant ζ. This direction is obtained from the cross product of vectors in the ξ and η directions. The direction of x_1' is perpendicular to x_3' and parallel to global xz plane. The direction of x_2' is defined by the cross product of vectors in the x_3' and x_1' directions. Since the ice covers being modeled are flat, the vector $\{v\}_{3k}$ will be perpendicular to the ice surface and the local x_1' and x_2' axes will coincide with the global x and y axes if the top and bottom nodal coordinates satisfy

$$x_{top} = x_{bot} \quad \text{and} \quad y_{top} = y_{bot}. \tag{4.1.4}$$

The five significant strain components for this element are:

$$\{\varepsilon\} = \begin{Bmatrix} \varepsilon_x \\ \varepsilon_y \\ \gamma_{xy} \\ \gamma_{xz} \\ \gamma_{yz} \end{Bmatrix} \tag{4.1.5}$$

Since the stress in the direction perpendicular to the mid-surface (σ_z) is assumed to be negligible, the five stress components considered in the local system are:

$$\{\sigma\} = \begin{Bmatrix} \sigma_x \\ \sigma_y \\ \tau_{xy} \\ \tau_{xz} \\ \tau_{yz} \end{Bmatrix} \tag{4.1.6}$$

In the thermal loading analysis, the temperature distribution through the thickness of the ice cover is non-uniform. In the present finite element code this is accommodated in a

simple and effective manner using a layered approach. It is assumed that the ice cover is built up from a series of layers. Each layer can have a different temperature and different material properties and the material properties can be a function of that layer's temperature. The stress components are computed at the stress points located on the mid-surface of the layers and the stresses are assumed to be constant over the thickness of each layer. Therefore, the actual stress distribution is modeled by a piecewise constant approximation (Fig. 4.1).

The numerical integration of isoparametric shell elements has received considerable attention in the literature, since it has an important effect on element behavior. For the integration in the ξ and η directions, full or exact integration of an unmapped element can be accomplished using a 3×3 Gaussian integration formula. However it is well known that if degenerate shell elements are fully integrated, they exhibit locking. Therefore, the beneficial effects of reduced (2×2) or selective (3×2) integration techniques have been established in a number of investigation (for example, Zienkiewicz, 1977). For the lower order elements, reduced integration is essential for thin shell applications; for higher order elements, significant improvements in accuracy are attained with reduced integration. In the reduced integration technique all of the components of the strain energy are integrated using the four sampling points. In the selective reduced integration technique, the energies corresponding to membrane strains (ε_x, $\varepsilon_{y,}$, and γ_{xy}), are integrated using the normal rule (3×3), and the energies corresponding to transverse shear strains (γ_{xz} and γ_{yz}), are computed using the reduced integration rule. The process involves the following steps. First the shear terms in the strain-displacement matrix are computed at the four Gauss points. Then using the shape function these terms are extrapolated to the nine Gauss points, where other terms are calculated. However, these techniques may occasionally lead to spurious zero energy modes appearing in the global equations. Usually the global stiffness matrix becomes singular if there is a small number of elements and the number of sampling points is small compared to the number of unrestrained degrees of freedom.

4.2 - Constitutive Law

The constitutive laws adopted for ice are most easily understood by considering their associated one dimensional rheological models as shown in Fig. 4.2. The strain under constant stress for this model is shown in Fig. 4.3. The curve shown in this figure is similar to the experimental curves obtained by Lindgren (Fig. 2.6) for the deformation of ice under constant load. The Maxwell unit consists of a linear spring, which represents the instantaneous elastic deformation, in series with a non-linear dashpot based on power law creep which models the non-recoverable viscous deformation. The Kelvin-Voigt unit consists of a linear spring in parallel with a non-linear dashpot. This unit models the delayed elastic deformation. The use of the Kelvin-Voigt unit is optional in the program.

In a uniaxial model consisting of a Maxwell unit and a Kelvin-Voigt unit subjected to temperature changes, the total strain consists of four parts

$$\varepsilon = \varepsilon_e + \varepsilon_v + \varepsilon_d + \varepsilon_\theta \tag{4.2.1}$$

where

ε = total strain

ε_e = instantaneous elastic strain

ε_v = permanent viscous strain

ε_d = delayed elastic strain

ε_θ = thermal strain.

The elastic strain is related to the applied stress, σ, by the stiffness E_1 of the elastic element in the Maxwell unit. This gives

$$\varepsilon_e = \frac{\sigma}{E_1}. \tag{4.2.2}$$

The viscous strain rate can be expressed as a function of the applied stress. This may be expressed as

$$\dot{\varepsilon}_v = \eta_1 \sigma^n \tag{4.2.3}$$

where n is a constant and η_1 is the fluidity parameter. The fluidity parameter is related to the viscosity (μ_1) by

$$\eta_1 = \frac{1}{\mu_1}. \tag{4.2.4}$$

The delayed elastic strain can be related to the stress, σ', in the elastic element of the Kelvin-Voigt unit by

$$\varepsilon_d = \frac{\sigma'}{E_2} \tag{4.2.5}$$

where E_2 is the stiffness of the spring in Kelvin-Voigt unit. The dashpot in this unit is also based on power law creep which gives the strain rate as

$$\dot{\varepsilon}_d = \eta_2 \sigma''^m \tag{4.2.6}$$

where m is a constant and η_2 is the fluidity parameter of the dashpot.

The applied stress, σ, is the sum of the stresses σ' and σ'', and can be written in terms of the delayed elastic strain and strain rate. This gives

$$\sigma = \sigma' + \sigma''$$

$$= E_2\varepsilon_d + (\frac{1}{\eta_2}\dot{\varepsilon}_d)^{\frac{1}{m}}. \tag{4.2.7}$$

The thermal strain is that due to temperature change and is given by

$$\varepsilon_\theta = \alpha\Delta\theta \tag{4.2.8}$$

where

α = coefficient of thermal expansion

$\Delta\theta$ = temperature changes.

In the finite element formulation, equations 4.2.2 to 4.2.8 are required in a three dimensional form. The three dimensional stress-strain relationship of the elastic element is straight forward and is given by

$$\{\sigma\} = [D_1]\{\varepsilon_e\} \tag{4.2.9}$$

Assuming orthotropic material symmetry and taking σ_3=0 for the finite element (4.2.9) takes the form:

$$\begin{Bmatrix}\sigma_1\\ \sigma_2\\ \sigma_{12}\\ \sigma_{13}\\ \sigma_{23}\end{Bmatrix}=\begin{bmatrix}D_{11} & D_{12} & 0 & 0 & 0\\ D_{12} & D_{22} & 0 & 0 & 0\\ 0 & 0 & D_{33} & 0 & 0\\ 0 & 0 & 0 & D_{44} & 0\\ 0 & 0 & 0 & 0 & D_{55}\end{bmatrix}\begin{Bmatrix}\varepsilon_{11}\\ \varepsilon_{22}\\ \gamma_{12}\\ \gamma_{13}\\ \gamma_{23}\end{Bmatrix} \tag{4.2.10}$$

where

$$D_{11}=\frac{E_{11}}{1-\nu_{12}\nu_{21}} \qquad D_{22}=\frac{E_{12}}{1-\nu_{12}\nu_{21}} \qquad D_{12}=\frac{E_{12}\nu_{12}}{1-\nu_{12}\nu_{21}} \qquad (\frac{\nu_{12}}{E_{11}}=\frac{\nu_{21}}{E_{12}})$$

$$D_{33}=G_{12} \qquad D_{44}=K_1G_{13} \qquad D_{55}=K_2G_{23}$$

K_1, K_2 = shear correction factor.

Assuming that the normal to the mid-surface remains straight, makes the transverse shear strain constant through the thickness. The correction shear factor is introduced to approximate on an average basis, the transverse shear strain energy. For a homogenous cross section, where the shear strain distribution is a parabolic function of z, the shear correction factor is equal to $\frac{5}{6}$.

The three dimensional formulation of the constitutive law for the viscous element is based on the equations suggested by Sanderson (1984). First, an effective stress, τ, is defined which is used to derive the generalized power law stress-strain rate relationship. For an isotropic material the effective stress is the second invariant of the stress deviator tensor and can be written as

$$2\tau^2=(\sigma_{11}-\sigma_{22})^2+(\sigma_{22}-\sigma_{33})^2+(\sigma_{33}-\sigma_{11})^2+6(\sigma_{12}^2+\sigma_{23}^2+\sigma_{13}^2). \tag{4.2.11}$$

For an anisotropic material, considering σ_{33}=0, this may be generalized to

$$\tau^2=a_{11}\sigma_{11}^2+a_{22}\sigma_{22}^2+2a_{12}\sigma_{11}\sigma_{22}+a_{33}\sigma_{12}^2+a_{44}\sigma_{13}^2+a_{55}\sigma_{23}^2. \tag{4.2.12}$$

where a_{11} to a_{55} are constants. In the matrix form it can be written as

$$\tau^2=\langle\sigma\rangle[A]\{\sigma\} \tag{4.2.13}$$

where

$$\langle\sigma\rangle=\langle\sigma_{11}\quad\sigma_{22}\quad\sigma_{12}\quad\sigma_{13}\quad\sigma_{23}\rangle$$

$$[A]=\begin{bmatrix} a_{11} & a_{12} & 0 & 0 & 0 \\ a_{12} & a_{22} & 0 & 0 & 0 \\ 0 & 0 & a_{33} & 0 & 0 \\ 0 & 0 & 0 & a_{44} & 0 \\ 0 & 0 & 0 & 0 & a_{55} \end{bmatrix}$$

For isotropic materials:

$a_{11} = a_{22} = 1.0$, $a_{12} = -0.5$, and $a_{33} = a_{44} = a_{55} = 3.0$.

Then a scalar potential function, Φ, is defined which allows the calculation of viscous strain rate from the effective stress. This function is given by

$$\Phi = \frac{\eta_1 \tau^{n+1}}{n+1} \tag{4.2.14}$$

where η and n have the same definition as in the one dimensional model. Finally the viscous strain rate may be expressed as

$$\dot{\varepsilon}_{v\,ij} = \frac{\partial \Phi}{\partial \sigma_{ij}} = \eta_1 \tau^n \frac{\partial \tau}{\partial \sigma_{ij}} \tag{4.2.15}$$

From (4.2.13) it follows that:

$$\frac{\partial \tau}{\partial \sigma} = \frac{1}{\tau}[A]\{\sigma\} \tag{4.2.16}$$

so the matrix form of (4.2.15) becomes:

$$\{\dot{\varepsilon}_v\} = \eta_1 \tau^{n-1}[A]\{\sigma\}. \tag{4.2.17}$$

The three dimensional formulation of the delayed elastic element is based on the constitutive equations suggested by Khoo (1989). The stress-strain relationship for the elastic component is similar to that of an elastic material. This is given by

$$\{\varepsilon_d\} = \frac{1}{E_2}[P]\{\sigma'_d\} \tag{4.2.18}$$

where

E_2 = modulus of elasticity for the elastic component of the delayed elastic element

$\{\sigma'_d\}$ = stress in the elastic component

and

$$[P]=\begin{bmatrix} 1 & -\nu & 0 & 0 & 0 \\ -\nu & 1 & 0 & 0 & 0 \\ 0 & 0 & 2(1+\nu) & 0 & 0 \\ 0 & 0 & 0 & \dfrac{2(1+\nu)}{K_1} & 0 \\ 0 & 0 & 0 & 0 & \dfrac{2(1+\nu)}{K_2} \end{bmatrix}$$

The stress in the viscous component of the delayed elastic element is equal to:

$$\{\sigma_d''\} = \{\sigma\} - \{\sigma_d'\} \tag{4.2.19}$$

The delayed elastic strain rate is obtained from $\{\sigma_d''\}$ in the form of

$$\{\dot{\varepsilon}_d\} = \eta_2(\sigma_{eff}'')^{m-1}[P]\{\sigma_d''\} \tag{4.2.20}$$

where

$$\sigma_{eff}'' = \sqrt{\sigma_{d\,11}''^2 + \sigma_{d\,22}''^2 + 2\sigma_{d\,12}''^2 + 2\sigma_{d\,13}''^2 + 2\sigma_{d\,23}''^2} \tag{4.2.21}$$

As explained by Khoo (1989), the parameter σ_{eff}'' takes into account the effect of biaxial stress on the strain rate. The influence of each component of σ'' on the rate is related by the matrix [P]. In the elastic part of the delayed elastic element, the delayed elastic strain ε_d is also related to each component of σ' by the matrix [P]. According to Khoo

> "The use of [P] in both elastic and viscous parts makes the delayed elastic term coordinate invariant."

4.3 - Some Features of the Computer Program

4.3.1 - Elastic Foundation

Natural ice covers are normally floating on the water. When there is no deformation the weight of the ice cover is in equilibrium with the buoyancy force, and because of the relationship between the specific weights of ice and water, 90% of the ice is below the water. Bending of the ice cover, causes downward and upward displacements at different

positions. The water resists such displacement. Since the hydrostatic pressure increases linearly with depth from the free surface, the force at each point is proportional to the displacement at that point. This effect can be modeled by a uniform linear elastic foundation. The stiffness of the unit area of the elastic foundation is equal to the unit weight of water. The force over a differential element of area is then equal to:

$$dF_w = S_w u dA \tag{4.3.1}$$

where

S_w = stiffness of the elastic foundation

u = vertical displacement of the small surface.

In the finite element formulation, the displacement of a point within an element can be expressed in terms of the displacements of the element nodes.

$$dF_w = S_w \sum_{i=1}^{nn} N_{zi} q_i dA \tag{4.3.2}$$

where

N_{zi} = nodal shape function for vertical displacements

nn = number of nodes

q_i = nodal displacements

In the matrix form it can be written as:

$$dF_w = S_w \langle N_z \rangle \{q\} dA \tag{4.3.3}$$

The total force acting on an element can be obtained by integration over the element surface.

$$F_{w\,el} = \int_{A\,el} S_w \langle N_z \rangle \{q\} dA \tag{4.3.4}$$

4.3.2 - Boundary Elements

In this study, boundary elements are used to model the effect of inclined shore lines and non-rigid boundaries. These elements are linear springs that are attached to the nodal points and can be oriented in any direction in space. The orientation and stiffness of these elements is given as a part of input data.

4.3.3 - Tensile Cracking

According to Metge's observations (section 2.11), dry cracks are the most common cracks in ice covers. These are tensile cracks which form during cooling periods when the upper region of the ice sheet tries to contract. They are called dry cracks because they do not penetrate through the entire thickness and hence do not fill with water. The contraction happens only in the upper part of the sheet and it is restrained by the rest. (Fig 2.13). The cracks observed by Metge had an average crack width of about 0.5 cm and an average spacing of about 25m. These kinds of cracks are important in the stress analysis, because they affect the stresses during and after cooling periods.

In this study a smeared crack approach is used to model the dry cracks. In this approach the cracked ice is assumed to remain a continuum and the effect of the cracks is smeared out in a continuous fashion. The initiation of cracking is governed by a maximum tensile stress criterion (tension cut-off). At each iteration and at each Gauss point, the maximum principal stress in the horizontal plane is compared to the specified tensile strength (f_t). Cracks are assumed to form only in planes perpendicular to the ice cover. If the maximum stress exceeds the tensile strength, a crack forms in a plane perpendicular to the direction of the maximum principal stress. After cracking has occurred, the elasticity modulus and the numerical value of the stress from the previous step are reduced to zero in the direction perpendicular to the cracked plane. The Poisson's ratio is also set to zero. The ice becomes orthotropic after the first crack occurs with one of the material axes being oriented along the direction of cracking. Denoting the two principal directions in the xy plane with the subscripts 1 and 2, the elasticity matrix referred to coordinates in these direction is :

$$[D]_{cracked} = \begin{bmatrix} 0 & 0 & 0 & 0 & 0 \\ 0 & E & 0 & 0 & 0 \\ 0 & 0 & G_{12}^{cr} & 0 & 0 \\ 0 & 0 & 0 & G_{13}^{cr} & 0 \\ 0 & 0 & 0 & 0 & \frac{5G}{6} \end{bmatrix} \qquad (4.3.5)$$

where G_{12}^{cr} and G_{13}^{cr} are the reduced shear moduli. The value for the reduced shear modulus should be obtained from tests. Due to the lack of information, these values are also set to zero in the present model. If the stress in the 2 direction reaches f_t, a second crack perpendicular to the first is assumed to form and all the terms in the elasticity matrix and all the stresses are set to zero. At each iteration, the strain perpendicular to the crack is calculated and if this strain becomes negative, it is assumed that the corresponding crack is closed so that it can carry tension again. Cracking can occur independently at different layers so that cracks need not penetrate through the whole thickness.

4.3.4 - Loading Due to Water Level Changes

When an ice cover is bonded to the shore or to a hydraulic structures, water level changes might decrease or increase the buoyancy force of water on the ice cover. This effect is modeled using a distributed uniform load. The time history of any water level changes is given as input to the program. At the start of the analysis the weight of the water replacing the ice cover is calculated and divided by the thickness. This gives the force per unit area per unit change in water level. At each increment this force is multiplied by the water level changes and applied to the ice sheet.

4.4 - Overall Formulation

In the finite element formulation the total time is divided into a number of steps or time increments. The temperature of the ice cover and the water level might vary during each step causing additional thermal and mechanical loading. Therefore in each time step there is a nonlinear problem to deal with. There are different ways of dealing with this situation. The procedure used here, is based on the implicit method discussed by Zienkiewicz (1977).

At the beginning of each time increment, all the displacements, stresses, and forces are known. The viscous and delayed elastic strain rate at each step are calculated from an

intermediate value of the stress within that time step. Since the stresses at the end of the step are not known, an iterative procedure is required to obtain an estimate for these stresses. In the following description of this procedure, the subscript, I, denotes the time increment number and the superscript, J, denotes the iteration number.

At the end of each time step there are two conditions that have to be satisfied:

1) The equilibrium condition:

The principal of virtual work can be used to obtain the equilibrium equations. The virtual work equation can be written as:

$$\int_v \sigma_{ij}\delta\varepsilon_{ij}dv + \int_A F_{wi}\delta u_{zi}dA = \int_s \overline{T}_i\delta u_i ds + \int_v \overline{F}_i\delta u_i dv \qquad (4.4.1)$$

In the finite element formulation, the virtual strains and displacements at each point within an element can be obtained from the nodal displacements.

$$\{\delta u\} = [N]\{\delta q\} \qquad (4.4.2)$$

$$\{\delta\varepsilon\} = [B]\{\delta q\} \qquad (4.4.3)$$

where

$\{q\}$ = nodal displacements

$[N]$ = shape function matrix

$[B]$ = strain-displacement matrix.

In matrix form the equation of virtual work becomes :

$$\int_v \langle\delta q\rangle[B]^T\{\sigma\}dv + \int_A S_w\langle\delta q\rangle\{N_z\}\langle N_z\rangle\{q\}dA = \int_s \langle\delta q\rangle[N]^T\{\overline{T}\}ds + \int_v \langle\delta q\rangle[N]^T\{\overline{F}\}dv \qquad (4.4.4)$$

Since (4.4.4) must be satisfied for an arbitrary $\langle\delta q\rangle$ (subject to $\langle\delta q\rangle = \langle 0\rangle$ on S_u), it follows that :

$$\int_v [B]^T\{\sigma\}_{I+1}dv + \int_A S_w\{N_z\}\langle N_z\rangle\{q\}_{I+1} - \{F\}_{I+1} = \{0\} \qquad (4.4.5)$$

where

$$\{F\} = \int_s [N]^T\{\overline{T}\}ds + \int_v [N]^T\{\overline{F}\}dv$$

Equation (4.4.5) is the equilibrium equation at the end of the time step.

2) Considering that the elastic properties may change during the time step, the incremental form of the elastic constitutive equation can be written as

$$\{\Delta\sigma\} = [D_1](\{\Delta\varepsilon\} - \{\Delta\varepsilon_c\} - \{\Delta\varepsilon_\theta\}) + [\Delta D_1]\{\varepsilon_e\} \tag{4.4.6}$$

or

$$\{\sigma\}_{I+1} - \{\sigma\}_I - [D_1]_I[B](\{q\}_{I+1} - \{q\}_I) + [D_1]_I\{\Delta\varepsilon_c\}_{I+\beta} + [D_1]_I\{\Delta\varepsilon_\theta\} - [\Delta D_1]_I\{\varepsilon_e\}_I = \{0\} \tag{4.4.7}$$

where

$[\Delta D_1]$ = Changes in elasticity matrix due to temperature changes

$\{\Delta\varepsilon_c\} = \{\Delta\varepsilon_v\} + \{\Delta\varepsilon_d\}$

$$\{\Delta\varepsilon_\theta\} = \begin{Bmatrix} \alpha\Delta\theta \\ \alpha\Delta\theta \\ 0 \\ 0 \\ 0 \end{Bmatrix}$$

The viscous and delayed elastic strain increment are calculated from intermediate values for the stresses that are obtained by a linear interpolation between the stresses at the start and end of the time step. This is done both for the total stress and for the stress, $\{\sigma''\}$, in the viscous part of the delayed elasticity element. This gives

$$\{\sigma\}_{I+\beta_1} = (1-\beta_1)\{\sigma\}_I + \beta_1\{\sigma\}_{I+1} \tag{4.4.8}$$

$$\{\sigma''\}_{I+\beta_2} = (1-\beta_2)\{\sigma\}_I + \beta_2\{\sigma\}_{I+1} - \{\sigma'\}_I \tag{4.4.9}$$

where β_1 and β_2 are constants with values between 0 and 1. As a matter of convenience, the values of β_1 and β_2 were taken to be equal. This value is denoted by β in the following.

The conditions (4.4.5) and (4.4.7) form a set of non-linear equations with $\{\sigma\}_{I+1}$ and $\{q\}_{I+1}$ as the unknowns. An iterative procedure can be used to solve this system of equations. The solution scheme starts with an initial estimate for $\{\sigma\}_{I+1}$ and $\{q\}_{I+1}$. The corresponding values at the start of the time step are used so that

$\{\sigma\}_{I+1} = \{\sigma\}_I$ and $\{q\}_{I+1} = \{q\}_I$.

Equation (4.4.7) can be written as:

$$\{\phi\}_{I+1}^{J+1} = \{\sigma\}_{I+1}^{J} - \{\sigma\}_{I} - [D_1]_I[B](\{q\}_{I+1}^{J} - \{q\}_I) + [D_1]_I\{\Delta\varepsilon_c\}_{I+\beta}^{J} + [D_1]_I\{\Delta\varepsilon_\theta\} - [\Delta D_1]\{\varepsilon_e\}_I$$

$$= \{0\} \tag{4.4.10}$$

where $\{\phi\}$ can be considered a residual that becomes zero when (4.4.7) is satisfied. A first order approximation for the residual at the start of the next iteration can be written in terms of changes in the stress and strain during the current increment.

$$\{\phi\}_{I+1}^{J+1} \approx \{\phi\}_{I+1}^{J} + \{\delta\sigma\}_{I+1}^{J} - [D_1]_I[B]\{\delta q\}_{I+1}^{J} + [D_1]_I[R]_{I+\beta}^{J}\beta\{\delta\sigma\}_{I+1}^{J} = \{0\} \tag{4.4.11}$$

where

$\{\delta\sigma\}_{I+1}^{J}$ = the change in stress in the J^{th} iteration

$\{\delta q\}_{I+1}^{J}$ = the change in the nodal displacements in the J^{th} iteration

$$[R]_{I+\beta}^{J} = \frac{\partial\{\Delta\varepsilon_v\}_{I+\beta}^{J}}{\partial\{\sigma\}_{I+\beta}} + \frac{\partial\{\Delta\varepsilon_d\}_{I+\beta}^{J}}{\partial\{\sigma\}_{I+\beta}}$$

Using the equation 4.2.17 for the viscous strain rate, an estimate of the viscous strain increment can be written as:

$$\{\Delta\varepsilon_v\}_{I+\beta} = \Delta t\{\dot{\varepsilon}_v\}_{I+\beta} = \Delta t\eta_1\tau_{I+\beta}^{n-1}[A]\{\sigma\}_{I+\beta} \tag{4.4.12}$$

where Δt is the time step. It follows that

$$\frac{\partial\{\Delta\varepsilon_v\}_{I+\beta}^{J}}{\partial\{\sigma\}_{I+\beta}} = \Delta t\eta_1((n-1)\tau_{I+\beta}^{n-3}[A]\{\sigma\}_{I+\beta}\langle\sigma\rangle_{I+\beta}[A]^T + \tau_{I+\beta}^{n-1}[A]). \tag{4.4.13}$$

The delayed elastic strain rate can be written as:

$$\frac{d}{dt}\{\varepsilon_d\} = \eta_2(\sigma''_{eff\ I+\beta})^{m-1}[P](\{\sigma\}_{I+\beta} - \{\sigma'\}_I) \tag{4.4.14}$$

where

$$\{\sigma'\} = E_2[P]^{-1}\{\varepsilon_d\} \tag{4.4.15}$$

Substituting equation (4.4.15) into (4.4.14) gives:

$$\frac{d}{dt}\{\varepsilon_d\} = \{c_1\} - c_0\{\varepsilon_d\} \tag{4.4.16}$$

where

$$\{c_1\} = \eta_2(\sigma''_{\text{eff } I+\beta})^{m-1}[P]\{\sigma\}_{I+\beta}$$

$$c_0 = \eta_2 E_2(\sigma''_{\text{eff } I+\beta})^{m-1}$$

Since $\sigma''_{\text{eff } I+\beta}$ and $\sigma_{I+\beta}$ are taken to be constant within the time step, $\{c_1\}$ and c_0 will also be constants.

The differential equation (4.4.16) was solved by Khoo (1989) and the result is the following:

$$\{\Delta\varepsilon_d\}_I = \left(\frac{1}{E_2}[P]\{\sigma\}_{I+\beta} - \{\varepsilon_d\}_I\right)\left(1 - \exp(-\eta_2 E_2(\sigma''_{\text{eff } I+\beta})^{m-1}\Delta t)\right) \tag{4.4.17}$$

The rate of change of the delayed elastic strain increment is approximated by:

$$\left[\frac{\partial\Delta\varepsilon_{d\,I}}{\partial\sigma_{I+1}}\right] = \frac{\beta[P]}{E_2}\left(1 - \exp(-c_0\Delta t)\right) \tag{4.4.18}$$

After some manipulation (4.4.11) becomes:

$$\left([I] + [D_1]_I[R]^J_{I+\beta}\beta\right)\{\delta\sigma\}^J_{I+1} = [D_1]_I[B]\{\delta q\}^J_{I+1} - \{\phi\}^J_{I+1} \tag{4.4.19}$$

Solving for the stress increment at iteration J gives:

$$\{\delta\sigma\}^J_{I+1} = \left([I] + [D_1]_I[R]^J_{I+\beta}\beta\right)^{-1}[D_1]_I[B]\{\delta q\}^J_{I+1} - \left([I] + [D_1]_I[R]^J_{I+\beta}\beta\right)^{-1}\{\phi\}^J_{I+1} \tag{4.4.20}$$

or

$$\{\delta\sigma\}^J_{I+1} = [\overline{D}]^J[B]\{\delta q\}^J_{I+1} - \{\overline{\phi}\}^J_{I+1} \tag{4.4.21}$$

where

$$[\overline{D}]^J = \left([I] + [D_1]_I[R]^J_{I+\beta}\beta\right)^{-1}[D_1]_I$$

$$\{\overline{\phi}\}^J_{I+1} = \left([I] + [D_1]_I[R]^J_{I+\beta}\beta\right)^{-1}\{\phi\}^J_{I+1}$$

The new estimates for the stress and displacement at the end of the iteration can be obtained from:

$$\{\sigma\}^{J+1}_{I+1} = \{\sigma\}^J_{I+1} + \{\delta\sigma\}^J_{I+1} \tag{4.4.22}$$

$$\{q\}^{J+1}_{I+1} = \{q\}^J_{I+1} + \{\delta q\}^J_{I+1} \tag{4.4.23}$$

Substituting (4.4.21) to (4.4.23) into the equilibrium equation(4.4.5) gives..

$$\int_v [B]^T \left(\{\sigma\}_{I+1}^J + \{\delta\sigma\}_{I+1}^J \right) dv + \int_A S_w \{N_z\}\langle N_z\rangle \left(\{q\}_{I+1}^J + \{\delta q\}_{I+1}^J \right) dA - \{F\}_{I+1} = \{0\} \quad (4.4.24)$$

$$\int_v [B]^T [\bar{D}]^J [B] \{\delta q\}_{I+1}^J dv + \int_A S_w \{N_z\}\langle N_z\rangle \{\delta q\}_{I+1}^J dA =$$

$$[F]_{I+1} - \int_v [B]^T \left(\{\sigma\}_{I+1}^J - \{\bar{\phi}\}_{I+1}^J \right) dv - \int_A S_w \{N_z\}\langle N_z\rangle \{q\}_{I+1}^J dA \quad (4.4.25)$$

This can be written in the form

$$[K]\{\delta q\}_{I+1}^J = \{f\}_{I+1}^J \quad (4.4.26)$$

where

$$[K] = \int_v [B]^T [\bar{D}]^J [B] dv + \int_A S_w \{N_z\}\langle N_z\rangle dA$$

$$\{f\}_{I+1}^J = \{F\}_{I+1} + \int_v [B]^T \left(\{\sigma\}_{I+1}^J - \{\bar{\phi}\}_{I+1}^J \right) dv - \int_A S_w \{N_z\}\langle N_z\rangle \{q\}_{I+1}^J dA$$

The iteration process is continued until the convergence criteria is satisfied. The following criteria is used for this purpose:

$$\frac{\|f\|}{\|F + F_\theta\|} \le \lambda_c \quad (4.4.27)$$

where λ_c is the error limit and F_θ is the load vector for the total thermal strain.

$$\{F_\theta\} = \int_v [B]^T [D_1] \{\varepsilon_\theta\} dv \quad (4.4.28)$$

4.5 - Flowchart of the Computer Program

The flowchart of the computer program is shown in Fig. 4.4. All the symbols in this flowchart are defined in section 4.4.

4.6 - Comparison with Available Analytical and Numerical Solutions

In this section the predictions of the model are verified by comparison with some available analytical and numerical solutions. The tests are selected so that they cover different aspects of the model. In the uniaxial tests the predicted stresses and strains in both constitutive models are compared to the analytical solution for the differential equation of the rheological model. Then the displacements in a model consisting of a Maxwell unit are compared to another finite element solution corresponding to the creep of plates under mechanical loading. In another series of tests the effect of the elastic foundation is verified for an elastic material and for both thermal and mechanical loading. Comparisons with laboratory and field data are performed in Chapter 5.

4.6.1 - Uniaxial Stress in a Model Consisting of a Maxwell unit

In a model consisting of a Maxwell unit (Fig. 4.2), the stress can be related to the elastic strain by

$$\sigma = E_1\varepsilon_e = E_1(\varepsilon - \varepsilon_v). \tag{4.6.1}$$

Differentiating 4.6.1 with respect to time and assuming that the exponent of the stress in dashpot is equal to one, gives

$$\dot{\sigma} = E_1(\dot{\varepsilon} - \dot{\varepsilon}_v) = E_1(\dot{\varepsilon} - \eta_1\sigma) \tag{4.6.2}$$

or

$$E_1\dot{\varepsilon} = \dot{\sigma} + E_1\eta_1\sigma. \tag{4.6.3}$$

Equation 4.6.3 is the governing differential equation for the rheological model consisting of a Maxwell unit.

For stress under constant strain, the strain rate, $\dot{\varepsilon}$, is zero. Assuming initial condition as

$$\sigma = E_1\varepsilon \quad \text{at } t = 0 \tag{4.6.4}$$

The solution to the differential equation would be

$$\sigma = E_1\varepsilon \exp(-E_1\eta_1 t) \tag{4.6.5}$$

A clamped beam is used to model the uniaxial conditions. All of the rotations and the displacements except the displacements in y direction are restrained. In order to simulate the uniaxial conditions Poisson's ratio is set equal to zero. Thermal loading is used to generate a constant strain. A temperature increase of 10°C is applied at the start of the analysis, and then the temperature is kept constant. In these conditions only the stress in x direction is non-zero. The modulus of elasticity is chosen to be 1000 MPa, the stress exponent is 1, and the fluidity parameter is $1\times10^{-7}s^{-1}MPa^{-1}$. The modulus of elasticity and fluidity parameter are both constant and do not change with temperature.

Figure 4.5 shows the comparison between the stress obtained from the analytical solution (4.6.5), and the finite element solution with different time steps. With time steps of 100s and 1000s the error is less than 1% and 5% respectively.

For stress under constant strain rate, the strain rate, $\dot{\varepsilon}$, is constant , and assuming the initial condition

$$\sigma = 0 \qquad \text{at } t = 0 \tag{4.6.6}$$

the solution of 4.6.4 is

$$\sigma = \frac{\dot{\varepsilon}}{\eta_1}\left[1-\exp(-E_1\eta_1 t)\right]. \tag{4.6.7}$$

A constant temperature rate of 3.6°C/h was applied to the same beam with the same material parameters as described for the previous test. With constant material parameters this thermal load will simulate a constant stain rate loading. Figure 4.6 shows the comparison between the stresses obtained from equation 4.6.7, and from the finite element program with different time steps. The results are found to agree to three figures when the time step is equal to 100s. Even when the time step is equal to half an hour, the error is less than 4% at the start of the problem and gets smaller with increasing time.

4.6.2 - Uniaxial Stress in a Model with Delayed Elasticity

For the rheological model in Fig. 4.2, assuming that the exponent of stress is equal to one in both dashpots, the stress strain relationship for different components of the model will be

$$\varepsilon_e = \frac{\sigma}{E_1}, \qquad \varepsilon_v = \eta_1 \sigma, \qquad \varepsilon_d = \frac{\sigma'}{E_2}, \quad \text{and} \quad \dot{\varepsilon}_d = \eta_2 \sigma''. \tag{4.6.8}$$

The total strain is the sum of the strain at the different components and is given by

$$\varepsilon = \varepsilon_e + \varepsilon_v + \varepsilon_d \tag{4.6.9}$$

The stress is also equal to the sum of the stresses in the spring and dashpot of the Kelvin-Voigt unit. This may be expressed as

$$\sigma = \sigma' + \sigma'' = E_2 \varepsilon_d + \frac{1}{\eta_2}\dot{\varepsilon}_d = E_2(\varepsilon - \varepsilon_v - \varepsilon_e) + \frac{1}{\eta_2}(\dot{\varepsilon} - \dot{\varepsilon}_v - \dot{\varepsilon}_e)$$

or

$$\sigma = E_2\left(\varepsilon - \varepsilon_v - \frac{\sigma}{E_1}\right) + \frac{1}{\eta_2}\left(\dot{\varepsilon} - \eta_1\sigma - \frac{\dot{\sigma}}{E_1}\right). \tag{4.6.10}$$

Differentiating 4.6.10 with respect to time, using the equations 4.6.8, and rearranging gives the governing differential equation of the rheological model as

$$\ddot{\varepsilon} + E_2\eta_2\dot{\varepsilon} = \frac{\ddot{\sigma}}{E_1} + \dot{\sigma}\left(\eta_2 + \eta_2\frac{E_2}{E_1} + \eta_1\right) + \sigma E_2\eta_1\eta_2. \tag{4.6.11}$$

When the stress is constant, equation 4.6.11 reduces to

$$\ddot{\varepsilon} + E_2\eta_2\dot{\varepsilon} = \sigma E_2\eta_1\eta_2. \tag{4.6.12}$$

In this case the initial conditions are

$$\varepsilon = \frac{\sigma}{E_1}, \quad \text{and} \quad \varepsilon_d = 0 \quad \text{at } t = 0 \tag{4.6.13}$$

The second condition gives

$$\sigma = \sigma' = \frac{1}{\eta_2}\dot{\varepsilon}_d = \frac{1}{\eta_2}(\dot{\varepsilon} - \dot{\varepsilon}_v) = \frac{1}{\eta_2}(\dot{\varepsilon} - \sigma\eta_1)$$

or

$$\dot{\varepsilon} = \sigma(\eta_1 + \eta_2). \tag{4.6.14}$$

The solution to 4.6.12 that satisfies 4.16.13 is:

$$\varepsilon = \frac{\sigma}{E_1} + \sigma\eta_1 t + \frac{\sigma}{E_2}[1 - \exp(-E_2\eta_2 t)]. \tag{4.6.15}$$

In the finite element simulation a tensile load is applied to the same beam as described earlier but with free movement at one end in x direction. The tensile stress produced is 2.0 MPa. The material properties are:

E_1=2000 MPa, E_2=1000 MPa, $\eta_1=1\times10^{-7}s^{-1}MPa^{-1}$, and $\eta_2=5\times10^{-7}s^{-1}MPa^{-1}$

Figure 4.7 shows the comparison between the results of the analytical solution and the finite element solution with different time steps. The strains agree to three figures when the time step is equal to 100s. When the time step is equal to 1000s the error is about 10% at the start of the problem and decreases with time.

When the strain is constant, assuming

$E_1 = E_2$, and $\eta_1 = \eta_2$

equation 4.6.11 reduces to

$$\ddot{\sigma} + 3E_1\eta_1\dot{\sigma} + E_1^2\eta_1^2\sigma = 0 \tag{4.6.16}$$

The initial conditions are

$$\sigma = E_1\varepsilon, \quad \text{and} \quad \varepsilon_d = 0 \quad \text{at } t = 0 \tag{4.6.17}$$

The second condition gives

$$\sigma = \sigma' = E_1\varepsilon = \frac{1}{\eta_1}\dot{\varepsilon}_d = \frac{1}{\eta_1}(-\frac{\dot{\sigma}}{E_1} - \eta_1 E_1\varepsilon)$$

or

$$\dot{\sigma} = -2E_1^2\eta_1\varepsilon. \tag{4.6.18}$$

The solution to 4.6.16 that satisfies 4.6.17 is

$$\sigma = 0.5(1+\frac{1}{\sqrt{5}})E_1\varepsilon\exp[-0.5(3+\sqrt{5})E_1\eta_1 t] + 0.5(1-\frac{1}{\sqrt{5}})E_1\varepsilon\exp[-0.5(-3+\sqrt{5})E_1\eta_1 t] \tag{4.6.19}$$

In the finite element analysis the clamped beam is subjected to an instantaneous temperature rise of 10°C. The material properties are:

$E_1 = E_2 = 1000$ MPa, and $\eta_1 = \eta_2 = 1\times10^{-7}s^{-1}MPa^{-1}$.

The comparison between the stresses obtained from the analytical solution using equation 4.6.19, and from the finite element program with different time steps is shown in

Fig. 4.8. The error with time steps of 100s and 1000s is less than 1% and 7% respectively.

4.6.3 - Steady State Creep of Plates Under Mechanical Loading

In this section the predictions of the finite model for creep of plates under constant load are compared to another finite element solution given by Hrudey (1973). In the analysis performed by Hrudey the constitutive law is the same as the present model with a Maxwell unit. The results are presented in a non-dimensional form for the displacement rate or velocity under steady state conditions. Figure 4.9 shows the comparison between the non-dimensional vertical velocities along the radius for a simply supported circular plate under point load, p_0. The numbers for n correspond to the stress exponent and the non-dimensional velocity is given by

$$v = \frac{\dot{w}}{\kappa_n a^2}\left(\frac{2\pi M_n}{p_0}\right)^n \tag{4.6.20}$$

where

$$\kappa_n = \frac{2\dot{\varepsilon}_n}{h}, \tag{4.6.21}$$

$$M_n = \frac{n\sigma_n h^2}{2(2n+1)}, \tag{4.6.22}$$

$\dot{w}$ = vertical displacement rate,

h = thickness of the plate,

$\dot{\varepsilon}_n$ = an arbitrary standard constant equal to the strain rate of uniaxial specimen under a stress σ_n .

Table 4.1 shows the comparison for non-dimensional steady state vertical velocities at the center of a uniformly loaded circular plate under a uniformly distributed load q_0. As can be seen the agreement is good for both loading conditions.

4.6.4 - Elastic Foundation

Analytical solutions are available for elastic rectangular plates on elastic foundations (Timoshenko and Woinowsky-Kreiger, 1959). In this section the results are compared for a simply supported square plate under uniformly distributed and point loads. In the finite element model using symmetry, a quarter of the plate is modeled with four elements. The material properties and the dimensions of the plate are:

$E = 200000$ MPa, $\nu = 0.3$,

$h = 0.2$m, dimensions = 6×6 m, $S_w = 100$ MN/m^2

uniformly distributed load = 1 MN/m, and point load = 10 MN.

The results for the vertical displacements along the center line of the plate are shown in Table 4.2. The results also depend on the integration technique. Therefore the results for both the complete and a reduced integration rule are shown in the table.

The analytical solution is also available for an elastic beam on elastic foundation under non-uniform thermal loading (Hrudey, 1992). The classical differential equation for a beam on elastic foundation is:

$$EI\frac{d^4w}{dx^4} + k_f w = 0 \qquad (4.6.23)$$

where w is the vertical displacement and k_f is the stiffness of the foundation. It is assumed that the beam under goes a temperature change which is non-uniform across the section but has the same distribution for all sections. This assumption means that in the absence of any constraint, including the foundation, the beam would deform into a state of constant curvature, denoted by κ_0. Therefore, when the foundation is included the bending moment in any cross section would be

$$M = -EI(\frac{d^2w}{dx^2} - \kappa_0) \qquad (4.6.24)$$

Assuming a symmetry with respect to the center of the beam, and free boundary conditions with zero moments and zero shears at the ends, the non-dimensional form of the solution to 4.6.23 is

$$\frac{w\lambda^2}{\kappa_0} = \frac{(\cosh\lambda l \sin\lambda l + \sinh\lambda l \cos\lambda l)\sinh\lambda l\xi \sin\lambda l\xi}{(\sin\lambda l \cos\lambda l + \sinh\lambda l \cosh\lambda l)} +$$

$$\frac{(\sinh\lambda l \cos\lambda l - \cosh\lambda l \sin\lambda l)\cosh\lambda l\xi \cos\lambda l\xi}{(\sin\lambda l \cos\lambda l + \sinh\lambda l \cosh\lambda l)} \qquad (4.6.25)$$

where

$$\lambda = \sqrt[4]{\frac{k_f}{EI}}, \qquad (4.6.26)$$

$$\xi = \frac{x}{l}.$$

The finite element analysis is performed for a beam with symmetric conditions at center and free conditions at other boundaries. In order to eliminate the two dimensional in-plane behavior, Poisson's ratio was set equal to zero. Figure 4.10 shows the comparison for the non-dimensional vertical displacements along the x axis, between the analytical and finite element solutions. In this case

$$\frac{\lambda l}{\pi} = 2.$$

There is a good agreement between the solutions and it can be seen that the elastic foundation flattens the beam in the central parts. The negative and positive displacements at the end of the beam result in foundation forces that form a moment that is sufficient to straighten the beam.

4.7 - Summary and Conclusion

In this chapter the issues regarding the finite element program were described, The finite element used was introduced, the constitutive law and important features of the program were explained, the solution algorithm and the program flowchart were presented, and finally the results obtained from the program were shown to be in good agreement with available analytical and other numerical solutions. The examples in section 4.6 covered different aspects of the program including, uniaxial visco-elastic

deformation with or without delayed elastic element, three dimensional steady state creep under mechanical loading, and beam and plate on elastic foundation with mechanical and thermal loading. Nevertheless the given examples were only a part of the numerous tests that were performed in the process of the development of the program. For example other features of the program like tensile fracture and boundary elements were tested in the situations were the results were known. In all of the tests the results of the program were satisfactory. In Chapter 5 some comparisons are made with the results of field measurements and boundary conditions.

	$\frac{\dot{w}}{\kappa_n r}\left(\frac{6M_n}{q_0 r^2}\right)^n$	
n	Hrudey, 1973	Present study
1	0.25781	0.25870
3	0.23618	0.23573
5	0.20552	0.20331
7	0.17650	0.17298
9	0.15076	0.14638

Table 4.1 - Non-dimensional velocity in a center of a simply supported uniformly loaded circular plate.

	Uniformly distributed load			Point load		
x/a	Analytical solution	Finite element (3×3)	Finite element (2×2)	Analytical solution	Finite element (3×3)	Finite element (2×2)
0.00	0.010464	0.010623	0.010675	0.010777	0.009270	0.011027
0.25	0.009850	0.009984	0.010034	0.008446	0.007960	0.008708
0.50	0.007925	0.007929	0.008088	0.005164	0.005217	0.005052
0.75	0.004560	0.004589	0.0046609	0.002364	0.002442	0.002414
1.00	0.0	0.0	0.0	0.0	0.0	0.0

Table 4.2 - Comparison between the analytical and finite element solutions with different integration techniques for displacement at the center of simply supported square plate on elastic foundation.

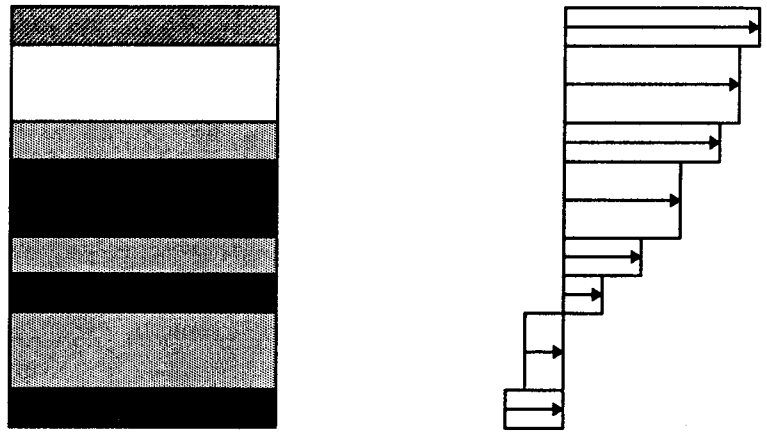

Figure 4.1 - Layered model and stress distribution through the thickness.

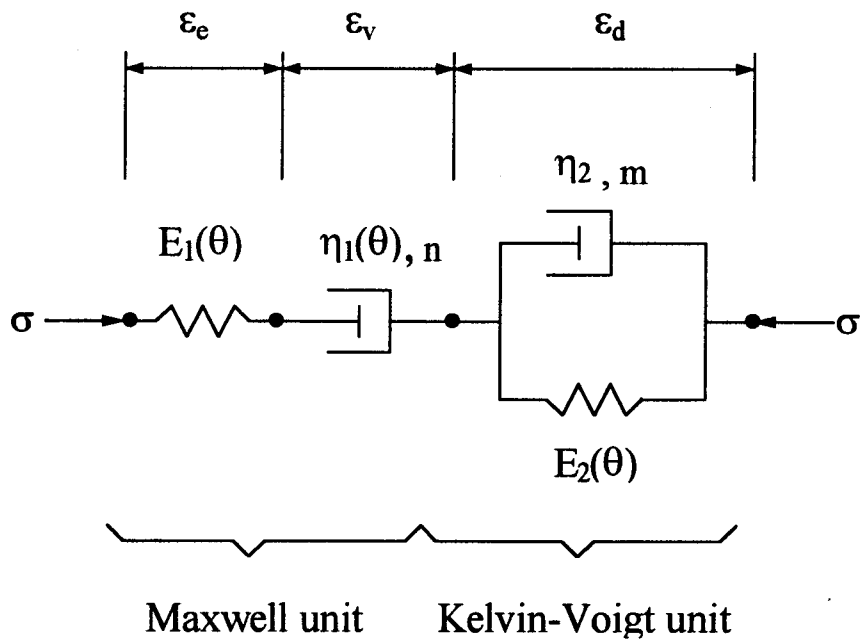

Figure 4.2 - Rheological model for constitutive law.

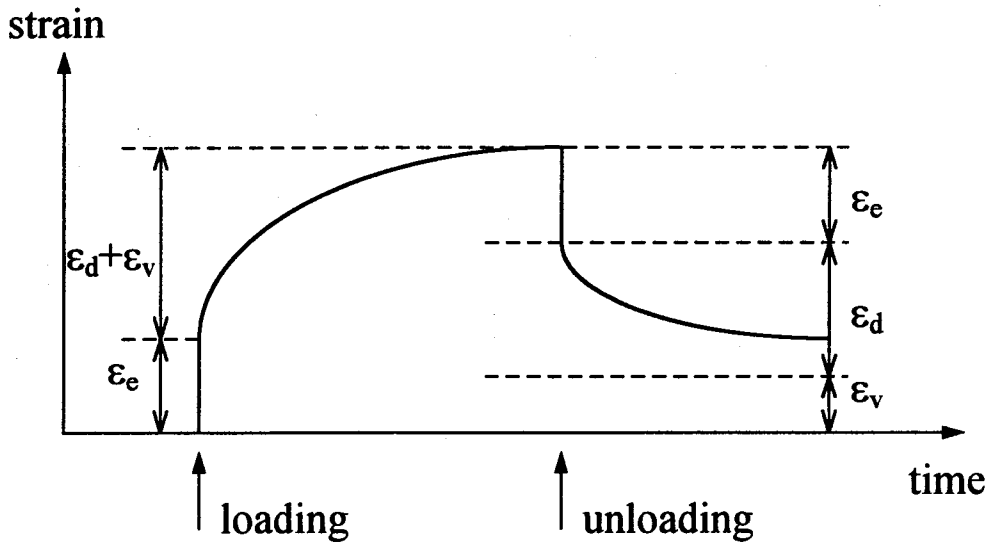

Figure 4.3 - Strain under constant stress for the rheological model shown in Fig. 4.2.

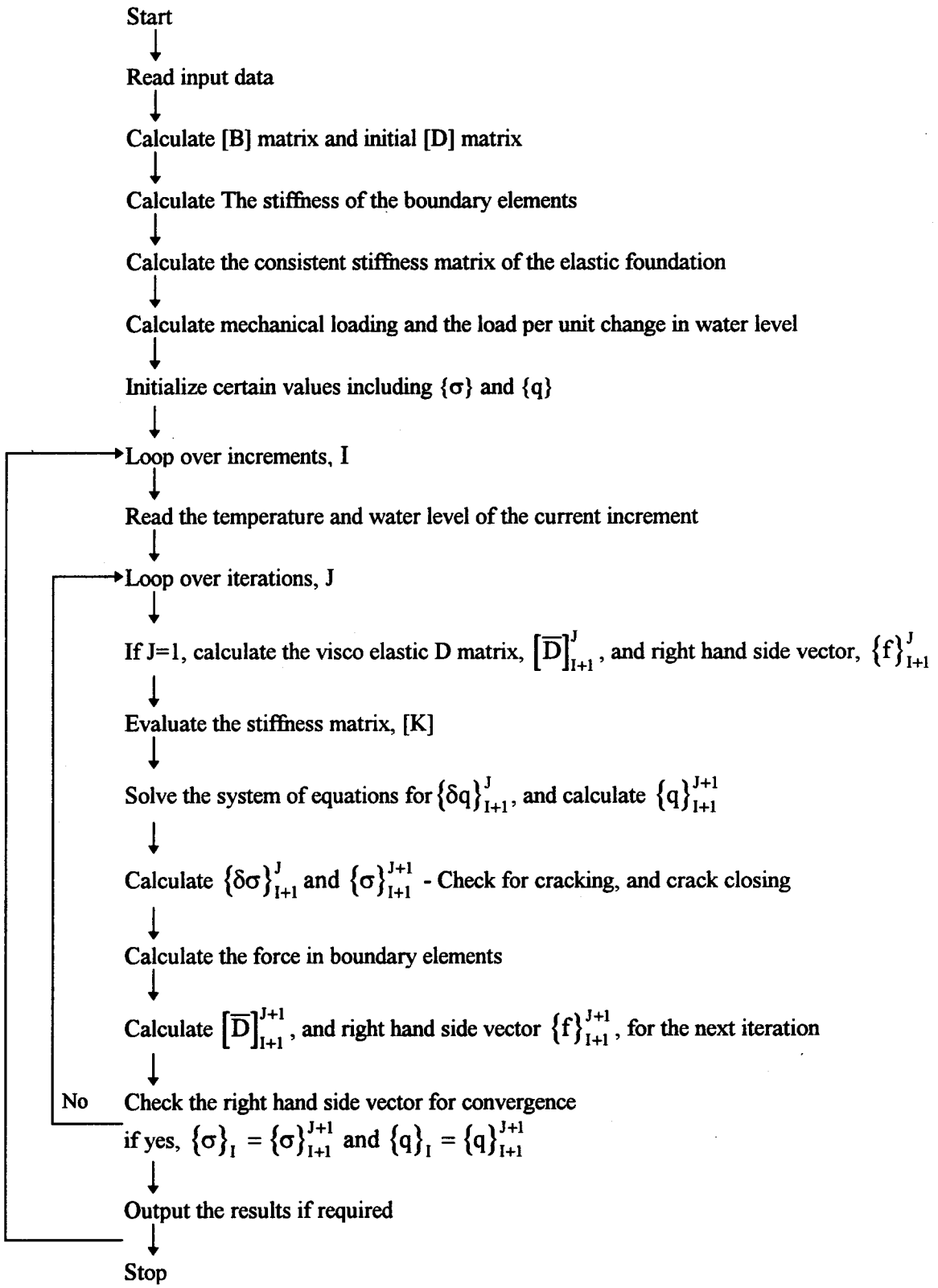

Figure 4.4 - Flowchart of the finite element program.

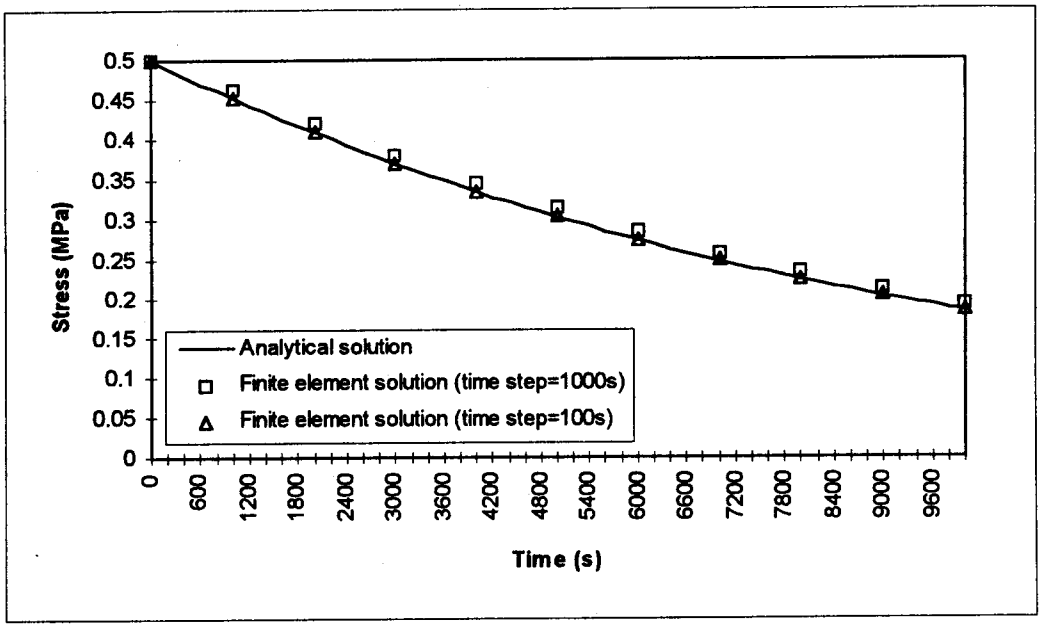

Figure 4.5 - Comparison between the analytical and finite element solutions for stress under constant strain in a uniaxial model consisting of a Maxwell unit.

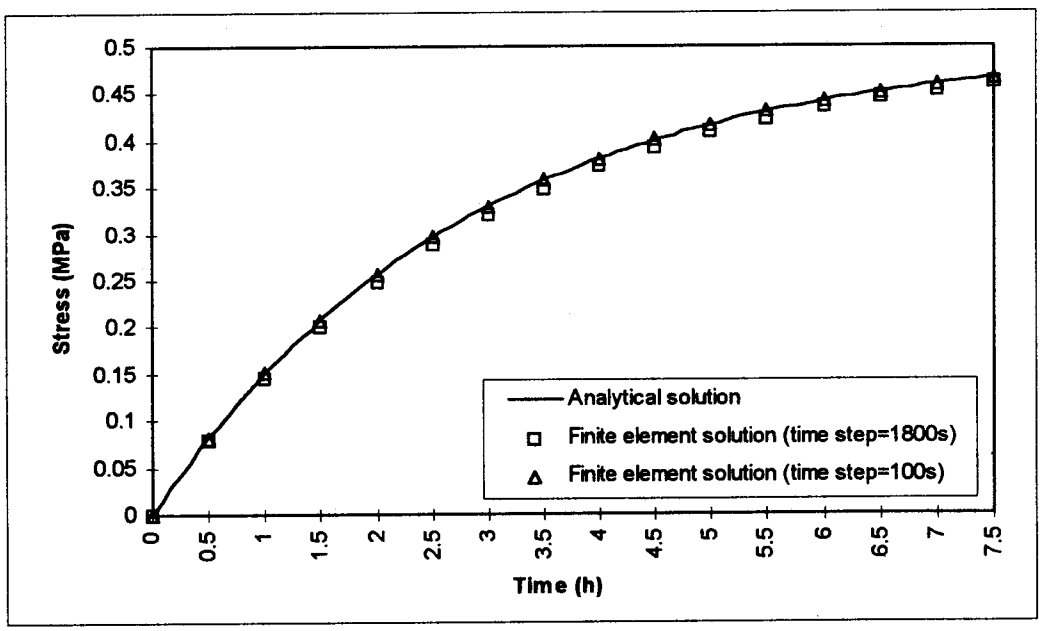

Figure 4.6 - Compariosn between the analytical and finite element solutions for stress under constant strain rate in a uniaxial model consisting of a Maxwell unit.

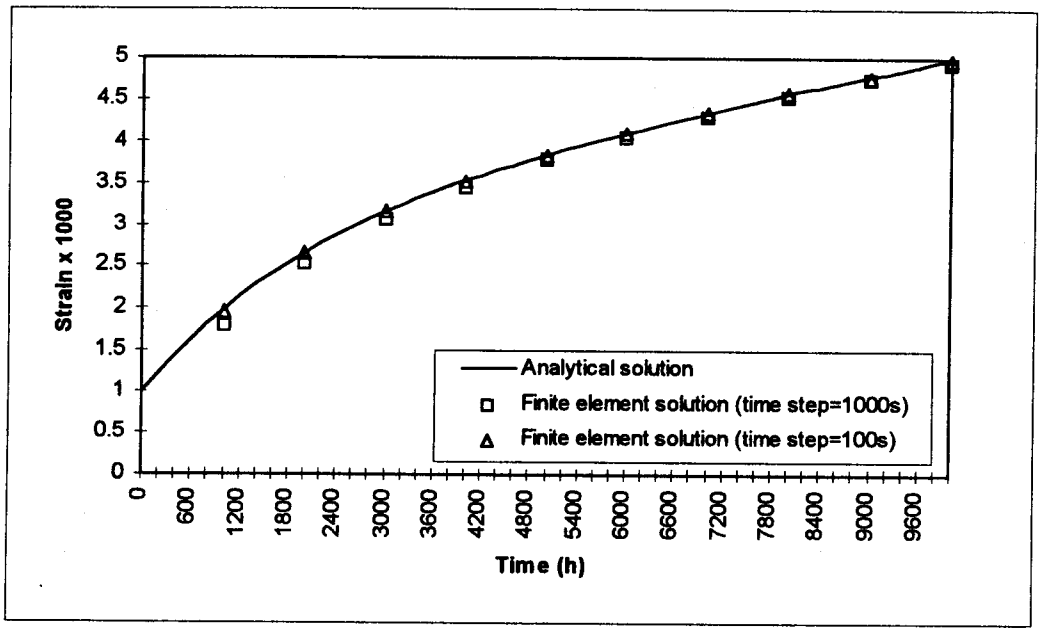

Figure 4.7 - Comparison between analytical and finite element solutions for strain under constant stress in a uniaxial model consisting of a Maxwell unit in series with a Kelvin-Voigt unit.

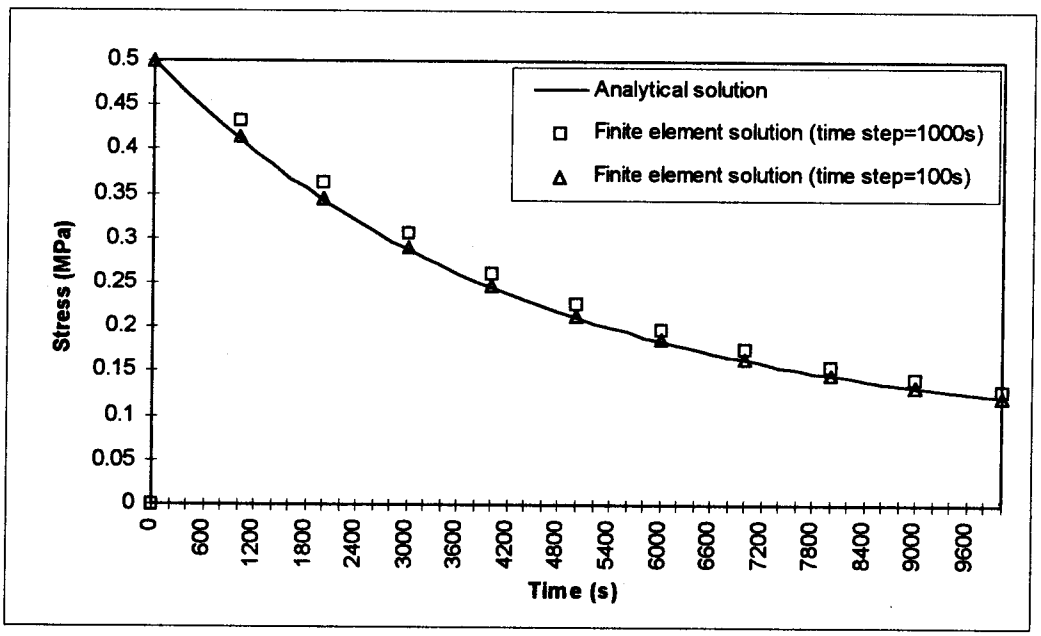

Figure 4.8 - Comparison between analytical and finite element solutions for stress under constant strain in a uniaxial model consisting of a Maxwell unit in series with a Kelvin-Voigt unit.

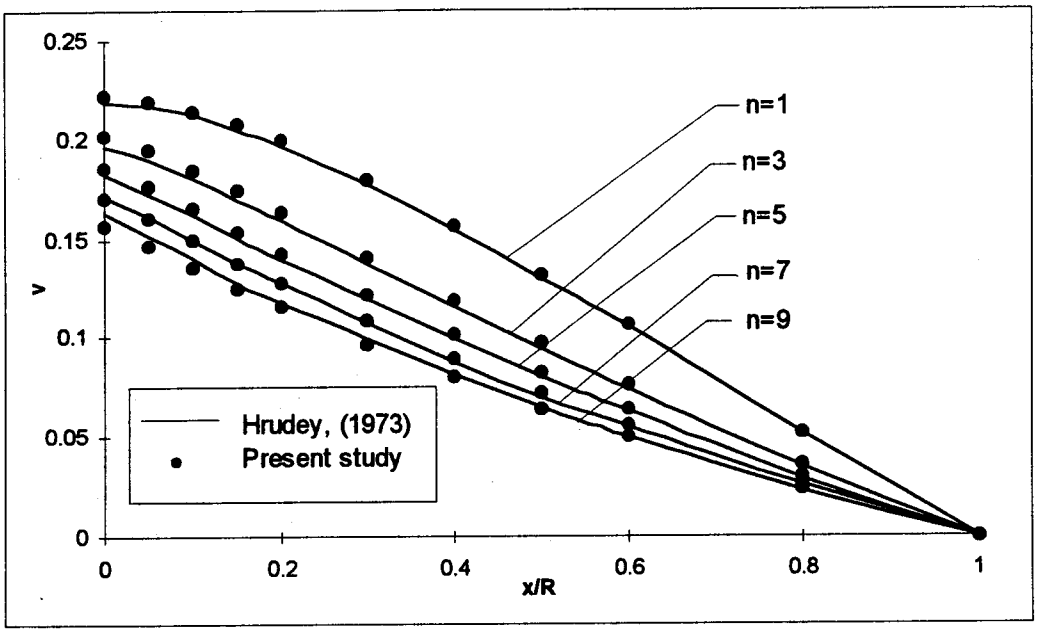

Figure 4.9 - Comparison between finite element solutions for steady state non-dimensional velocity along the center line of a simply supported circular plate under point load.

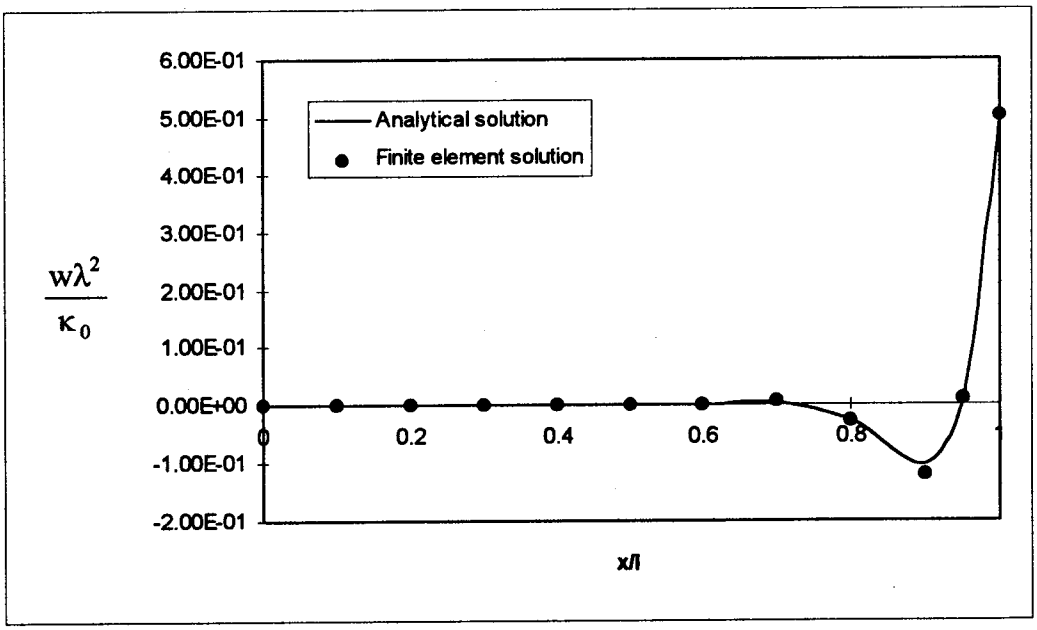

Figure 4.10 - Comparison between the analytical and finite element solutions for non-dimensional vertical displacement of a beam under thermal loading on elastic foundation.

5 - COMPARISON WITH EXPERIMENTS AND FIELD MEASUREMENTS

The objective of this part of the study is to calibrate and evaluate the analytical model, so that it can be used for a qualitative study of ice behavior under thermal loading. In the first part of this chapter, published experimental results are compared to predictions of the model obtained using different mechanical properties for ice. Determining the material properties for ice can itself be the subject of a very vast investigation and it was not in the scope of this study. Therefore, only published values for material properties were used in these comparisons. In the second section the predictions of the model are compared to field measurements. The data collected by Fleet Technology Ltd., as described in section (2.21) were used for this study.

5.1 - Mechanical Properties of Ice

The mechanical properties of ice have been the subject of investigation for a long time. Compared to other engineering materials, ice has relatively large crystals and normally exists at a temperature very close to its melting point. The response of ice under loading, depends on many parameters such as the ice type, the stress and strain levels, the stress and strain rate, and the temperature.

Ice types are classified according to their formation, and the size, shape, and orientation of the crystals (Michel, 1979). A summary of the classification system is presented in Table 5.1. The letter P denotes primary ice which forms first on a water body. The letter S indicates secondary ice which grows below the primary ice in a direction parallel to the heat flow. The ice types designated with a T are superimposed ice types that form on the top of the primary ice due to flooding of the ice.

The grain size is divided into five ranges:

a) Fine - Grain diameter is less than 1 mm.

b) Medium - Grain diameter is 1 to 5 mm.

c) Large - Grain diameter is 5 to 20 mm.

d) Extra large - Grains have diameters greater than 20 mm.

e) Giant - Grains have dimensions in meters.

Among the different types of ice, there are really only two broad categories of ice found in most lakes and reservoirs.

1) Granular ice - This category of ice consists of fine, randomly oriented crystals. The grain size is between one and three millimeters. This ice is usually found in the surface layers of lakes and reservoirs. Due to the random orientation of the crystals, the mechanical properties of this ice are isotropic. The most common ice type in this category is the snow-ice.

2) Columnar ice with c-axes horizontal or S2 ice - This type of ice is usually found in the lower layers of ice covers in lakes and reservoirs. The grain size is usually in the range of three to one hundred millimeters and the crystals are elongated in the vertical direction. This ice is considered transversely isotropic (orthotropic) and the properties are the same in all directions in the horizontal plane.

Most laboratory investigations on ice are performed on snow-ice, S2, and S1 ices (Table 5.1) and the most common loading modes are constant strain-rate, constant load and constant loading rate. In the field, temperature changes strain the ice covers and the loading conditions are similar to those in constant strain rate tests. The behavior of ice depends on strain rate and at strain rates higher than 10^{-4} to 10^{-3} s^{-1} the behavior changes from ductile to brittle. Figures 5.1 and 5.2 show the results of some of the constant strain rate tests performed on granular and columnar ice at different strain rates. It can be seen that at higher strain rates the stress reaches a maximum and drops. This drop in stress is less at lower strain rates.

Drouin and Michel studied the air temperature changes in Quebec City. The climatological data used in this study were those recorded at the Quebec City airport from 1944 to 1967. The largest recorded change in air temperature was 3.3°C in 30 minutes. For other regions of Canada, some data can be found in a paper by Kendall on the meteorological information relevant to ice pressures (Kendall, 1968). The maximum air

temperature spreads in January with duration of six hours and periods of recurrence of 5, 15, and 25 years are given for 23 locations in Canada. Those values are shown in Table 5.2. The maximum value in this table is 27.8°C which corresponds to an average rate of 4.6°C per hour. In some places like the Chinook belt of Southern Alberta, the air temperature can increase in a relatively short time by as much as 10 to 20°C. It can also happen that the temperature increase is followed by a rapid decrease. All of the values in the table and the ones being discussed are for the air temperature. The corresponding temperature change in an ice cover usually happens at a lower rate. According to the parametric study performed for this project, when the short-wave solar radiation is not considered, the change in ice surface temperature for daily temperature changes can be less than 80 percent of the change in air temperature. In the measurements made by Fleet Technology Ltd., as described in section 2. , the rates of rise in ice surface temperature were less than 2°C/h. Considering a rate of 5°C/h the strain rate would be:

$$\dot{\varepsilon} = \alpha\dot{\theta} = \frac{0.54 \times 10^{-4} \times 5}{3600} = 7.5 \times 10^{-8}\,s^{-1}$$

Therefore, the mechanical properties used for stress analysis should be based on tests performed at strain rates in the range of 10^{-8} to 10^{-7} s^{-1}. Nevertheless, this is a very low strain rate and most of the reported laboratory tests are performed in rates above $10^{-7}s^{-1}$.

In the finite element program there are two options for the rheological model. The first is a Maxwell unit consisting of a linear spring in series with a non-linear dashpot. This model requires values for E_1, ν, η_1, and n. The second model has a Maxwell unit in series with a Kelvin-Voigt unit. The parameters required are: E_1, ν, η_1, n, E_2, η_2, and m. In the constitutive model suggested by Khoo (1989), η_1 changes as a function of strain. This accounts for the softening after the peak stress. Drouin and Michel's tests show that for snow-ice and S2 ice at low strain rates, the stress at constant strain rate reaches a maximum and then remains almost constant at that level. Thus in the present study, the post-peak softening effect is not included. Only the effect of temperature on the material parameters is considered. Among the various mechanical properties for ice reported in the literature, only those used in determining thermal pressures and those obtained in tests performed at low strain rates (10^{-8} to $10^{-7}s^{-1}$) are considered for use in the present model.

What follows is a discussion of material properties suggested by others which were considered to be suitable for thermal stress analysis.

Drouin and Michel (1971) -

Drouin and Michel performed uniaxial and biaxial tests on snow-ice and columnar ices (S1 and S2). The uniaxial tests were constant strain rate tests performed at different temperatures. The strain rates were in the order of 10^{-8} to 10^{-7} s^{-1} which is in the range of thermal strain rates occurring in natural ice. Drouin and Michel used the test results to determine the constants for their rheological model. They plotted the stress versus strain curves and found the best fit for the slope at the origin, and the relationship between the maximum stress and strain rate. Then considering the effect of the stiffness of the test assembly they calculated the stress versus strain curves for the ice plus testing machine and compared it to the test results. The stress-time curves for ice alone were also calculated using the rheological model and the apparent Young's modulus for ice alone.

Snow-ice-

The snow-ice used in the tests was made in the laboratory. Its density was about 890 kg/m^3. The grains were spherical with random crystallographic orientation and the average grain size was about 1 mm. The tests were performed at constant rates varying from 1.8×10^{-8} to 1.8×10^{-7} and at temperatures from -28.3 to -3.9°C. In the majority of the tests the stress reached a maximum and remained almost constant at that level. In other cases it diminished slightly and then assumed a constant value. The maximum stress was reached at an average strain of 0.15 percent. The following relationships were given for the apparent Young's modulus of ice and the relationship between the maximum stress and strain rate (converted to SI units).

$$E = 4.52 \times 0.0981 \exp\left(\frac{2060}{T}\right) \qquad \text{(E in MPa and T in K°)} \qquad (5.1.1)$$

$$\dot{\varepsilon} = 2.961 \times 10^{9} \exp\left(\frac{-83684}{8.314T}\right)\sigma^{4} \qquad (\sigma \text{ in MPa, T in K°, and } \dot{\varepsilon} \text{ in } s^{-1}) \qquad (5.1.2)$$

Columnar ice with optical axis vertical - S1

The specimens were made in the laboratory by simulating the natural conditions (calm surface and small temperature gradient). The tests were performed at constant strain rates

varying from 3.7×10^{-8} to 1.8×10^{-7} s^{-1} and at temperatures varying from -26.8 to -4.1°C. It was observed that the stress increased at an almost constant rate for about two to four hours. Then the rate of increase gradually diminished until the stress reached a maximum. Following that, the stress dropped very rapidly and then stabilized at a nearly constant value. The maximum stress was reached when the specimens had been deformed in the range of 0.08 to 0.2 percent. The sudden drop in stress was attributed to the buckling of crystals when strained in compression in the direction parallel to the basal plane. Drouin and Michel studied the relationship between the maximum stress and strain rate. The analysis showed a scatter in values which prevented the establishment of a single relationship between the strain rate and maximum stress. The scatter was greater for tests performed at higher temperatures. The average value measured for the stress exponent was 3.7 and the following relationships were defined for different temperatures and rates.

$$\dot{\varepsilon} = c\exp(\frac{-Q_c}{RT})\sigma^n \qquad (5.1.3)$$

where

n=3.7

R=8.314 j/(mol.K°)

and

$Q_c = 56170$ j/mol for $\dot{\varepsilon} = 10^{-3}s^{-1}$ and θ = -30°C to -10°C

$Q_c = 60773$ j/mol for $\dot{\varepsilon} = 10^{-7}s^{-1}$ and θ = -30°C to -10°C

$Q_c = 269199$ j/mol for $\dot{\varepsilon} = 10^{-3}s^{-1}$ and θ = -10°C to 0°C

$Q_c = 215476$ j/mol for $\dot{\varepsilon} = 10^{-7}s^{-1}$ and θ = -10°C to 0°C

The constant c was given only for low temperatures (-30°C to -10°C). Finally the following equation was given which is valid only for low temperatures but was used by Drouin and Michel to simulate the test results at higher temperatures as well.

$$\dot{\varepsilon} = 2.961\times10^{9}\exp(\frac{-83684}{8.314T})\sigma^{3.7} \qquad (5.1.4)$$

The apparent Young's modulus for ice alone was obtained as a function of temperature and strain rate.

$$E = 344 \times 0.0981 \dot{\varepsilon}^{0.079} \exp(\frac{1335}{T}) \quad (5.1.5)$$

Columnar ice with optical axis horizontal - S2

For this kind of ice, Drouin and Michel only reported two tests. The test durations were on the order of 100 hours and the appearance of the stress versus time curves was substantially the same as those for snow-ice. The maximum stress, however, occurred at a much greater deformation. The corresponding strain was 1.3 and 2.4 percent in these two tests. Drouin and Michel did not calculate the Young's modulus or the relationship between the maximum stress and the strain rate. Most of the parameters in the rheological model were taken to be the same as those for snow-ice and the value used for the stress exponent was 4. The test results were compared to the predicted values for the ice plus testing machine but the stress time curves for ice alone were not calculated.

Bergdahl (1978) -

The model used by Bergdahl, to estimate thermal ice pressure, consisted of a linear spring in series with a non-linear dashpot. The following values were used for the various constants.

$$\eta_1 = 3235 \exp(\frac{-59800}{8.314T}) \quad (T \text{ in } K^\circ) \quad (5.1.6)$$

$$n = 3.651 \quad (5.1.7)$$

$$E_1 = 6100(1-0.012\theta) \quad (\theta \text{ in } C^\circ) \quad (5.1.8)$$

The values for η_1 and n were based on Drouin and Michel's experiments on S1 ice and the value for E was based on the material properties given by Lindgren (1968).

Cox (1984) -

Cox used the same model as Bergdahl but with different values for mechanical properties. Cox argued that the numbers used by Bergdahl for E were very high and therefore selected a reduced value given by the relationship

$$E_1 = 4000(1-0.012\theta) \quad (5.1.9)$$

For the stress-strain rate relationship Cox used the following equations.

$$\eta_1 = 3.9 \times 10^{-7} |\theta|^{-1.97} \quad (5.1.10)$$

$$n=3.7 \quad (5.1.11)$$

Equation (5.1.9) was found by curve fitting the experimental data for S1 ice given by Drouin and Michel. The values for η_1 from different tests, versus test temperature were plotted with a logarithmic scale. In order to obtain a linear fit, it was assumed that the 0°C tests were performed at -1°C. As a result, this equation gives quite large values for temperatures close to 0°C.

The values for E and η obtained from different equations are compared in Tables 5.3 and 5.4. It can be seen that the values for E suggested by Bergdahl and Cox are much higher than those suggested by Drouin and Michel for different kinds of ice.

In order to verify the present model, the mechanical properties suggested by Drouin and Michel for different ice types were used in a model consisting of a spring and a dashpot. To simulate a uniaxial condition, Poisson's ratio was set to zero in the finite element model. The results of this analysis were compared to the curves calculated by Drouin and Michel for ice alone.

Figure 5.3 shows the comparisons for snow-ice. The curves given by Drouin and Michel for ice alone compare well with the calculated curves. There is only a small difference in the maximum stresses. In Fig. 5.4 the results are compared for S1 ice. The present model is not able to simulate the drop in stress but the agreement in the initial part of the curves is good. Except for the first two curves which are calculated at high temperatures where Drouin and Michel's equation is not valid, the overall agreement is acceptable. In the experimental curves for ice plus testing machine the drop in stress is more than that for the theoretical curves for ice alone (Fig. 2.9). Since this kind of ice is not very common in lakes and reservoirs, no attempt was made to model the drop in stress. Figure 5.5 shows the comparisons for S2 ice. In this case, for the present model, the properties for S1 and snow-ice suggested by Drouin and Michel, and those suggested by Cox were used and the results were compared to the experimental curves which included the effect of the flexibility of the testing machine.

Drouin and Michel also performed biaxial tests on different types of ice. In these tests circular discs of ice were placed in an invar ring. Invar has a very low coefficient of thermal expansion compared to ice, so that the test approximates one of complete restraint against thermal expansion. The thickness of the ice was 0.05 m and the diameters ranged

from 0.15 to 0.3 m. The specimens were subjected to an increase in temperature and the stress was calculated by measuring the strain in the ring. In the Figs. 5.6 to 5.8 the experimental stress in these tests is compared with the prediction of the present model using different mechanical properties. In the analysis, Poisson's ratio was equal to 0.33 and the coefficient of thermal expansion for ice was taken as a function of temperature as suggested by Drouin and Michel (1971).

$$\alpha = (54 + 0.18\theta) \times 10^{-6} \qquad (5.1.12)$$

In all these cases, the mechanical properties suggested by Cox, which have a high value for E_1, gave very high stresses compared to the measured stresses. The properties suggested by Bergdahl gave even higher stresses and are not shown here. In the case of snow-ice, the stress versus time curves obtained using snow-ice properties from Drouin and Michel are closer to the measured stresses. In the case of S2 ice, the initial part of the curves, which is controlled by the value of E_1, is modeled better by the snow-ice properties and the remaining part of the curves are between the snow-ice and S1, or close to snow-ice. In some cases for S1 ice the measured stress is closer to that for snow-ice and in some cases it is between that for the S1 and snow-ice. The curves calculated using the E_1 value for S1 ice and the η_1 expression of Cox give good agreement in some tests. However, equation (5.1.10) gives a very high value of η_1 for temperatures near 0°C and it might cause numerical problems.

According to these numerical tests the values suggested by Drouin and Michel for snow-ice give reasonable stress prediction for most cases. The stresses calculated using the mechanical properties of S1 ice are also close to the measured stresses but these properties have the limitation that the equation given for η_1 is not valid for temperatures above -10°C. The material properties suggested by Bergdahl give very high stresses which seem unrealistic for thermal loading analysis. The stresses calculated using the mechanical properties suggested by Cox were also higher than the measured stresses in the experiments of Drouin and Michel. All of these results offer guidance on the choice of mechanical properties. However a final decision on which properties to use in the analytical studies requires consideration of field data.

5.2 - Comparison with Field Measurements

5.2.1 - General Discussion

As discussed in section (2.21), field measurements of ice were conducted by Fleet Technology Ltd. and sponsored by Canadian Electricity Association (CEA). Field data were collected during the winters of 1991-92 to 1993-1994, at Hydro-Quebec's Paugan Dam on the Gatineau River at Low, Quebec and Ontario Hydro's dam at Arnprior, Ontario. Large scale tests were also conducted at a 120 m by 60 m outdoor basin at the National Research Council (NRC) in Ottawa. The purpose of these tests was to measure and study the loads resulting from temperature and water level changes. The data collected included temperature and stress profiles, ice thickness and snow cover measurements, and meteorological data. The results were reported by Fleet Technology Ltd. in three phases. The reports of phase I (winter 1991-92), phase II (winter 1992-93), and computer data on solar radiation, wind speed, temperature profiles, and some of the local stresses at the NRC basin test were obtained for use in this study (Comfort and Abdelnour, 1993; Comfort, Abdelnour, and Gong, 1994). The data were used to verify the analytical models.

A number of questions and difficulties were encountered in simulating the field conditions. These problems were common to most of the simulations. Therefore before studying each case separately, some of these problems and their resolution are discussed .

1) Ice type, constitutive model, and mechanical properties-

One of the most difficult problems in preparing a simulation model is to decide which ice type existed in the field and which constitutive model and which mechanical properties should be used in the simulations. There is no simple solution to this problem. The ice type and the associated mechanical properties depend on the conditions at the time of formation. This makes it difficult to predict exactly what type of ice would have existed at a particular site. Observations show that the upper parts of the ice cover usually consist of granular ice and the lower parts of columnar ice with optical axis horizontal (S2). The

finite element model offers two options for the constitutive model. In the first, which consists of a spring and a dashpot, mechanical properties suggested by previous investigators can be used directly. For the second, which includes a delayed elastic element, the properties are not well defined and must be obtained by trial and error to fit the measured data. Therefore, some of the major thermal events (periods of temperature increase) were first simulated using model (1) with different mechanical properties. It was observed that in all the events except one (described later), the best agreement was obtained using the material properties suggested by Drouin and Michel for snow-ice. Two thermal events from the NRC basin tests are used here to demonstrate how the stress is affected by the choice of different mechanical properties. Figure 5.9 shows the comparison between the measured and calculated stress versus time curves. The first thermal event begins at the start of the simulation and is followed by a cooling period. The second thermal event starts at about 60 hours and lasts till the end of the simulation. It can be seen that the curve calculated using mechanical properties for snow-ice, as given by Drouin and Michel follows the measured data reasonably well. Stresses obtained using the mechanical properties suggested by Cox are very high for both events and the stresses obtained using S1 ice properties are high in the first event and low in the second event. The same pattern was observed in most other cases. The good agreement using snow-ice properties might be due to the fact that the temperature changes mostly affect the upper parts of the ice sheet which usually consist of granular ice.

In the next step, the results of the second constitutive model were compared to those of the first model with snow-ice properties, and the measured data. As mentioned earlier the formulation of this model was done by Khoo (1989) who had used it for indentation problems. Khoo found the parameters that gave the best agreement with published experiments. These parameters were as follows:

a) Sinha's uniaxial tests on columnar ice at -10°C (Sinha, 1982),

$E_1 = 7000$ MPa $\qquad E_2 = 3500$ MPa

$\eta_{1i} = 1.4\times10^{-7}$ $(MPa)^{-n}s^{-1}$ $\qquad \eta_2 = 0.6\times10^{-6}(MPa)^{-m}s^{-1}$

$n = 2.7$ $\qquad m = 2$

The parameter η_{1i} is the initial value of η_1 which varied as a function of strain and strain rate in Khoo's original model.

b) Mellor and Cole's tests on fine grained ice at -5°C (Mellor and Cole, 1982),

$E_1 = 9500$ MPa $\qquad E_2 = 1267$ MPa

$\eta_{1i} = 3.2\times10^{-7}(\text{MPa})^{-n}s^{-1}$ $\qquad \eta_2 = 3\times10^{-6}(\text{MPa})^{-m}s^{-1}$

$n = 3$ $\qquad m = 3$

c) Frederking's test on columnar ice at -10°C (Frederking, 1977),

$E_1 = 4500$ MPa $\qquad E_2 = 9000$ MPa

$\eta_{1i} = 2.1\times10^{-7}(\text{MPa})^{-n}s^{-1}$ $\qquad \eta_2 = 0.8\times10^{-6}(\text{MPa})^{-m}s^{-1}$

$n = 3.1$ $\qquad m = 1$

Most of the above tests were performed at strain rates higher than $1\times10^{-7}s^{-1}$. Sanderson (1988), suggested a value of 9500 MPa for E_1. This is the elastic modulus of ice which does not depend on temperature but could be measured only at very high loading rates. The values obtained at normal tests are usually lower than that and are called the apparent elastic modulus of ice.

In order to determine the effect of each of these parameters on the stresses a number of numerical tests were performed. In these tests a biaxially restrained ice sheet was subjected to a uniform temperature increase. The material properties were constant and did not change with temperature. In each test one of the mechanical properties was changed while the others were kept constant and the stress versus time curves were plotted. It was known that the maximum stress is controlled by the value of η_1, and therefore this parameter was not changed. In all of the tests the temperature rate was 5°C/h and the following parameters were used as the base constants.

$E_1 = 5000$ MPa $\qquad E_2 = 5000$ MPa

$\eta_1 = 3.0\times10^{-7}(\text{MPa})^{-n}s^{-1}$ $\qquad \eta_2 = 1.0\times10^{-6}(\text{MPa})^{-m}s^{-1}$

$n = 3.0$ $\qquad m = 3$

Figure 5.10-a shows the stress versus time curves for different values of E_1 (1000, 5000, and 9500 MPa). It can be seen that the initial slope is controlled by this parameter. In Fig. 5.10-b the comparison is made for different values of E_2 (1000, 5000, and 9500 MPa). It was observed that lower values for E_2 decrease the stresses after the initial

part and before reaching the maximum stress. Figure 5.10-c shows the comparisons for different values of η_2 (1.0×10^{-7}, 1×10^{-6}, and 1×10^{-5} $MPa^{-m}s^{-1}$). The value of η_2 controls the curvature before reaching the maximum stress.

Using a high value for E_1, for example 9500 MPa as suggested by Sanderson, increases the initial slope of the stress versus strain or stress versus time curves. This value was used in the simulations and it was observed that the calculated stresses at the start of the simulation are much higher than the measured stresses. In order to obtain better stress predictions when using a high value for E_1, it is necessary to use a low value for E_2. However the computation time increases as the difference between E_1 and E_2 is increased, because the stress changes rapidly and more iterations are required in each time step. Therefore, lower values for E_1 were used in the simulations and the parameters that gave the best agreement with measured data were obtained by trial and error. Figure 5.11 shows results for the same events as Fig. 5.9, where the measured stress-time curve is compared to the curves calculated using different constitutive models. Snow-ice properties were used for the first model and in the second, the following properties were used:

$E_1 = 2000$ MPa $\qquad$ $E_2 = E(T)$ as for snow-ice

$\eta_1 = \eta(\theta)$ as for snow-ice $\qquad$ $\eta_2 = 1\times10^{-6}(MPa)^{-m}s^{-1}$

$n = 4$ $\qquad$ $m = 4$

As seen in Fig. 5.11 the agreement for the first event is somewhat better with model 2, but model 1 gives better agreement for the second event. It was observed that the first model is capable of predicting the ice stresses and there is not much improvement in the results when the second model is used. Since the second model has the disadvantages that it requires more computing time and does not have well defined parameters it was decided to use the first model with snow-ice material properties for subsequent parametric studies.

2) Finite element mesh-

An important question that arises when designing the finite element mesh is whether or not to model the entire ice cover or a much smaller region in the vicinity of the resisting structure. In order to answer these questions several options were tried. For the NRC basin test, it was possible to model the entire basin (using symmetry), with a relatively fine

mesh containing 20 elements. In the case of the Arnprior Dam, a coarse mesh was used and the complete reservoir was modeled using 20 elements. For the Paugan Dam, the ice cover in front of the gates and piers of the spillway was modeled using a very fine mesh. The effect of geometry and number of elements was also studied in the parametric study.

It was observed that when there is only thermal loading and all the displacements and rotations on the reservoir boundary are restrained, the effect of reservoir geometry and number of elements is negligible. In this case due to existence of an homogenous stress field, the displacements and rotations at all of the nodal points are equal to zero and it is possible to get the same results using a single element. A typical single element mesh is shown in Fig. 5.12. The element has eight nodes and all of the displacements and rotations are restrained except for the mid-side displacements in the direction parallel to the element boundary. The size of the element is arbitrary but the thickness should be equal to the thickness of the ice sheet at the time of simulation. Eight to ten layers are used through the thickness of this element. Most of the simulations and tests (e.g. Figs. 5.9 and 5.11) were performed using this one element mesh.

3) Stress history-

When comparing the measured and predicted stress, the effect of the stress history should be considered. The ice cover is continuously under stress and when simulating an event, the analysis must necessarily start somewhere in the middle of an ongoing process. Figure 5.13 shows a sample from the parametric study where the surface temperature of the ice cover varies as a cosine function having a 24 hour period. The air temperature starts from -20°C and rises to 0°C and drops back to -20°C. The temperature distribution in the ice sheet is calculated using the finite difference thermal analysis program. The thickness of the ice cover is 0.2 m. Eight cycles occurring over eight days are shown. Although the maximum and minimum temperatures are the same for all the cycles, the maximum stress is greatest during the first cycle. After a few cycles an equilibrium is reached beyond which the maximum stress does not change. Imagine now that this figure represents measured stresses. If a simulation is started at the fourth or fifth cycle, the calculated stresses would initially be under first cycle conditions. Therefore for the same

temperature changes, the calculated stresses would be higher than the measured stresses. This effect usually causes an over estimation of the stresses at the start of a simulation.

Another problem is that when two thermal events happen within a short interval of time, the stress from the first event may not have dissipated completely before the next event. In this case, if the simulation starts from a zero stress at the beginning of the second event, the measured stresses will be higher than the calculated stresses. This effect usually causes an under estimation of the ice stresses at the start of the simulation.

In order to overcome these difficulties the duration of all simulations was made as large as possible. A problem in simulating events over long periods however, is that the thickness of the ice may change. Therefore, the following steps were taken in some of the simulations.

a) If possible the simulation started at a time when the measured stresses were close to zero.
b) An interval that covered a number of events (2 to 5 days) was used.
c) The initial thickness was chosen to be equal to the thickness of the ice cover at later events.
d) For the first events the thickness was not correct and the effect of the stress history was still present. Therefore the first events were disregarded in the comparisons.

The difference between the measured and calculated stresses, due to the effect of stress history, usually diminishes after one or two days. Therefore, the stresses in later events will be closer to the measured stresses.

4) Ice surface temperature-

In order to achieve good simulation of the ice stresses, it is necessary to use accurate temperature data. Due to the difference between the conductivities of the air, snow, and ice, there is a steep temperature gradient at the ice surface which is in contact wiht the air or snow cover. Therefore the positioning of the thermocouple that measures the surface temperature is very critical. Figure 5.14-a shows a comparison between the measured and calculated temperatures for the NRC basin test. The calculated temperature distribution was obtained using the air temperature, wind speed, solar radiation, and considering the snow cover. The calculated and measured temperatures are in good agreement except at

the surface of the ice. The reason for this discrepancy is not clear. It may have been that the thermocouple was positioned in the snow cover rather than in the ice.

Figure 5.14-b shows the measured temperature profile from an earlier event at the NRC basin test. In this case, the only temperatures recorded were at the ice surface and 0.1 m below the surface. There is a large difference between the surface and 0.1 m temperatures. Considering that the temperature at the bottom of the ice sheet is at the freezing point, and the ice sheet is very thin ($h<0.2$ m) the stress distribution through the thickness should be close to linear. But in this case the line joining the measured temperatures at the top surface, 0.1 m, and the bottom surface is very far from a straight line or even a smooth line. It is very likely that in this case also, the positioning of the thermocouple that measured the surface temperature was not right.

In order to overcome this problem, the measured temperatures were checked by performing a thermal analysis. When the surface temperatures did not seem to be accurate, it was assumed that the measured surface temperature was actually a temperature in the snow cover. Then a new surface temperature was calculated using a thermal analysis with one centimeter of snow on top of the ice sheet.

5) Effect of water level changes-

The field data obtained by Fleet Technology Ltd. (Comfort et al., 1993 and 1994) indicate that water level changes have an effect on measured stresses. Although the thermal events were the main contributor to the ice pressure, it was apparent that the stresses also fluctuated with changes in water level.

The effect of water level changes can be included in the finite element model by changing the buoyancy force on the ice cover. This was done by adding a uniform gravitational force at each time step during which there was a decrease in water level. The magnitude of the force is proportional to the water level change during the time increment. During periods of increasing water level, the incremental forces were applied in the opposite direction (upward). This approach is valid as long as the change in water level is not more than the ratio of densities times the thickness of the ice cover (~90% of the thickness). This numerical approach was verified by comparing the calculated deflections with the prescribed water level changes.

Calculations showed that changing the buoyancy force on the ice cover does not have a major effect on the calculated stresses. The stresses calculated with this approach compared very well with the measured stresses at the NRC basin test but this approach could not model the stress fluctuations that occurred in the dam sites. Changing the buoyancy forces causes only bending stresses in the ice sheet and cannot have a major effect on the in-plane stress resultant. In the dam sites the stress resultants calculated from the measured stresses also fluctuated with the water level changes. This suggests that the stress fluctuations might be caused by another mechanism rather than the change in buoyancy force, a mechanism which causes a relatively uniform stress distribution through the thickness.

One possible mechanism is arching action. Arching action was known to be the reason of the failure of a dam in Minneapolis in 1899 (The Engineering Record, 1899) and was also discussed in a paper by Wilmot (1952). When the water level drops, the ice cover, which is bonded to the reservoir walls, forms a basin and cracks at the edges (Fig. 5.15). These cracks can freeze and form a continuous arch. Subsequent increases in water level are resisted by arching action which causes a pressure through the whole thickness of the ice cover.

5.2.2 - NRC Basin Test - Winter 1992-93

As described in section 2.21, large scale tests were conducted at an outdoor basin at the National Research Council (NRC) in Ottawa, Ontario. The basin was 3 m deep, 60 m by 120 m in area and had vertical concrete walls. Freeze-up commenced in early December and the stress sensors were installed during the period from December 16 to 22. During the early part of the winter, the ice was allowed to grow and the stresses resulting from the changes in air and ice temperature were monitored. By the middle of January, a large amount of snow (0.2 m) had accumulated on the surface. To facilitate the occurrence of large temperature changes in the ice sheet, the snow was cleared on January 19 using mechanical equipment. Due to low conductivity of the snow, the snow layer acts like an insulation layer and does not let the ice cover lose heat to the air.

Therefore with increasing thickness of the snow layer the ice temperature increases. Consequently removing the snow cover and exposing the ice cover to the cold air produced a temperature shock and cracks in the ice sheet. The cracks subsequently refroze. The thermal load monitoring part of the test continued until January 23. During this period the water level in the basin remained constant.

On January 24 two slots were cut in the ice sheet (Fig. 5.16). The purpose of these was to produce a simple two dimensional geometry by eliminating the biaxial restraint. On January 25, tests to investigate the effect of water level changes were started. These continued till February 26. The tests were conducted by pumping water into or out of the basin. The snow was cleared again on February 19 by flooding. This was done by pumping water onto the ice surface and draining water from the basin at the same time. During all water level tests, with the exception of the last, the ice remained solidly bonded to the basin walls.

The thickness of the ice cover was relatively uniform over the basin's area. During the period January 8 to February 12, the ice near the walls was about two to five centimeters thinner than at the center of the basin. This was attributed to heat transfer from the ground. After February 22 the difference in thickness increased to about 10 centimeters. This was due to heavy snow falls and flooding operations which deflected the center of the ice sheet downward. The surface ice growth was very small before January 12 (1 cm). During the middle of the January it increased to about five centimeters and remained almost constant till the flooding operation (February 19). The water from the flooding remained on the ice and a large amount of surface growth occurred subsequently.

The ice temperature was measured continuously through the winter. In the early winter (December 24 to January 8) the ice temperature was measured at two points through the thickness: at the ice surface and 0.1 m below the surface. On January 8 a string of 12 thermocouples was installed which measured the air-ice-water temperature profile. When initially installed, the temperatures were measured at 1.5 m and 0.05 m above the ice surface, every 0.05 m through the ice thickness, and 1.4 m below the ice surface. Due to surface ice growth, the surface thermocouples gradually became embedded in the ice. No attempt was made to reposition the thermocouple string. Thus

the temperature at 0.05 m above the original surface was considered to be the ice surface temperature after January 25. After February 19 the same temperature was considered to be the temperature at 0.1 m below the ice surface.

The in-coming solar radiation and wind speed were also recorded during the period from December 22 to April 1. The in-coming solar radiation had daily fluctuations but increased with time over the winter, reaching a maximum of 890 W/m^2 on March 3. The maximum wind speed recorded was 6.95 m/s which occurred on March 16.

Three different types of sensors were installed in the ice sheet. One rosette of Hexpack panel meters was located at the center of the basin. These sensors, which were developed in 1983 by Fleet Technology Ltd., are thin wide panels that extend through the full thickness of the ice cover and measure the depth averaged pressure. Twelve BP local sensors (developed by British Petroleum) were arranged in four vertical arrays to measure the stress profile acting perpendicular to the basin walls. These are small disc shaped sensors which measure the average pressure over an area of 0.075 m diameter. The BP sensors were arranged so that they measured the average stresses at depths of 0.025 to 0.10, 0.125 to 0.20, 0.225 to 0.30, and 0.325 to 0.40 m. Three oil-filled flatjack sensors were also deployed which measured the average stress over an area of 0.15 m diameter. Since the stresses are very depth dependent, the data measured by the BP sensors, which have a smaller diameter, are preferred for the comparisons with the numerical simulations. The data record for the stresses measured by the upper sensors (0.025 to 0.10 m) were made available by Fleet Technology Ltd.

Several thermal events occurred during the thermal part of the test program. Figure 5.17 shows the measured temperatures during the December 24 to February 8 period, when only the ice surface and 0.1 m temperatures were measured. A number of thermal events can be seen in this figure. The stresses due to the temperature changes were calculated using the finite element program, ICEP. At first a finite element mesh spanning one quarter of the basin (using symmetry) was prepared. Subsequently, a single element model as described in section (5.2.1) was used. It was found that the results from the two models were the same and the single element model required less computing time. Therefore it was easier to model the long periods with the single element model. All the

results presented here for the thermal part of the program were simulated with the one element model.

Figure 5.18 shows the comparison between the calculated and measured stresses for the two events that occurred during the period December 24 to December 29. The material properties suggested by Drouin and Michel for snow-ice were used in the simulation. The first event begins at the start of the simulation. The stresses increase for about 15 hours and then decrease during the cooling period that follows the first event. The second event starts at about 60 hours from the start of the simulation and lasts about three days. During these events the thickness of the ice cover was about 0.15 m. The temperature distribution between the ice surface and 0.1 m was obtained from a thermal analysis, considering one centimeter of snow on the surface, as discussed in section (5.2.1). The temperature distribution between 0.1 m and the bottom of the ice sheet was also obtained from the thermal analysis. The stresses were calculated using snow-ice properties from Drouin and Michel.

The predicted stresses follow the measured stresses reasonably well during the first event. During the cooling period that occurred after the first temperature peak, the measured stresses remain compressive. This is probably due to the presence of cracks that reduce the tensile strength. First the analysis was performed using a very high tensile strength (1000 MPa). The calculations were then repeated using a very small tensile strength (0.01 MPa), which resulted in cracking of the ice sheet. The stresses calculated using the cracking model match the measured stresses quite well at the start of the second event (from 60 to 65 hours). This shows the importance of including the cracking in the simulation of the thermal stresses. At the end of the second event, the measured stresses decrease while the calculated stresses do not. Since the temperatures are still high (near 0°C) during this part of the event, the drop in the measured stresses might be due to compressive cracking or softening of the ice which could have led to unbonding of the sensors.

Figure 5.19 shows a comparison between the measured and calculated short wave solar radiation data during the first event (January 25 and January 26). The heat flux due to short-wave solar radiation that is shown in Fig. 5.19 was calculated for three different

values of cloud cover (C). For a clear sky, C is equal to 0/8 and it increases to 8/8 for the case of complete cloud cover. The heat flux due to short wave radiation can have a major effect on the temperature distribution in the ice cover, and as can be seen in Fig. 5.19 it can change significantly with the cloud cover. The amount of cloud cover is not usually included in meteorological data. Even when this data is available, it must be remembered that it is not obtained using sophisticated instrumentation. It is based on the subjective judgment of an observer.

Figure 5.20 shows the comparison between the measured and calculated stresses for the thermal event that occurred during the period from January 2 to January 4. The thickness of the ice cover at that time was 0.2 m. The temperature profile was obtained by the same method as described for the previous events. As can be seen, the calculated values match very well with the measured stresses. However at the end of the event, the measured stresses drop to zero due to melting of the ice. Above freezing temperatures were recorded through the thickness of the ice cover. After this event, the measured stresses were affected by freezing stresses for a while. The freezing stresses are the stresses that occur due to volume increase during freezing. Very high stresses (0.75 MPa) due to freezing were recorded by sensor BP21. The surface ice growth of one centimeter probably occurred after this event when the snow cover that was melted due to increase in temperature froze in the following cooling period.

On January 8 a string of thermocouples was installed which measured the air temperature and temperature in the ice sheet at every 0.05 m through the thickness. Figure 5.21 shows the measured temperatures during the period from January 8 to January 14. The air temperature data and the data recorded for incoming solar radiation were used to calculate the temperature distribution through the thickness of the ice cover. Figure 5.22 shows a comparison between the measured and calculated temperatures at 0.05 m and 0.1 m depth on January 10 and 11. The thickness of the ice cover at the time was 0.28 m. A layer of snow (0.03 m) was also considered on top of the ice sheet. Since the incoming short-wave solar radiation was measured, only the coefficient of reflection of the surface was used in the analysis. Many different values are suggested for the coefficient of reflection of snow in the literature. It depends on many parameters such as

age, wetness, and grain size of the snow cover. It also depends on the wave length and angle of the incident light. In general the coefficient of reflection of fresh and dry snow is high (0.8 to 0.9), but decreases once the snow cover gets older and begins to melt (0.5 to 0.6) (Gray and Male, 1981). It is also higher for short wave lengths. Bergdahl suggested values of 0.9 for wave lengths between 350-700 nm, 0.7 for 700-1200 nm, and 0.6 for 1200-4000 nm. These values were used in the temperature simulations. It was observed that the measured temperatures were higher during the daytime, therefore the value of 0.9 was reduced to 0.7 and good agreement was obtained. The measured temperatures match the calculated temperatures during the first day but are higher during the second day showing that probably the snow layer was melting and a lower coefficient of reflection was required. In Figs. 5.23-a and 5.23-b the measured and calculated temperature profiles are compared at five hours and 15 hours after the start of the simulation. The agreement is good except for the ice surface temperature. As mentioned earlier it is possible that the measuring point at the surface was located inside the snow layer. Figure 5.24 shows the comparison between the measured and calculated temperatures on January 12. The thickness of the ice sheet had increased to 0.3 m but the thickness of the snow cover was still 0.03 m. In this case the reflexivity is put equal to 0.5 for all wave lengths. Figures 5.25-a and 5.25-b show the measured and calculated temperature profiles at four hours and nine hours after the start of the event.

Above freezing temperatures were recorded on the surface and through the thickness of the ice cover during January 4, 5, 7, 8, and 9. Therefore the measured stresses might be high or low during and after these dates due to melting or freezing of the ice cover. In Fig. 5.26 the measured and calculated stresses are compared for the period from January 11 to January 14. The calculation was started earlier to include the effect of prestressing. This figure shows three thermal events, two daily events and one event that lasted more than one day. On January 13 and 14 there was a heavy snow (0.15 m) and the ice temperature increased despite a decrease in air temperature. The calculated stresses are higher than the measured stresses during all three events but the agreement with the measured stresses is best during the third event.

After January 15 the surface ice growth increased from 1 cm to about 5 cm on January 25 and remained almost constant till the flooding operation (February 19). Above freezing temperatures were recorded in the ice sheet on January 17. It is probable that some of the snow cover melted and froze subsequently. Therefore for the thermal events occurring between the January 17 and 25, the depths for the recorded temperatures are not quite clear. The snow cover was cleared on January 19 and some thermal events happened after that. Figure 5.27 shows a comparison between the measured and calculated stresses for the thermal events happening in the period from January 20 to 22. Three thermal events can be seen in this figure: one at the start of the simulation, the second after 24 hours, and the third after 36 hours. In this simulation the temperature at 5 cm above the original ice surface was assumed to be the surface temperature. The stresses were also calculated at 7.5 to 15 cm below the ice surface. It can be seen that the calculated stresses are higher than the stresses measured by all of the sensors during the first event, but are lower than those measured by BP21 during the second and third event. As the amount and rate of temperature change are similar in the first and second event it is not clear why such high stresses were recorded by BP21. Since clearing the snow on January 19 caused a thermal shock that produced some cracks in the ice, it is possible that stresses in all the sensors and particularly sensor BP21 were effected by opening and refreezing of the cracks.

On January 24 two slots were cut in the ice sheet to create a system of uniaxial restraint for performing the tests on water level changes. A finite element mesh covering the ice sheet between these slots (using symmetry) was prepared, and free boundary conditions were used at the location of the slots. The element sizes were selected so that the position of the Gauss points would be as close as possible to the location of the stress sensors. In Fig. 5.28 the measured and calculated stresses are compared for a period from February 1 to 7. In order to include the effect of the prestressing, the simulations started at January 30 and also a temperature increase of five degrees at the ice surface was applied at the start of the simulation. The calculation was performed twice, with and without the effect of the water level changes. The vertical displacements at the central point of the ice sheet are added to the initial water level and the results are presented as the calculated

water levels in Fig. 5.28. As can be seen, although the calculated water levels track the actual water levels, there is not much difference between the stresses calculated with or without water level changes and the stresses are mainly thermally induced. The increase in water level has resulted in a negative bending moment. Since the stresses are compared for the upper part of the ice cover, the bending stresses have reduced the compressive stresses due to thermal loads. The calculated stresses compare very well with the measured stresses except for the cooling period at about 96 hours. As can be seen the amount and the rate of temperature decrease from 80 hours to 96 hours are more than those in the cooling period from 28 to 40 hours and yet there is a large decrease in the measured stresses in the first cooling period. Since above freezing temperatures were recorded in the ice sheet at about 80 hours, it is possible that the measured stresses after that were affected by the freezing stresses.

5.2.3 - Arnprior Dam - Winter 1992-93

The Arnprior dam is located on the Madawaska River at Arnprior (about 50 km from Ottawa), Ontario. In addition to the dam wall there is a turbine intake section, gates and a sluiceway. The dam itself consists of a vertical concrete face and a sloped berm. Since the gates were heated, the stresses were measured only at a position close to the dam's vertical face. Six BP sensors arranged in two vertical arrays, with three sensors in each array, were used to measure the stress perpendicular to the dam face. The sensors measured the stress at depths of 0.025 to 0.10, 0.125 to 0.20, and 0.225 to 0.30 m below the ice surface. Initially (on December 9), the sensors were installed near the dam wall, but due to relatively large water level fluctuations, the ice near the dam broke up and an ice bustle consisting of ice, water layers, and air voids was produced. The sensors were repositioned on December 18 and January 5. By January 5 the ice conditions near the dam had stabilized and the sensors were located in the ice sheet in front of the bustle. A vertical string of thermistors was used to measure the air-ice temperature profile. The thermistors were also repositioned to the stable ice sheet in front of the dam.

Due to water level fluctuations a crack was formed in mid-January at about 10 m from the dam face. This crack refroze subsequently and another crack was formed further offshore in early February. The February crack was open during the winter and absorbed a part of the rotations produced by water level fluctuations. Therefore the local conditions at the dam face were no longer affected by the water level changes.

Figure 5.29 shows a comparison between the measured and calculated temperatures at depths of 0.1, 0.2, and 0.3 m below the ice surface during a period from February 12 to 15. The maximum line load occurred during this event. The temperatures through the thickness of the ice cover were calculated using the surface temperatures. There is a good agreement between the measured and calculated temperatures at 0.1 m and 0.2 m depths but the calculated temperatures are higher than the measured temperatures at 0.3 m. Measured and calculated temperature profiles 8 and 40 hours after the start of the simulation are shown in Fig. 5.30. It can be seen that the calculated temperatures at 0.3 m below the surface coincide with the temperatures at other depths. It is possible that the thermistor at 0.3 m was positioned at a higher level.

A finite element mesh covering a large part of the reservoir (about 1.25×2.5 km) was prepared for the stress analysis. The elements in front of the dam face were finer than elsewhere in the mesh. The stress resultants obtained from the calculated stresses are compared to those calculated from the measured stresses in Fig. 5.31. The material properties suggested by Drouin and Michel for snow-ice gave the best agreement. The temperature changes and the water level fluctuations are shown as well. Since the actual numbers for the water levels were very large, they are not used here, and the numbers shown in Fig. 5.31 are only used to show the fluctuations. The calculated water levels are obtained by adding the vertical displacements at a node in the middle of the reservoir to the initial water level. The calculated water levels show the same fluctuations as the measured ones but there is not much difference between the stress resultants calculated with or without water level changes. This was expected because the loading due to water level changes causes only bending stresses which do not have a significant effect on the stress resultants. The calculated stress resultants agree on an average basis with the measured values but do not exhibit the same fluctuations. The fluctuations in the

measured loads coincide with the water level changes. Since the calculated stresses do not show these fluctuations, it is possible that other mechanisms such as arching action are responsible. The February crack also may have affected the stress distributions. The stresses measured at different depths were roughly equal at one of the sensors but at the other, higher stresses were recorded at the lowest sensor.

5.2.3 - Paugan Dam - Winter 1991-92 And 1992-93

The Paugan Dam is a hydro-electric power plant located on the Gatineau River near Low (about 100 km north of Ottawa), Quebec. The spillway is located about 300 m from the dam and has six steel gates, each with a span of 15.2 m, and six concrete piers. Two of the steel gates are heated. The dam is located next to the power plant and has a combination of vertical and sloped faces. The reservoir is about 500 m wide and has moderately steep and rocky sides.

During the 1991-92 winter, temperatures and stresses were measured at two sites: near the spillway (site 1), and near the dam face and power house (site 2). The air-ice-water temperature profile was measured using thermistor strings consisting of six thermistors at 10 cm intervals. Two thermistor strings were deployed at each site. One measured the temperatures in the vicinity of the structure and the other measured the far field temperatures. A combination of BP and panel stress meters were used to measure the local and depth averaged pressures. The BP sensors were located at depths of 0.07 to 0.145 and 0.195 to 0.27 m below the ice surface. At site 1 the stress sensors were placed in the vicinity of gates 2 and 3 (which were unheated), near piers 2 and 3, and at 32 m and 67 m from gate 2. At site 2 the sensors were installed along the face of the dam, along the nearby steep rock face, and also at 30 m from the dam.

By early January, the reservoir was covered with a stable ice sheet with little snow cover (less than 10 cm). Near the surface the ice sheet consisted of large grained P2, and fine grained P3, P4, and S1 ices. At depths below 20 cm the ice was of columnar S2 type. The stress sensors were installed during January 4 to 7 by cutting a slot in the ice, placing the sensor in the slot, and pouring water around it. From January 1 to January 15 the

water fluctuations were small (about 5 cm). During January 15 to 17 a large crack formed in the vicinity of the structures and along the reservoir boundaries due to a water level drop of about 25 cm. After January 20 several snow falls took place and the ice sheet was gradually depressed by the weight of the snow. In early February the ice sheet became submerged below the water level. As described in the reports of Fleet Technology Ltd., water reached the surface and a mixture of snow, surface ice crusts, and water was formed on top of the original ice surface. Therefore in the regions away from the boundaries, the recorded ice temperatures through the thickness of the ice cover were at the freezing point. Although at the boundaries the ice temperature was below the freezing point, the relatively soft ice that covered most of the reservoir prevented the occurrence of thermal loads during the remainder of the winter.

Significant thermal events occurred during January 8 to January 19. In Fig. 5.32 the measured and calculated stresses are compared for the period from January 9 to January 15. Two thermal events occurred during this period, one from January 8 to 10, and the other from January 12 to 15. The temperature data was obtained from the temperature profiles given in the figures of the report at four hour intervals. In the time intervals between the times of the given profiles the temperature profile was obtained from a linear interpolation between the given temperatures. The measured stresses are the maximum principal stresses obtained from the rosette located 30 m from the vertical face at a depth of 0.07 to 0.145 m. This location was selected for the comparison because it was stress free at the start of the simulation and was unaffected by the local conditions in the vicinity of the structures. The finite element analysis was performed using a single element mesh. The material properties suggested by Cox were used in the analysis because the material properties of snow-ice resulted in low stresses compared the measured stresses. The stress analysis was performed, with and without cracking. The stresses obtained with the cracking model agree best with the measured stresses.

The maximum line load obtained from the measured stresses in the reservoir which occurred during the first event was 115 kN/m. The loads on the pier were significantly higher than those on the gate. The maximum loads on the pier and gates were 288 and 82 kN/m respectively. The difference in the loads on the piers and the gates was probably

due to flexibility of the gates. Since there was not enough information to assign a value for the stiffness of the steel gate, a parametric study was performed with different values for the stiffness of the gate and the results are presented in Chapter 6.

During the winter of 1992-93 temperatures and the stresses were measured only at site 1. The air-water-ice temperature profile was measured at two locations: at 1 m from gate 2, and 30 m from it. A panel stress meter that measured the depth averaged pressure through the whole thickness of the ice cover was installed 30 m from the gates. BP sensors were deployed near gate 2 and pier 3 at depths of 0.025 to 0.10, 0.125 to 0.20, and 0.225 to 0.30 m below the ice surface. The sensors were initially installed on December 11 on floats. Due to a large drop in the water level the sensors were repositioned on December 14. The thermal loads occurred during the period from December 22 to February 13. In mid-February the far field ice temperature profile became uniform at the freezing point due to snow accumulation. In early winter the ice temperature profile was similar at both positions. Later, the ice near the gates was colder and had more temperature variations than the ice at far field. However, since a relatively soft ice covered most of the reservoir, the loads were very low near the spillway.

The highest stresses were recorded during the first thermal event which occurred on December 24. Unfortunately the temperature data for this event is not considered reliable because two quite different temperatures were recorded near the ice surface. In other thermal events, the stresses recorded 30 m from the gates were below 0.12 MPa, therefore despite the ambiguous temperatures, an attempt was made to simulate the stresses for the first event. Since for the 1991-92 winter the stresses obtained using the material properties suggested by Cox gave the best agreement, it was necessary to know if those properties would give the best agreement for the 1992-93 winter as well. Therefore, the material properties suggeted by Cox and those suggested by Drouin and Michel for snow-ice were both used in the simulations. The agreement was better when the snow-ice properties were used. Figure 5.33 shows the results of the stress analysis for the period from January 24 to January 26. Between the two different temperatures which were recorded for the ice surface, the lower one was used for the analysis. The thermal event that starts at 19:00 on January 24, was preceded by a cooling period. Prior to this cooling

period, which lasted about one day, above freezing temperatures were recorded through the entire thickness of the ice cover. Therefore the compressive stresses during this cooling period are probably due to the freezing of the ice cover. Two different start times were selected for the stress analysis: one from a stress free condition during the cooling period, and the other from the start of the thermal event. Cracking of the ice was included in the analysis. The simulation that started from the beginning of the thermal event resulted in stresses that were higher than the measured stresses. The other analysis that includes the cooling period, gives the best agreement with the measured stresses during the latter part of the thermal event.

The temperature analysis was done for a period during which the graphs containing the temperature data were plotted on an extended scale. The measured surface temperature was used as the surface boundary condition in calculating the temperature distribution through the whole thickness of the ice cover. In Fig. 5.34 the measured and calculated temperatures at the depths of 0.1 and 0.2 m are compared for a period from January 12 to 14. The agreement is very good for the temperatures at 0.1 m, but the temperatures measured at 0.2 m are slightly lower than the calculated temperatures. The difference is less than 0.5 degrees.

5.3 - Summary and Conclusion

In this chapter the temperature and stress predictions of the programs prepared in this study, were compared to the results of experiments and field measurements. The experimental studies of Drouin and Michel, and the field data collected by Fleet Technology Ltd. at the NRC Test Basin, Arnprior Dam, and Paugan Dam were used in the comparisons. Most of the measured data used in the comparisons of the NRC Basin Test were available in digital form, but the other data were read from the graphs and were subjected to reading errors. Some of the general conclusions from the comparisons are discussed here.

It was observed that good temperature predictions are possible with the thermal analysis program, ICET. However, the results depend on the boundary conditions. Two types of boundary conditions were used. In the NRC Basin Test, where the data for the wind speed and solar short wave radiation were available, the air temperatures were used to calculate the temperature distributions through the thickness of the ice cover including the ice and snow surface temperature. The agreement was good except for the ice surface temperature. This was attributed to the high temperature gradient that exists at the ice surface. The results were also sensitive to the amount of solar short wave radiation. At the dam sites, where the wind speed and solar radiation data were not available, the ice surface temperatures were used to calculate the temperatures through the thickness of the ice cover. The agreement was good in most of the cases.

In the stress simulations, it was observed that the predicted stresses depend very much on the choice of mechanical properties. The mechanical properties suggested by Drouin and Michel for snow-ice gave the best agreement for most of the experiments and field measurements. For the Paugan Dam however, during the 1991-92 winter, the stresses obtained using the snow-ice properties were very low compared to the measured stresses while the mechanical properties suggested by Cox gave the best agreement. Also, information concerning grain structure was incomplete. Therefore, it was not possible to reach to a firm conclusion with the available information about which mechanical properties are the best. More field measurements in different regions are required to obtain a better understanding about the mechanical properties of ice.

A constitutive model consisting of a linear temperature dependent spring and a nonlinear temperature dependent dashpot was used in the simulations (Maxwell unit in Fig. 4.2). This model can give a reasonable prediction of the ice stresses, has well defined mechanical properties and requires less computing time than a model including the delayed elastic element. A single element mesh was used in most of the simulations with thermal loading (i.e. no water level changes). The stress history was observed to have a significant effect on the predicted stresses. In order to include the effect of stress history, long periods were used and in some cases the simulations started one or two days before a particular thermal event. Cracking of the ice should also be considered in the analysis. In

the simulations, the tensile strength of ice was set very close to zero (0.01 MPa), since the tensile stresses measured were close to zero. This is probably the effect of cracks that are present in the ice. The effect of water level changes was included by adding a uniform gravitational force which changed according to water level fluctuations. The calculated deflections matched with the prescribed water level changes. The stresses obtained by this method compared very well with the stresses for the NRC Basin Test but did not show the fluctuations that occurred in the stresses at the dam sites. It was suggested that probably other mechanisms such as arching action produced the stress fluctuations. The agreement between the measured and calculated stresses was good in most of the cases. In situations where above freezing temperatures were recorded in the ice sheet, some discrepancies were observed between the measured and calculated stresses. During these periods the calculated stresses were usually higher than the measured stresses and after these periods the measured stresses were higher. In some cases even compressive stresses were recorded during the cooling periods. These discrepancies were attributed to the melting and freezing of the ice cover. The cracks that were caused by water level changes or snow removal operations also affected the stresses in the ice cover.

Name	Formation	Grain size and shape	Orientation of c-axis	Location
P1	calm surface, small temperature gradient	large to extra large, irregular	vertical	reservoirs, lakes, calm rivers
P2	calm surface, large temperature gradient	medium to extra large, tabular or needle like	random or vertical	lakes, reservoirs, calm rivers
P3	agitated surface, nucleated from snow	fine to medium, tabular	random	lakes, reservoirs, rivers, seas
P4	nucleated by snow	fine to medium	random	lakes, reservoirs, seas
S1	calm water, like P1 and P2	large to extra large, columnar	vertical	lakes, reservoirs, calm rivers
S2	like P2, P3, and P4	large to extra large, columnar	random in horizontal plane	lakes, reservoirs, seas
S3	bottom of thick ice sheets	columnar	aligned in horizontal plane	frozen lakes, thick sea ice, arctic ice islands
S4	congealed frazil slush	fine to medium, tabular	random	turbulent flows
S5	drained congealed frazil slush	fine to medium, angular	random	where water has drained from slush
T1	snow-ice	fine to medium, round to angular	random	where saturated snow freezes
T2	drained snow-ice	fine to medium, well rounded	random	where water level varies rapidly
T3	layers of columnar ice on top of primary ice			
R	agglomerate ice	various ice types and forms		

Table 5.1 - Classification of different ice types (Michel, 1979).

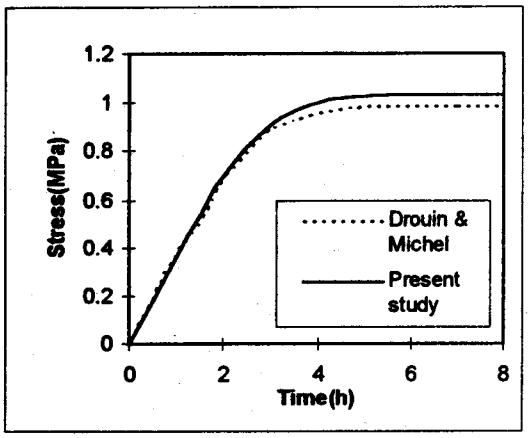

a) $\theta = -8.9^{\circ}C$, $\dot{\varepsilon} = 9.31 \times 10^{-8} s^{-1}$

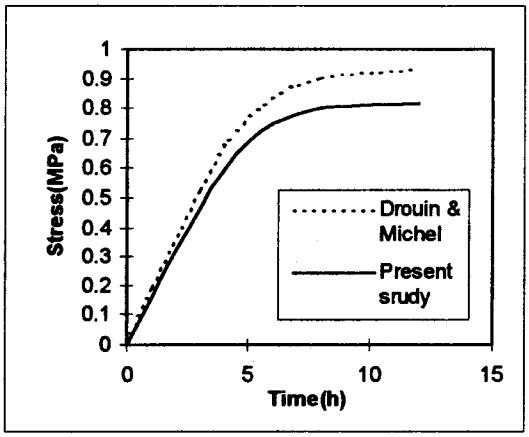

b) $\theta = -12.2^{\circ}C$, $\dot{\varepsilon} = 3.68 \times 10^{-8} s^{-1}$

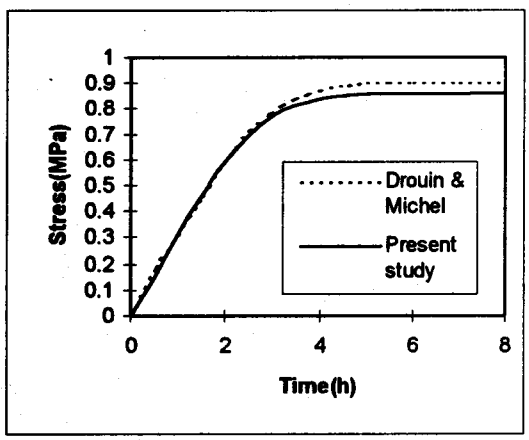

c) $\theta = -3.9^{\circ}C$, $\dot{\varepsilon} = 9.29 \times 10^{-8} s^{-1}$

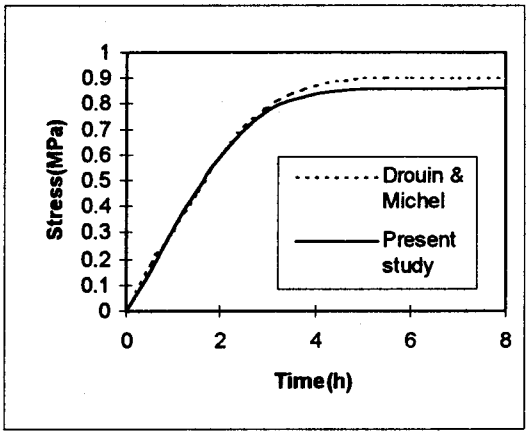

d) $\theta = -27.4^{\circ}C$, $\dot{\varepsilon} = 5.56 \times 10^{-8} s^{-1}$

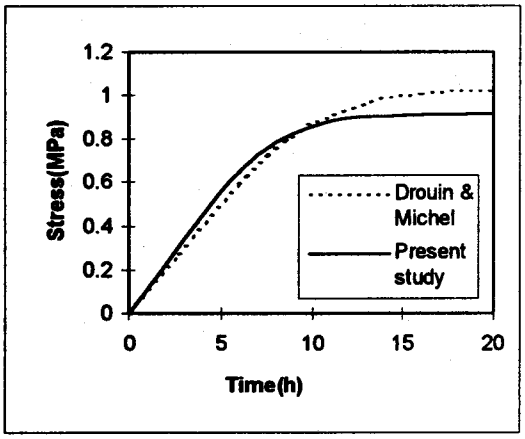

e) $\theta = -14.8^{\circ}C$, $\dot{\varepsilon} = 2.46 \times 10^{-8} s^{-1}$

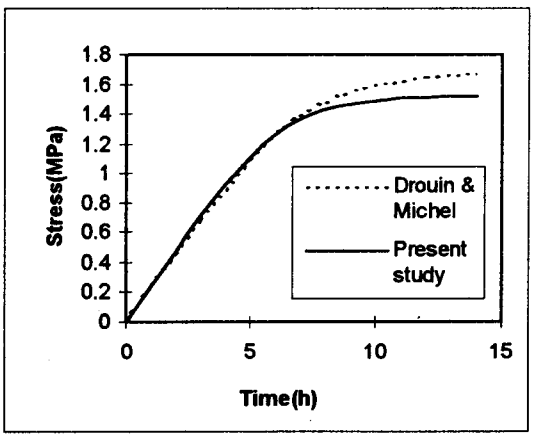

f) $\theta = -25.1^{\circ}C$, $\dot{\varepsilon} = 3.68 \times 10^{-8} s^{-1}$

Figure 5.3 - Stress under constant strain rate, based on the uniaxial experiments of Drouin and Michel on snow-ice.

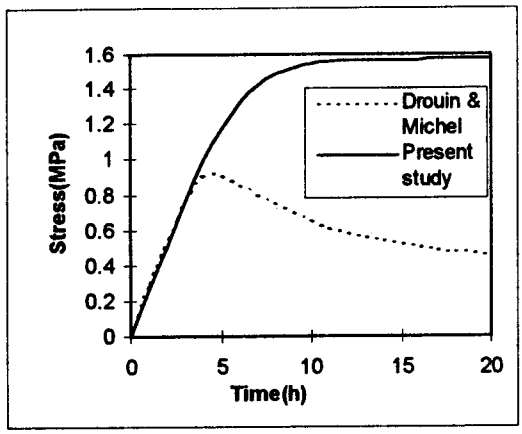

a) $\theta = -4.1^{\circ}C$, $\dot{\varepsilon} = 5.56 \times 10^{-8} s^{-1}$

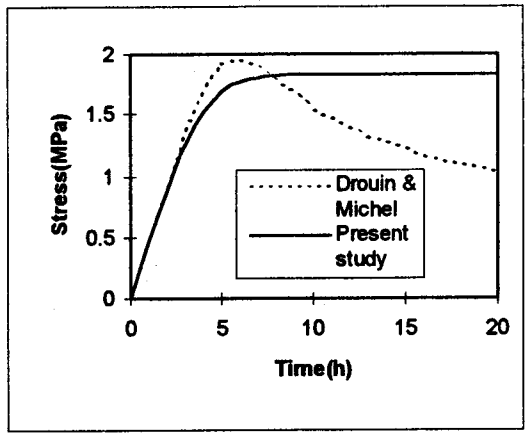

b) $\theta = -4.9^{\circ}C$, $\dot{\varepsilon} = 9.08 \times 10^{-8} s^{-1}$

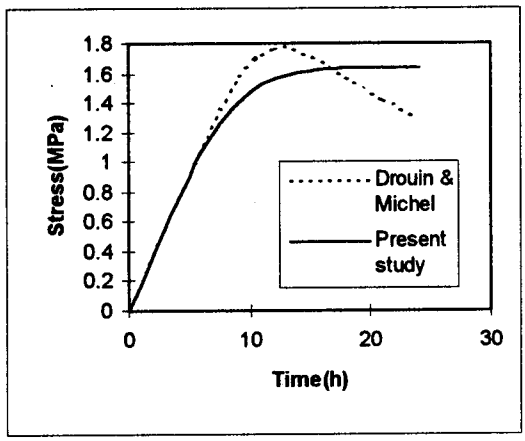

c - $\theta = -9.6^{\circ}C$, $\dot{\varepsilon} = 3.72 \times 10^{-8} s^{-1}$

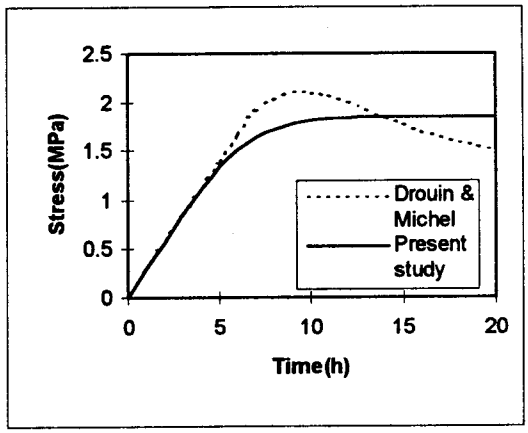

d) $\theta = -10.1^{\circ}C$, $\dot{\varepsilon} = 5.52 \times 10^{-8} s^{-1}$

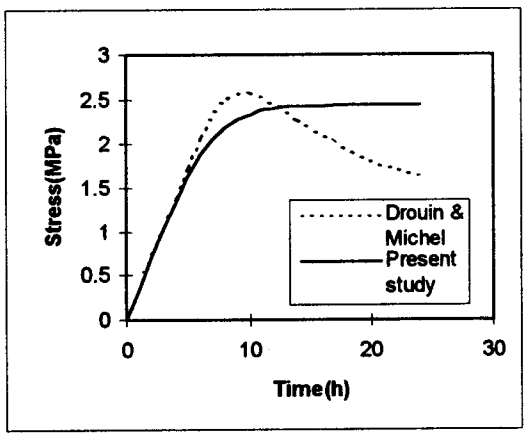

e) $\theta = -19.4^{\circ}C$, $\dot{\varepsilon} = 5.5 \times 10^{-8} s^{-1}$

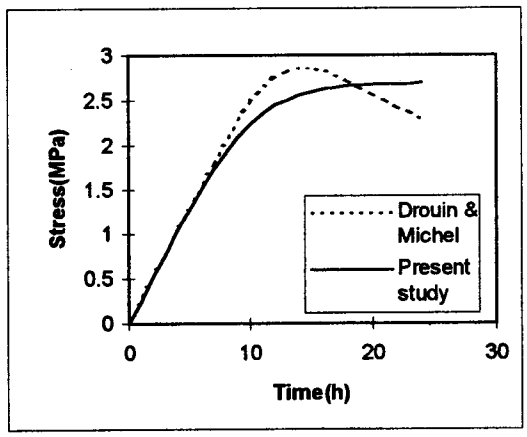

f) $\theta = -26^{\circ}C$, $\dot{\varepsilon} = 3.7 \times 10^{-8} s^{-1}$

Figure 5.4 - Stress under constant strain rate, based on the uniaxial experiments of Drouin and Michel on S1 ice.

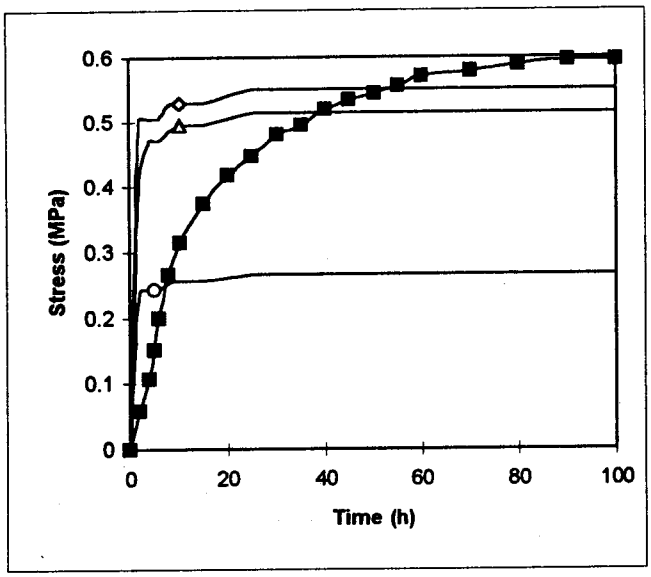

a) $\theta = -9.4^{\circ}C$, $\dot{\varepsilon}_1 = 5 \times 10^{-8} s^{-1}$, $\dot{\varepsilon}_2 = 6.94 \times 10^{-8} s^{-1}$

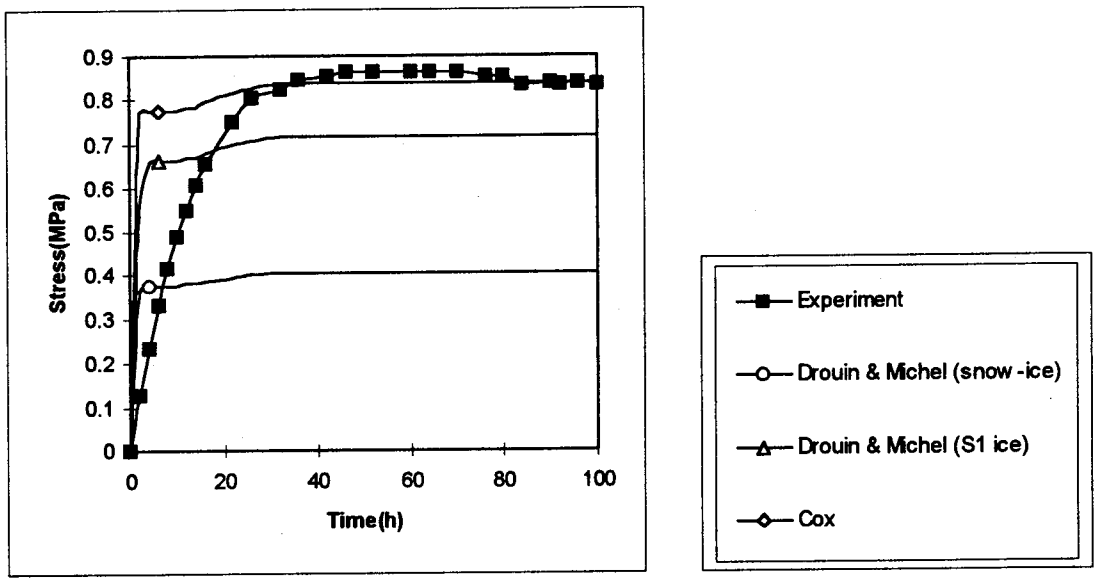

b) $\theta = -20.6^{\circ}C$, $\dot{\varepsilon}_1 = 5.2 \times 10^{-8} s^{-1}$, $\dot{\varepsilon}_2 = 6.9 \times 10^{-8} s^{-1}$

Figure 5.5 - Stress under constant strain rate, based on the uniaxial experiments of Drouin and Michel on S2 ice.

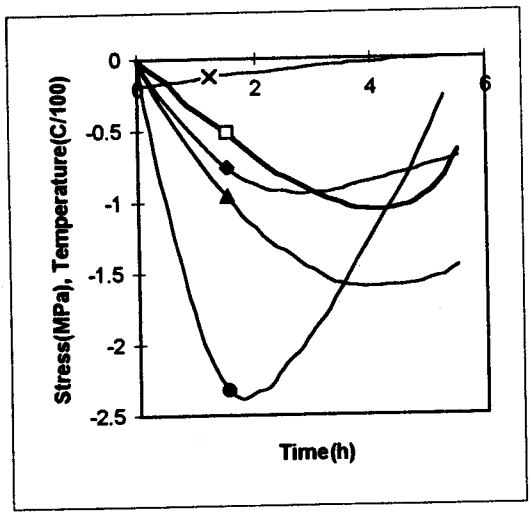

a) $\theta_i = -19^\circ C,\ \dot{\theta} \approx 3.65^\circ C / h$

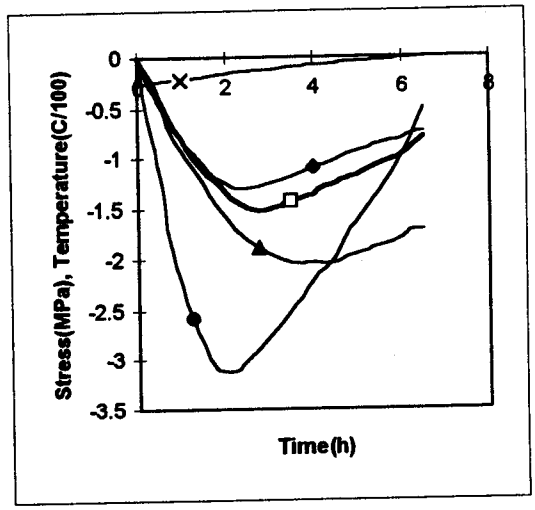

b) $\theta_i = -28^\circ C,\ \dot{\theta} \approx 4.15^\circ C / h$

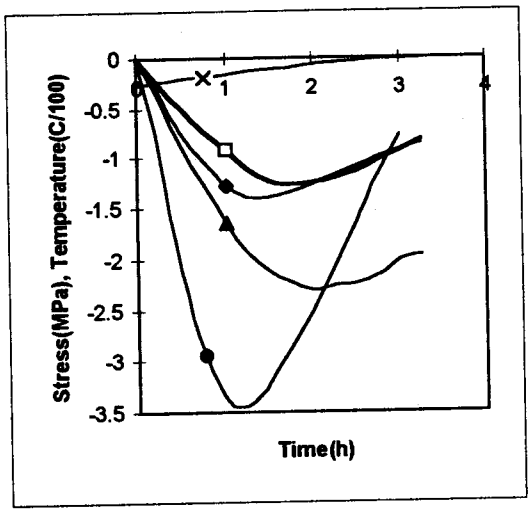

c) $\theta_i = -27^\circ C,\ \dot{\theta} \approx 7.6^\circ C / h$

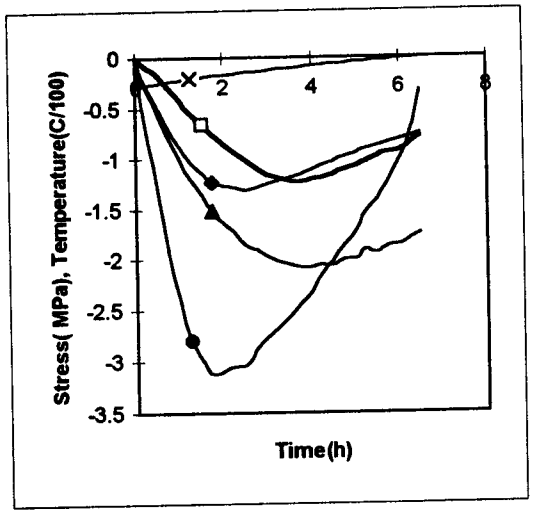

d) $\theta_i = -28^\circ C,\ \dot{\theta} \approx 4.5^\circ C / h$

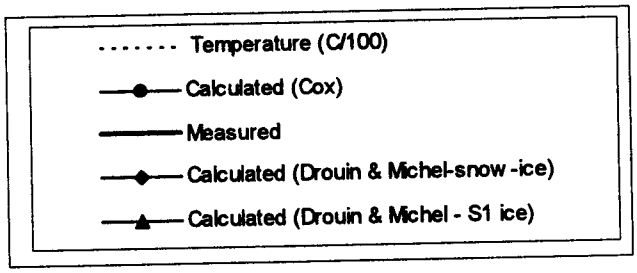

Figure 5.6 - Stress under linear temperature increase, based on the biaxial experiments of Drouin and Michel on snowice.

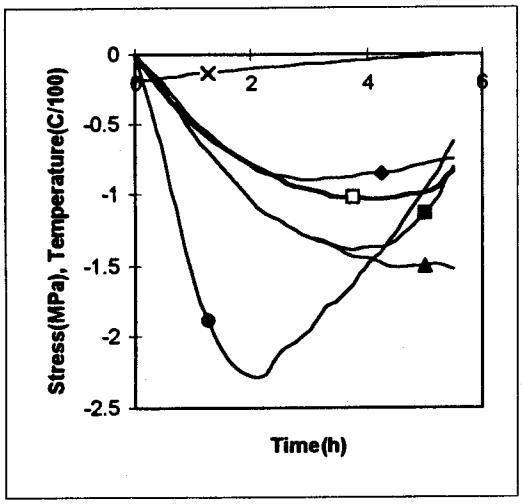

a) $\theta_i = -19°C,\ \dot{\theta} \approx 2.9°C/h$

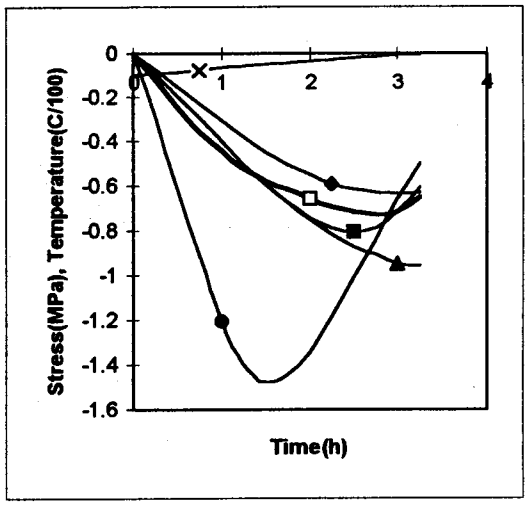

b) $\theta_i = -10°C,\ \dot{\theta} \approx 2°C/h$

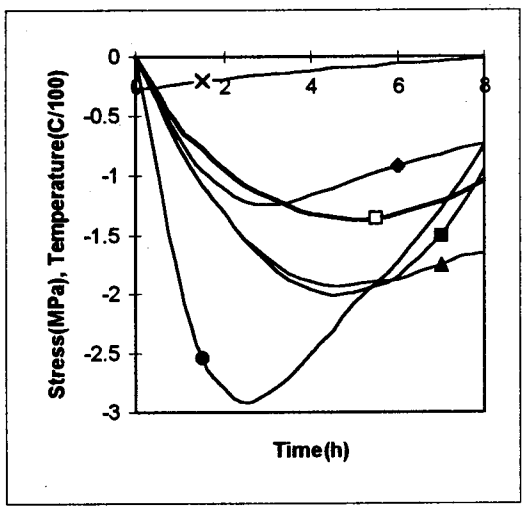

c) $\theta_i = -28°C,\ \dot{\theta} \approx 2.9°C/h$

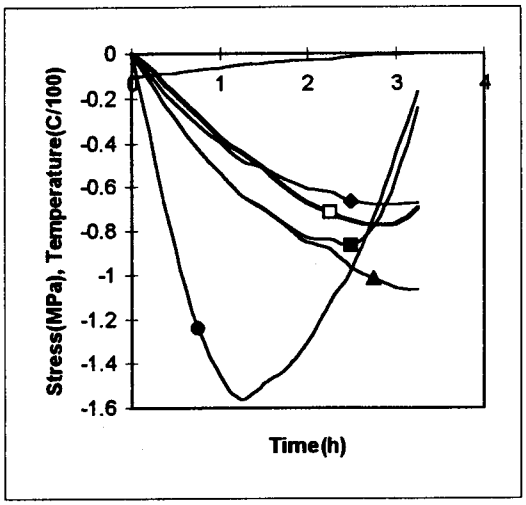

d) $\theta_i = -11°C,\ \dot{\theta} \approx 2.3°C/h$

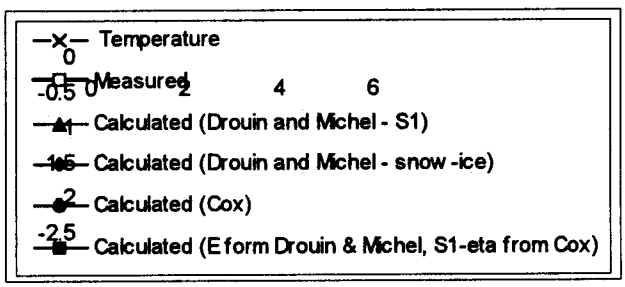

Figure 5.7 - Stress under linear temperature increase, based on biaxial experiments of Drouin and Michel on S1 ice.

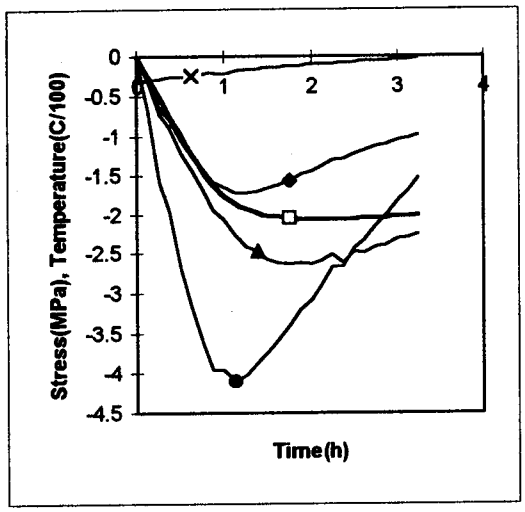

a) $\theta_i = -32^\circ C,\ \dot{\theta} \approx 7.1^\circ C / h$

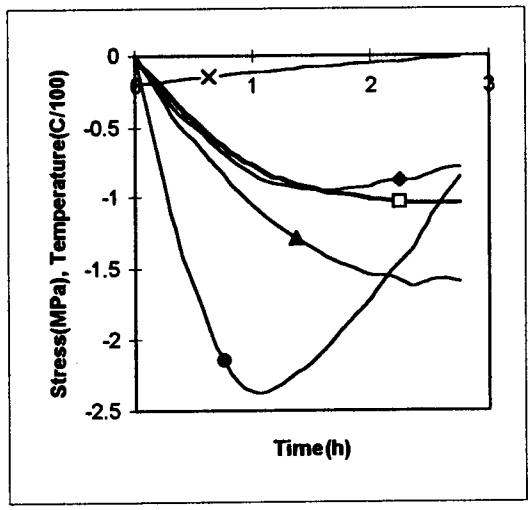

b) $\theta_i = -19^\circ C,\ \dot{\theta} \approx 1.8^\circ C / h$

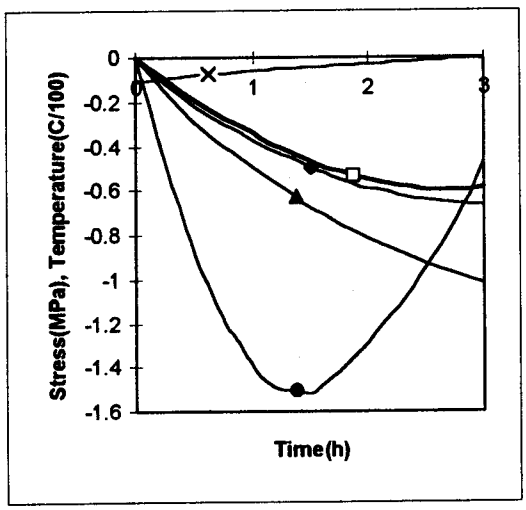

c) $\theta_i = -11^\circ C,\ \dot{\theta} \approx 2^\circ C / h$

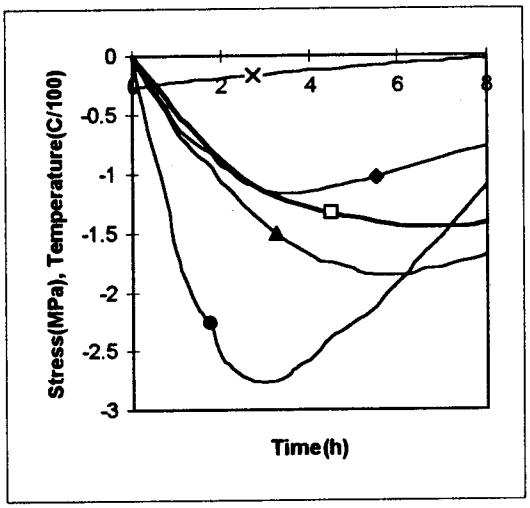

d) $\theta_i = -26^\circ C,\ \dot{\theta} \approx 2.4^\circ C / h$

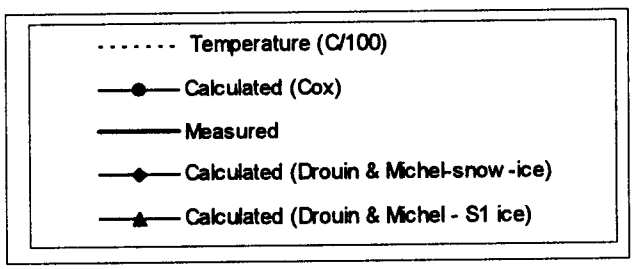

Figure 5.8 - Stress under linear temperature increase, based on Drouin and Michel's biaxial experiments on S2 ice.

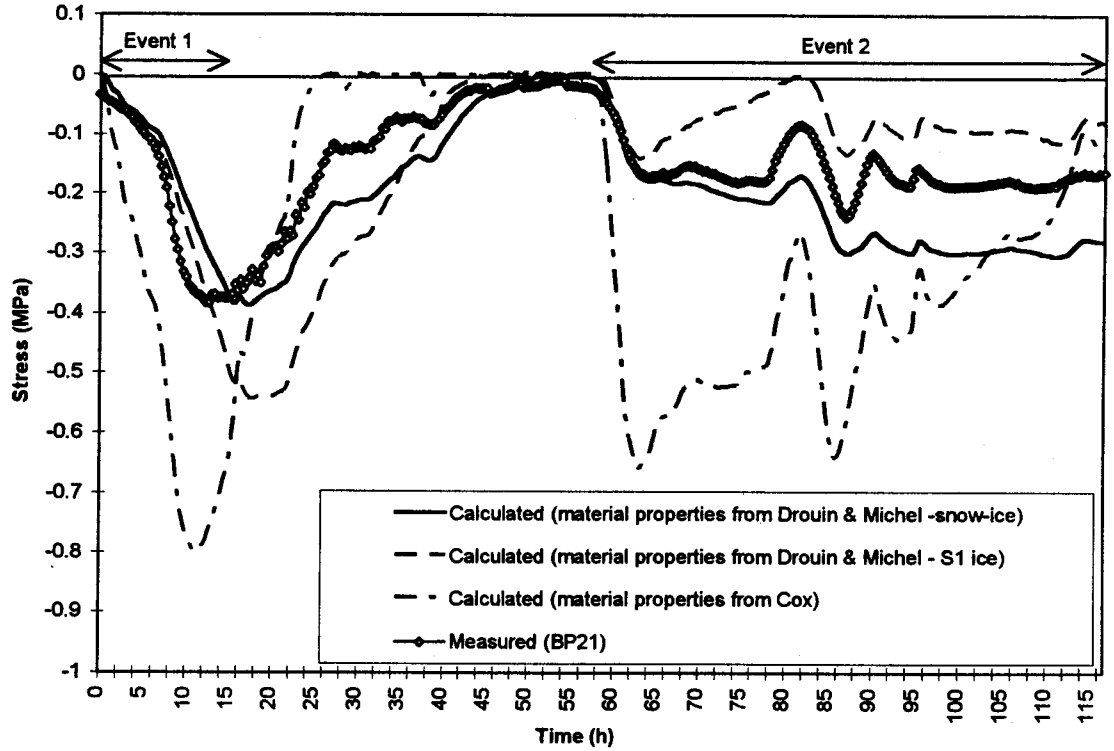

Figure 5.9 - NRC basin test (12/24 to 12/29), comparison between the measured stresses and the stresses calculated with different material properties.

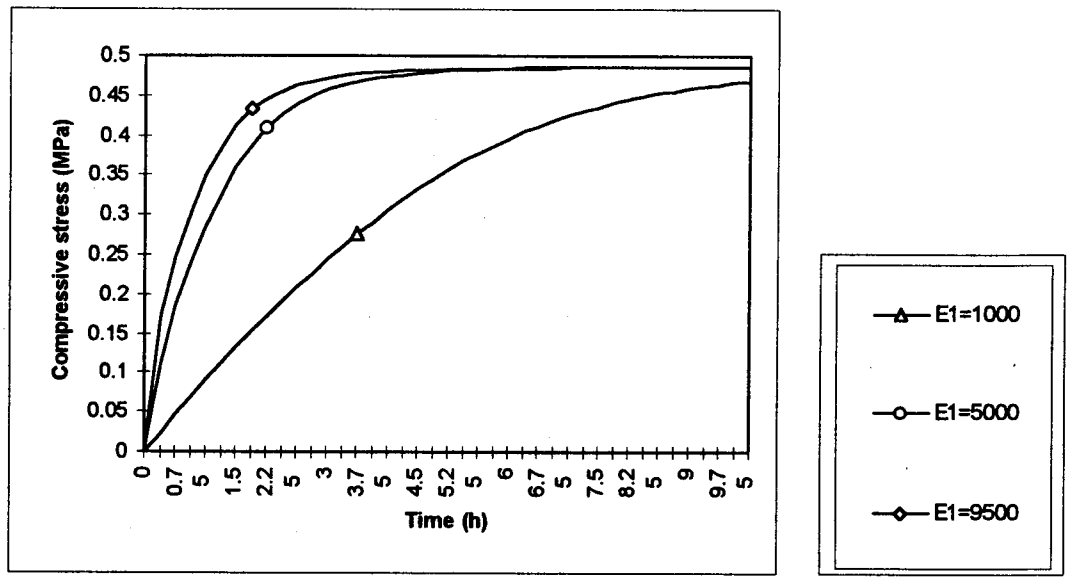

Figure 5.10-a - Stress under constant strain rate, calculated with the constitutive model 2 and different values for E_1.

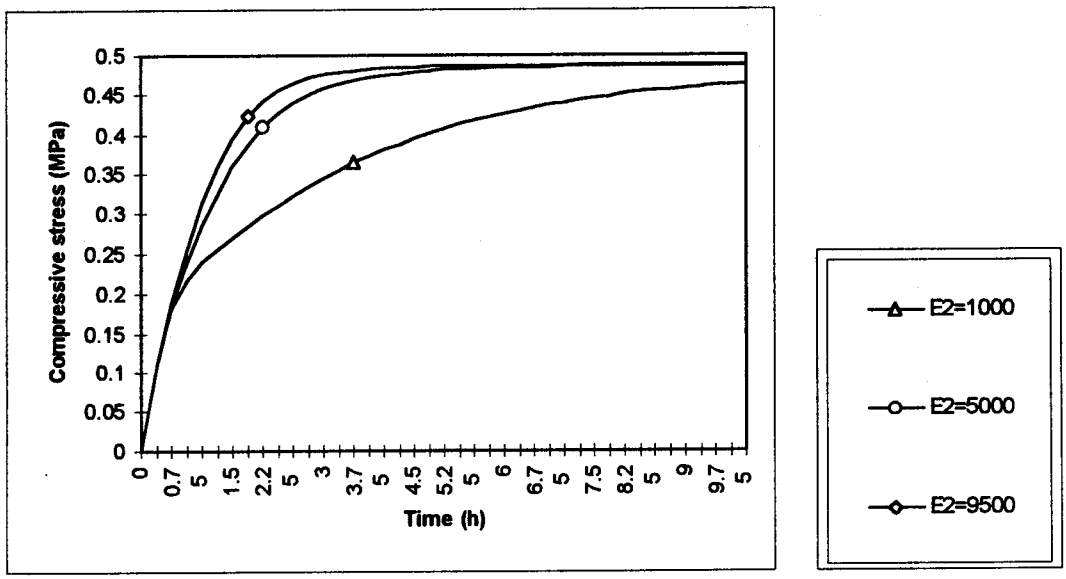

Figure 5.10-b - Stress under constant strain rate, calculated with the constitutive model 2 and different values for E_2.

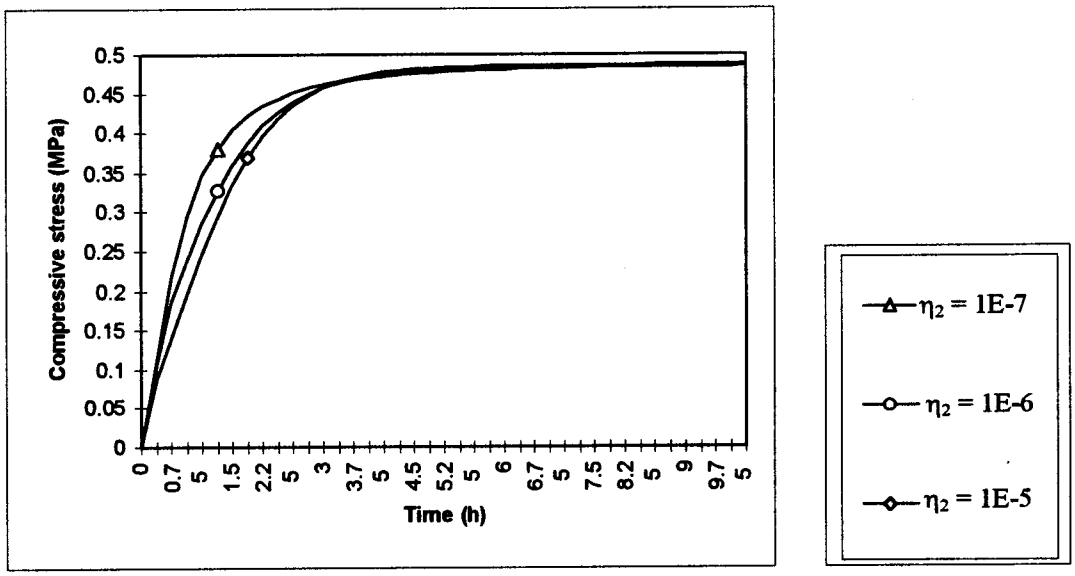

Figure 5.10-c - Stress under constant strain rate calculated with the constitutive model 2 and different values for η_2.

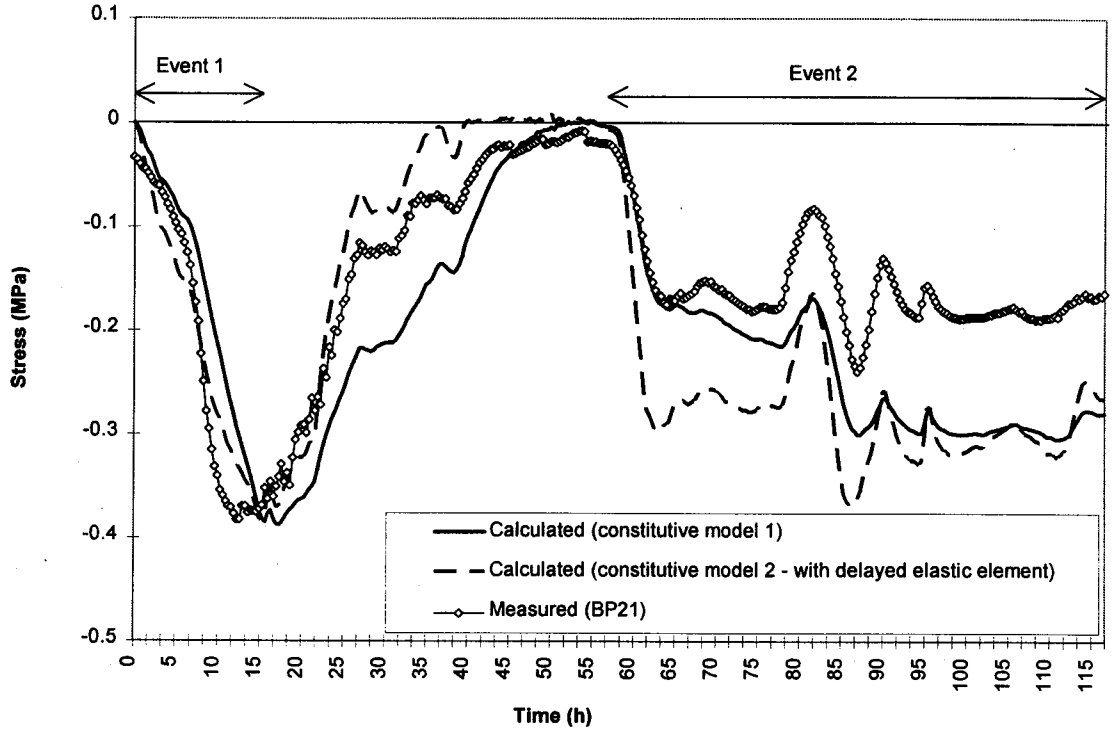

Figure 5.11 - NRC basin test (12/24 to 12/29), comparison between the measured stresses and the stresses calculated with different constitutive models.

Nodes restrained except for motions indicated.

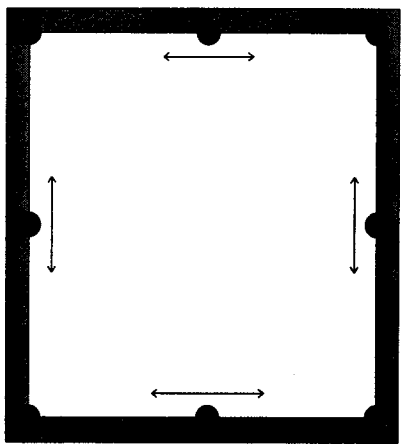

Figure 5.12 - A typical one element mesh for thermal loading analysis.

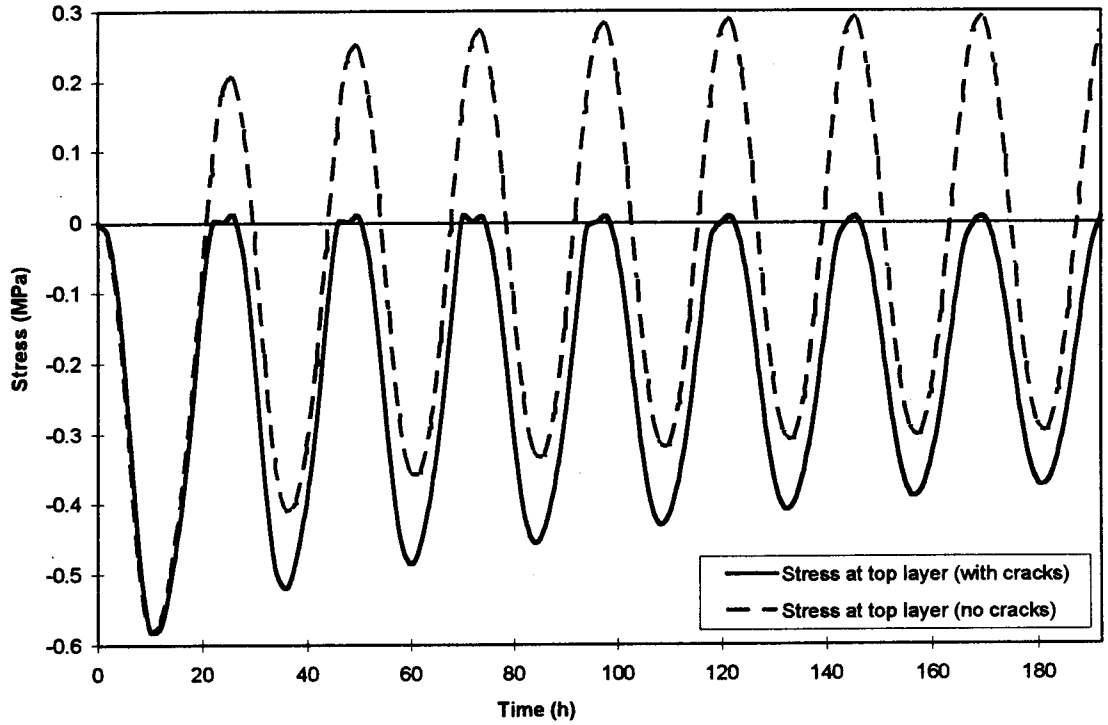

Figure 5.13 - Effect of stress history on ice stresses.

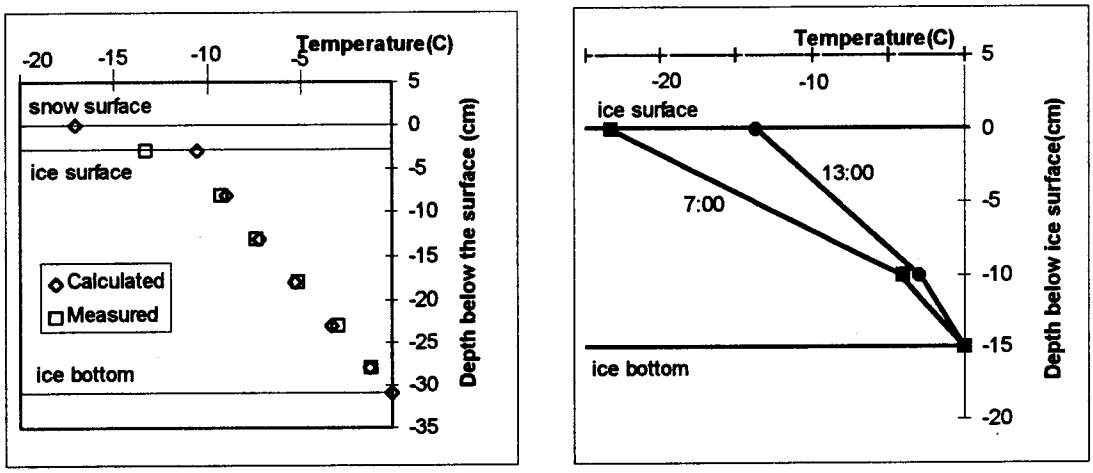

a)Temperatures at 1/10/1993 9:20 b)Measured temperatures at 12/27/1992

Figure 5.14 - Measured and calculated temperature profiles at NRC basin test.

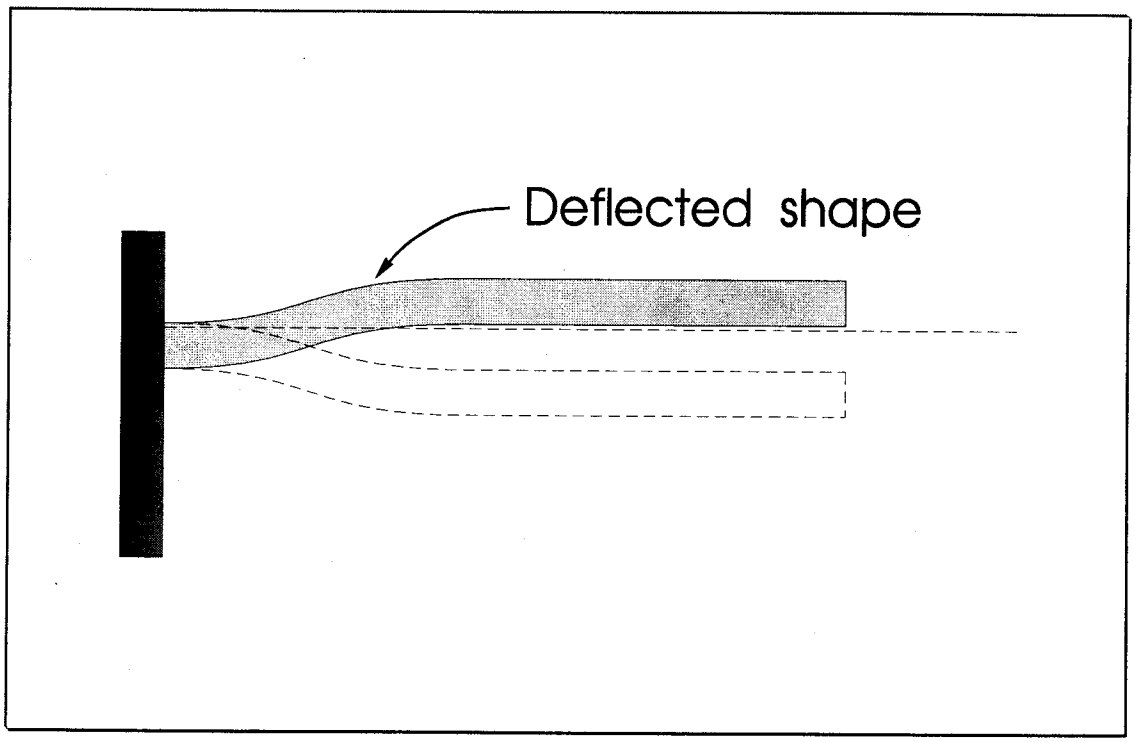

Figure 5.15 - Deflected shape of the ice cover during water level changes.

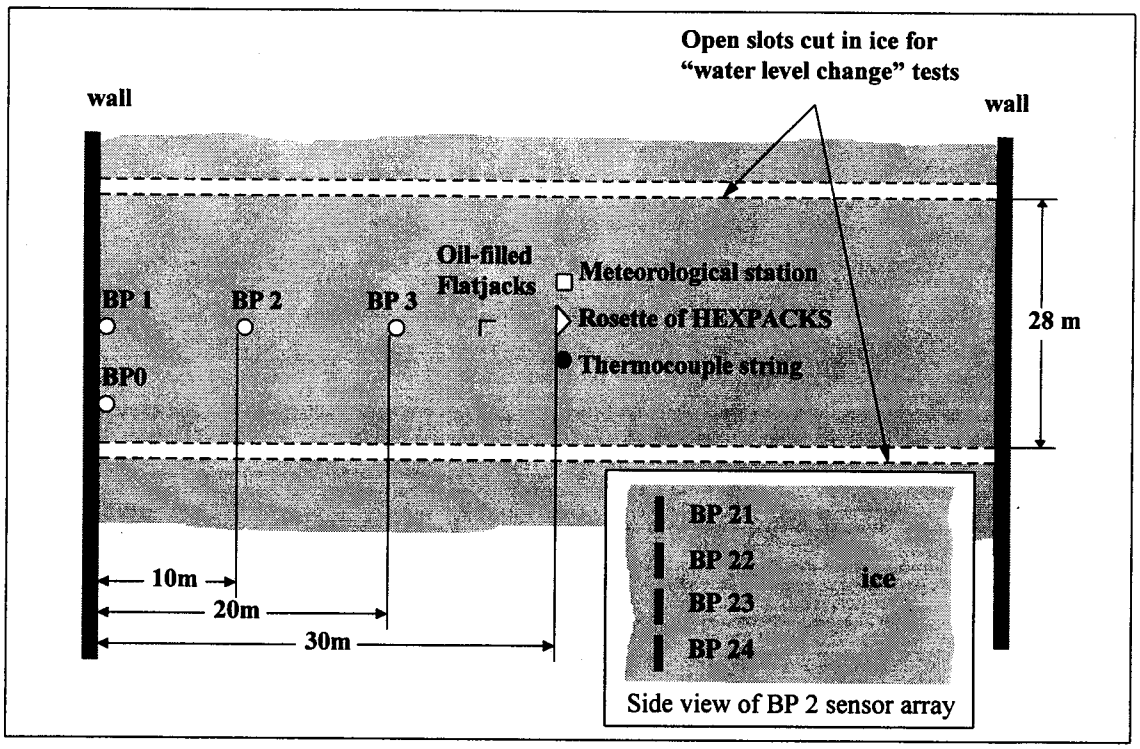

Figure 5.16 - Layout of sensors and the slots, and side view of a typical sensor array at NRC Basin Test.

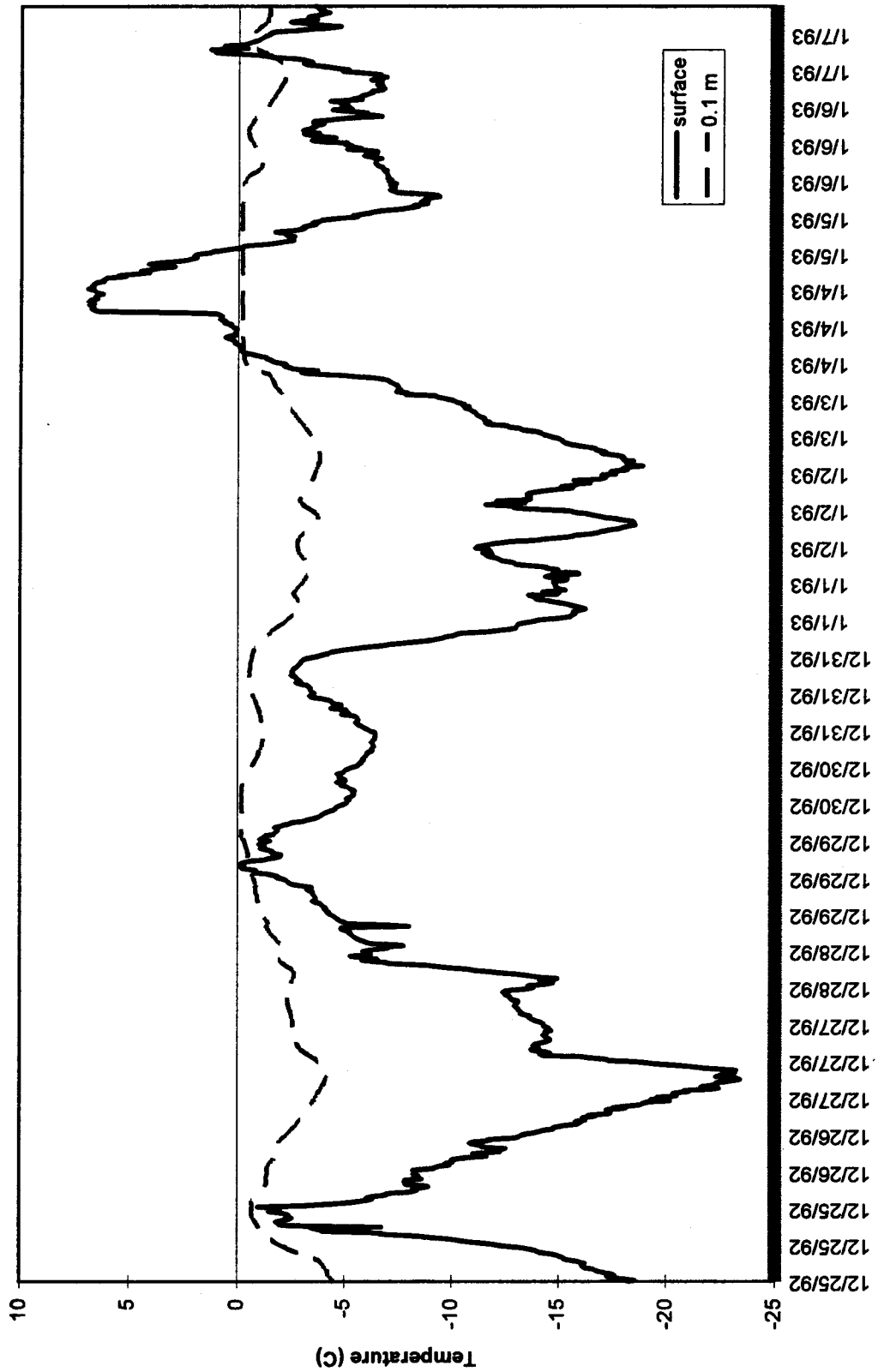

Figure 5.17 - Measured temperatures at NRC Basin Test (12/25 to 1/7).

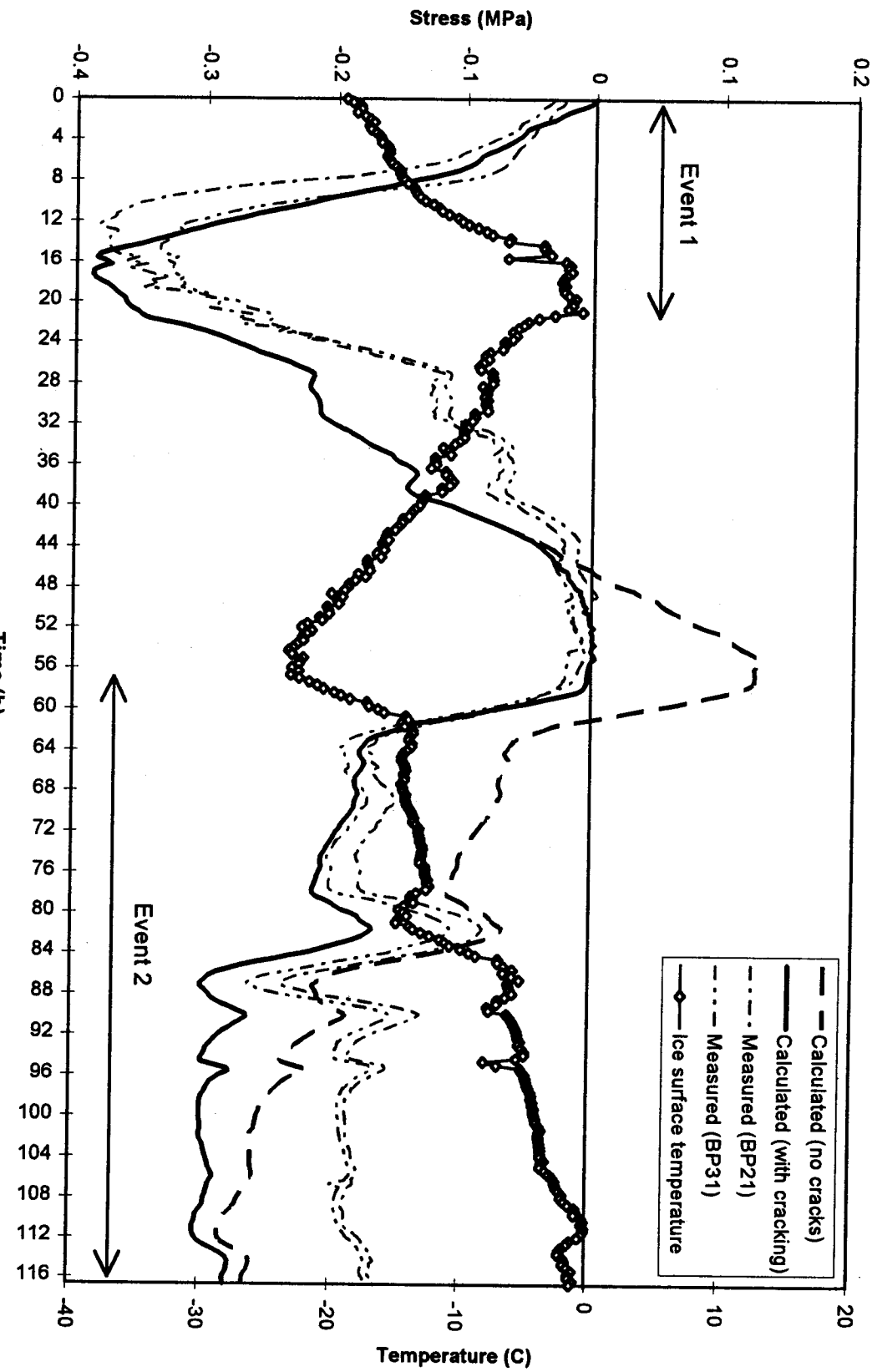

Figure 5.18 - Measured and Calculated temperatures at NRC Basin Test (12/24 to 12/29).

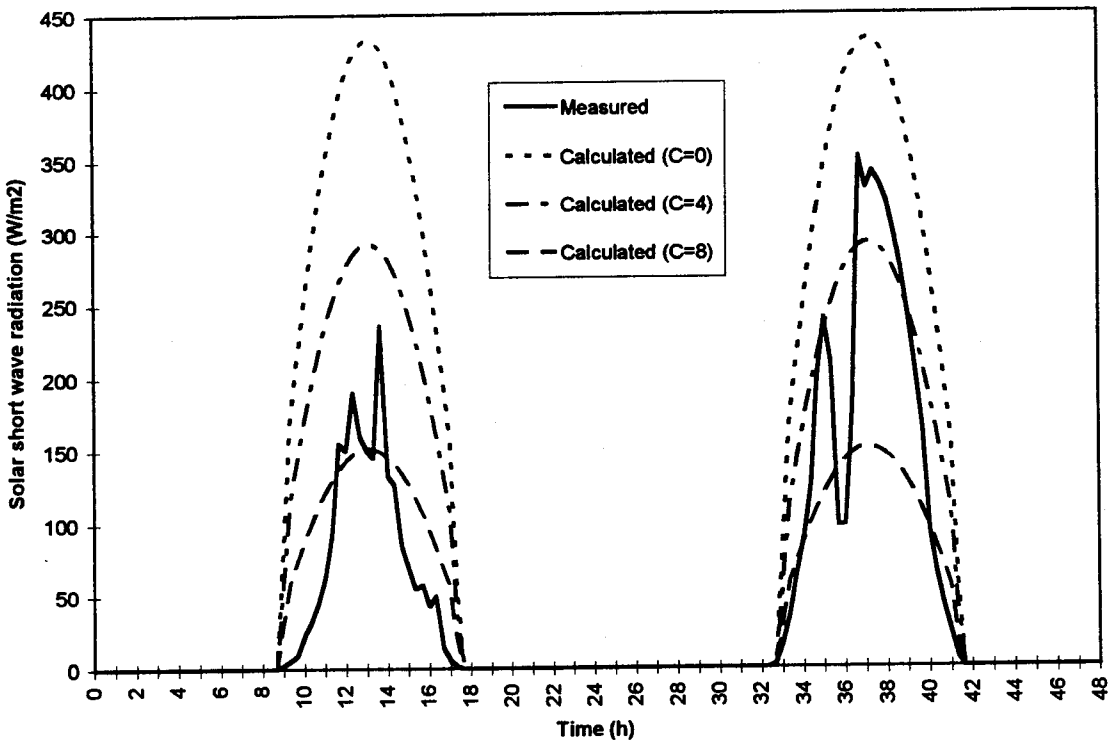

Figure 5.19 - Measured and calculated short-wave solar radiation at NRC Basin Test (12/25 and 12/26).

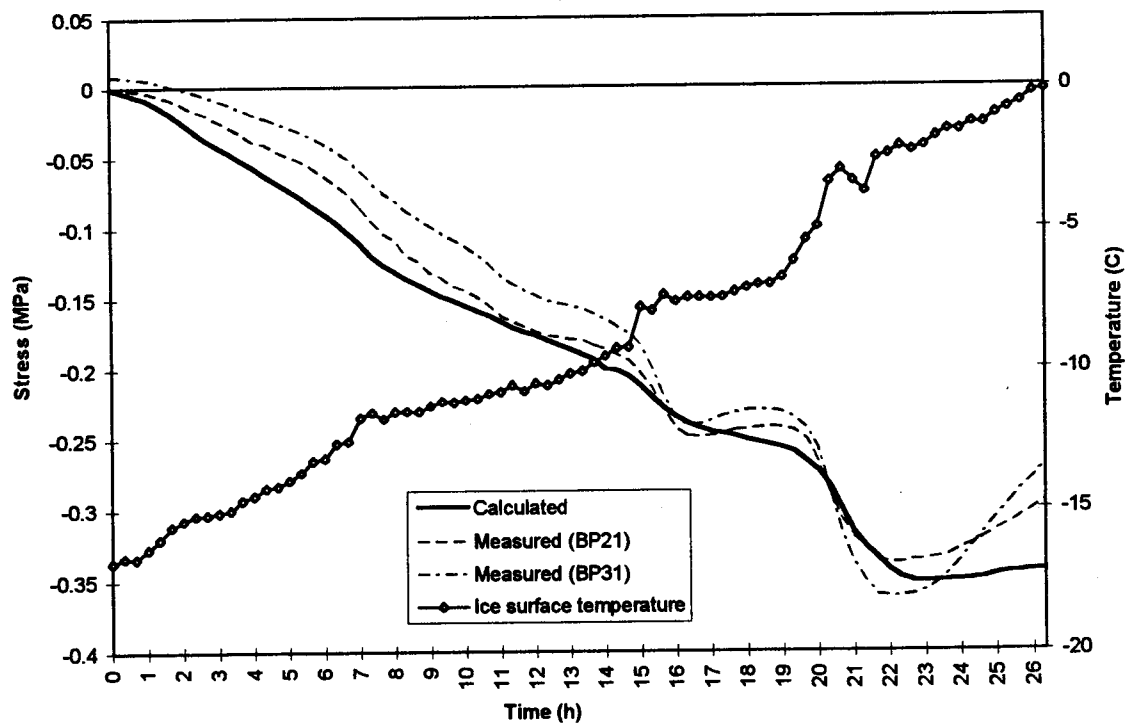

Figure 5.20 - Measured and calculated stresses at NRC Basin Test (1/2 to 1/4).

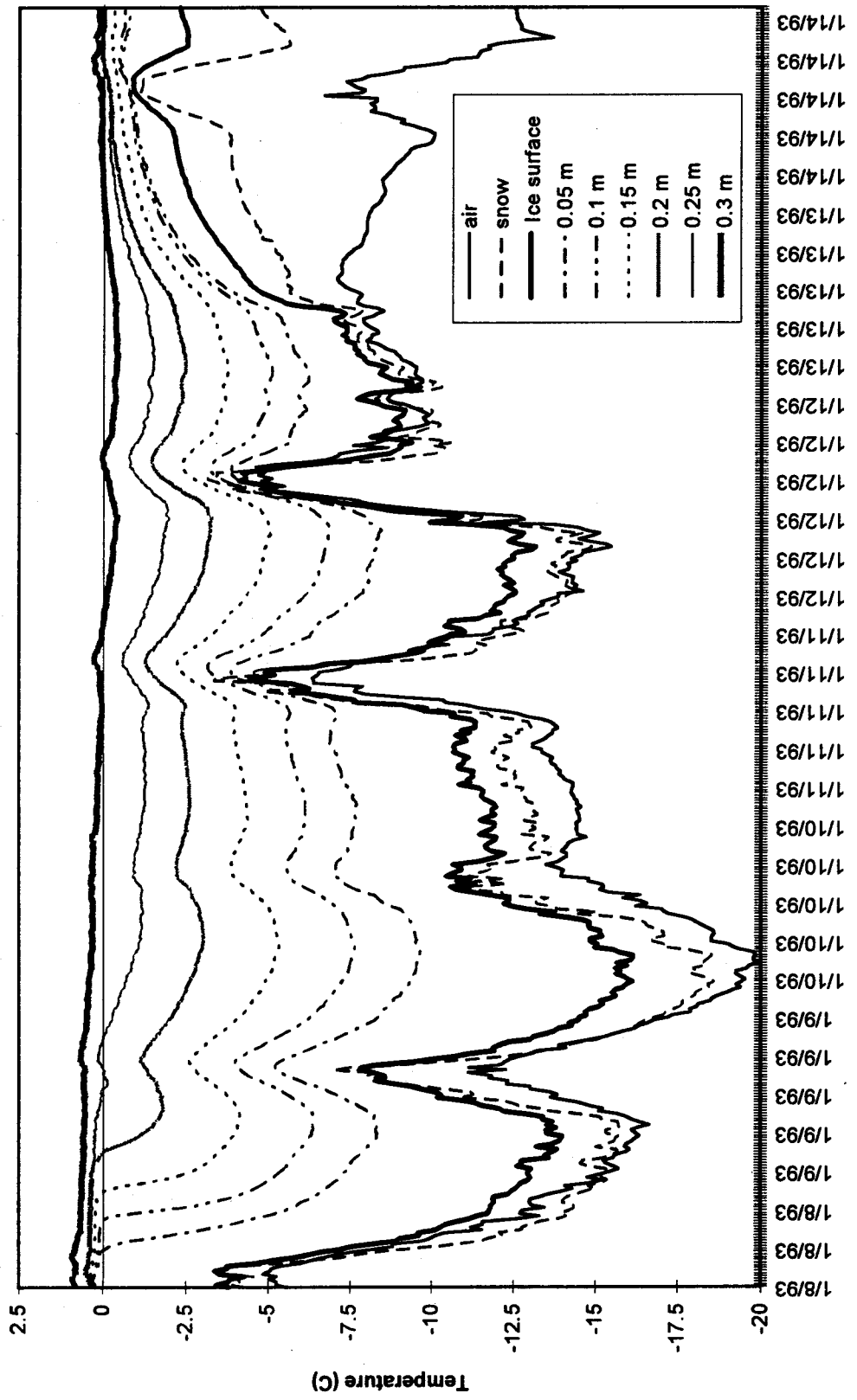

Figure 5.21 - Measured temperatures at NRC Basin Test (1/8 to 1/14).

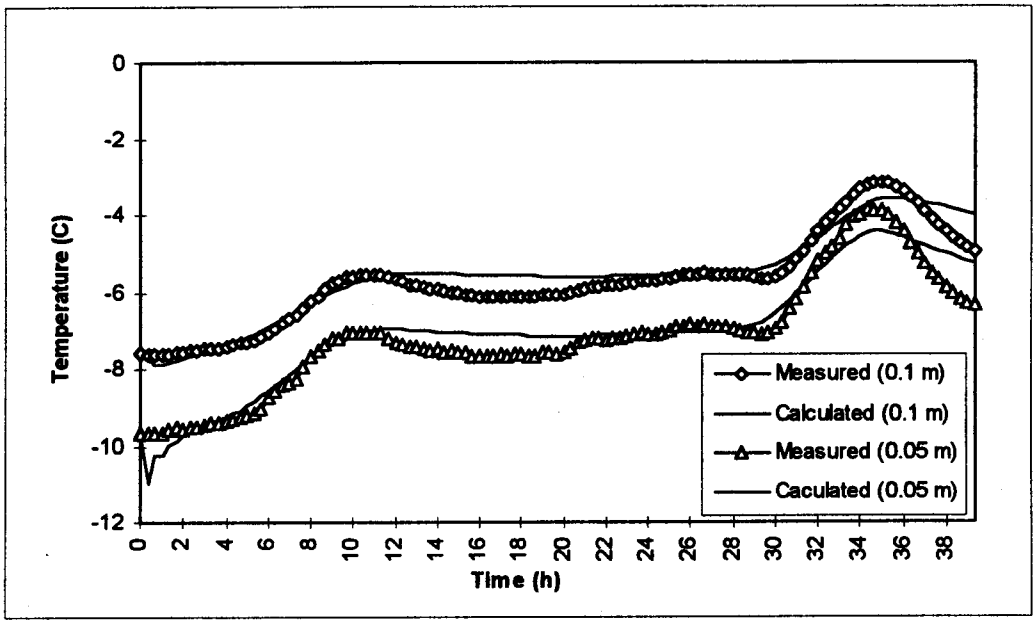

Figure 5.22 - Measured and calculated temperatures at NRC Basin Test (1/10, 4:20 to 1/11, 19:40)

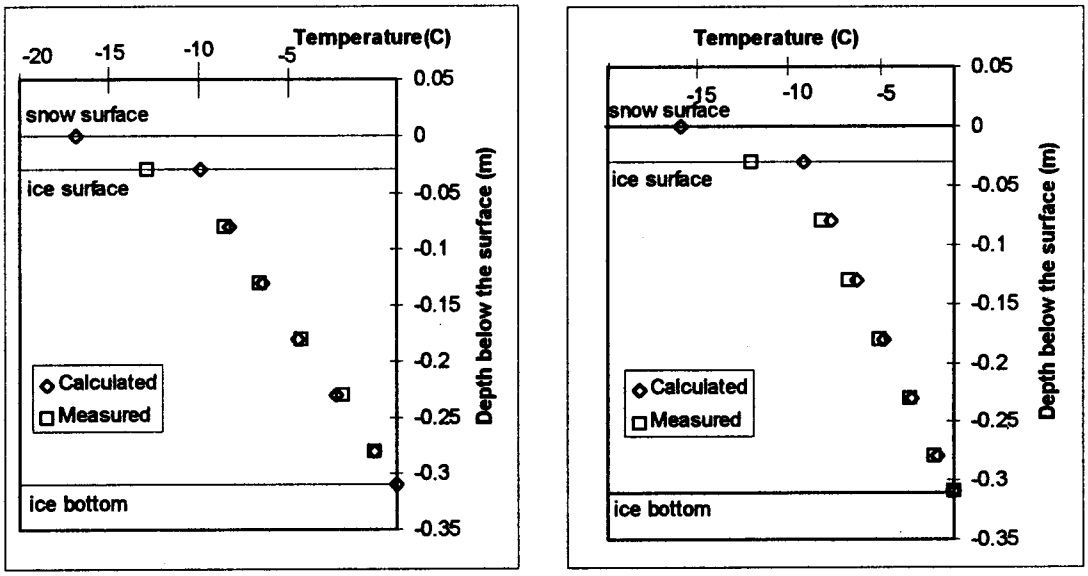

a) Temperatures at 1/10/1993 9:20 b) Temperatures at 1/10/1993 19:20

Figure 5.23 - Measured and calculated temperature profiles at NRC Basin Test after a) 5 hours and b) 15 hours from the start of the simulation.

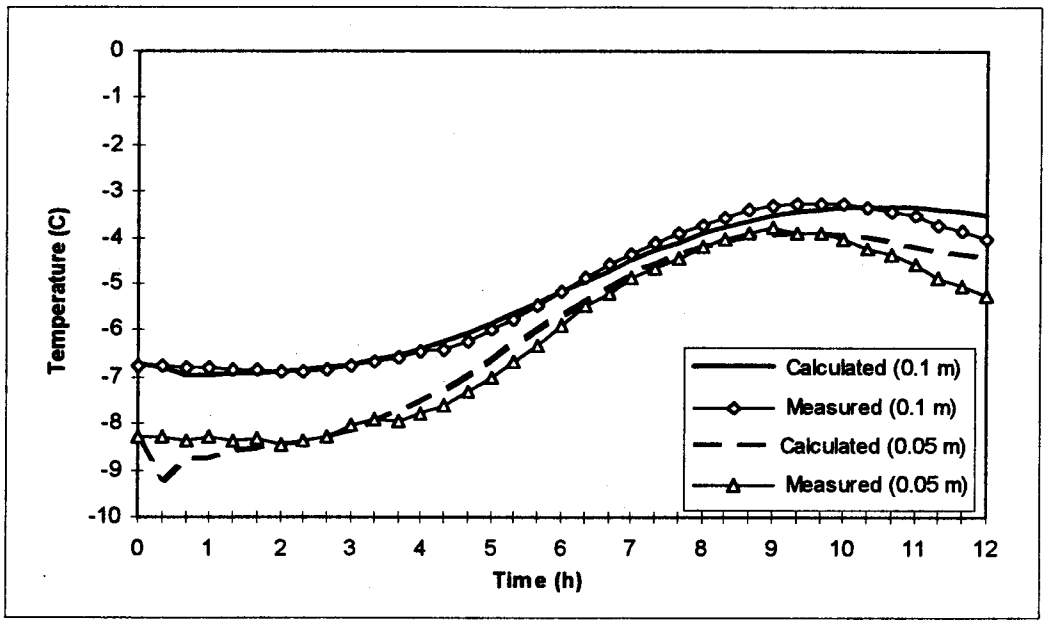

Fig 5.24 - Measured and calculated temperatures at NRC Basin Test (1/12, 6:00 to 1/12, 18:00)

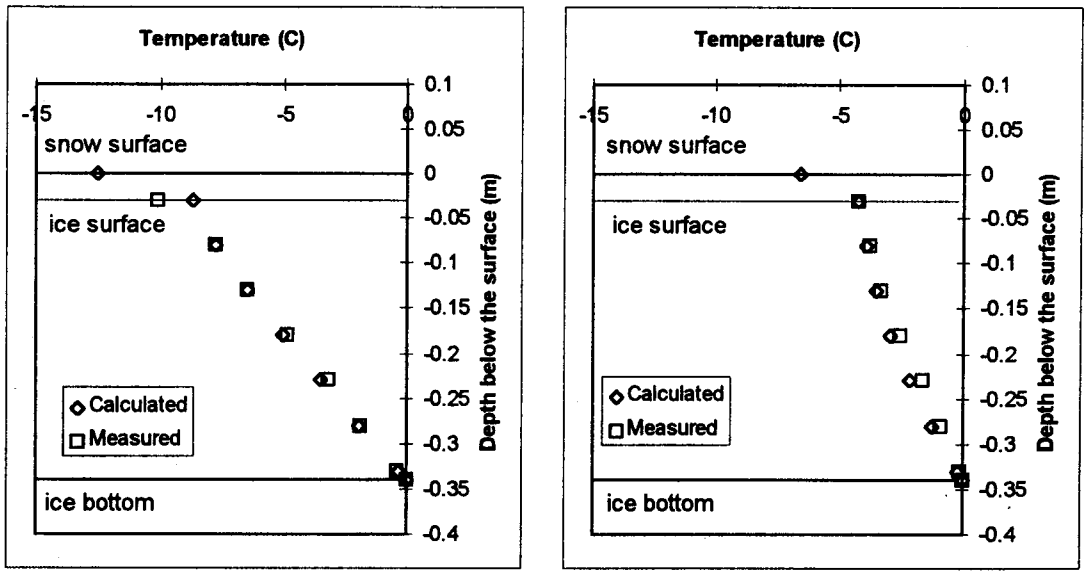

a) Temperatures at 1/12/1993, 10:00 b) Temperatures at 1/12/1993, 15:00

Figure 5.25 - Measured and calculated temperature profiles at NRC Basin Test after a) 4 hours and b) 9 hours from the start of the simulation.

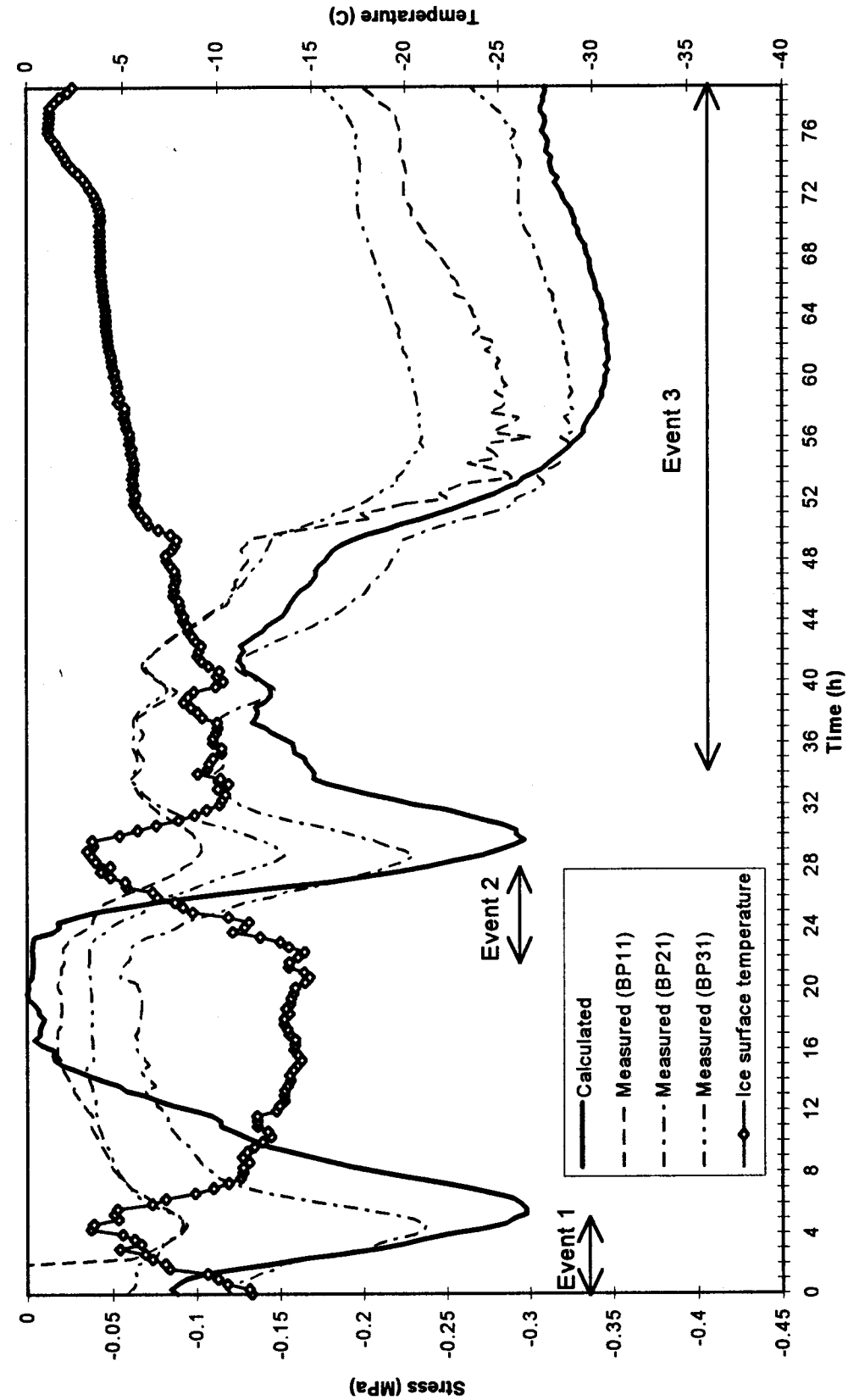

Figure 5.26 - Measured and calculated stresses at NRC Basin Test (1/11 to 1/14).

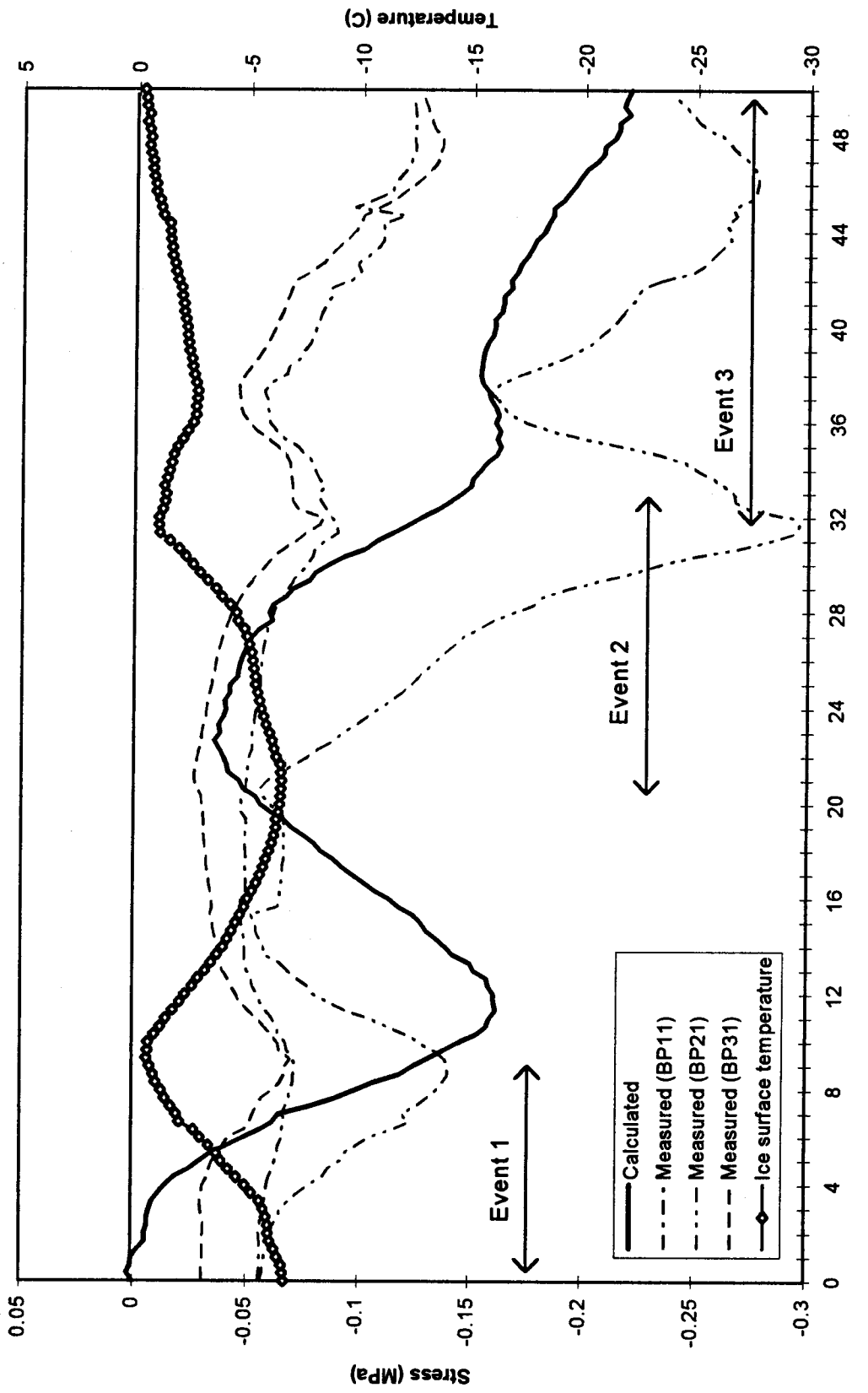

Figure 5.27 - Measured and calculated stresses at NRC Basin Test (1/20 to 1/22).

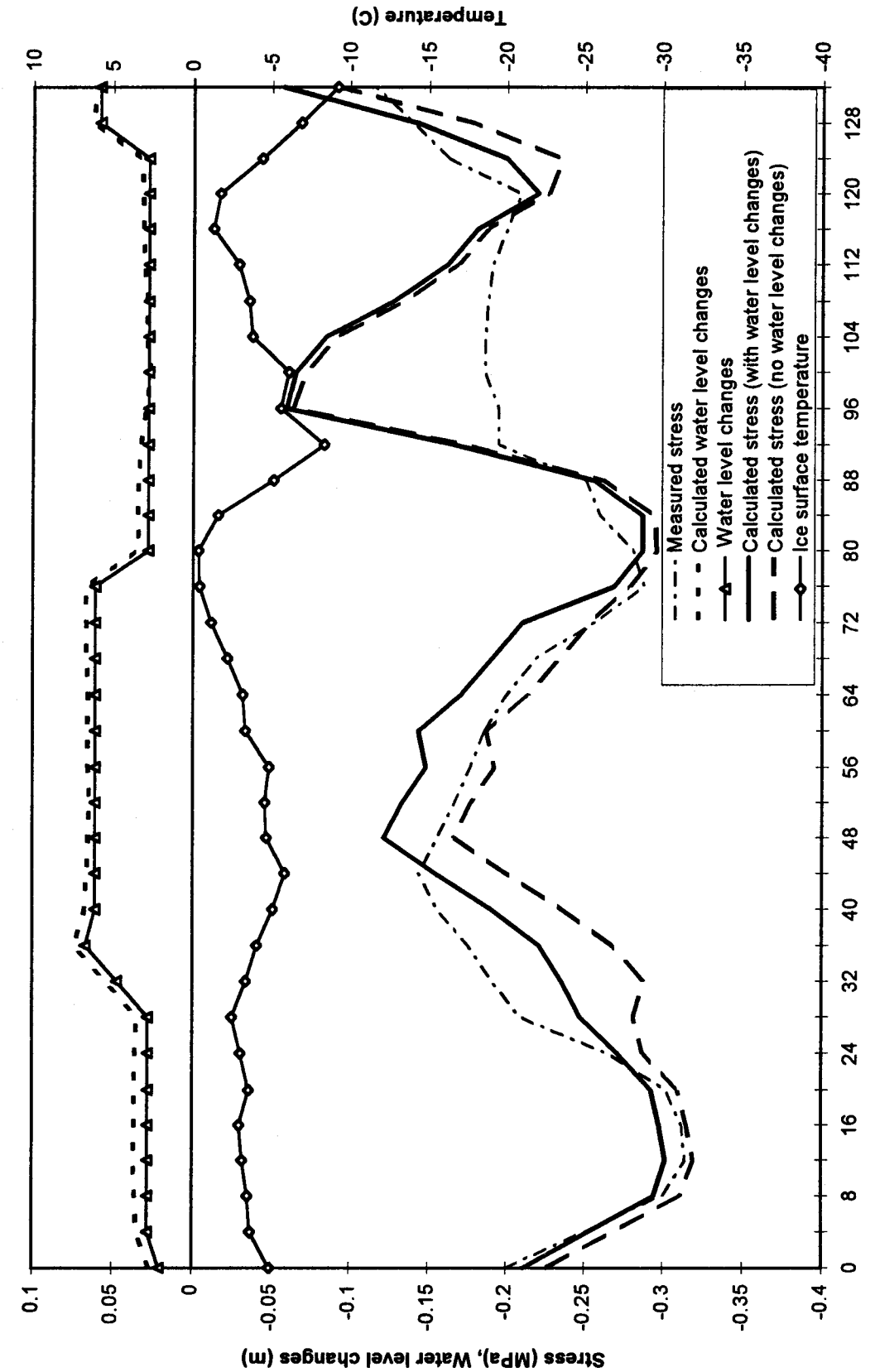

Figure 5.28 - Measured and calculated stresses at NRC Basin Test, (2/1 to 2/7).

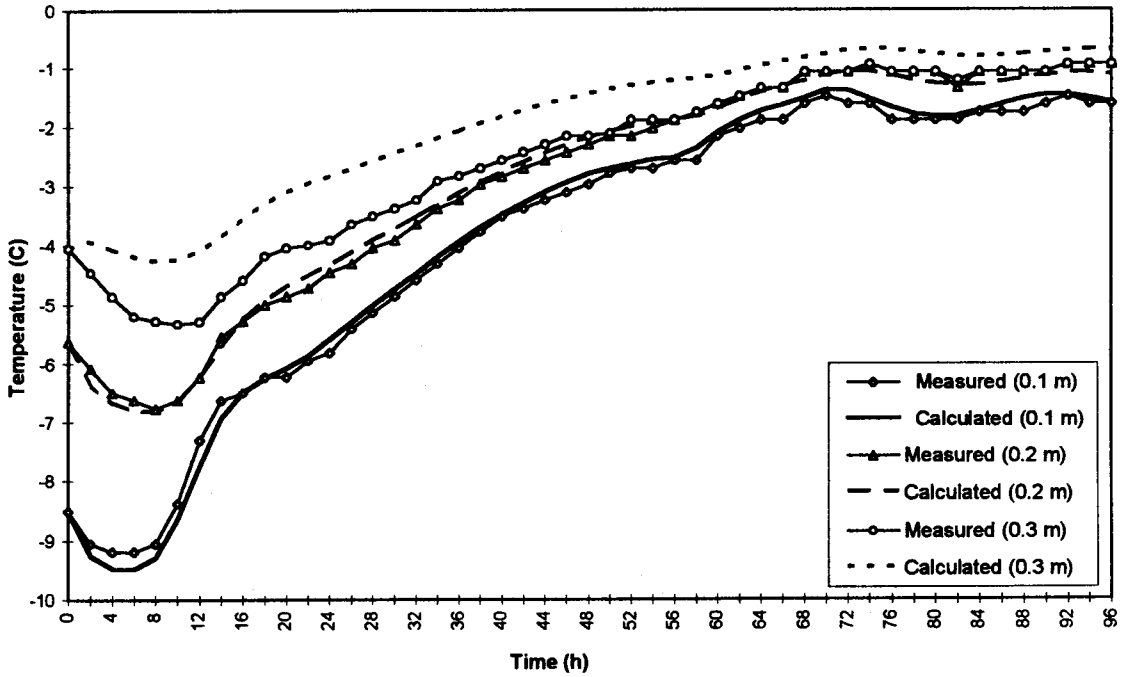

Figure 5.29 - Measured and calculated temperatures at different depths below the ice surface at Arnprior Dam (2/12, 0:00 to 2/16, 0:00).

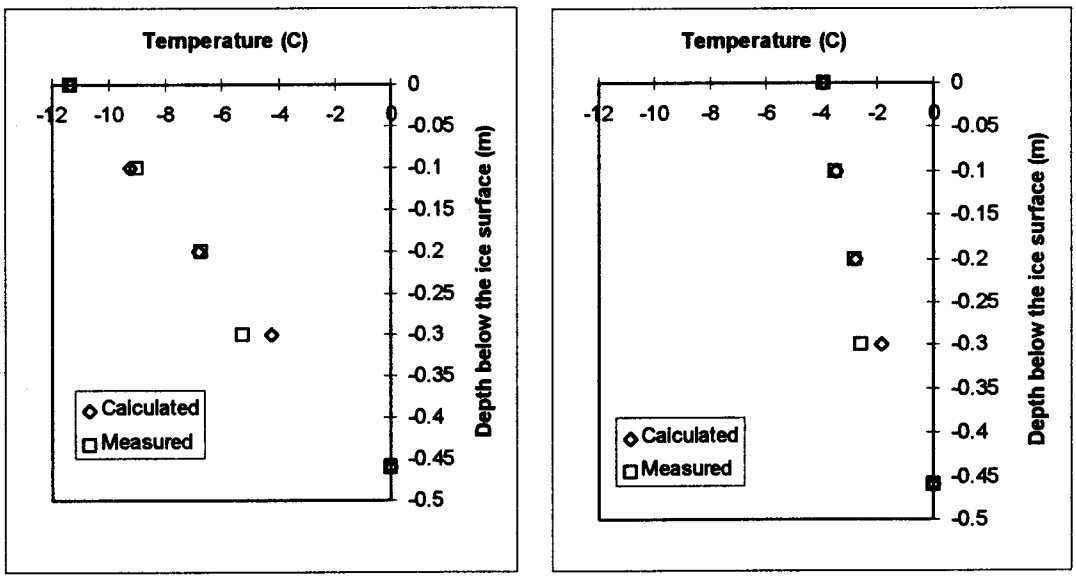

a) Temperatures at 2/12, 8:00 b) Temperatures at 2/13, 16:00

Figure 5.30 - Measured and calculated temperature profiles at Arnprior Dam after a) 8 hours and b) 40 hours from the start of the event.

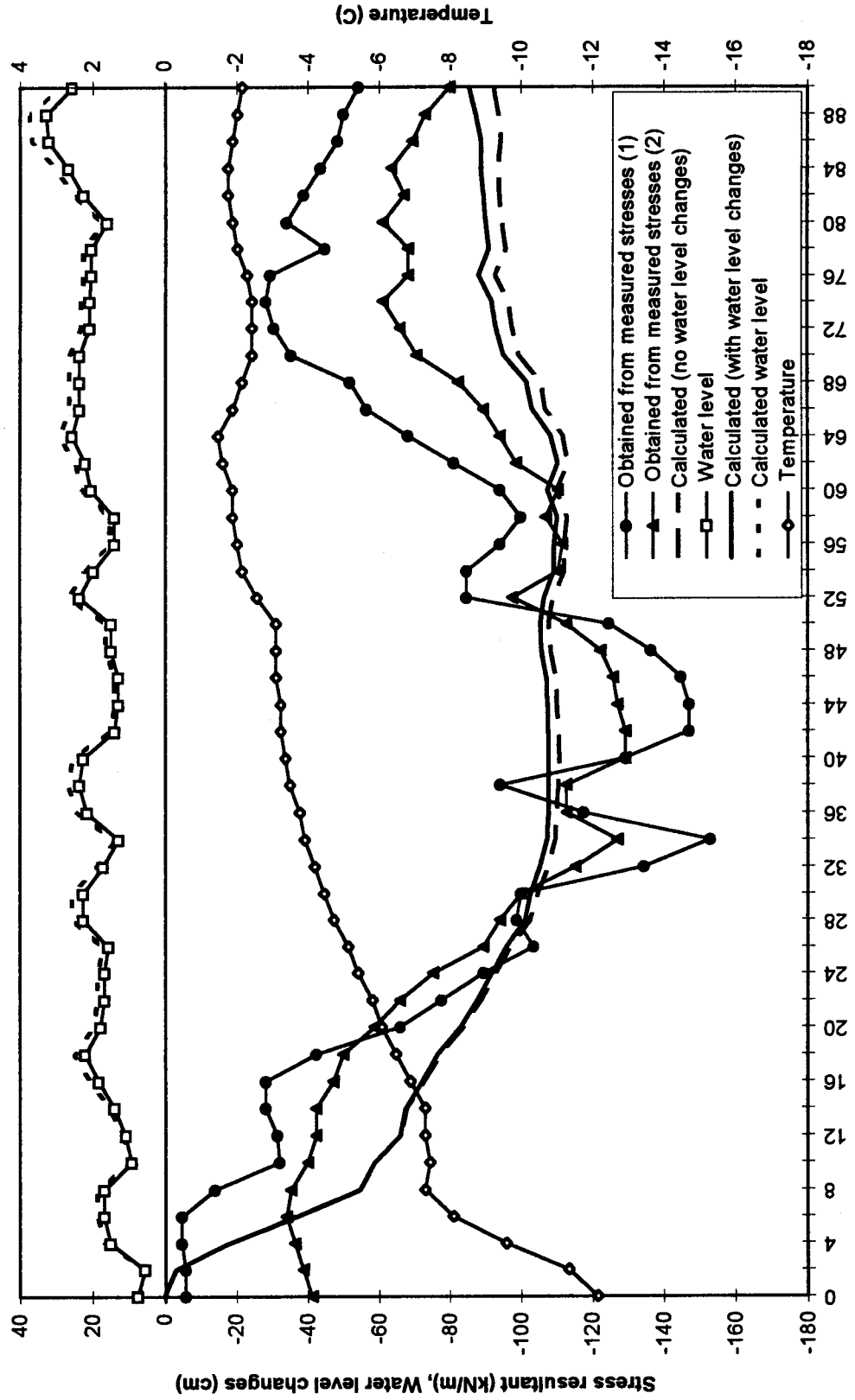

Figure 5.31 - Measured and calculated line loads at Arnprior Dam (2/12 to 2/15).

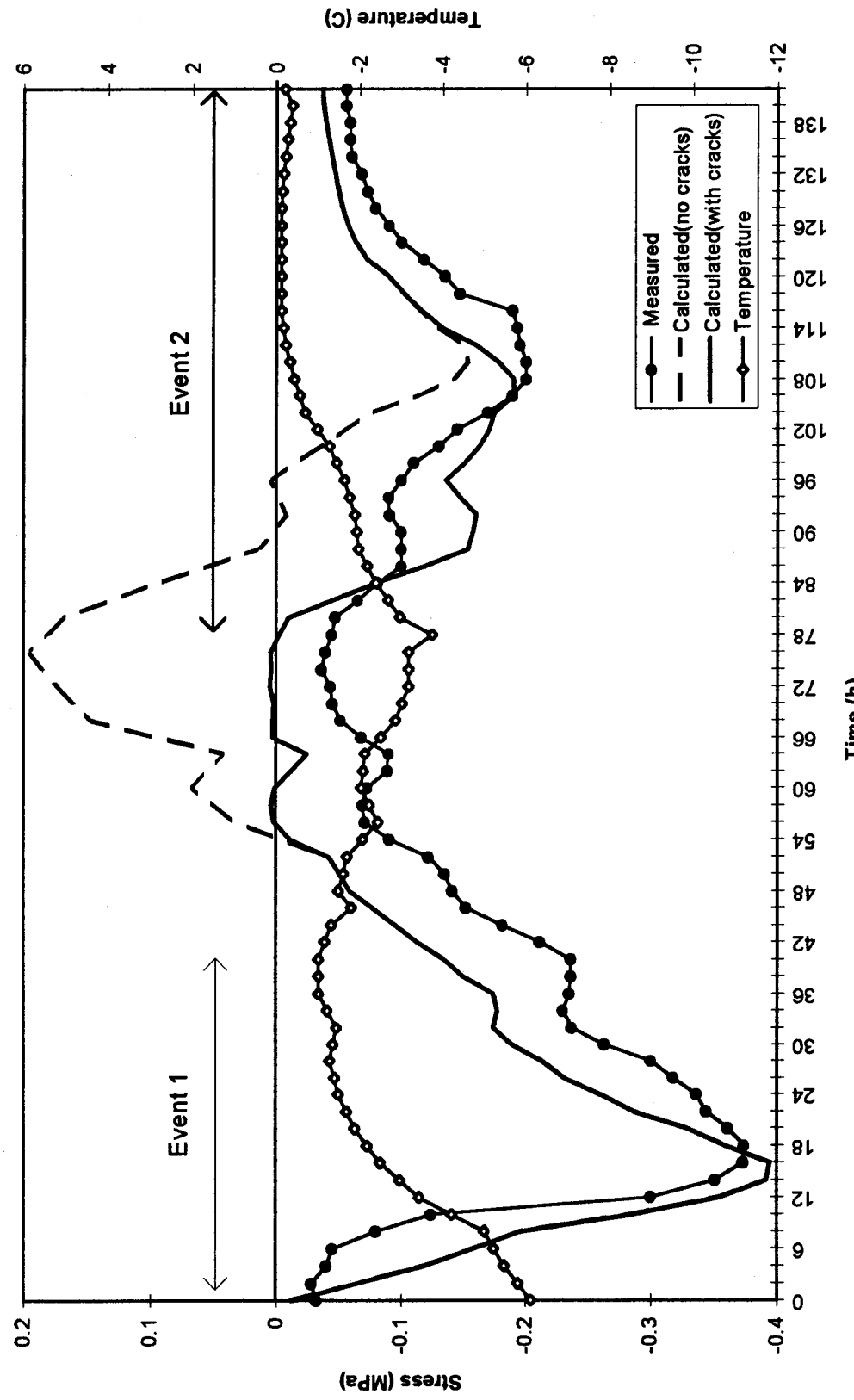

Figure 5.32 - Measured and calculated stresses at Paugan Dam, site 2, 30 m from the vertical face (1/9/92, 0:00 to 1/15/92, 0:00).

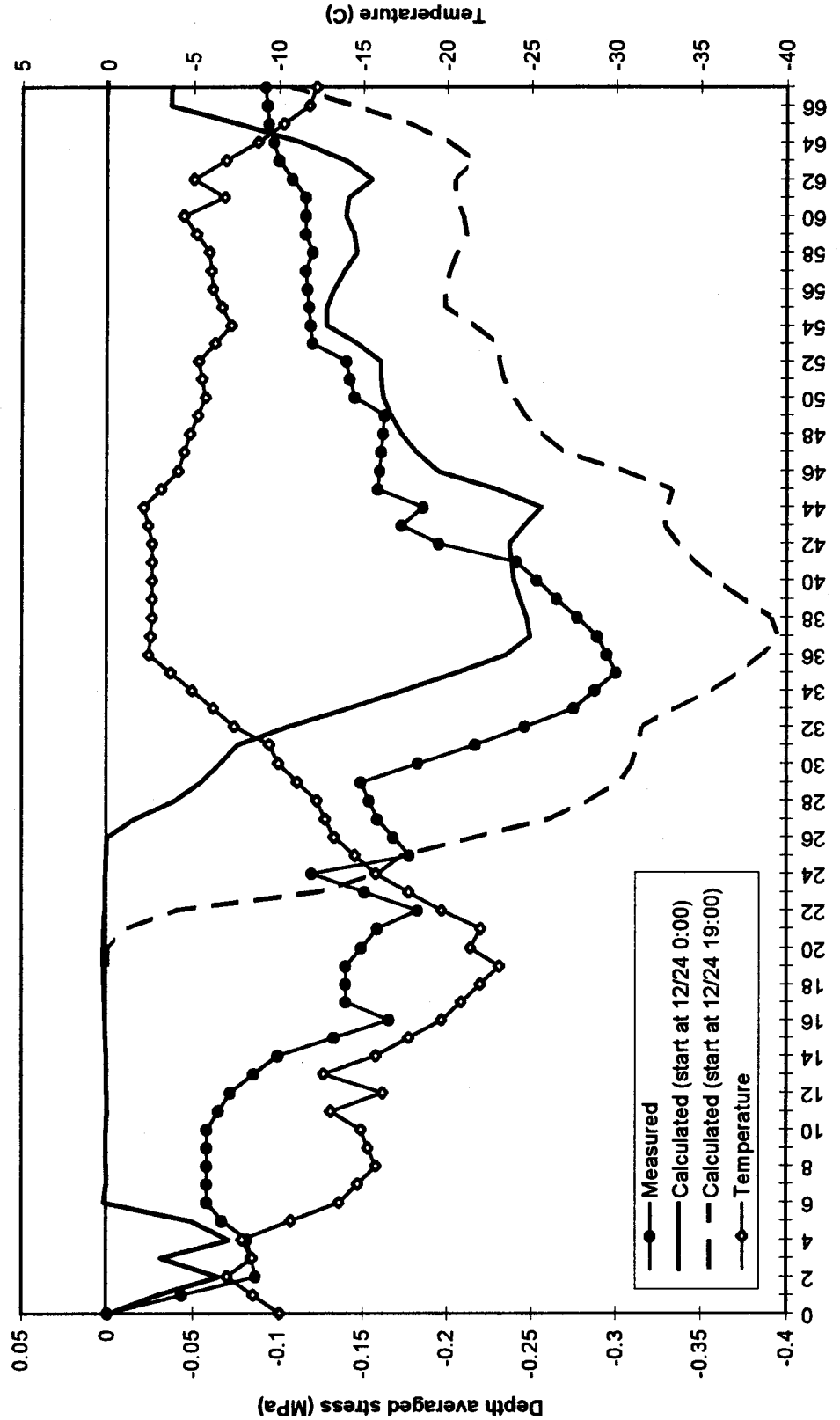

Figure 5.33 - Measured and calculated stresses at Paugan Dam, 30 m from gates (12/24/92, 0:00 to 12/27/92, 16:00).

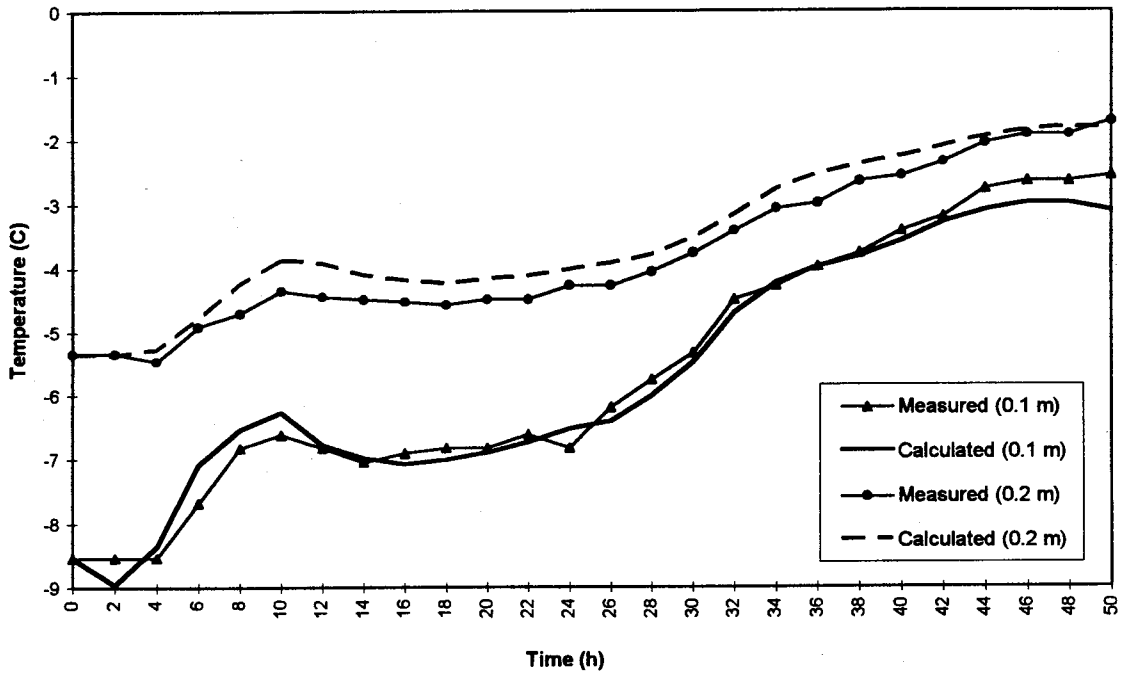

Figure 5.34 - Measured and calculated temepratures at Paugan Dam (1/12/93 to 1/14/93).

6 - A STUDY OF INDIVIDUAL FACTORS INFLUENCING THERMAL ICE LOADS

The amount of pressure exerted by an expanding ice sheet depends on many factors. Some factors such as the meteorological conditions affect the temperature field in the ice and others such as the rigidity of the resisting structure affect the stress distribution. Factors such as the ice thickness affect both. Understanding the role of all these factors is necessary for the prediction of ice pressures. This chapter contains an investigation, the purpose of which is to identify the parameters that have the most effect on ice pressures and to determine how ice pressures are affected by changes in these parameters. The investigation is divided into two parts. In the first, the focus is on the thermal aspects of the problem and parameters that influence the temperature distribution in the ice. The second part is concerned with the mechanical aspects of the problem and deals with factors such as boundary conditions. In the thermal part of the study the investigation covers most of the parameters that affect the temperatures. However, in the mechanical part of the investigation it was not possible to cover all the different factors. For example when considering reservoir geometry, it is impossible to model all of the possible cases. Therefore the study is limited to some specific situations chosen with the objective of gaining some understanding of this aspect of the problem.

When reading this chapter, it should be remembered that the results presented are based on a numerical model. As such they depend on a number of inherent assumptions, particularly those in the constitutive model. The constitutive model used is considered to be valid because it includes the basic features of ice behavior and it has been verified by comparison with experimental and field data. The material properties used are those that in most cases gave the best agreement with experimental and field data. However, due to complexity of the ice behavior and the many factors involved in the problem being studied, care must be taken when interpreting the numerical predictions. The objective

here is not to produce results that can necessarily be relied upon in a quantitative sense, but rather to investigate behavior and to assess the role that individual factors play.

As part of the process of formulating the analysis presented in this chapter, it was necessary to choose a suitable form for the temperature time history. Usually linearly varying or sinusoidally varying temperatures are used for the thermal stress analysis. Drouin and Michel performed a study on air temperature variations in Quebec City and concluded that most often they exhibited a sinusoidal shape (Drouin and Michel, 1971). The type of the temperature variation used in their study was half a cosine wave varying between $-\pi$ and π. If one wants to analyze situations involving cooling, this type of temperature history is a convenient choice. The temperature variation applied in this study is similar to that used by Drouin and Michel and is obtained from the following equation:

$$\theta = \theta_i + \theta_{am}(1 - \cos\frac{2\pi t}{T_\theta}) \tag{6.1}$$

where

θ_i = initial temperature

θ_{am} = amplitude of temperature variation

T_θ = period of temperature variation.

In the thermal analysis, equation 6.1 is used as the time history for the air temperature. If short -wave solar radiation is not included in the analysis, the temperature history at any point through the thickness of the ice cover, will have a periodic form. For stress analysis the temperature variation is applied to the ice surface. Then the temperatures through the thickness of the ice cover are obtained from the thermal analysis. The period selected for most of the cases is 24 hours which represents a daily temperature variation. Other periods that are used to study the effect of duration are 6, 12, 48 ,and 96 hours. The initial temperature is the minimum temperature, and the maximum temperature is reached after the time corresponding to the half of the period. For example in Fig 6.1 it is assumed that the air temperature is -20°C at the start of the problem (mid-night), reaches to 0°C at noon, and decreases again to -20°C by mid-night.

In the thermal parameter study the comparisons are made for ice surface temperature and are based on the maximum temperature, minimum temperatures, and maximum

temperature change or twice the amplitude of temperature wave. In the stress analysis the comparisons are made for the maximum stress in the top layer, and the stress resultants at the Gauss points. In some cases the reactions or the forces in boundary elements are used to assess the line load on the structure. The stress resultants are obtained by integrating the stresses through the thickness. The stress in each layer is multiplied by the thickness of that layer, and the results are added.

The range of the thicknesses considered in this chapter cover the range encountered for fresh water ice in most parts of Canada (below 60° latitude). Ice covers with a thickness of 0.1 m to 0.2 m are considered thin, and ice covers with a thickness above 0.7 m are called thick.

6.1 - Parametric Study, Thermal Factors

When performing a thermal analysis in an attempt to simulate a particular field situation it may not be possible to obtain all the input data required unless an effort has been made to measure all of the weather data and ice conditions. If this data is not available, there is a need to know which factors are important and which factors are not, as far influencing the temperature distribution in the ice. In the first part of this section a sensitivity analysis is performed on a number of parameters, and the effect of each on the temperature distribution is studied. These parameters include: ice type and material properties, wind speed, relative humidity, cloud cover, latitude, time of the year, and snow cover. In these cases the initial air temperature is -20°C, the amplitude is 10°C and the period is 24 hours. In the next part the temperature distribution in the ice cover is studied for different amplitudes and periods of air temperature increase and different ice thickness.

6.1.1 - Ice Type and Thermal Properties

The thermal and mechanical properties of ice depend on the ice type, which in turn depends on the conditions that existed at the time the ice was formed. At any particular

site, it is difficult to predict which type of ice will form. Thus there is value in understanding how the ice type affects both thermal and mechanical behavior of an ice cover.

Although many different types of ice occur naturally (Table 5.1), there are actually two broad categories of ice found in most lakes and reservoirs. These are granular ice like snow-ice, and columnar S2 ice. A thermal analysis is performed to compare the temperatures obtained for these two ice types at the same time, site, and ambient conditions. The thermal properties used in the analysis are those suggested by Bergdahl (1978) (Table 3.6). The comparison is made for two different ice thicknesses, with and without short-wave solar radiation. It is assumed that the sky is clear, the wind speed is 2 m/s, and the relative humidity is 80%. In the analysis that includes short-wave solar radiation, the date is set equal to January 1 and the latitude is assumed to be 60°. The time at the start of the problem is assumed to be 12:00 a.m.

Figures 6.1 and 6.2 show the ice surface temperature versus time curves obtained from the analysis. It can be seen that with no short-wave solar radiation, there is not much difference in the temperatures obtained for different ice types. When the short-wave solar radiation is considered, the temperatures are higher for snow-ice. Since in nature ice covers usually consist of columnar ice with a layer of snow-ice on top, another case is included in the study. In this case the ice cover is assumed to be of columnar ice, but the coefficient of reflection from the surface is chosen to be equal to the coefficient of reflection for snow-ice. The results for this case are included in Figs. 6.1 and 6.2 and are identified by the caption, columnar ice (snow-ice at surface).

Compared to columnar ice, the coefficient of reflection for snow-ice is lower and the coefficient of absorption is higher. Therefore when the short-wave solar radiation is considered the temperatures in snow-ice are higher. The temperatures predicted for columnar ice with snow-ice at the surface are not much different from the temperatures for columnar ice. This indicates that most of the difference between the temperatures in the columnar ice and those in the snow-ice are due to the different coefficients of absorption.

If the effects of short-wave solar radiation are not considered, then three material properties affect the temperature distribution in the ice. These are the density ρ, the conductivity k, and the specific heat C_p. The combined role of these parameters in the equation of thermal diffusion (equation 3.1.2) is through the diffusivity ($k/\rho C_p$). Some guidance as to the range of values for the diffusivity of naturally occurring ice, can be found in the study by Drouin and Michel (1971). The values suggested by different investigators for the thermal properties of ice can be combined in such a way as to obtain extreme values for the diffusivity. The resulting maximum and minimum values for the diffusivity, and the associated values for ρ, k and C_p can be summarized as follows.

k_{max}=2.508 J/(C°.m.s) k_{min}=2.090 J/(C°.m.s)

Cp_{min}=1800 J/(kg.C°) Cp_{max}=2120 J/(kg.C°)

ρ_{min}=850 kg/m^3 ρ_{max}=925 kg/m^3

diffusivity$_{max}$=1.64×10^{-6} m/s^2 diffusivity$_{min}$=1.07×10^{-6} m/s^2

Thermal analyses are performed using these extreme values of diffusivity. The wind speed, relative humidity, and cloud cover are the same as those described at the start of this section. The results for the ice surface temperature are shown in Fig. 6.3 for two ice thicknesses, 0.2 m and 1.0 m. The surface temperatures obtained using the maximum diffusivity are slightly higher but the difference is not significant (less than 1°C). It can be seen that the difference between the maximum and minimum surface temperature, which is of importance as far as thermal stresses are concerned, is almost the same for the two extremes of diffusivity. For thin ice sheets where the temperature distribution through the thickness is almost linear, the amplitude of the temperature changes is a maximum at surface. Therefore the difference between the maximum and minimum temperatures will be even less through the thickness. For thick ice covers however, the difference between the maximum and minimum temperatures may be higher at points within the ice sheet compared with the ice surface. It was observed that even for a thickness of 1.0 m the change in the difference between the maximum and minimum temperatures for the extreme values of diffusivity was less than 0.8°C. The conclusion is that when short-wave solar radiation is not considered the temperatures are not very sensitive to the thermal properties of the ice.

6.1.2 - Relative Humidity, Cloud Cover, and Wind Speed

In this section the effect and relative importance of the ambient conditions on the temperature distribution is studied. The effect of short-wave solar radiation is not included in the analysis since it is studied in another section. The three factors considered are the relative humidity, the cloud cover, and the wind speed.

The relative humidity is normally expressed as a percentage of the saturation vapor pressure for the corresponding air temperature and can vary from zero to one hundred percent. The cloud cover is expressed as a fraction, in eighths, with the extremes 0/8 and 8/8 corresponding to clear sky and complete cloud cover respectively. In nature, the wind speed typically does not remain constant for very long. In a thermal analysis for a specific time and site, it is possible to read the wind data from an input data file. But when the wind data is not available a constant value is assumed in the analysis. The possible wind speeds cover a very wide range and it is difficult to assign an extreme maximum value for wind speed. Therefore the wind data recorded by Fleet Technology Ltd. at the NRC Basin test was used as a guide in selecting values for this study. Most of the recorded data were below 5 m/s. The maximum wind speed recorded, which occurred for a very short time only, was 6.95 m/s. Values of 0 m/s and 6 m/s were subsequently selected as the minimum and maximum wind speeds. A wind speed of 2 m/s, a cloud cover of 4, and a relative humidity of 80% are adopted as the normal conditions. In each test two variables are kept constant at the normal value, while the other varies between the maximum and minimum range.

The results for this part of the study are summarized in Table 6.1. The table shows the minimum and maximum calculated surface temperatures along with the maximum temperature change, for different combinations of wind speed, cloud cover, and relative humidity. The first two rows show the effect of wind speed. With higher wind speed, the amount of heat transfer due to convection increases. Therefore the maximum temperature increases, the minimum temperature decreases, and the difference between these temperature extremes increases. Rows three and four show the effect of cloud cover.

The cloud cover affects the absorbed long-wave radiation. With complete cloud cover the long-wave radiation emitted from the atmosphere, and the part that is absorbed by the ice cover increase. The effect is that both the minimum and maximum temperatures increase. It can be seen that when short-wave radiation is not considered, the effect of cloud cover is not significant compared to the other parameters considered in Table 6.1. Rows five and six show the effects of relative humidity. The relative humidity affects the heat fluxes due to both convection and absorbed long-wave radiation. It can be seen that with increasing relative humidity, both the minimum and maximum temperatures increase as well as the difference between the extremes. In the last three rows the combination of the extreme cases are compared to the normal condition. In row seven the extreme cases are combined in a way that would increase the maximum temperature. This combination also increases the difference between the maximum and minimum temperatures. In row nine the other extremes are combined, and row eight shows the normal conditions.

6.1.3 - Parameters that Affect the Short-wave Solar Radiation

In this section the parameters that affect the short-wave solar radiation are studied. These include: time of the year, latitude, and cloud cover. The other parameters are selected to represent a relatively normal condition. The wind speed is chosen to be 2.0 m/s, and the relative humidity is chosen to be 80%. The results are presented for two ice thicknesses (0.2 m and 1.0 m) and for both snow-ice and columnar ice.

Table 6.2 shows how the maximum temperature at the ice surface is affected by changes in the parameters that affect the short-wave solar radiation. The results shown in rows one and two are for two reference cases having 0/8 and 8/8 cloud cover respectively, and in which short-wave radiation is not included. The difference in the calculated maximum temperature due to the change in cloud cover is about 1.5°C for the thin ice and about 2°C for the thicker ice. In the third and fourth row the effect of the cloud cover is shown when the short-wave solar radiation is considered in the analysis. When the short-wave radiation is included the effect of the cloud cover is not very significant for the columnar ice, especially for the thin ice. Snow-ice has a higher coefficient of absorption.

Therefore the difference is larger for this type of ice. However, even for snow-ice the difference is small compared to the effect of other parameters.

In the fifth row of Table 6.2, results are shown for a case with a lower latitude. It can be seen that the latitude has a significant effect on the temperatures, especially for snow-ice. Note that the thermal analysis program does not account for melting and therefore positive temperatures are obtained for this case. The results in rows three, six, and seven show the effect of the time of the year. As might be expected, the temperatures are lowest on the first of January compared to the first of December or March. The differences are most significant for the snow-ice.

6.1.4 - Snow Cover

The conductivity of snow is very low compared to that of columnar ice or snow-ice. Therefore a snow cover on an ice sheet acts as an insulating layer and reduces the effect that air temperature changes have on the temperature distribution through the ice cover. In this section the effect of the snow layer on the ice surface temperature is studied. The study is performed for a thin and a thick ice cover. The effect of the short-wave solar radiation is not included in the analysis. The wind speed is 6 m/s, the relative humidity is 100%, and the cloud cover is 8/8.

In Fig. 6.4 the maximum and minimum ice surface temperature, and the difference between these values are shown for different ice thicknesses. With increasing thickness of the snow cover, the temperature inside the ice cover approaches the temperature at the bottom surface which is 0°C. Since in the analysis the maximum air temperature is 0°C, the maximum ice surface temperature does not change very much with changing snow thickness. However the minimum temperatures increase and the maximum and minimum values get closer with increasing snow thickness. The difference between the maximum and minimum value of ice surface temperature decreases from about 13 to 2.7 degrees. Therefore with a 10 cm snow layer the variation in ice surface temperature is only 2.7°C even though the air temperature varies from -20°C to 0°C. Although the maximum and

minimum temperatures are different for thin and thick ice covers, the temperature changes are almost the same.

The insulating effect of snow covers is well known and it is confirmed in the field data collected by Fleet Technology. It was observed that significant thermal stress events did not occur after heavy snow falls. The effect of the snow cover in the field situation is due to both the insulating effect and the fact that the weight of the snow can cause the ice sheet to become submerged. In this case water can reach the surface and the ice surface temperature remains constant until freezing occurs.

6.1.5 - Thickness of the Ice Cover, and Period and Amplitude of Temperature Increase

In order to study the effect that ice thickness has on the vertical temperature distribution, ice covers with thicknesses ranging from 0.1 m to 1.0 m are analyzed. The numerical tests are performed for the extreme conditions with the wind speed taken as 6.0 m/s, complete cloud cover, and a relative humidity of 100%. Short-wave solar radiation is not included in the analysis. The air temperature is varied according to equation 6.1 with the minimum air temperature ranging from -40°C to -10°C, and the maximum air temperature fixed at 0°C. Two values are used for the period, 24 and 48 hours.

Figures 6.5 and 6.6 show the maximum and minimum ice surface temperatures versus ice thickness. The results are presented for different minimum air temperatures and different periods. It can be seen that with increasing thickness both maximum and minimum temperatures decrease and the curves become flatter. Also with increasing period the maximum temperatures increase and the minimum temperatures decrease.

In a thin ice sheet the temperature distribution is affected by the temperature at the bottom surface, but with increasing thickness the effect of the bottom temperature reduces. Thus for thick ice covers the temperature distribution gets closer to the temperature distribution corresponding to a semi-infinite body with a heat source (or sink) at the surface. The temperature at the bottom surface of the ice sheet is at the freezing

point which can be considered a high temperature compared to the air temperature. Therefore with increasing thickness, as the effect of the bottom boundary decreases, the maximum and minimum temperatures decrease and the curves become flatter. Also with increasing period the temperatures get closer to the air temperature. This is shown more clearly in Figs. 6.7 and 6.8 where the maximum ice temperature change (maximum temperature minus minimum temperature) is normalized with respect to the maximum change in the air temperature. Figure 6.7 corresponds to ice surface temperature, and Fig. 6.8 shows the temperature change at 1/4 thickness below the ice surface. It can be seen that for a 24 hour (open symbols), and 48 hour periods (closed symbols), all the curves corresponding to different minimum temperatures fall on top of one another. This means that the amplitude of the temperature waves through the thickness depends on the amplitude of the air temperature history and not on the average air temperature during the cycle. Results for a 12 hour period and for a 96 hour period are also plotted for comparison. These results indicate that with increasing period the ice surface temperature amplitudes get closer to the air temperature amplitude.

The amplitude of temperature variation through the thickness of an ice cover for a sinusoidal variation in surface temperature was discussed by Sanderson (1984). It was stated that an ice surface temperature wave becomes attenuated with depth according to equation (2.14.1). Therefore for a constant diffusivity and period, the amplitude of the temperature wave at a certain depth will depend on the air temperature amplitude. The results in this section indicate this is also true for the case where convective heat transfer and long wave radiation are also considered. For small thicknesses the amplitudes are affected by the bottom boundary condition, but with increasing thickness the effect of the bottom boundary condition becomes less, and the normalized amplitudes at the ice surface become relatively independent of ice thickness.

Figure 6.8 shows results for a point located 1/4 thickness from the top surface. Since the actual distance to the quarter point depends on the full thickness, it is observed in Fig. 6.8 that the relative temperature amplitude decreases with increasing thickness.

Figure 6.9 shows the temperature distribution through the thickness at the times of maximum and minimum surface temperature, and also the temperature changes between

these two cases. Results are presented for two different periods and four different thicknesses. It can be seen that for the thinnest case of 0.2 m, the temperatures and the temperature change are both linear through the thickness and the effect of the period is slight. For a medium thickness (h=0.4 m), temperature change still occurs through essentially the whole thickness but the results are more affected by the period. For a 24 hour period the distributions of temperature and temperature change show more non-linearity compared to those for the 48 hour period. Also, the temperature change is less significant in the lower half of the ice sheet. For the two thickest cases (0.7 m and 1.0 m) the results are similar with only the upper part of the ice sheet undergoing significant temperature variation with time. The thickness of this active zone increases from 0.3 m for the 24 hour period to 0.4 m for the 48 hour period.

6.2 - Mechanical Factors

In this section the factors that affect the stress distribution in ice covers are studied. These factors include, thickness of the ice cover, period of temperature increase, initial temperature, amplitude of temperature change, underlying water, boundary conditions, geometry of the reservoir, different shore lines, and stiffness of the resisting structure. For some factors, like the geometry of the reservoir, it is not possible to cover all of the different possibilities. Therefore the study is performed for some special situations that would give an understanding of the problem.

The stress analysis is performed for a periodic change in the ice surface temperature. The temperature distribution through the ice thickness is obtained by a thermal analysis. In the following, unless stated otherwise, it can be assumed that the initial ice surface temperature is -10°C, the amplitude of the temperature variation is 5°C, and the period is 24 hours.

Issues concerning the mechanical properties of ice were discussed in Chapter 5. In the present chapter only one set of mechanical properties is selected to study the effect of the other parameters that affect the ice pressure. Since in the previous studies the

mechanical properties suggested by Drouin and Michel for snow-ice gave the best agreement in most cases, those properties are used here. Cracking of the ice is considered with the tensile strength of ice taken to be 0.01 MPa. The choice of this value is made on the basis of the field data which showed tensile stresses were very close to zero. In most of the numerical tests presented in this section the analysis is performed for clamped boundary conditions, and a single element mesh as described in section 5.2.1(Fig. 5.12), with ten layers through the thickness is used. The exceptions are cases where the geometry of the ice sheet is considered important. This happens when the rotations or displacements are not restrained at the boundaries.

6.2.1 - Number of Layers. Through the Thickness

Since the finite element analysis makes use of a number of layers through the ice thickness, the question arises as to the proper choice for the number of layers. Increasing the number of layers increases the computing time while using a small number of layers decreases the accuracy of the analysis. To address this issue a simple test is performed using two different choices for the number of layers (eight and ten). The stress resultants and the stresses in the top layer are then compared for three different thickness cases, 0.2 m, 0.4 m, and 1.0 m. The maximum values are shown in Table 6.3. Comparing the results for the eight and ten layer cases, the largest differences in maximum stress resultant and stress in the top layer are less than 0.5 kN/m and 0.015 MPa respectively. These changes are considered to be small and indicate there is no need to use more than ten layers.

6.2.2 - Thickness of the Ice Cover

Thickness of the ice cover is a factor that affects both the temperature and the stress distributions. During the study on the effect of the thickness on temperature, it was observed that in a thin ice sheet the whole thickness undergoes temperature change, while in a thick ice sheet the temperature changes are significant only in the upper part. The

stress distribution in an ice cover depends on both temperature changes and boundary conditions. For a clamped case where the rotations and displacements are restrained at boundaries the stress at each layer will depend only on the temperature changes of that layer. Therefore the pattern of the stress distribution will be similar to the pattern of the temperature changes. For example in a thin ice sheet the whole thickness will be stressed, but in a thick ice sheet the stress in the lower parts will be close to zero. When the ice sheet has freedom to move or rotate along parts of the boundary, the interaction between the layers will change the pattern of the stress distribution. In these cases the stresses due to bending and in-plane deformation will be superimposed on stresses due to temperature changes. In this section only the stresses and the stress resultants in the clamped case are studied. It will be seen later that the stress resultants for the clamped situation provide a benchmark case for comparing the stress resultant for other boundary conditions.

To assess the role that ice thickness plays in the thermal stress problem a series of numerical tests are performed. In these tests the ice thickness is varied from 0.1 to 1.0 m. The thermal loading includes two cycles and a single element mesh is used. For this element the stresses at all Gauss points, in both the x and y direction are identical. The comparisons are based on the maximum stress in the top layer and the stress resultant at one of the Gauss points.

Figure 6.10 shows a comparison between the stresses in the top layer versus time for three different thicknesses, 0.2 m, 0.4 m, and 1.0 m. The first two values are reasonable for early and late season. For example in the data collected by Fleet Technology Ltd. most of the thermal events occurred when the thickness of the ice cover was between 0.15 m and 0.5 m. The thickness of 1.0 m was selected to represent a very thick ice sheet.

Figure 6.10 shows that the stress in the top layer does not change very much with the thickness and only slightly decreases with the increasing thickness. In the power law creep the maximum stress depends on the strain rate and fluidity parameter, η, which is a function of temperature. In the layered model the stress, the temperature and the temperature rate in the top layer are those corresponding to the mid-point of that layer. Since the number of layers is constant, with increasing thickness, the thickness of each layer increases and the mid-point gets further from the surface. The temperature rate is

the highest at the ice surface and is the same for different thicknesses. The temperature rate at the mid-point of the top layer however, decreases slightly with increasing thickness because it gets further from the surface. Therefore the stress in the top layer also does not change significantly with thickness but decreases slightly with increasing thickness. The peak stress calculated during the second cycle is observed to be lower than that during the first cycle and the magnitude of the stress during the second cycle depends on the tensile strength of the ice sheet. The maximum stress resultant, the maximum stress in the top layer, and the times of their occurrence during the first cycle are shown in Table 6.4 for different ice thicknesses Similar results, but for the second cycle, are shown in Tables 6.5 and 6.6 for tensile strengths of 0.01 and 0.5 MPa respectively. It can be seen that with a higher tensile strength the maximum compressive stress during the second cycle decreases. The reason for this behavior is explained subsequently in section 6.2.10, which deals with tensile cracking.

Tables 6.4 to 6.6 also show that with increasing thickness there is a greater delay before the maximum stresses and stress resultants occur. It can be seen that the peak stress in the top layer occurs before the peak stress resultant. Also the time delay between the two peaks increases with increasing thickness. This indicates that the penetration into the ice sheet of the effects of the transient surface temperature is an important factor affecting the maximum load. Figure 6.11 shows the stress distribution through the thickness of the ice cover at the time of the maximum stress resultant. Results are shown for three different thicknesses. It can be seen that in all of the cases stress is very depth dependent. For the thinnest ice sheet (0.2 m), the time at which the maximum stress resultant occurs is close to that for the maximum stress. Therefore the stress is highest in the first layer. For the two thicker cases (0.4 m and 1.0 m), the maximum stress resultants occur after the temperature at the ice surface has started decreasing. Therefore the stress in the top layer is lower than the stress in the second layer. Figure 6.11 also shows that for a thick ice cover the effect of temperature variation with a period of 24 hours does not reach the bottom layers and the stresses are close to zero in the lower parts of the ice sheet.

Figure 6.12 shows the stress resultant versus time for the same conditions as Fig. 6.10. It can be seen that for the relatively thin 0.2 m ice sheet the maximum stress resultant occurs simultaneously with the maximum surface temperature and the value of the maximum stress resultant does not change between temperature cycles. As the ice thickness increases there is a greater delay between the maximum temperature and the maximum stress resultant. Also for the thickest case considered, a cumulative effect between cycles is observed. This indicates that the stresses from the first temperature cycle are not dissipated before the second cycle begins. Thus for the 1.0 m ice, the predicted peak stress resultant increases between the first and second temperature cycle.

As seen in Fig. 6.12, the peak value of stress resultant depends on the ice thickness and can be different between temperature cycles. The stress resultant during the second cycle is also affected by tensile cracking and thus by the tensile strength. These affects are shown in Fig. 6.13 where the peak stress resultant for both the first and second temperature cycles are plotted as functions of ice thickness. Second cycle results are shown for two values of tensile strength, 0.01 and 0.5 MPa. It is observed that the maximum stress resultant during the first temperature cycle increases with ice thickness until around 0.5 to 0.6 m after which it remains relatively constant. The peak stress resultant for the second cycle is less than that for the first cycle for thicknesses less than 0.6 m. Beyond a thickness of 0.6 m the second cycle peak is higher and it continues to increase with thickness. However, since the slope of the curve decreases with increasing thickness, it is expected that the second peak value will eventually flatten out. Increasing the tensile strength of the ice cover slightly decreases the maximum stress resultant during the second cycle.

6.2.3 - Period of Temperature Increase

The magnitude of the prescribed temperature change and the time over which it occurs both affect the stress distribution and the stress resultant in the ice cover. The role played by the period of the temperature change is complex. On one hand, increasing the duration of the temperature rise, reduces the strain rate and the hence the stress in the ice. On the

other hand, a longer duration provides more time for conduction of heat into the ice, and the zone undergoing significant temperature change will be thicker. In order to study these effects, ice covers with different thicknesses are analyzed for prescribed harmonic surface temperature variations having different periods. The minimum temperature is -10°C, and the amplitude is 5°C. A 24 hour period approximates a typical daily temperature cycle.

Figure 6.14 shows the predicted maximum stress in the top layer versus the period of the prescribed surface temperature. As expected the stress in the top layer decreases with increasing period due to the lower strain rate. At small periods there is not enough time for the penetration of heat, and high stresses exist only near the surface. Since in the finite element model the number of layers through the thickness is constant, with increasing total thickness the thickness of each layer increases. For a thin ice sheet, the mid-point of the top layer is very close to the ice surface, and shows the high stress that occurs near the surface for small periods. With increasing thickness the mid-point of the top layer gets further from the ice surface and therefore the stress decreases. However, as the period increases the peak stress tends to become independent of ice thickness. For the 1.0 m ice sheet the top layer does not capture the high strain rate corresponding to the 6.0 hour period, so the stress increases when the period increases from 6 hours to 12 hours.

Figure 6.15 shows the maximum stress resultants versus the period of the temperature cycle. In the thin ice sheet, due to the relatively linear distribution of the temperature changes and the stresses, the maximum stress resultant is determined mainly by the magnitude of the stress at the surface. Therefore the stress resultant decreases when the period increases. For the thick ice sheets however, the maximum stress resultant is produced when the heat penetrates into the ice sheet, and the maximum stress resultant increases with increasing period. Figures 6.16 and 6.17 show the maximum stress in the top layer and the maximum stress resultant versus the thickness of the ice cover. The same trends as discussed earlier in the paragraph can be seen in these figures as well. It is generally believed that the ice pressure does not increase with the thickness when the thickness of the ice cover is more than 0.5 m. According to Fig. 6.17 this is true for daily temperature changes. However for long duration (periods of the order of 48 hours or

greater) temperature changes, the stress resultant is thickness dependent for thicknesses greater than 0.5 m.

6.2.4 - Initial Temperature

Under a constant strain rate the stress in ice increases with time until it reaches a level where the viscous strain rate corresponding to that stress equals the strain rate. Then the stress remains almost constant at that level. The maximum stress is therefore controlled by the fluidity parameter, η_1, and the stress exponent, n. With increasing fluidity parameter, the maximum stress decreases, for a given strain rate. The time to reach to the maximum stress depends on the modulus of elasticity, E_1. With increasing modulus of elasticity the time to reach the maximum stress decreases. The apparent modulus of elasticity and the fluidity parameter are both temperature dependent. Table 5.3 shows the values of E_1 and η_1 at different temperatures. It can be seen that at lower temperatures E_1 is higher and η_1 is lower. Therefore with the same strain rate the maximum stress is greater for lower temperatures and the time to reach the maximum is less. Consequently higher stresses are produced at low temperatures. For the snow-ice the rate of change of E_1 with temperature is higher at low temperature, and the rate of change in η_1 is lower. The fluidity parameter increases rapidly at temperatures close to zero. Therefore with a constant strain rate as the temperature increases the stress rate decreases until the stress reaches a maximum value. Then due to significant relaxation at high temperatures despite the increase in temperature the stress decreases.

With the periodic surface temperature history used in this study, for a particular prescribed amplitude and period, the final stress distribution and stress resultant will depend on the initial temperature at which the process started. In this section the effect of the initial temperature is studied and the stress and stress resultant are compared for different initial temperatures. The period and the amplitude in all of the tests are 24 hours and 5°C respectively. The initial temperature ranges from -30°C to -10°C.

In Figs. 6.18 and 6.19, the maximum stresses in the top layer and the maximum stress resultant for different ice thicknesses are plotted against the initial ice surface temperature.

As expected the stresses and stress resultants both decrease with increasing initial temperature. It was observed that the time to reach the maximum stress does not change very much with increasing initial temperature. This indicates that the change in fluidity parameter plays the main role in changing the maximum stresses.

6.2.5 - Amplitude of Temperature Increase

Changing the rate of temperature increase changes the strain rate which in turn affects the stress. At a prescribed temperature (in which case E_1 does not change), with increasing strain rate, the peak stress increases and the time to reach the peak decreases. With increasing temperature the stresses are affected not only by the strain rate corresponding to a temperature rate, but also by the magnitude of the temperatures.

In this section the amplitude of the temperature variation is changed while maintaining the period at 24 hours. The amplitude is varied from 2.5°C to 15°C which correspond to maximum temperature changes of 5°C and 30°C respectively. Also, since the mechanical properties of ice are temperature dependent, a change in the mean temperature of the cycle will affect the stress and stress resultant. Therefore in one series of tests the initial temperature is kept constant at -30°C, and in the other series, the maximum temperature is constant at 0°C.

Figures 6.20 and 6.21 show the maximum stress in the top layer and the maximum stress resultant versus the amplitude of the temperature cycle for two different ice thicknesses. It can be seen that the maximum stress and maximum stress resultant both increase with increasing temperature amplitude but the shape of the curves depends on the mean temperature.

In Fig. 6.20 for the tests where the initial temperature is kept constant at -30°C (lower mean temperature), the slope of the maximum top layer stress curve decreases as the temperature amplitude increases. For the tests where the maximum temperature is constant (higher mean temperature), the curve is almost linear and there is an almost uniform increase in the maximum top layer stress as a function of temperature amplitude.

This can be explained by the manner in which η_1 changes with temperature. As discussed earlier, η_1 increases very rapidly at high temperatures. As the amplitude of the temperature cycle increases there are two effects. On one hand the strain rate increases which increases the maximum stress, while on the other hand η_1 increases which accelerates the relaxation in the stress. Consider for example the curve in Fig. 6.20 for 0.2 m ice with minimum temperature fixed at -30°C. When the amplitude increases from 5 to 10 degrees, the strain rate doubles but η_1 remains almost constant because of the low mean temperature. For the same curve, as the temperature amplitude increases from 25 to 30 degrees, the increase in strain rate is almost offset by the increase in stress relaxation, due to the relatively high mean temperature.

The shape of the curves in Fig. 6.21 are similar to the those in Fig. 6.20, but there are two differences between Figs. 6.20 and 6.21. First in Fig. 6.21 the magnitudes are quite different for two different thicknesses while they were almost the same in Fig. 6.20. Secondly, the curves for 0.2 m thickness are closer than the curves for 1.0 m.

The difference in magnitudes is the effect of thickness which was discussed in section 6.2.2. It was observed that with increasing thickness the stress in the top layer remains almost constant while the stress resultant increases. The closeness of the curves for the thin ice sheet can be attributed to the range of temperatures. Figures 6.9 and 6.11 show that in a thin ice sheet the temperature and the stress distributions through the thickness are almost linear. In this case the stress resultant is the sum of the stresses through the whole thickness which occur in a wide range of temperatures from the minimum surface temperature up to 0°C. In a thick ice cover however, the significant stresses occur only in the upper layers which are affected primarily by the surface temperature. For example when the surface temperature varies from -30 to -25°C, in a thin ice sheet the stresses develop in the temperatures from -30 to 0°C, while in the thick ice sheet the stresses develop in the temperatures which are probably below -15°C. Therefore for a thin ice sheet there is not much difference between the curves for different temperatures.

In Fig. 6.22 the stress in the top layer is plotted versus time for two different temperature amplitudes, and two different thicknesses. The initial temperature is the same in all cases. In Fig. 6.22 the strain rates corresponding to the larger amplitude (-30 to 0)

are higher. Also with increasing thickness the mid-point of the top layer gets further from the surface and therefore the strain rate decreases at this point. It can be seen that the maximum stress occurs earlier with higher strain rates. As explained earlier this happens because there is less time for relaxation.

Figure 6.23 shows the stress resultant versus time for the same cases that are described for Fig. 6.22. It can be seen that for the thin ice (0.2 m), the maximum stress resultant also occurs earlier when the strain rate is higher. There is not much difference between the shape of the two 0.1 m curves, only the maximum values are different. This is due to the fact that for relatively thin ice sheets the maximum load is controlled by the maximum stress, whereas in a thick ice sheet, the maximum stress resultant occurs when the effects of the surface temperature change have had time to penetrate well into the ice sheet.

6.2.6 - Underlying Water and Boundary Conditions

The elastic foundation behavior of the underlying water, and the shoreline boundary conditions are all expected to have some influence on the stress field in the ice and hence on the resultant line load. However to some degree the effects of these factors are related and it is not possible to separate them.

For example consider an ice cover which is free to expand or rotate. Under a non-uniform and non-linear temperature variation through the thickness the ice cover bends and expands (or contracts) and the stresses through the thickness distribute in a way that the stress resultant and bending moments in each cross section becomes equal to zero and the normals to mid-surface remain normal. In this case due to interaction between the horizontal layers, some of the layers will be under tensile stress and some under compressive stress.

If the ice cover is floating on water, the underlying water will resist the bending and flatten the ice cover in the regions away from the boundary. The effect of the underlying water was shown in a beam example in section 4.6.3. In that case the bending displacements near the end of the beam, in conjunction with the elastic foundation, result in bending moments being applied at the ends. The size of the flat region for both a beam

and a plate, will depend on the lateral dimensions, thickness, and stiffness of the foundation.

When the displacements are restrained on the boundary but the rotations are free, expansion is prevented and the stress resultant will not be equal to zero. However the normal bending moment near the boundary will still be equal or close to zero.

Under clamped boundary conditions, where the displacements and rotations are both equal to zero on the boundary, a normal bending moment and resultant force, both generated as reactions, act on the ice cover. The effect of the bending moment reaction will be similar to the effect of the bending moment generated by the underlying water in the case where rotations are free on the boundary. Both tend to flatten the ice cover. However in the clamped case, this flattening occurs with or without an elastic foundation.

In regions where the ice cover remains flat, and there is no horizontal displacement, the stress distribution through the thickness is the same as would occur if each layer were allowed to expand and contract independently under the action of the temperature history in the layer.

Despite the difficulties cited in separating the effects of the elastic foundation and boundary conditions, several test cases are conducted to gain some insight into the role of these factors.

Two types of boundary condition at the edge of the ice plate are considered: one has clamped boundaries with no displacement or rotation, and the other has displacements restrained but free rotations about both the x and y directions. Other types of boundary conditions are studied in the section about the different shore line types. The effect of the underlying water is also studied for both clamped and free rotation boundary conditions. The analyses are performed on circular ice plates with radius ranging from 3.0 m to 30000 m. Different radii are studied to investigate the effect of the scale on the stress distribution when the elastic foundation is considered in the analysis. In the finite element analysis, considering symmetry one quarter of the circular ice cover was modeled using a total of 18 elements.

The results obtained for the clamped boundary conditions indicated that the stresses are exactly the same in the x and y directions for all values of radius, both with and

without an elastic foundation. The results do not change even for irregular geometries or different number of elements. The rotations are close to zero in all elements and there is no bending deformation in the ice cover. As well, all in-plane displacements are zero, indicating as discussed previously, that each layer acts independently under the effect of its own temperature history. In order to verify this, a simple test was performed in which the whole ice cover was subjected to a uniform temperature variation identical to the temperature variation in the upper layer of the previous cases. It was observed that stresses in the whole ice cover are identical to those generated in the upper layer of the previous case with non-uniform temperature variation. This conclusion simplifies the analysis for estimating the ice pressure. It indicates that in fully confined conditions, where the reservoir boundary conditions are equivalent to clamped, it is possible to use only one element with clamped boundary condition for estimating the thermal pressure. The size of the element is arbitrary. The single element mesh was also used to simulate the field measurements in Chapter 5. The agreement was good in most cases and it was concluded that in certain circumstances the single element mesh is capable of estimating the stresses in the ice sheet.

When the rotations are free at the boundaries, the stress distribution is affected by both the presence of an elastic foundation and the radius of the ice plate. Tables 6.7 and 6.8 show the maximum stress in the top layer and the maximum stress resultant for circular ice plates with different radius. The results are presented for two thicknesses, with and without an elastic foundation. It can be seen that for small values of the radius, the stress in the top layer is much lower than for the clamped case, but there is not much change in the stress resultant. Figure 6.24 shows the stress distribution through the thickness at the time of maximum stress resultant for two different thicknesses. The radius in each case is 3.0 m, and the stresses shown are at the Gauss point closest to the center of the plate. The temperature changes are larger in the upper layers, therefore the ice covers takes a convex shape when it is free to bend. This reduces the stress in the top layers and produces compressive stresses in the bottom layers. Since the dimensions of the plate are small and the normal moments are zero at the edges, the stresses even in the central regions are redistributed in a way such that the resultant bending moment is close to zero.

Since the plate is not free to expand in the xy plane, a resultant force is generated, which is found to be similar to that for the clamped case. As can be seen in Table 6.7, with increasing radius the stresses do not change very much when the effect of the underlying water is not considered. For these cases however, the vertical displacements at the center of the plate get very large and become unrealistic. The underlying water resists the vertical displacements and tends to flatten the ice cover. Therefore when the elastic foundation is included in the analysis, as the radius get larger the stress distribution at points away from the boundary gets closer to that for the clamped case. At the edge of the ice plate the stress distribution should produce a zero bending moment. The stresses shown in the Table 6.7 as the edge stresses are obtained in the Gauss points. Since the element configuration does not change with increasing radius the Gauss point at the elements located on the edge of the ice plate get further from the edge. Therefore for large radius these values also get close to those for the clamped condition and do not represent the stress distribution right at the edge, which should have a zero normal bending moment. This shows that for large ice sheets, as occur on lakes and reservoirs, the effect of the underlying water is to create a condition for a large part of the ice cover, which is the same as would exist if the boundaries were clamped. Thus even when the ice cover is free to rotate at the boundaries, a single element mesh is able to give good estimate of the stresses that exist in regions away from the boundary.

6.2.7 - Different Shore Types

When the shores are not very steep, the ice cover has some freedom to expand in the direction perpendicular to the shore line. This tends to reduce the stresses that would otherwise occur. Field measurements confirm that stresses due to thermal expansion tend to be lower in reservoirs having shorelines with relatively shallow inclines. For example the highest thrusts measured by Monfore (1954) were 292 kN/m at a reservoir with rocky and steep walls, 137 kN/m at a reservoir with moderately steep shores, and 85 kN/m at a reservoir with flat shores. The freedom to expand also changes the stress distribution through the thickness of the ice cover. The expansion of the upper layers is resisted by the

lower layers which experience smaller temperature changes. Therefore tensile stresses are produced in the lower layers. The expansion of the ice cover is also affected by the thickness. With increasing thickness, there is more resistance against the expansion of the upper parts of the ice cover. Therefore the horizontal displacement of the whole ice cover decreases with increasing the thickness.

While it is accepted that the incline of the shore has an effect on the thermal stresses generated in an expanding ice sheet, it is difficult to study this effect in isolation from other factors such as the geometry of the reservoir. Consider for example a reservoir where the shore is relatively flat in one region and quite steep in others. The effect of the flat region on the stresses in the ice cover depends on the geometry of the reservoir. If the flat region is small compared to the whole boundary, only the stresses at the vicinity will be affected.

Since it is not possible to cover all the different geometries possible, a simple square geometry is used to gain some understanding of the behavior of ice when it has some freedom to expand on a part of the boundary. It is assumed that the shore is flat on one of the sides of the rectangle, and steep on the other sides. The finite element mesh of the ice plate, which is a 300 m square, is shown in Fig. 6.25. Two series of analysis are performed. In the first series, the plate is clamped on three sides (BD, CD, and AC) with all rotations and displacements equal to zero. On the fourth side (AB), only the displacements in the vertical direction are restrained. The springs shown in Fig. 6.25 are used in the second series of tests and do not apply to these tests. This is intended to represent a flat shore that provides negligible resistance against movements in the horizontal direction or rotations.

In this series of tests, the horizontal movement of the ice cover, the stress distribution in the vicinity of the free boundary (location 1, Fig. 6.25), the effect of thickness, and the stress resultant at a location far form the free boundary (location 2, Fig. 6.25) are investigated under two loading conditions. In the first, the minimum temperature is -10°C and the amplitude is 5°C. In the second, which represents a more severe thermal loading, the minimum temperature is -20°C and the amplitude is 10°C. The period is 24 hours in both cases. In order to study the tensile stresses, cracking is not included in the analysis.

Figure 6.26 shows both the maximum displacement of the ice cover in the y direction, and the stress resultant at location 2, versus the ice thickness. In order to facilitate the comparison of results for different thicknesses, the stress resultants are normalized with respect to the stress resultant corresponding to each thickness under completely clamped conditions. As expected, with increasing thickness, the in-plane displacement of the ice cover decreases. When the expansion of the ice cover decreases, the normalized load decreases.

Figure 6.27 shows the stress distribution through the thickness of the ice cover at the time of maximum expansion. Results are shown for different thicknesses, at different locations (as shown in Fig. 6.25), and for the two loading conditions. The maximum tensile stress is about 0.45 MPa, which occurs in the 0.1 m ice sheet under the severe loading condition. The values suggested in the literature for the tensile strength of ice, which are obtained from laboratory tests, are about 2 MPa (Haynes, 1973). In the upper layers, due to presence of pre existing cracks and flaws, the sort of global tensile strength is reduced. Since most of the cracks are observed to be open at upper layers (Metge, 1976) the ice in the bottom layers might be able to tolerate higher levels of tensile stress. This should be verified by field measurements. The magnitude of the tensile stress decreases as the thickness increases. With increasing thickness, the thickness of the region that is affected by temperature changes becomes a smaller fraction of the total thickness. Therefore the tensile resistance against the expansion is shared by a larger portion of total thickness. Note also that the time at which the maximum expansion occurs increases with increasing thickness. Some similar numerical tests under the same conditions but with a lower tensile strength were also performed. It was observed that cracking in the ice cover increases the expansion and the stress resultants.

In the second series of tests, boundary elements are used on side AB to model an inclined shore (Fig. 6.25). The boundary elements are linear springs that are fixed at one end and attached to boundary nodes at the other. These springs can be given any desired orientation. A spring with a relatively large stiffness prevents movement of the attached node in the direction of the spring. Therefore when the springs are aligned in a direction perpendicular to the shore, as shown in Fig. 6.25, the ice cover cannot move in that

direction. If the other displacements are not restrained, this can model the sliding of the ice cover up the shore. In order to study the effect of the rotations on side AB on the stresses two cases were studied, in one case the rotations were restrained and in the other were free. In this particular example, the rotations are restrained and there is freedom to move only in the direction perpendicular to the boundary elements. The case with free rotations on side AB is discussed in the next part of this section. The thickness of the ice cover is 0.2 m, and the minimum temperature is -10°C with an amplitude of 5°C.

Figures 6.28 and 6.29 show the maximum stress in the top layer and the maximum stress resultant for different angles of shore inclination. The stresses are for two locations, far from the free edge (location 2, Fig. 6.25) and near the free edge (location 1, Fig. 6.25). As the inclination angle becomes larger the boundary condition approaches a clamped condition and both the maximum top layer stress and the stress resultant increase. For angles near zero or ninety degrees, the stress and the stress resultant are somewhat unaffected by changes in the angle. The effect of change in the angle on the stresses is larger for angles from 30° to 60°. The amount of reduction in the stresses with respect to clamped conditions depends on the location of a particular point with respect to the shore with shallow incline. Since the expansion of the ice cover occurs in the y direction the reduction in the stresses with respect to clamped conditions is more for the stresses and forces in the y direction than in the x direction. But due to Poisson's effect, a part of the stresses in the x direction is also released. The stresses also depend on the boundary conditions on the other sides (BD, CD, and AC). All boundary points other than AB have a displacement constraint in the y direction. Thus points that are far removed from the free edge will be affected by this constraint, and a higher stress in y direction will result.

Since the stresses are affected by the boundary conditions, two other combinations of boundary condition are also considered. Figures 6.30 and 6.31 show the maximum stress in the top layer and the maximum stress resultant for three different boundary conditions. Boundary condition 1 represents the case that was described in the previous part of this section where the sides AC, BD, and CD are clamped, and the rotations are restrained along AB. Boundary condition 2 has clamped conditions on sides AC, BD, and CD. On side AB the rotations about the x axis and displacements in x direction are free. Boundary

condition 3 has the same conditions as boundary condition 2 but with free displacements in the y direction along on AC and BD. It can be seen that free rotations along AB mainly affects the stresses at location 1 for angles above ten degrees. This can be explained by the fact that with large angles the ice cover has to bend near the shore in order to be able to slide up the incline. Figures 6.30 and 6.31 also indicate that the maximum top layer stress and the stress resultants at location 2 depend very much on boundary conditions on sides AC and BD. The stresses and the loads decrease significantly when the plate is free to move along the y axis on those sides.

6.2.8 - Stiffness of the Resisting Structure

As an ice sheet expands against a structure, the interaction force generated between the ice sheet and the structure will be influenced by the stiffness of the structure. An extremely flexible structure, which allows relative freedom for the ice sheet to expand, will encounter smaller loads than would a very stiff structure. The latter would in effect behave much like a rigid and very steep shoreline. The situation is more complex when different regions of the structure have quite different stiffnesses. For example, concrete piers are much stiffer that the steel gates of a spillway. As the stiffness of the flexible parts decreases, so would the loads on these parts, while at the same time, the loads on the stiffer parts would increase. This effect has been confirmed by field data. For example the data collected by Fleet Technology Ltd. show that at the spillway of Paugan Dam, the loads exerted on piers were three or four times the loads on gates (Comfort et al., 1993, 1994).

In the finite element program, boundary elements are used to model flexible structures. A spring with a very high stiffness represents a rigid structure, and a small stiffness represents a flexible one. A real structure exhibits a distributed stiffness somewhat like an elastic foundation. However ultimately in a finite element model, the effect of a distributed stiffness will still be discrete stiffnesses added to the nodes. The objective in this part of the study is not to characterize a specific structure but rather to adjust the stiffness over a wide enough range as to encompass many real structures.

In this section two different geometries are studied. In the first case the finite element mesh shown in Fig. 6.25 is used. The springs lie in the horizontal plane and are oriented in the y direction. Sides AC, BD, and CD have clamped boundaries. This corresponds to the situation where the part of the structure in contact with the ice has a vertical face, and the ice has adhered to the structure. The problem is analyzed using different values for the spring stiffness and in each case the maximum stresses in the top layer and the maximum stress resultants are obtained. The thickness chosen for the ice cover is 0.2 m. The values selected for the stiffness of the boundary elements ranged from 1 MN/m which represents almost a free expansion to 1×10^5 MN/m for which the results are identical to the clamped conditions.

Figures 6.32 and 6.33 show the maximum stress in the top layer and the maximum stress resultant in the y direction for different values of stiffness. It can be seen that both the maximum top layer stresses and the stress resultants decrease with decreasing stiffness of the structure. The stresses in the x direction also decrease, but since the springs are in the y direction, there is more decrease in the y direction than the x direction. The sides AC and BD are clamped, therefore the stresses at location 1 are affected by the structure stiffness more than those at location 2.

In the second case, the geometry of the ice cover in the vicinity of the spillway at the Paugan Dam is used to study the effect of the flexibility of the gates on the load sharing between the gates and piers. The finite element mesh used for this analysis is shown in Fig. 6.34. The pier is assumed to be rigid and the springs model the flexible gate. The length L is 70 m in this analysis. The analysis is performed for four different thicknesses: 0.2, 0.4, 0.7, and 1.0 m. Two thermal loading conditions are considered: in the first, the minimum temperature is -10°C and the amplitude is 5°C, and in the second, the minimum temperature is -20°C and the amplitude is 10°C. The period is 24 hours in both cases. The tensile strength in this analysis is set equal to 0.5 MPa.

Figures 6.35 and 6.36 show the maximum average line load on the gate and the maximum stress resultant near pier tip versus stiffness of the gate, for different thicknesses. The term line load is used to show the load per unit length that is exerted on a structure and in this case is obtained by dividing the sum of the forces in the boundary

elements by the length of the gate. The stress resultant at the pier tip is obtained from the stresses in the ice at the Gauss point closest to the pier tip. The stress resultants and the line loads are normalized with respect to the stress resultant for the same thickness but with a rigid clamped condition along the face of the structure. Figure 6.35 shows the results for a minimum temperature of -10°C, and Fig. 6.36 is for a minimum temperature of -20°C.

It can be seen that with decreasing stiffness of the gate, the load on the gate decreases while the load on the pier increases. Also with increasing thickness the normalized line load on the gate decreases while the normalized stress resultant near the pier tip increases.

It seems that for intermediate stiffnesses, in the middle region of these figures, there is load sharing between the pier and the gate. As a check, the sum of the forces in the springs and the reactions on the pier in the y direction, was divided by the total length of the pier and the gate. This value was found to be close to, but less than the stress resultant for completely clamped conditions. The data collected by Fleet Technology Ltd. also showed that the average load on the combination of the gate and pier is almost equal to the load measured at far field. As discussed in section 6.2.7, the lower regions of a thick ice sheet provide some internal resistance against expansion. Thus the normalized load on the gate decreases with increasing thickness, and due to load sharing the normalized load on the pier increases.

As the stiffness decreases the stress condition approaches the free expansion case that was discussed in section 6.2.7. In this case the load on the gate gets close to zero and the load on the pier decreases with increasing thickness.

In Fig 6.37 the normalized loads for two ice thicknesses, 0.2 m and 1.0 m, are compared for two different loading conditions. It can be seen that for the medium to high range of stiffness (above 50 MN/m), the curves corresponding to two different loading conditions fall on top one another. It indicates that the load sharing is independent of the thermal loading condition and depends only on the stiffness of the gate.

The line loads and the stress resultants also depend on the tensile strength of the ice. When tensile cracking is included in the analysis, the internal resistance against expansion provided by the lower part of the ice sheet is reduced. Figure 6.38 shows the effect of

tensile cracking on the line load on the gate and the stress resultant near the pier tip. It can be seen that as the tensile strength is reduced, both the stress resultant near the pier tip and the load on the gate increase.

In order to study the effect of scale, the length L in Fig. 6.35 is changed and the normalized stress resultants at the pier tip are compared for two different ice thicknesses and two different gate stiffnesses. The results are shown in Fig. 6.39. It can be seen that over the range $10\ m \leq L \leq 100\ m$, the stress resultants increase with respect to L at first but eventually tend toward constant values. When the stiffness is small the effect of the length is the same for both thicknesses, but with a higher stiffness the results are different for different thicknesses.

When the length L is very small the part of the ice cover in front of the pier is confined between the pier tip and the upper boundary which is clamped. Therefore the stresses will be close to those corresponding to clamped boundary conditions. When the length L increases the dimensions of the ice cover increase. With increasing dimensions, the displacements due to expansion and the strain rates increase. Thus the stresses also increase and the force exerted on the pier gets lager. However, with increasing L the size of the gates becomes small compared to the length of the reservoir and therefore the stress resultants tend to constant values. The difference in the normalized stress resultants in the case of higher stiffness is the effect of the load sharing between the gates and piers that was described in the previous section.

6.2.9 - Isolated Structures

An isolated structure is one that is located away from the shores and is surrounded by the ice cover. In the literature this is usually applied to offshore structures which are located in salt water, and at distances of the order of kilometers from shore. In this study however the term is restricted to inland water situations and structures such as water intakes or spillways that are located away from the main structure.

When the external boundaries of an ice sheet are clamped, the in-plane stress field is homogeneous and hydrostatic. In this case the load exerted on an isolated structure is the

same as the load on the boundaries and can be obtained from the stress resultant under clamped conditions in a single element mesh.

Now consider a case such as a rectangular reservoir where three sides are clamped and the fourth side is free. This is like the geometry used in section 6.2.7. The situation is no longer homogenous nor hydrostatic. A point located in the middle of the ice cover can go under considerable horizontal displacement, the magnitude of which depends on the dimensions of the reservoir and boundary conditions. Usually the larger the reservoir dimension, the larger is the expansion of the ice cover and the displacement of a typical point in the middle. Now if a fixed structure with dimensions that are small compared to the dimensions of the reservoir is located in the interior of the ice cover, a substantial force can be exerted on the structure. In this case, due to the large displacements, the strain rates also get larger than the strain rates corresponding to clamped conditions. Therefore the stresses increase. The thickness of the ice cover also affects the loads. In a thick ice cover the bottom layers that are not affected by the temperature changes of the upper layers will resist against the expansion and the strain-rates will be less than for a thinner ice sheet.

In this section the purpose is to assess the loads that can be exerted on an isolated structure in free expansion conditions. As discussed earlier the loads depend very much on the geometry, boundary conditions, and dimensions. Since it is not possible to study all of the different situations, a simple geometry is used. The finite element mesh is shown in Fig. 6.40. On side AB the displacements and rotations are all free except for the displacements in the vertical direction. Along CD and BD clamped boundary conditions are used. Line AC is an axis of symmetry so that the actual problem solved spans a region twice the size of that shown in Fig. 6.40. The isolated structure occupies the shaded region EFGH. Clamped boundary conditions are applied to the ice sheet along the boundary of the structure .

It could be argued that it is not realistic to apply rigid boundary conditions around the entire boundary of the structure. For example on side EF high tensile stresses are produced which in a field situation could result in the ice debonding from the structure. However in a field situation, the structure would not be totally rigid and this would tend to

decrease the compressive stresses on the front face of the structure. Therefore the forces obtained using the present model are considered to be upper bound.

The sides EF, FG, and GH of the structure are all five meters. The dimensions of the elements adjacent to the structure are 5.0×0.5 m. Other dimensions are varied in different tests. In order to study the effect of the geometry in each series of tests, the length L1 in Fig. 6.40 is kept constant, and the change in the maximum stress in the top layer in front of the structure and the average line load on the structure is determined for different values of length L2. The tests are repeated for three different values of L1. The minimum surface temperature is -10°C, the amplitude is 5°C, and the period is 24 hours. The average line load on the structure is obtained by calculating the total reaction in the y direction on side GH and then dividing by the length of side GH (5.0 m). In presenting the results, the line loads are normalized with respect to those for the same geometry and thickness but with clamped boundary conditions on sides AB, BD, and CD. This kind of normalizing facilitates the comparison of the results for different thicknesses

Figure 6.41 shows the maximum stress that occurs in the top layer in front of the isolated structure, near point G. The results are presented for two different thicknesses and three different values of L1. There is a stress concentration at G and the stresses at this region are higher than the stresses close to H. It can be seen that for a prescribed value of L1 stresses increase as the dimension L2 increases and tend to constant values. Increasing dimension L1 also increases the stresses. Figure 6.41 also shows that the stresses in the 1.0 m ice cover are much smaller than the stresses in the ice cover with the same geometry and 0.2 m thickness.

Increasing the dimension L2 directly increases the size of the expanding ice cover in front of the isolated structure. Therefore the strain rates due to displacements and the resulting stresses increase. However the clamped boundary conditions on side BD limit the expansion of the ice cover, and thus beyond a certain value of L2 the stresses do not change very much. Increasing the length L1 however, moves the clamped boundaries further from the structure and increases the stresses. The smaller stresses in the thick ice cover can be explained by the fact that with increasing thickness , the portion of the ice

cover that resists the thermal expansion becomes larger and reduces the displacement due to thermal expansion.

Figure 6.42 shows the maximum average normalized line load on the isolated structure for different values of L1 and L2 and for two different thicknesses. It can be seen that the normalized line load increases as the dimension L1 increases. Following any of the individual curves in Fig. 6.41, which corresponds to holding the dimension L1 constant and increasing the dimension L2, the normalized line load increases initially, but eventually tends to a constant value. The increase in line load is initially almost linear on the logarithmic scale. Figure 6.41 indicates that for small values of L1 the normalized results are not much different for different thicknesses, but the difference between the normalized line loads for two different thicknesses increases with increasing L1.

It can be seen that loads as high as 20 times the loads for clamped conditions are exerted on the structure. Nevertheless, these values are considered to be upper bounds because in a real case flexibility of the structure and compressive cracking at high stresses will reduce the load. Due to the complexity of this problem it is difficult to assess all of the different aspects of ice behavior that arise. Many different parameters including the finite element mesh affect the results. In order to gain a better understanding of the different aspects of the problem, future studies are necessary. In particular comparisons should be made between the predictions of the model and field measurements of the loads on isolated structures in lakes or reservoirs with flat shores.

6.2.10 - Tensile cracking

It was observed in sections 5.2.2 and 5.2.4, in which simulation results were compared with field measurements, that tensile cracking has a significant effect on the stresses that occur during and after cooling periods. In the finite element analysis cracking occurs when the principal stress at a Gauss point exceeds the tensile strength. A value for the tensile strength is therefore required as an input parameter. The uniaxial tensile strength of ice measured in laboratory tests is reported in the literature to be around 2.0 MPa (Haynes, 1973), and is almost independent of strain rate over the range of 10^{-6} to 10^{0} s^{-1}.

In the tests performed by Haynes (1973), the tensile strength under hydrostatic pressure, was reduced to about 0.5 MPa and decreased with increasing strain rate. All of the tests were performed at strain rates higher than $10^{-6}s^{-1}$. Based on the available data it can be argued that at stain rates lower than $10^{-6}s^{-1}$ the tensile strength is the same or higher. In the data collected by Fleet Technology Ltd., during the cooling periods the stresses in the majority of cases were close to zero (see for example Fig. 5.18). In some cases however tensile stresses were recorded. The tensile stresses near the surface (0.025 m-0.10 m) were in most of the cases below 0.05 MPa (see for example Fig. 5.20). At depths between 0.125 m and 0.3 m the maximum recorded tensile stresses were below 0.2 MPa. This was attributed to cracking in the upper layers of the ice sheet where the largest tensile stresses, and hence cracking, would be expected to occur. It could also be argued that the presence of natural flaws and imperfections that are more likely in the field situation would result in the effective tensile strength being lower than the laboratory values. If the ice fails at a low stress due to a weakness at one location, the tensile stress in the vicinity of that area drops essentially to zero despite the fact that some parts of the ice are still capable of carrying a much higher tensile stress. In other words on a global basis for the scenario described, the observed strength would be the low stress value. Therefore on the basis of field measurements a very low tensile strength (0.01 MPa) was used in the simulations and the studies involving clamped boundary conditions

It was observed during the simulations and analyses conducted for this chapter, that the tensile cracks that occur during cooling periods under clamped boundary conditions usually do not penetrate through the whole thickness so that the lower region of the ice cover remains intact. In the analyses for the free expansion case however it was observed that tensile stresses can also occur in the lower regions of the ice cover. Most of the cracks described by Fleet Technology Ltd. and Metge (1976) were open in the upper half of the ice sheet, and the recorded tensile stresses were also small in the upper half. Therefore it may be that an ice sheet can carry a higher tensile stress in the bottom layers. However with the data available, it is difficult to reach any conclusions regarding the tensile strength under free expansion conditions. The question of what magnitude to use for the tensile strength in this case requires further field measurements.

Stresses that develop in the numerical model after cracking has occurred depend on the criteria used for crack healing. In a finite element code that includes plasticity, Hinton and Owen (1984), have used the total strain perpendicular to the crack for evaluating the crack closure. A particular crack was assumed to be closed when the total strain perpendicular to the crack became negative. Thermal loading was not considered in that study. In the present study, due to temperature changes the situation is somewhat different. As an example consider an elastic beam with clamped ends, that is subjected to a non-uniform temperature decrease through the thickness. Non-uniform tensile stresses develop and in the layers with high tensile stress cracking might occur. If the temperature continues decreasing the cracks may open. Now if the beam is subjected to a temperature increase the crack openings will decrease and eventually the cracks will close. However due to the clamped boundary conditions, the beam remains straight and the total strains are zero everywhere. Therefore the total strain is not suitable for use in a crack closing criterion.

The beam example suggests that for an elastic case, the difference between the total strain and the thermal strain be used in the crack closing criterion. Now consider a visco-elastic material. In this case, during periods of temperature decrease, some stress relaxation can occur before cracking. The relaxation changes the stress free configuration and the beam will not be stress free if the temperature distribution was to suddenly return to the initial condition. The question arises as to whether or not the viscous part of the strain should also be subtracted from the total strain. In other words assuming that the cracks heal when the crack opening strain (ε_{co}) becomes zero, two different criteria may be used for crack healing. These are given by:

1) $\varepsilon_{co} = \varepsilon - \varepsilon_{\theta} = 0$ (6.2.1)

2) $\varepsilon_{co} = \varepsilon - \varepsilon_{\theta} - \varepsilon_{v} = 0.$ (6.2.2)

In order to evaluate the differences between these criteria, a simple analysis is performed using clamped boundary conditions and two different thermal loading conditions. The temperature variation is uniform through the thickness, and the upper layer of ice is allowed to crack. Under clamped boundary conditions the stresses are independent in each layer. The temperature history and the stresses in the cracked layer

are shown in Figs. 6.43 and 6.44. The difference between the analyses conducted for these figures is the initial temperature. For the analyses presented in Fig. 6.43 the temperature starts from the mean temperature in the cycle, which is -10°C. The temperature then increases to the maximum value of 0°C after which it decreases to -20°C. This gives a cooling period during which the temperature is less than the initial temperature. For the analyses presented in Fig. 6.44 the temperature starts from the minimum value, which is -20°C, and never goes below this temperature. In Figs. 6.43 and 6.44 the number (1) that appears in the legend indicates the first crack healing criteria, which is based on equation 6.2.1. Similarly the number (2) indicates the second crack closing criterion which uses equation 6.2.2. In both Figures 6.43 and 6.44, open symbols are used for stresses obtained from analyses that include cracking. The tensile strength is 0.01 MPa and in the elastic case the modulus of elasticity is constant and equal to 1200 MPa. For the visco-elastic case the material properties of snow-ice are used.

For the elastic analyses represented in Fig. 6.43, cracking occurs as soon as the temperature goes below the initial temperature. The cracks open during the cooling period, start closing when the temperature rises, and they heal when the temperature gets above the initial temperature. For the snow-ice during the first half period of the temperature cycle the stress is compressive and negative creep strains occur. Thus during the first cooling period (0°C to -20°C) when the stress is increasing, the stress reaches zero before the temperature returns to the initial value, -10°C. Cracking occurs shortly after, when the largest principal stress reaches the tensile strength. During the remainder of the cooling period (~ -7°C to -20°C) the cracks open wider. Then during the first part of the subsequent warming period (-20°C to ~ -7°C) they begin to close. When the cracks heal depends on which of the two criteria is used. For the first criterion, the cracks heal when the temperature reaches the initial temperature (-10°C). For the second criterion, healing is later due to the accumulated negative viscous strain. For both healing criteria, the maximum stress during the second half cycle above the initial temperature, is less than the maximum stress if cracking is not included in the analysis.

Considering the analyses for Fig 6.44, the important distinguishing feature from the analyses for Fig. 6.43 is that the temperature never goes below the initial temperature,

which in this case is -20°C. Thus for an elastic material there is no cracking. This might be thought to indicate the same would be true when the constitutive model for ice is used. Interestingly, the results in Fig. 6.44 show that cracking does in fact occur. This is because during the first three quarters of the first temperature cycle, when the stress is compressive, the accumulation of negative viscous strains results in considerable relaxation of the compressive stress. Thus during the first cooling period, tensile stresses are produced when the temperature gets close to the initial value (-20°C). Again, cracking occurs when the principal stress exceeds the tensile strength. The subsequent behavior is again different depending on the healing criteria adopted. With the first criteria the cracks do not open because the thermal strain is always negative. Furthermore, the cracks heal as soon as the temperature starts rising (at -20°C) and compressive stresses are generated. Comparing this behavior with that for the ice model in which cracking is not included, it is observed for the latter, tensile stresses exist when the warming period starts at -20°C. Thus the maximum compressive stress that is reached during the warming period is less for the non-cracking model. The behavior observed for the second criteria is different again. In this case, due to the negative viscous creep strains, the cracks open and close during the period when the stress is zero. Thus during the warming period part of the thermal strain is taken up in closing the cracks. This results in a peak compressive stress less than that for either the non-cracking model or the cracking model using the first healing criteria.

The question of which healing criteria is the most accurate is one which can only be resolved by performing appropriate laboratory tests. On intuitive grounds, the second criteria seems more reasonable, since both the thermal and viscous strains can be considered permanent strains and there is no fundamental basis for excluding one or the other from the healing criterion. However comparisons between simulation results and field measurements show that the stresses obtained using the first criteria give the best agreement. In all cases the magnitude of the measured compressive stresses began to rise immediately as the temperature started rising. Also, the measured compressive stresses were significantly higher than those predicted using the non-cracking model (see for

example Figs. 5.18 and 5.32). This indicates the importance of including cracking but why the first healing criterion agrees best with field results is unclear.

When considering different aspects of the problem it should also be noted that the model is based on a smeared cracking approach while the cracks in nature are discrete. In nature, due to the effect of bottom layers, tensile stresses exist between the cracks. Therefore it is possible that some relaxation occurs which reduces the crack openings, and the compressive stresses develop immediately when the temperature starts rising.

Resolution of this question requires laboratory tests in which crack opening and closing is studied under periodic thermal loading conditions. In the absence of such experiments, the first healing criterion was adopted in the simulations and analyses, on the basis that it agrees best with field results. This criteria was used in the analyses of the previous chapters but due to complex nature of the problem the discussion was left to the present chapter.

6.3 - Summary and Conclusion

In this chapter the role of various factors that affect the temperature and stress distribution in an ice cover, was studied. For temperature distribution, the factors considered included: different ice types, wind speed, cloud cover, relative humidity, time of the year, latitude, snow cover, thickness of the ice cover, and period and amplitude of temperature variation. For the stress analysis, factors considered were the number of layers through the thickness, the thickness of the ice cover, period of temperature variation, initial temperature, amplitude of temperature variation, underlying water, geometry of the reservoir, boundary conditions, different shore lines, stiffness of the resisting structure, isolated structures, and tensile cracking of the ice.

The air and ice surface temperature variation used in the thermal and stress analysis was a periodic temperature history. Therefore some of the conclusions, for example those referring to amplitude and period or maximum and minimum values, are all based on this kind of temperature variation. The words maximum and minimum indicate the maximum

or minimum values with respect to time. For the thermal analysis if not mentioned, the conclusions are based on the ice surface temperature, and for the stress analyses are based on the stress in the top layer or the stress resultants. In these conclusions, ice covers with a thickness of 0.1 to 0.2 m are considered to be thin, and those with a thickness larger than 0.7 m are called thick. The conclusions reached from these studies are summarized in the following:

1. When the effects of solar short-wave radiation are not included in the calculation of the temperature distribution through the ice sheet, the results are relatively insensitive with respect to the thermal properties of the ice.
2. When solar short-wave radiation is considered, the maximum temperatures depend very much on the value used for the coefficient of absorption.
3. When solar short-wave radiation is not considered, increases in the wind speed, cloud cover, and relative humidity, all increase the maximum temperature and the difference between minimum and maximum temperatures. Among these parameters, the wind speed has the greatest effect on the temperature changes.
4. Including short-wave solar radiation in the thermal analysis can increase the maximum temperature significantly. The more energy absorbed, the greater the temperature increase. Lowering the latitude, reducing the cloud cover, increasing the coefficient of absorption, and decreasing the coefficient of reflection, all cause an increase in the absorbed energy.
5. The insulating property of a snow cover is an extremely significant factor affecting the temperature distribution in an ice cover. In the cases studied, which involved 5 cm and 10 cm snow covers, the predicted ice surface temperature amplitude decreased by 66% and 72% respectively from the predictions for the clear ice case.
6. When short-wave solar radiation is not considered, the amplitude of the ice surface temperature variation depends on the amplitude of the air temperature variation and ice thickness. With increasing thickness however, the effect of the thickness diminishes. As the period of the temperature history increases, the ratio between the amplitude of the ice surface temperature and the amplitude of the air temperature gets closer to one.

7. For a given period of the air temperature history, both the minimum and maximum ice surface temperatures decrease with increasing thickness and tend to constant values.
8. In thin ice sheets, the temperature changes occur through the whole thickness and the temperatures are almost linear through the thickness. With increasing thickness the temperature distributions become non-linear, and in a thick ice sheet only the upper part is active. The depth of the active zone depends on the period of the temperature cycle. The depth of the active zone is about 0.3 m for daily temperature changes (24 hours), and 0.4 m for 48 hour period.
9. Under clamped boundary conditions the maximum stress resultant in a thin ice sheet is controlled by the maximum stress in the top layer and occurs when the stress in the top layer is a maximum. Depending on the temperature rate and duration of temperature increase, the maximum may occur prior to the maximum temperature. In thick ice covers, the maximum stress resultant occur when the effect of the surface temperature changes have penetrated into the ice sheet. This may occur after the maximum temperature.
10. Under clamped boundary conditions for two identical cycles of ice surface temperature, the maximum stress resultant during the first cycle tends to a constant value with increasing thickness. For thick ice covers the stress due to the first cycle might not dissipate during the cooling period. In this case the maximum stress resultant during the second cycle may be higher than the maximum stress resultant during the first cycle.
11. With increasing period of temperature variation, the maximum stress resultant under clamped conditions for thin ice covers decreases, where the maximum stress resultant for thick ice covers increases.
12. For a given period and amplitude of temperature variation, the stresses and stress resultants under clamped conditions both decrease with increasing initial temperature.
13. For clamped boundary conditions where the rotations and the displacements are zero, the ice cover does not have bending deformation. In this case the stress in each layer is controlled only by the temperature changes of that layer and does not depend on the

geometry of the reservoir. Therefore, it is possible to get a good estimate of the stresses, with only one element in a finite element analysis.

14. When the displacements are restrained on the boundaries but rotations are free, the ice cover undergoes bending deformation which is resisted by the underlying water. This affects the stress distribution through the thickness, but has negligible effect on the stress resultants. Near the boundaries the stresses in the upper layers decrease while the stresses in the lower layers increase. For large ice sheets the bending deformation is resisted by the water. Therefore with increasing distance from the boundaries, the stress distribution gets closer to that for the clamped case. In this case, a single element mesh can still give a good estimate of the stresses.
15. When the ice cover is free to expand along some parts of the boundary, a part of the thermal stress releases and the stress resultants decrease. The expansion might be due to a non-vertical shore, or a flexible structure. The in-plane displacements due to thermal expansion are larger for thin ice sheets, where the whole thickness is activated by the surface temperature changes.
16. When a resisting structure has a combination of flexible and rigid parts, the ice load is distributed between these parts. In this case the flexible part carries a load that is smaller than the load corresponding to a clamped condition, and the rigid part carries a larger load. As the stiffness of the flexible part is decreased the load on that part decreases while the load on the rigid part increases.
17. When an ice cover is free to expand on one shore, and there is a fixed isolated structure in the interior of the ice sheet, a substantial force can be exerted on the structure. The magnitude of the force depends very much on the dimensions and geometry of the reservoir. In some of the studied cases the exerted forces were about 20 times the load under clamped boundary conditions.
18. In the clamped boundary condition tensile stresses usually occur in the upper layers during cooling periods. In the case of free expansion, however, tensile stresses are produced during warming period in the lower layers which are less affected by the rise in surface temperature.

19. In the clamped boundary conditions the predicted stresses during and after cooling periods depend on the tensile strength and crack healing criterion. Due to existence of flaws and cracks in ice covers, the tensile strength in a global sense under field conditions might not be as high as the tensile strength obtained from laboratory specimens. It was observed that a crack healing criteria using the total strain minus thermal strain gives a good agreement with the field measurements.

Wind speed (m/s)	Cloud cover	Relative humidity (%)	Minimum temperature (C^o)	Maximum temperature (C^o)	Maximum temperature change (C^o)
0	4/8	80	-13.01	-5.55	7.46
6	4/8	80	-15.99	-3.84	12.15
2	0/8	80	-14.54	-5.12	9.42
2	8/8	80	-13.70	-3.71	9.99
2	4/8	0	-15.74	-8.27	7.47
2	4/8	100	-13.99	-3.96	10.03
6	8/8	100	-15.11	-2.07	13.04
2	4/8	80	-14.33	-4.76	9.57
0	0/8	0	-14.44	-8.74	5.7

Table 6.1 - Effect of ambient conditions on the maximum and minimum temperatures.

Date	Latitude	Cloud cover	h = 0.2 m		h = 1.0 m	
month/day	(Degrees)	(/8)	Snow-ice	Columnar ice	Snow-ice	Columnar ice
		8	-3.78	-3.71	-9.44	-9.47
		0	-5.22	-5.12	-11.66	-11.66
1/1	60	0	+0.68	-3.66	-4.47	-9.71
1/1	60	8	-1.71	-3.21	-6.93	-8.81
1/1	45	0	+6.14	-2.69	+3.53	-8.28
12/1	60	0	+1.11	-3.59	-3.90	-9.59
3/1	60	0	+7.26	-2.64	+4.13	-8.06

Table 6.2 - Maximum temperatures with different parameters that affect the short-wave solar radiation.

	Maximum stress resultant		Maximum stress at top layer	
Thickness (m)	8 layers	10 layers	8 layers	10 layers
0.2	60.31	60.28	0.534	0.539
0.4	105.00	104.94	0.526	0.533
1.0	135.96	135.48	0.491	0.505

Table 6.3 - Comparison between stress resultants and stresses calculated with different number of layers through the thickness of the ice cover.

	Stress resultant		Stress at top layer	
Thickness (m)	Time (h)	Maximum (kN/m)	Time (h)	Maximum (MPa)
0.1	11.00	30.77	9.67	0.540
0.2	11.67	60.28	9.67	0.539
0.3	12.33	85.81	9.67	0.536
0.4	13.33	104.94	10.00	0.533
0.5	14.33	117.64	10.33	0.528
0.6	14.67	125.37	10.33	0.524
0.7	15.00	129.89	10.67	0.519
0.8	15.33	132.60	10.67	0.514
0.9	15.33	134.28	11.00	0.510
1.0	15.67	135.48	11.00	0.505

Table 6.4 - Maximum stress resultants, maximum stresses at top layer, and the time of their occurrence at the first cycle.

Thickness (m)	Stress resultant		Stress at top layer	
	Time (h)	Maximum (kN/m)	Time (h)	Maximum (MPa)
0.1	35.00	29.543	34.00	0.497
0.2	35.67	57.4	34.00	0.497
0.3	36.67	79.92	34.33	0.491
0.4	37.67	96.24	34.67	0.483
0.5	38.33	110.56	35.00	0.475
0.6	38.67	124.51	35.00	0.471
0.7	38.67	137.70	35.33	0.465
0.8	38.67	150.09	35.33	0.458
0.9	38.67	160.30	35.33	0.452
1.0	39.00	168.51	35.67	0.450

Table 6.5 - Maximum stress resultants, maximum stresses at the top layer, and the time of their occurrence at the second cycle (tensile strength = 0.01 MPa).

Thickness (m)	Stress resultant		Stress at top layer	
	Time (h)	Maximum (kN/m)	Time (h)	Maximum (MPa)
0.1	35.67	25.84	35.33	0.389
0.2	36.33	50.99	35.33	0.388
0.3	37.00	73.37	35.67	0.388
0.4	38.00	91.40	35.67	0.387
0.5	38.33	106.45	35.67	0.388
0.6	38.67	120.76	36.00	0.389
0.7	38.67	134.41	36.00	0.390
0.8	38.67	146.41	36.00	0.391
0.9	39.00	156.73	36.00	0.391
1.0	39.00	164.66	36.33	0.392

Table 6.6 - Maximum stress resultants, maximum stresses at the top layer, and the time of their occurrence at the second cycle (tensile strength = 0.5 MPa).

	With elastic foundation				Without elastic foundation			
	Near center		Near edge		Near center		Near edge	
Geomtery	x	y	x	y	x	y	x	y
h=0.2 m, clamped	0.5389	0.5389	0.5389	0.5389	0.5389	0.5389	0.5389	0.5389
r=3 m, h=0.2 m, hinge	0.3383	0.3383	0.3193	0.3236	0.3162	0.3163	0.3158	0.3159
r=30 m, h=0.2 m, hinge	0.5404	0.5415	0.4314	0.4590	0.3337	0.3325	0.3153	0.3159
r=300 m, h=0.2 m, hinge	0.5404	0.5415	0.4314	0.4590	0.3337	0.3325	0.3153	0.3159
r=3000 m, h=0.2 m, hinge	0.5394	0.5387	0.5385	0.5386	0.3501	0.3330	0.3200	0.3197
r=30000 m, h=0.2 m, hinge	0.5389	0.5389	0.5389	0.5389	0.3501	0.3329	0.3200	0.3197
h=1.0m, clamped	0.5049	0.5049	0.5049	0.5049	0.5049	0.5049	0.5049	0.5049
r=3 m, h=1.0 m, hinge	0.3246	0.3246	0.3246	0.3246	0.3245	0.3245	0.3245	0.3245
r=30 m, h=1.0 m, hinge	0.5341	0.5344	0.3752	0.4022	0.3257	0.3257	0.3244	0.3246
r=300m, h=1.0m, hinge	0.5341	0.5341	0.3752	0.4022	0.3257	0.3257	0.3244	0.3246
r=3000 m, h=1.0 m, hinge	0.5125	0.5096	0.5016	0.5023	0.3565	0.3448	0.3274	0.3274
r=30000 m, h=1.0 m, hinge	0.5049	0.5049	0.5049	0.5049	0.3641	0.3441	0.3276	0.3274

Table 6.7 - Maximum stress (MPa) at top layer for a circular ice plate with and without elastic foundation, for different boundary conditions, different radius, and different thicknesses.

	With elastic foundation				Without elastic foundation			
	Near center		Near edge		Near center		Near edge	
Geomtery	x	y	x	y	x	y	x	y
h=0.2 m, clamped	60.2834	60.2834	60.2834	60.2834	60.2834	60.2834	60.2834	60.2834
r=3 m, h=0.2 m, hinge	64.4301	64.4299	64.4325	64.4307	64.3437	64.3431	64.3434	64.3443
r=30 m, h=0.2 m, hinge	60.9312	60.8444	60.8693	59.5525	64.2295	64.1994	64.3376	64.3446
r=300 m, h=0.2 m, hinge	60.9312	60.8444	60.8693	59.5525	64.2295	64.1994	64.3376	64.3446
r=3000 m, h=0.2 m, hinge	60.2892	60.2817	60.2735	60.2695	63.0944	62.5804	64.3234	64.3451
r=30000 m, h=0.2 m, hinge	60.2834	60.2834	60.2834	60.2834	63.0938	62.5796	64.3234	64.3451
h=1.0 m, clamped	135.477	135.477	135.477	135.477	135.477	135.477	135.477	135.477
r=3 m, h=1.0 m, hinge	142.650	142.650	142.650	142.650	142.654	142.654	142.654	142.654
r=30 m, h=1.0 m, hinge	139.995	139.922	140.877	137.964	142.713	142.689	142.668	142.647
r=300 m, h=1.0 m, hinge	139.995	139.922	140.877	137.964	142.713	142.689	142.668	142.647
r=3000 m, h=1.0 m, hinge	140.615	142.567	135.839	135.023	145.806	145.215	142.275	142.410
r=30000 m, h=1.0 m, hinge	135.477	135.466	135.475	135.475	145.937	145.397	142.289	142.414

Table 6.8 - Maximum stress resultant (kN/m) for a circular ice plate with and without elastic foundation, for different boundary conditions, different radius, and different thicknesses.

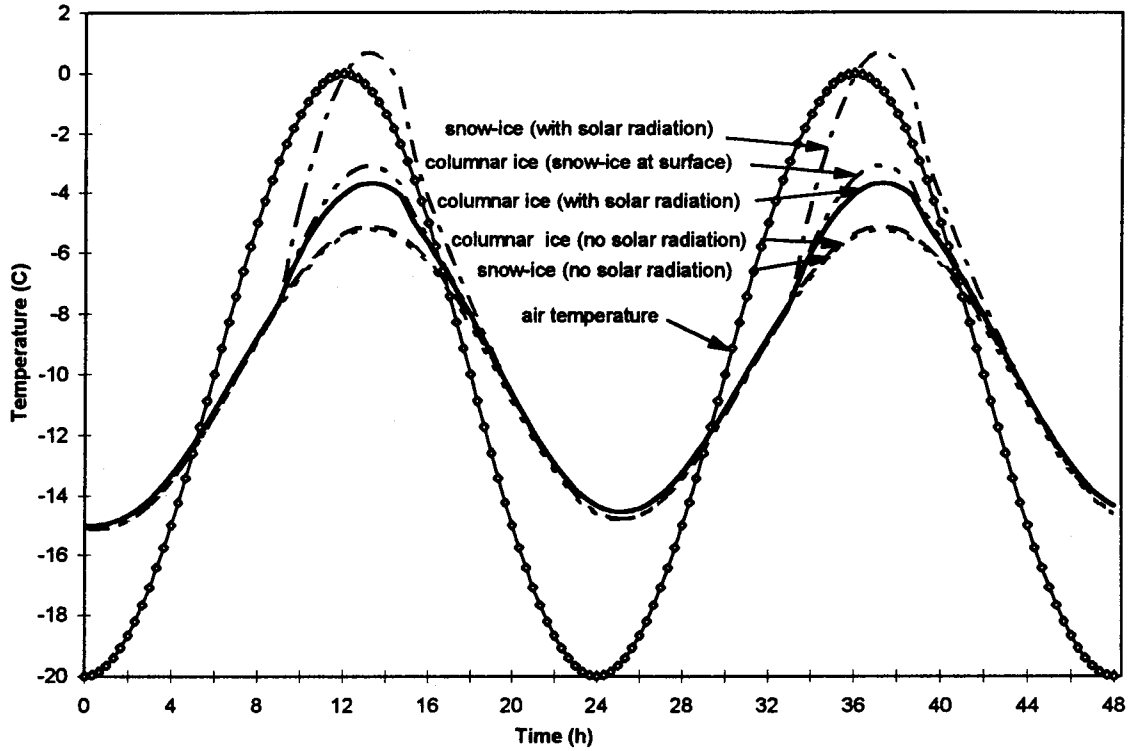

Figure 6.1 - Ice surface temperature for different ice types (ice thickness = 0.2 m).

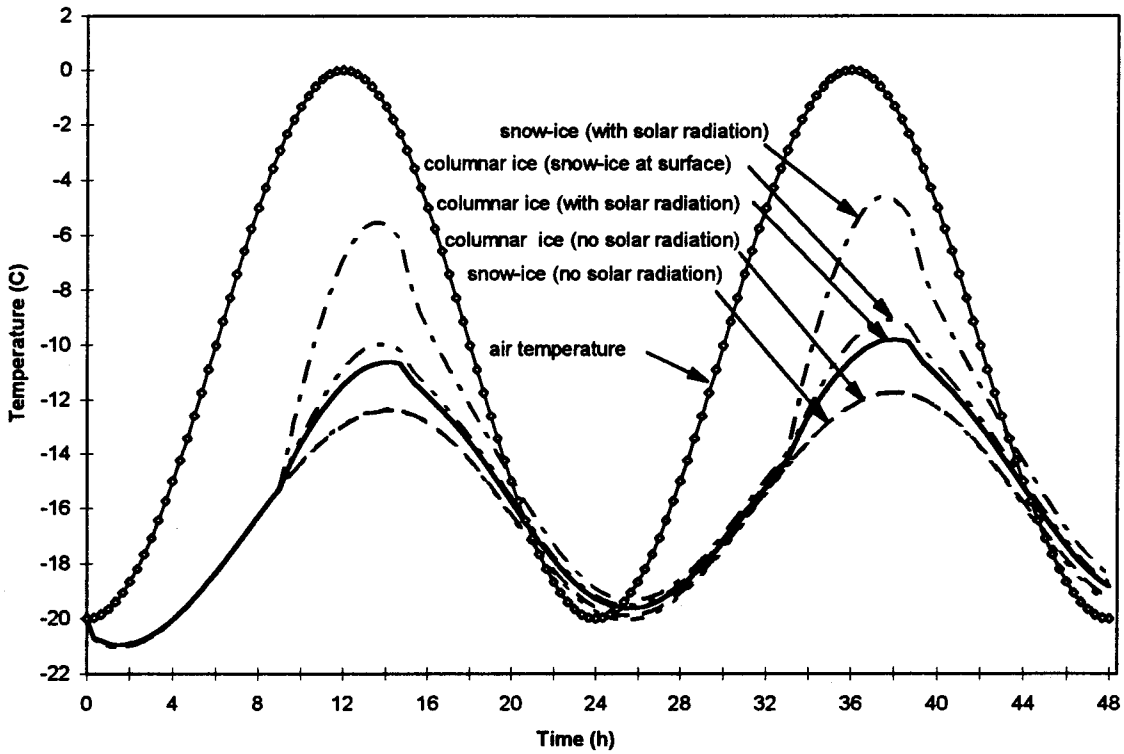

Figure 6.2 - Ice surface temperature for different ice types (ice thickness = 1.0 m).

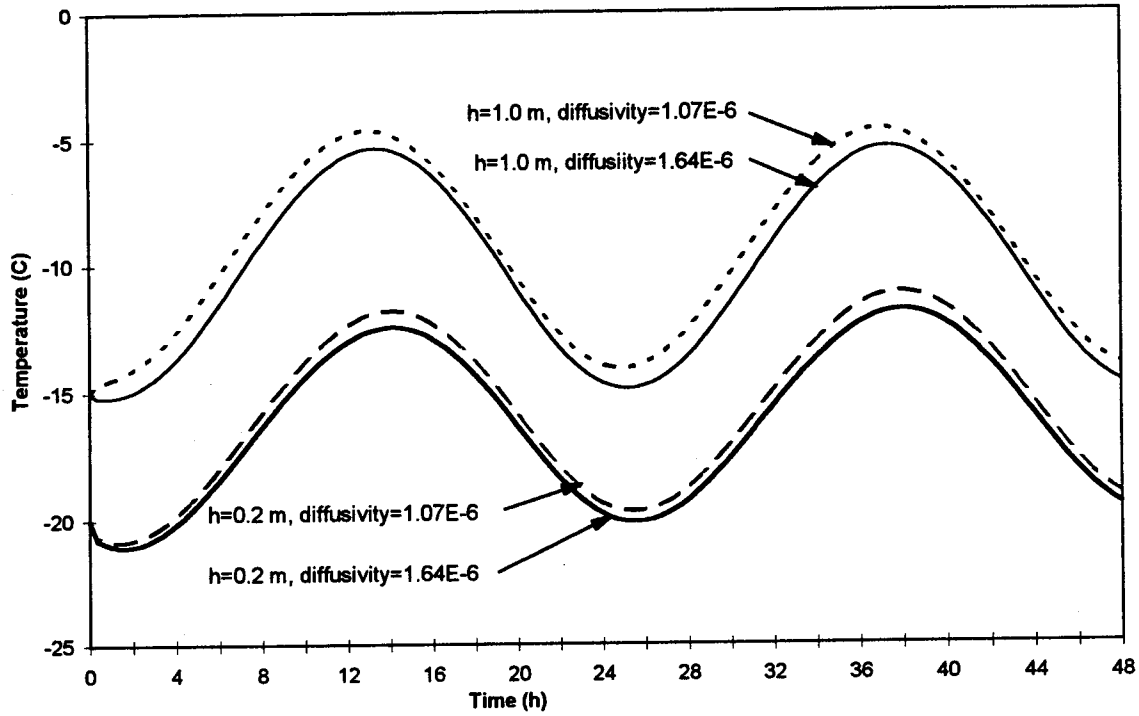

Figure 6.3 - Ice surface temperature with different diffusivity and different ice thicknesses.

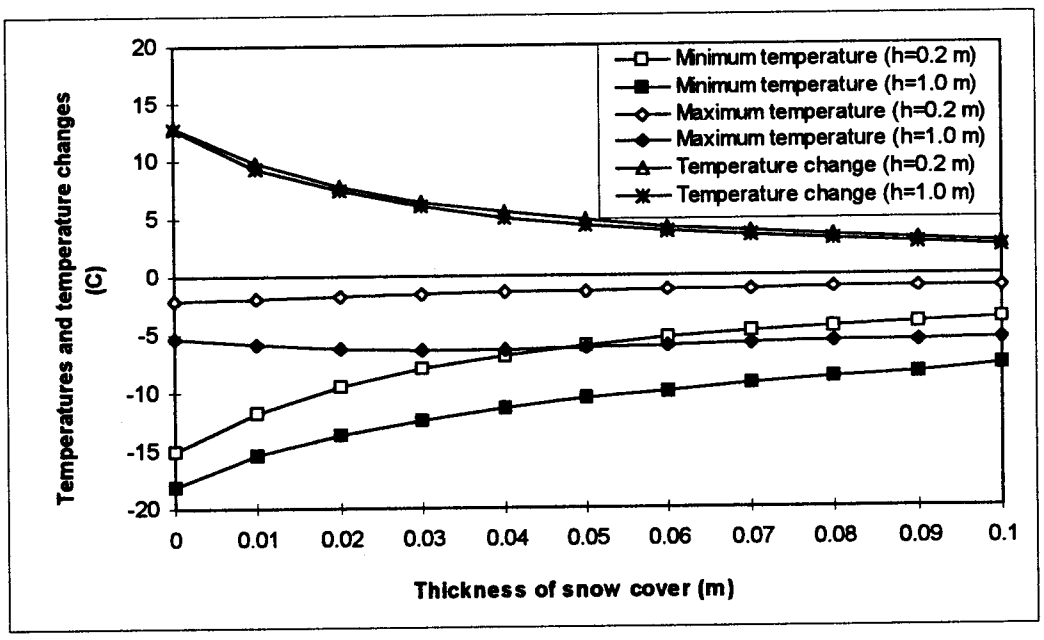

Figure 6.4 - Effect of the snow cover on maximum, minimum, and change of ice surface temperature.

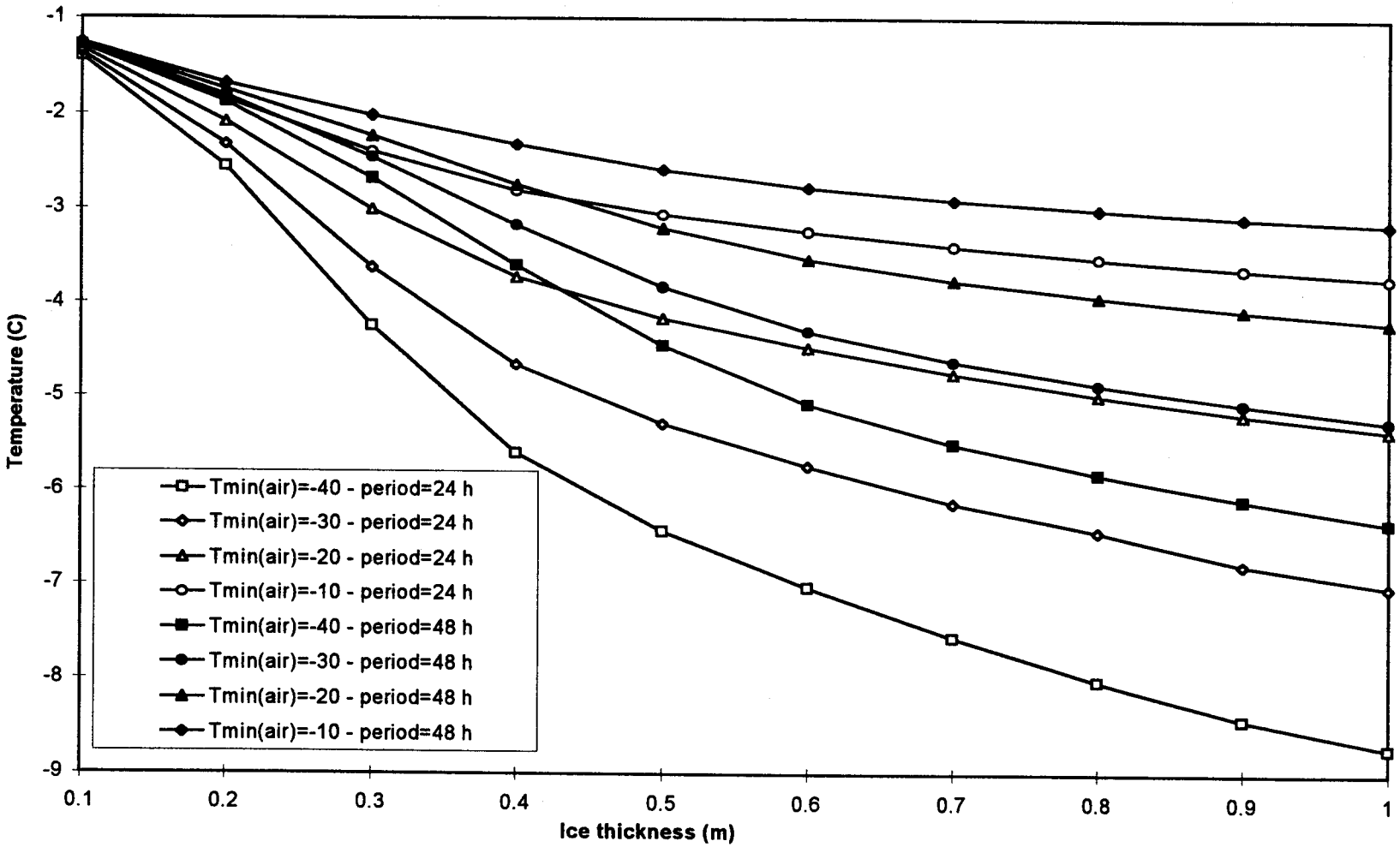

Figure 6.5 - Maximum ice surface temperature versus ice thickness for different amplitudes and periods of air temperature variation.

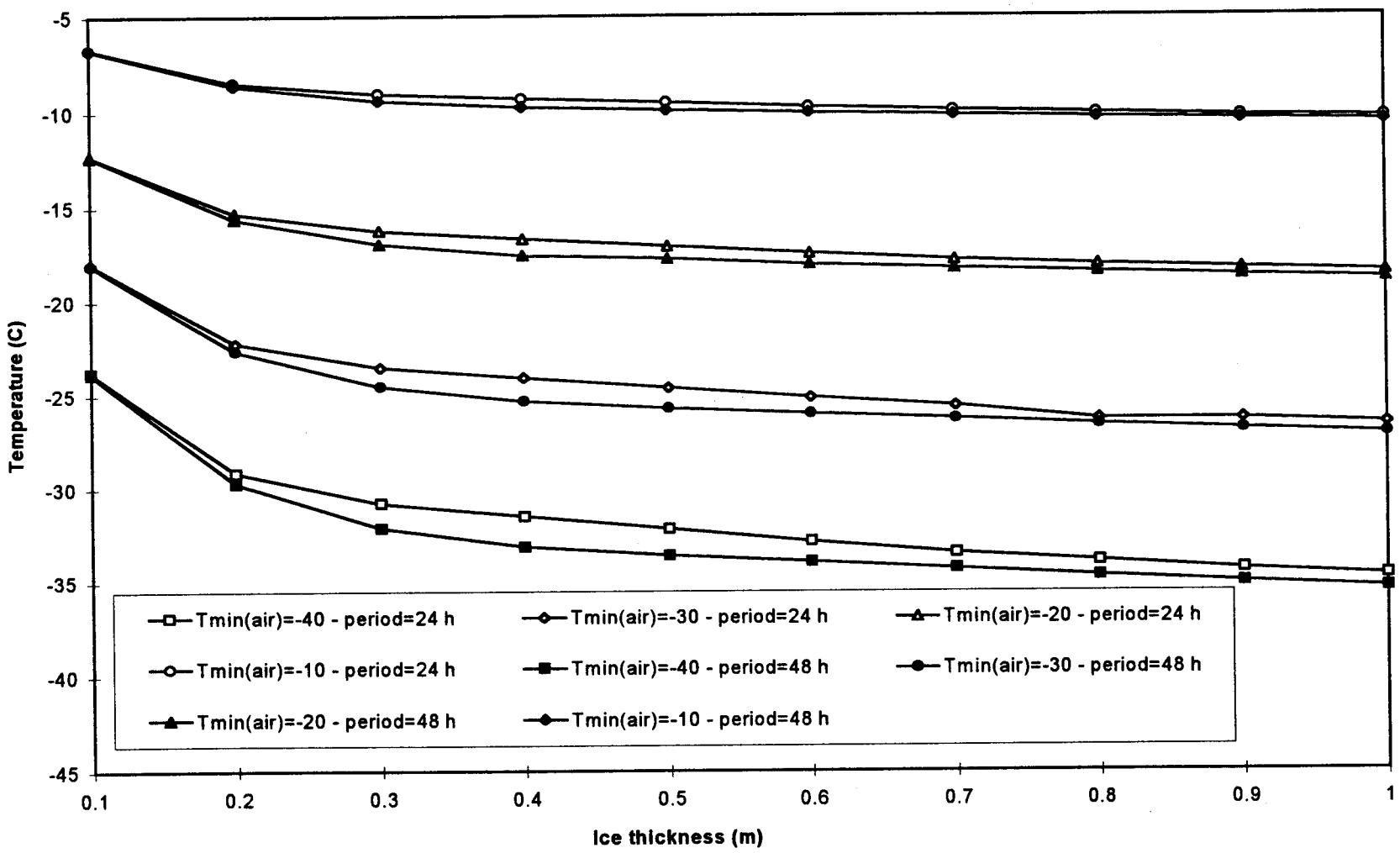

Figure 6.6 - Minimum ice surface temperature versus ice thickness for different amplitudes and periods of air temperature variation.

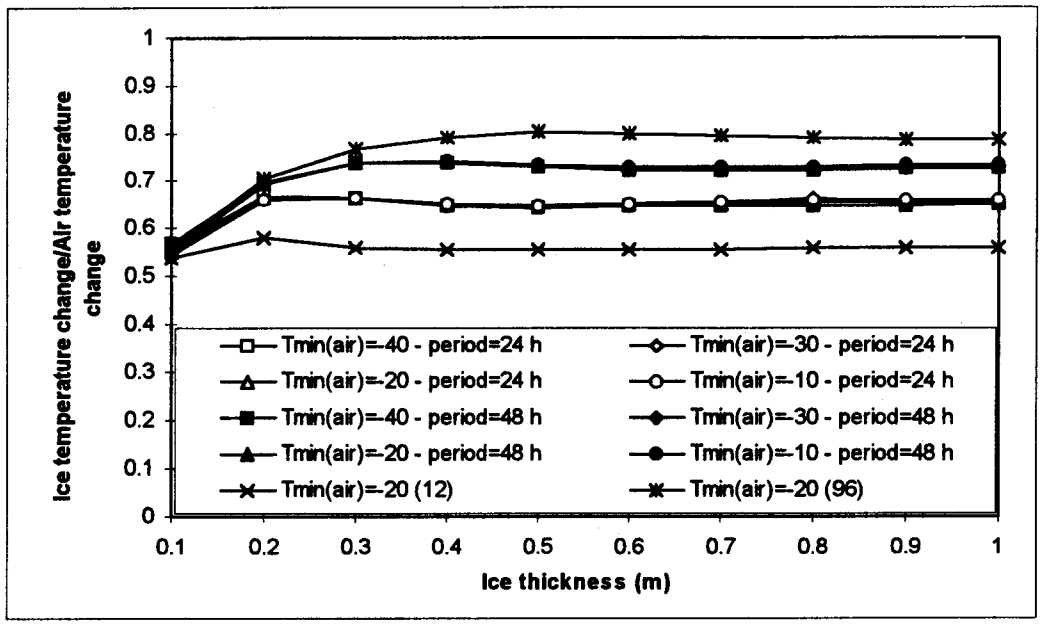

Figure 6.7 - Maximum normalized change in ice surface temperature versus ice thickness, for different amplitudes and periods of temperature increase.

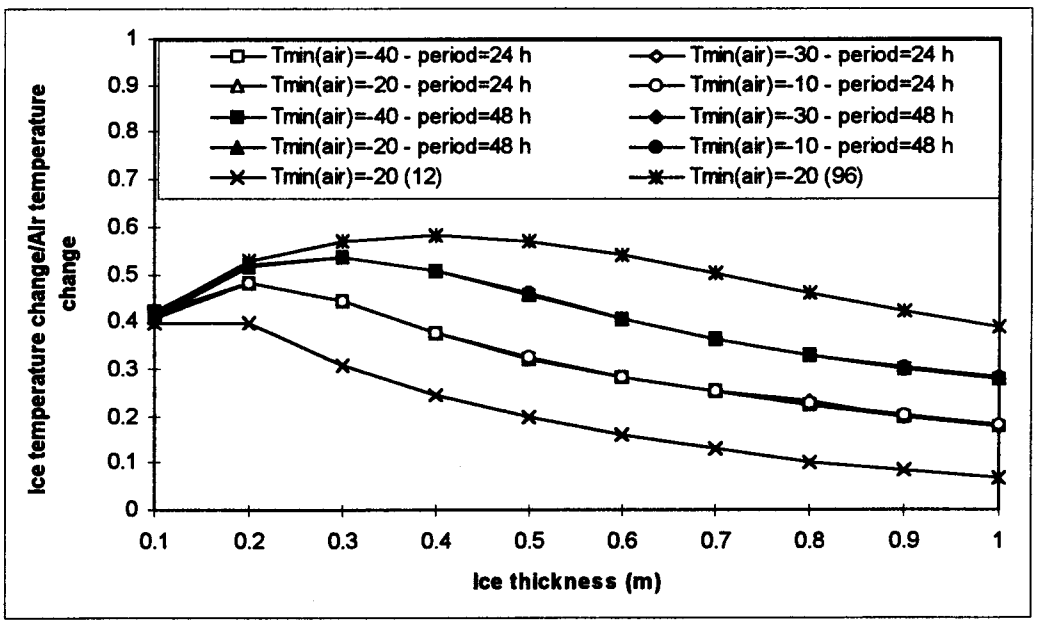

Figure 6.8 - Maximum normalized change in temperature at 1/4 depth of the ice cover, for different amplitudes and periods of air temperature variation.

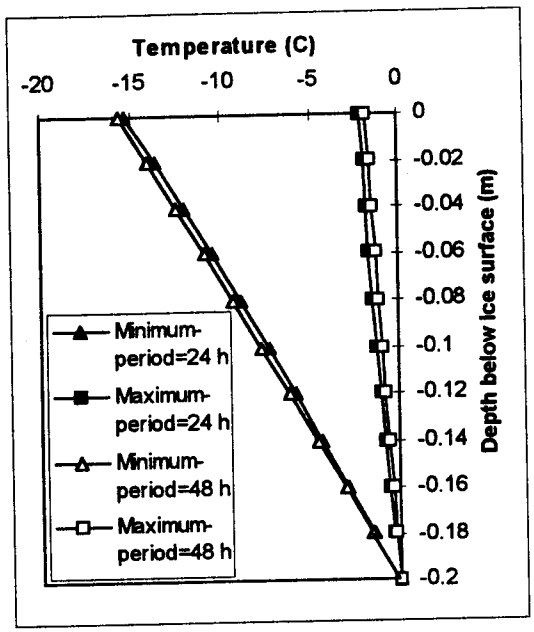

a)Temperature profiles (h = 0.2 m)

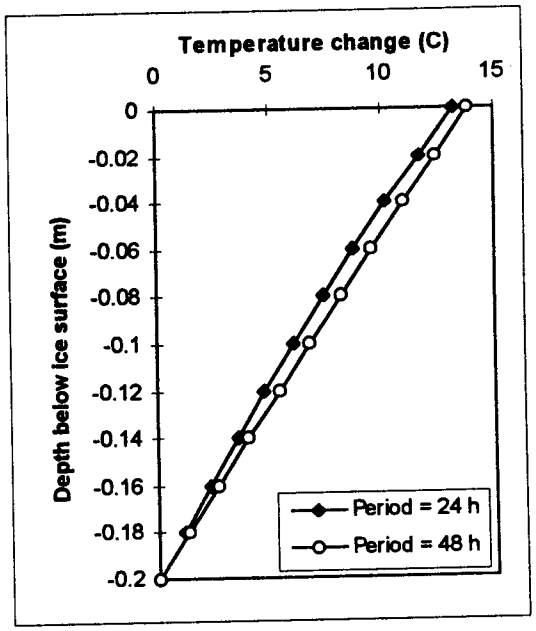

b)Change in temperatures (h = 0.2 m)

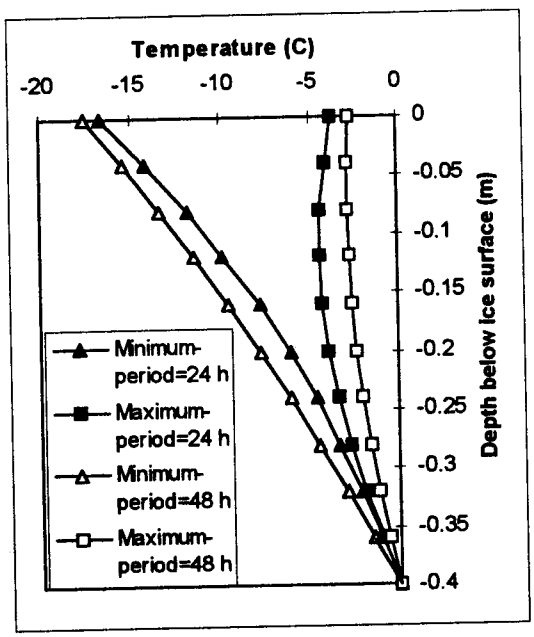

c)Temperature profiles (h = 0.4 m)

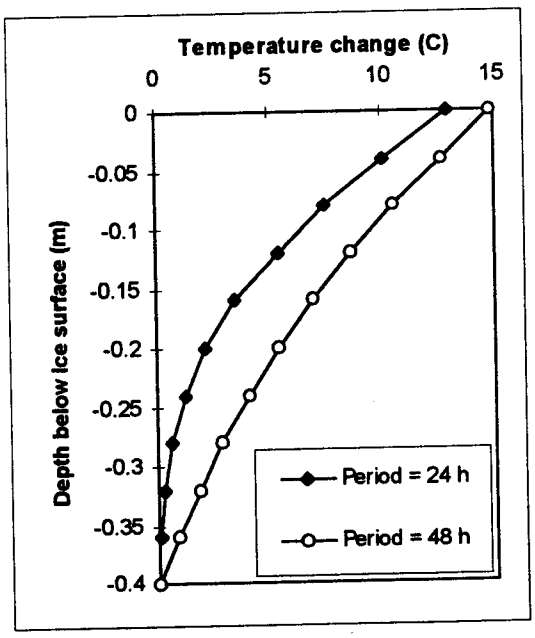

d)Change in temperatures (h = 0.4 m)

Figure 6.9 - Temperature profiles at the time of maximum and minimum surface temperatures, and temperature changes through the thickness of ice cover (continued on next page).

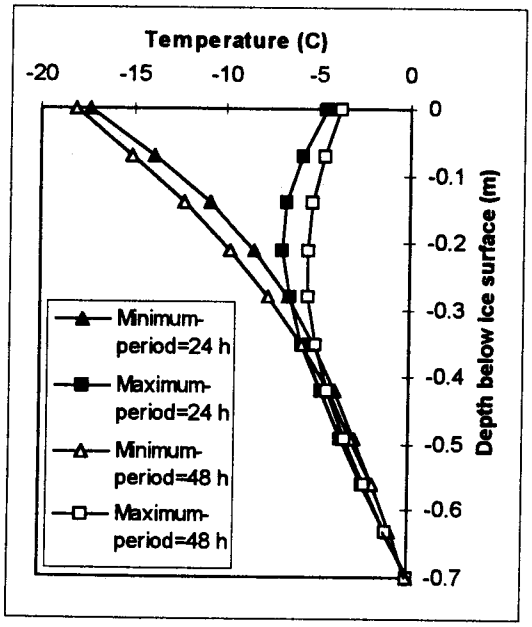

e)Temperature profiles (h = 0.7 m)

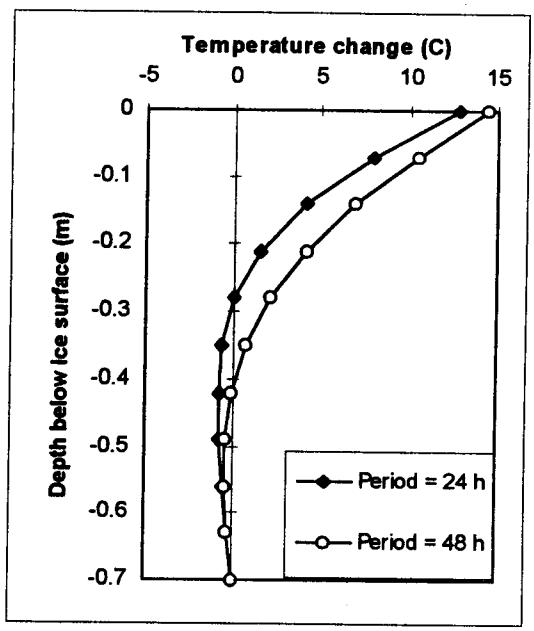

f)Change in temperatures (h = 0.7 m)

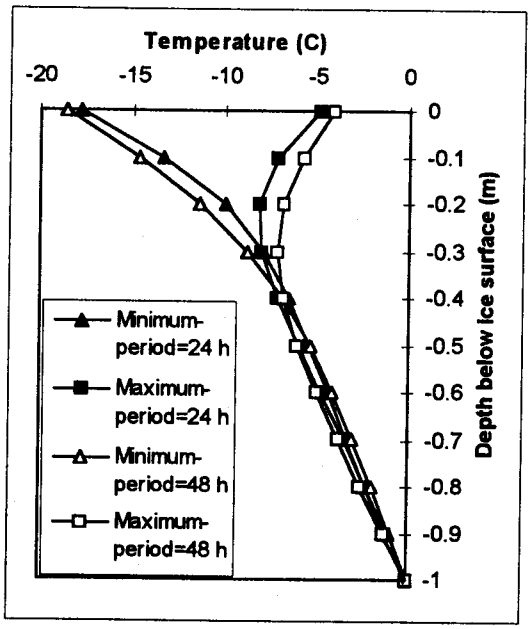

g)Temperature profiles (h = 1.0 m)

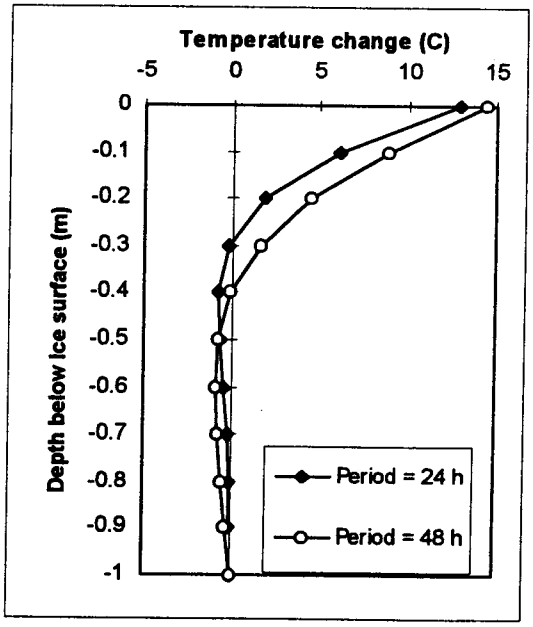

h)Change in temperatures (h = 1.0 m)

Figure 6.9 - Temperature profiles at the time of maximum and minimum surface temperatures, and temperature changes through the thickness of ice cover (continued from previous page).

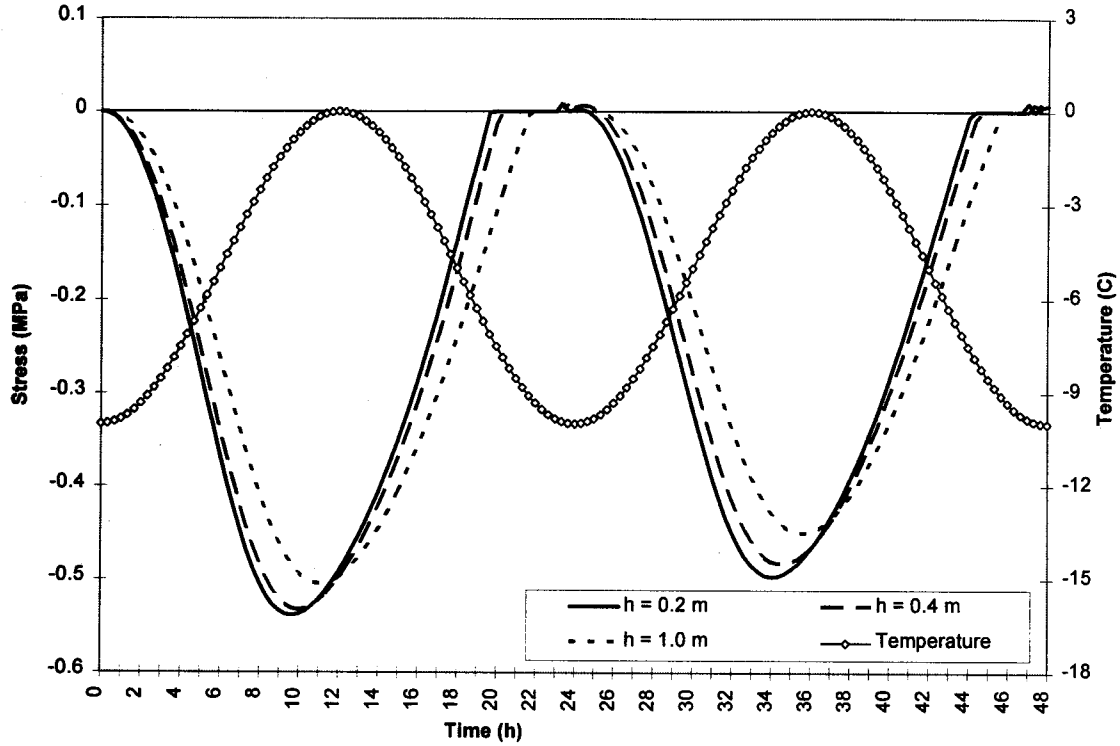

Figure 6.10- Stresses in the top layers for ice covers with different thicknesses.

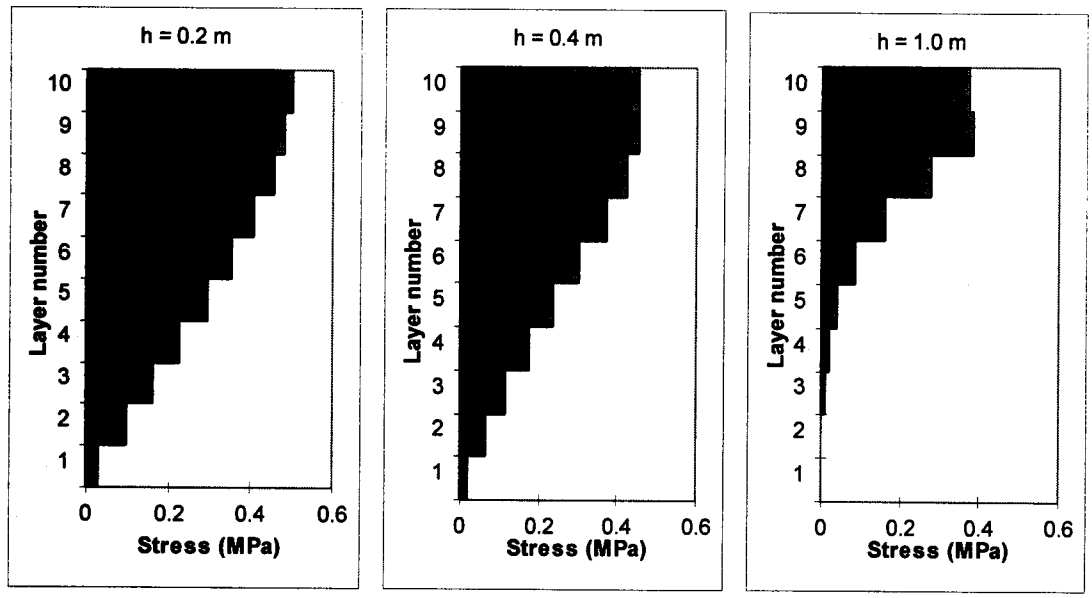

Figure 6.11 - Stress distribution through the thickness of the ice cover for three different thicknesses.

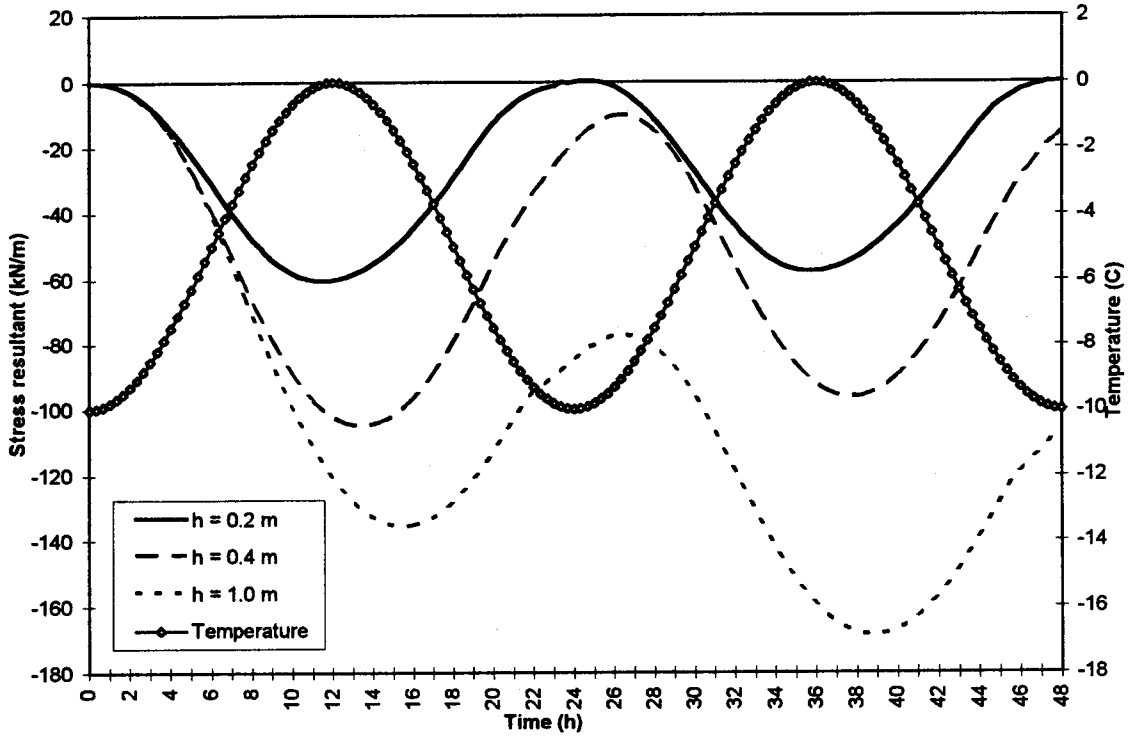

Figure 6.12 - Stress resultant versus time for ice covers with different thicknesses.

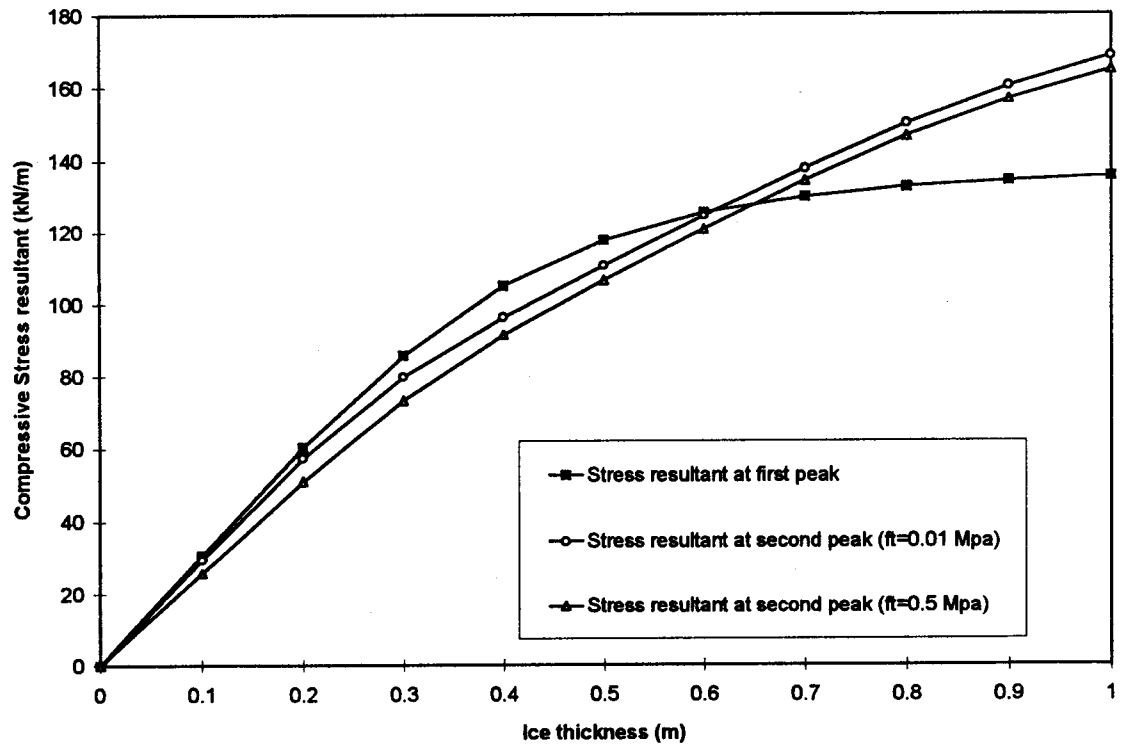

Figure 6.13 - Maximum stress resultant versus thickness of the ice cover.

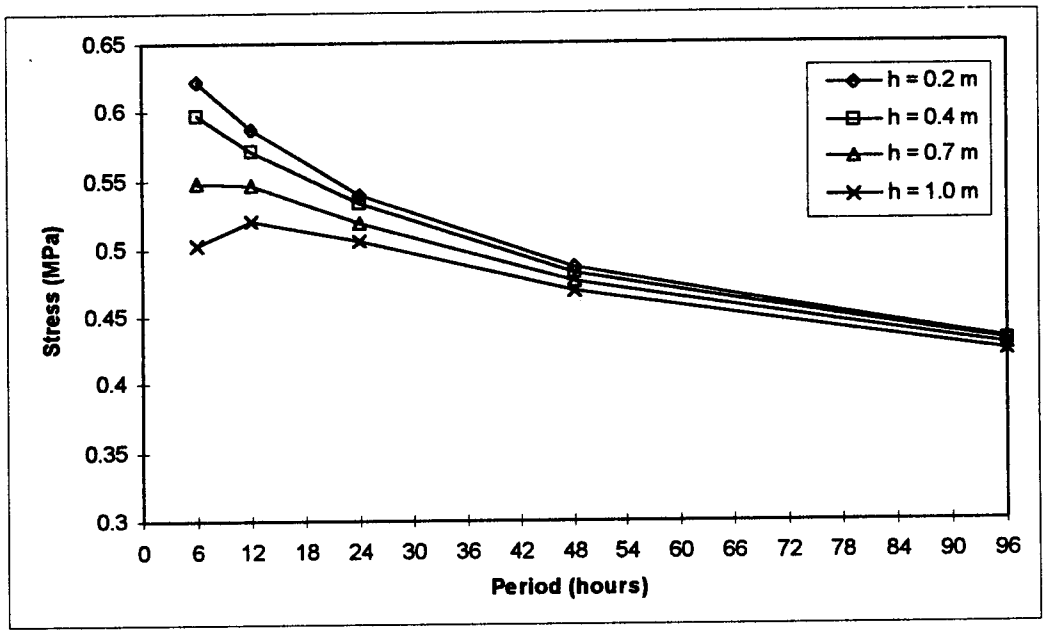

Figure 6.14 -Maximum stress in the top layer versus period of temperature increase for different ice thicknesses

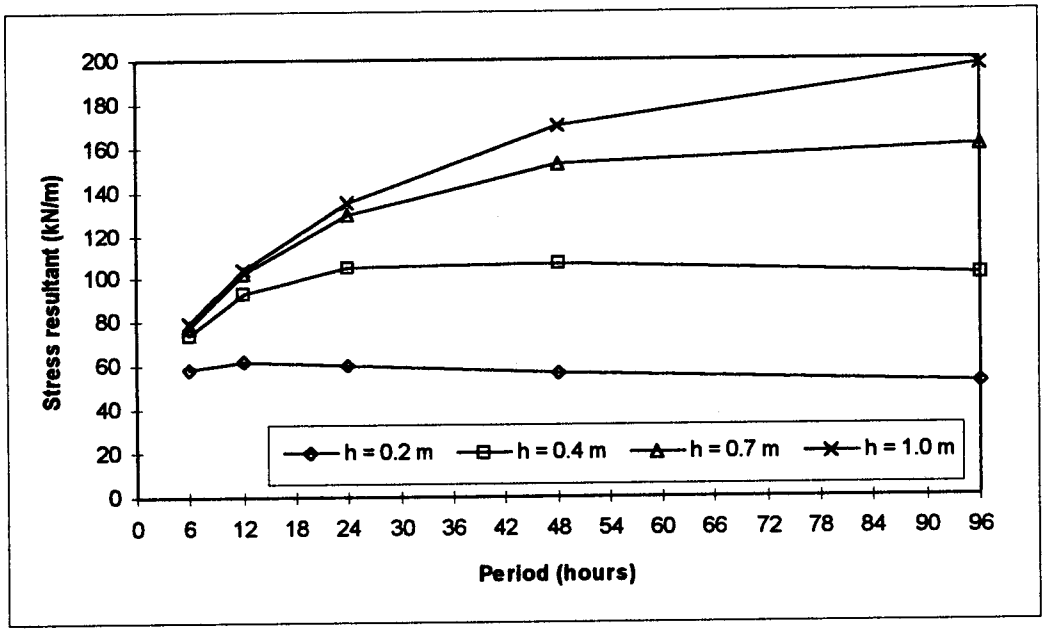

Figure 6.15 - Maximum stress resultant versus period of temperature increase for different ice thicknesses.

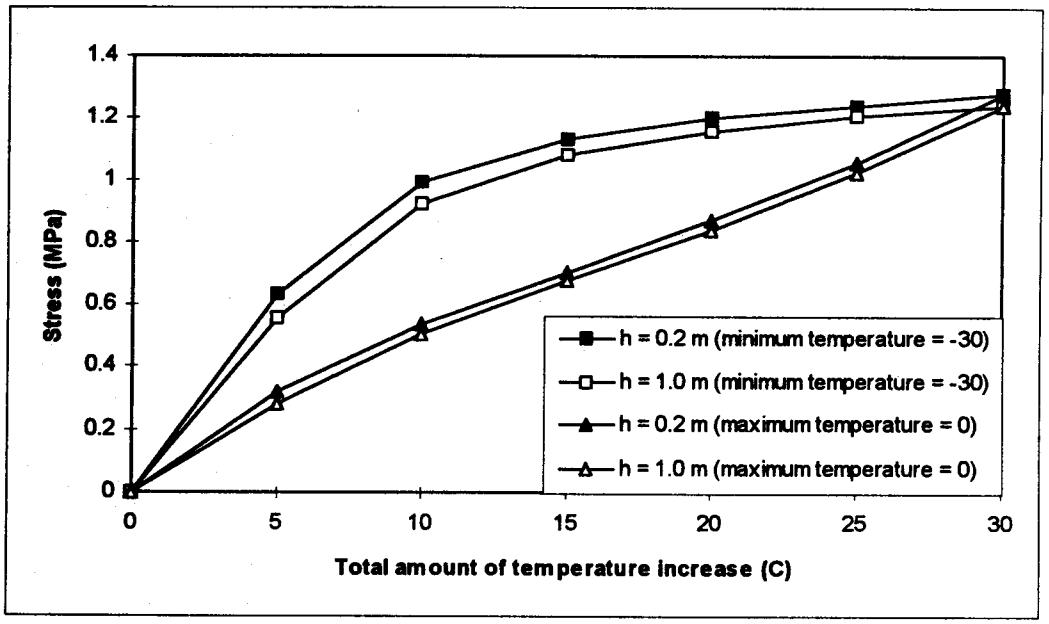

Figure 6.20 - Maximum stress in the top layer versus total amount of temperature increase.

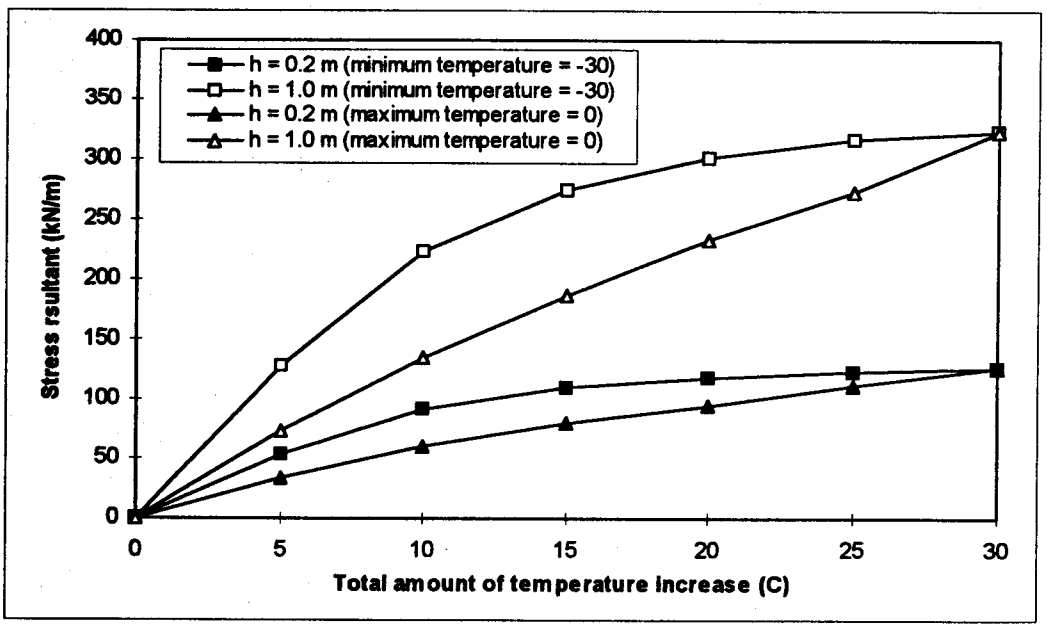

Figure 6.21 - Maximum stress resultant versus total amount of temperature increase.

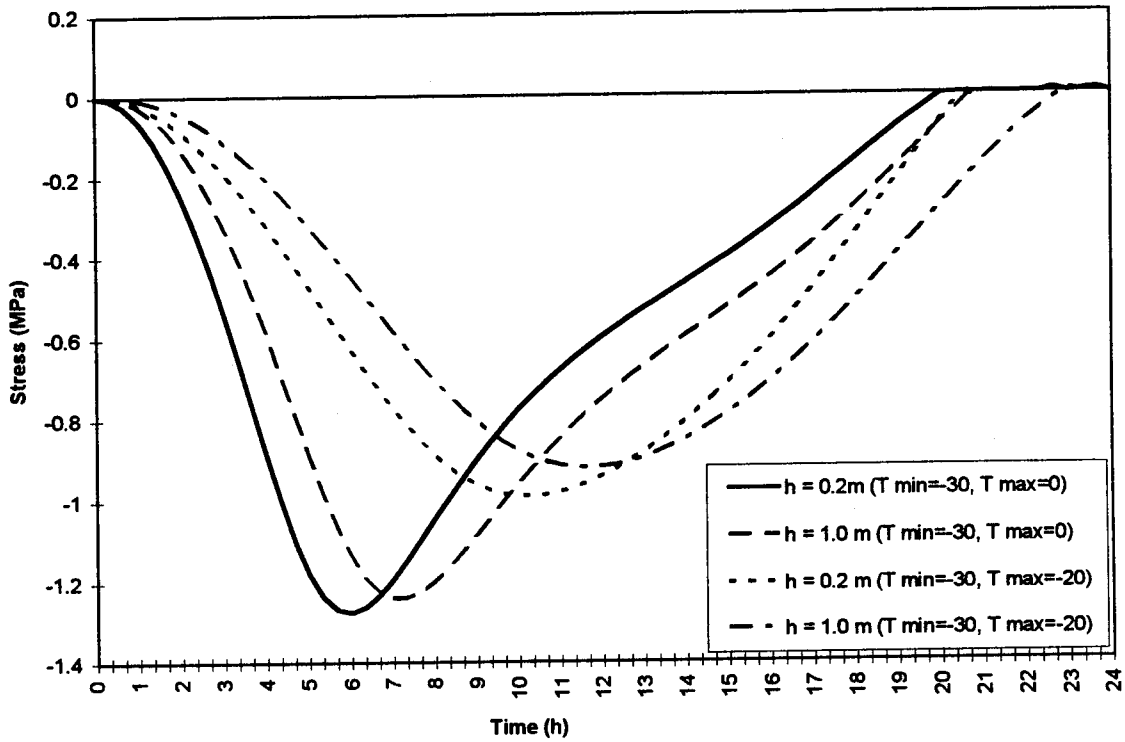

Figure 6.22 - Stress in the top layer for different amplitudes of temperature increase.

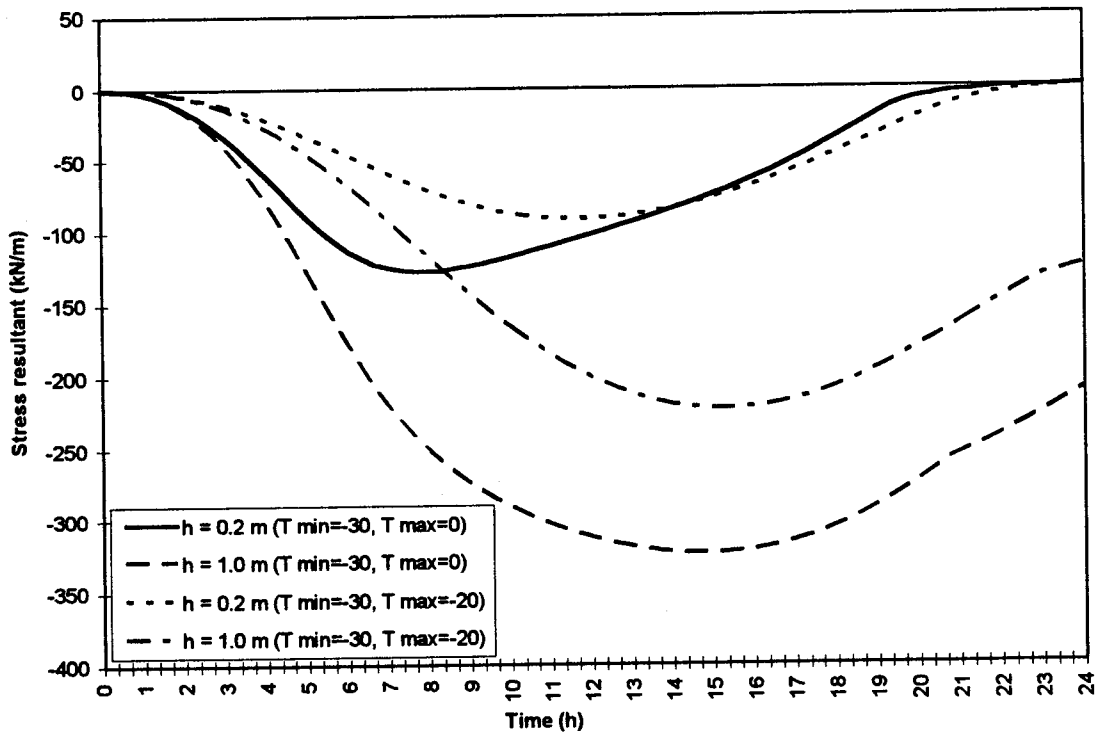

Figure 6.23 - Stress resultants for different amplitudes of temperature increase.

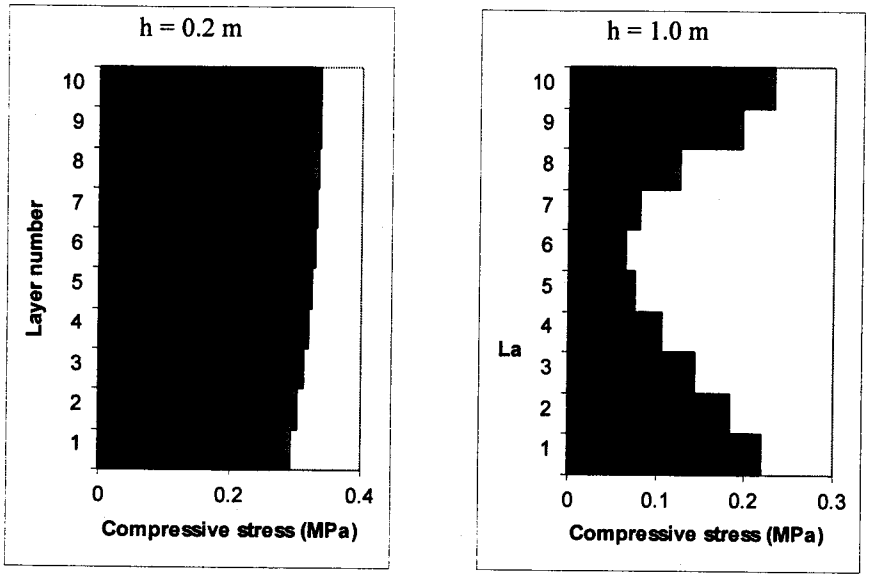

Figure 6.24 - Stress distribution through the thickness near the center of a circular ice plate with free rotation at the edges (r = 3.0 m).

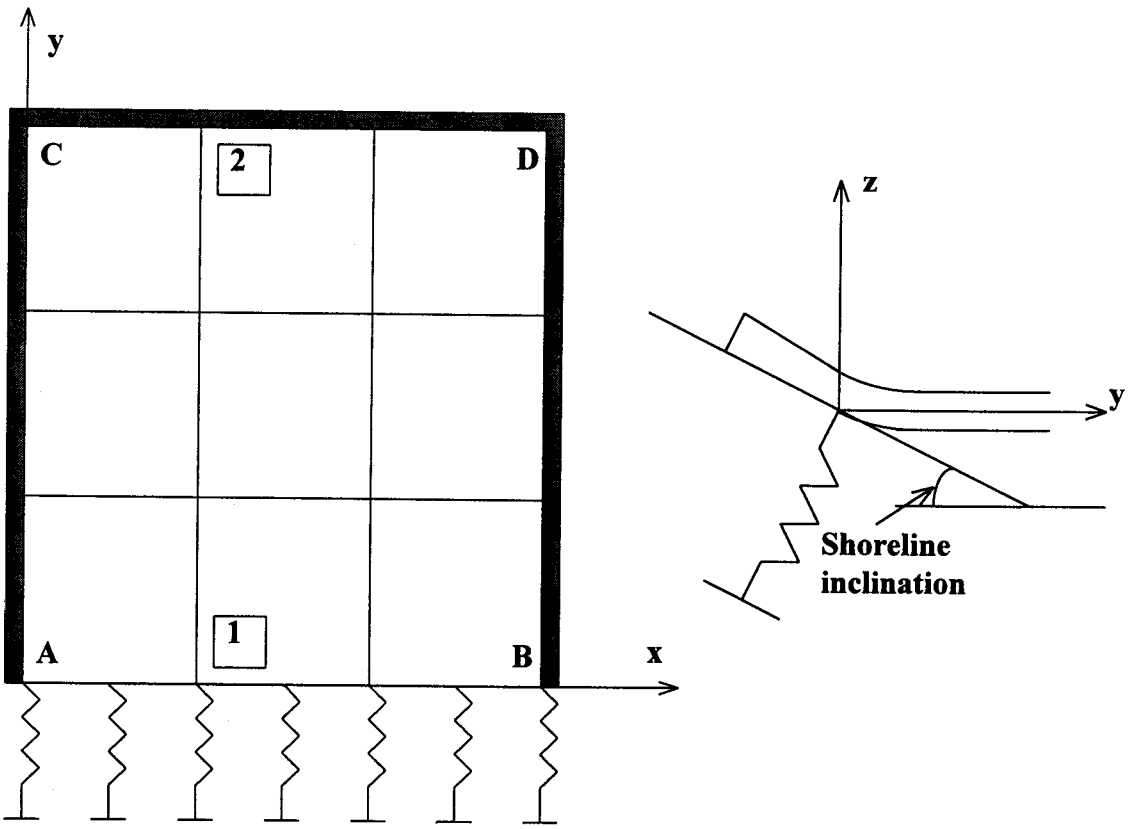

Figure 6.25 - Finite element mesh for studying different shore types.

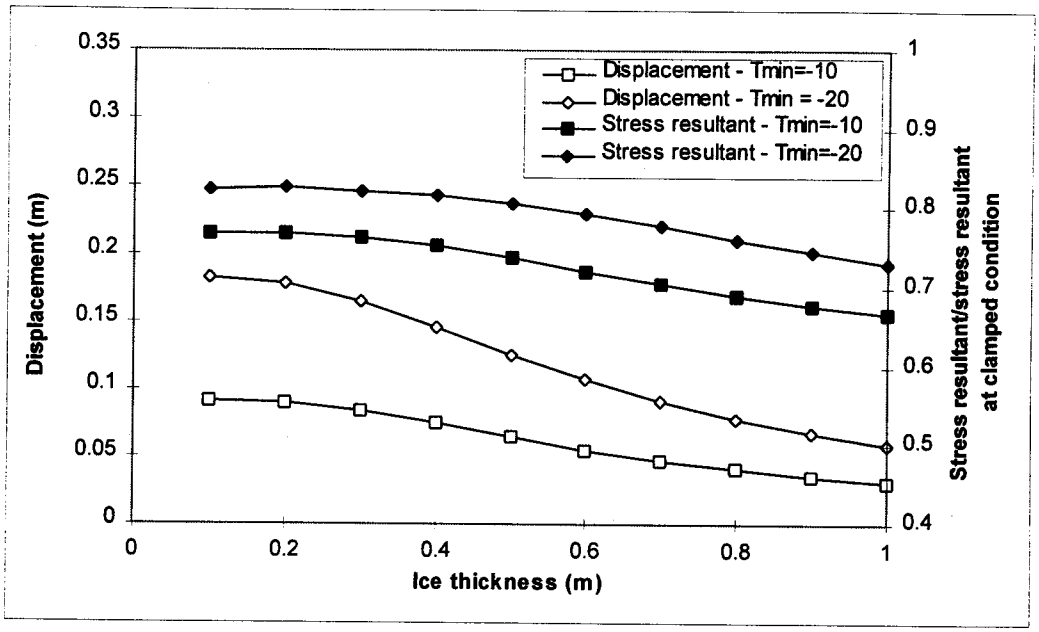

Figure 6.26 - Maximum displacement at a flat shore (near location 1 in Fig. 6.25) and maximum normalized stress resultant at location 2 in Fig 6.25, versus ice thickness.

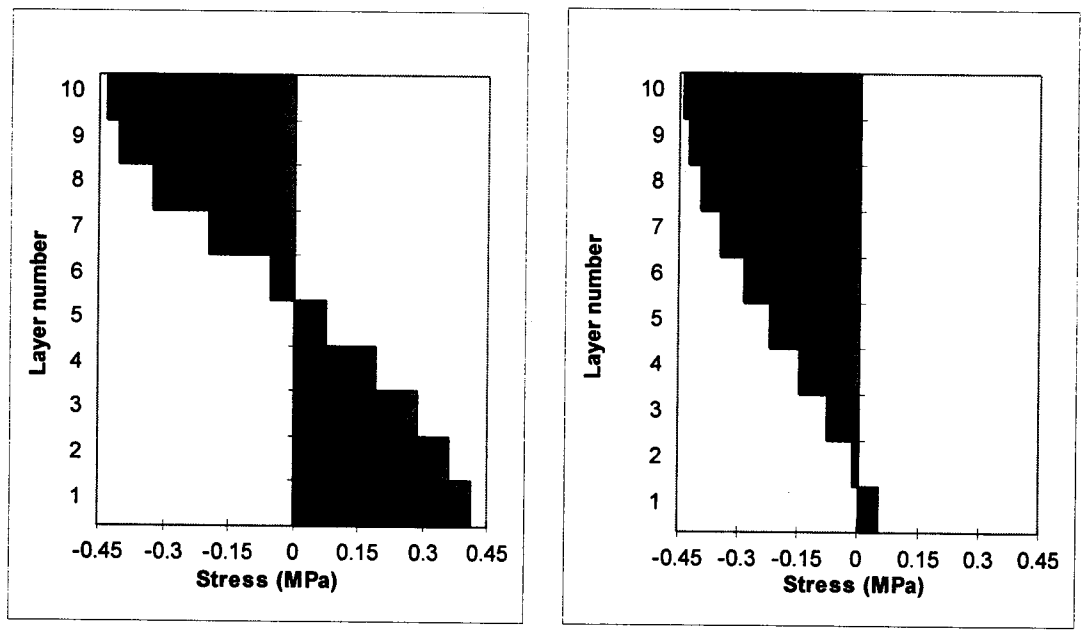

a)h=0.2 m,θ_{min} =-20, time=13 h, location 1. b) h=0.2 m, θ_{min}=-10, time=13 h, location 2.

Figure 6.27 - Stress distribution through the thickness of the ice cover at locations 1 and 2 in Fig. 6.25 (continued on next page).

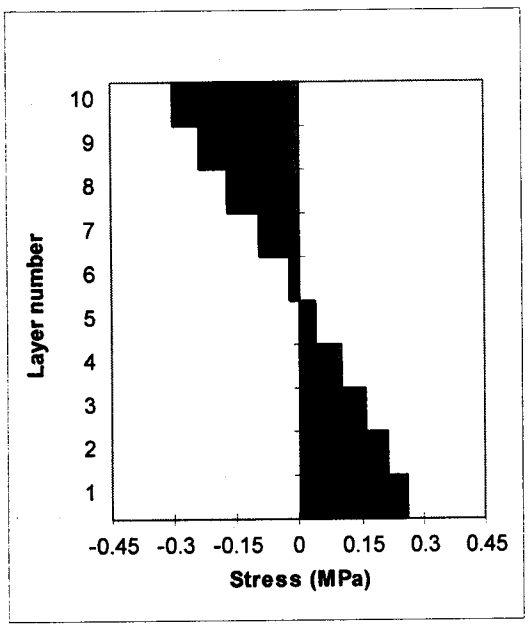

c)h=0.2 m,θ_{min} =-10, time=13 h, location 1.

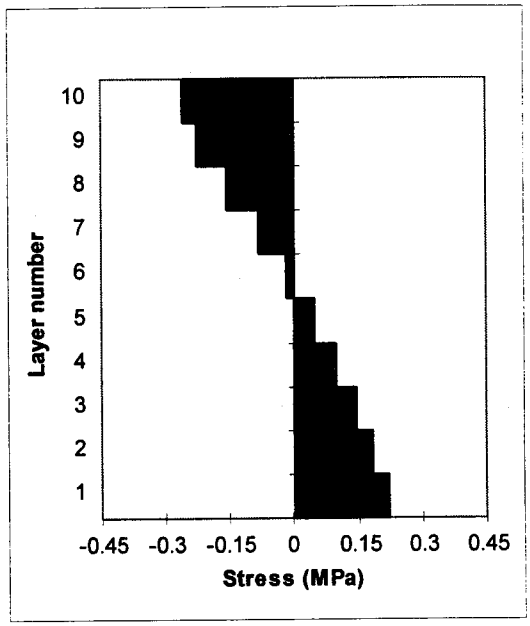

d)h=0.4 m, θ_{min} =-10,time=15 h, location 1.

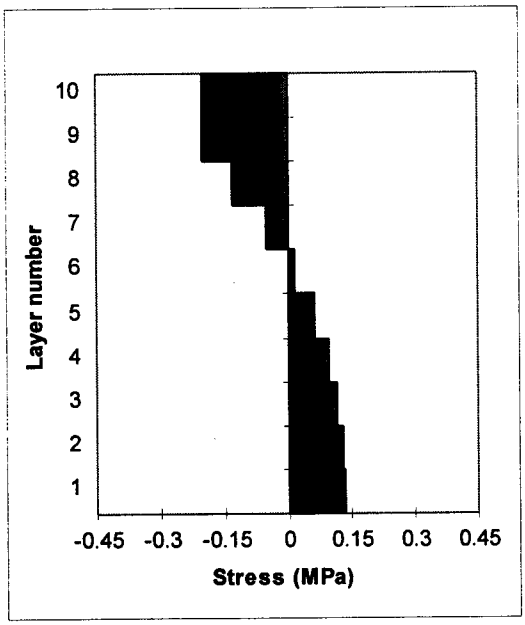

e)h=0.7 m, θ_{min} =-10, time=17 h, location 1.

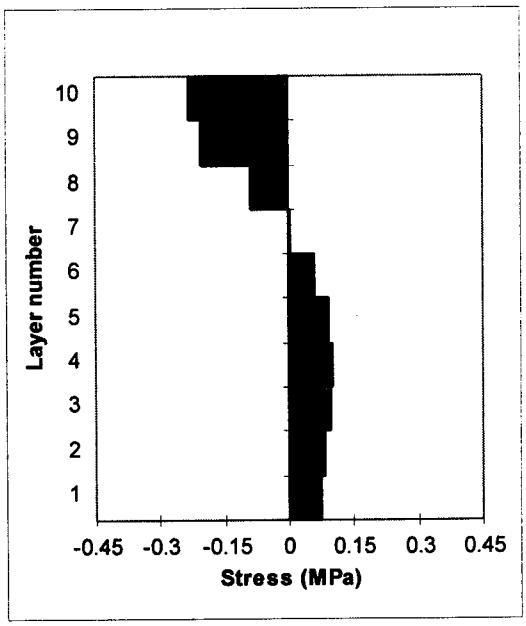

f)h=1.0 m, θ_{min} =-10, time=17 h, location 1.

Figure 6.27 - Stress distribution through the thickness of the ice cover at locations 1 and 2 in Fig. 6.25 (continued from previous page).

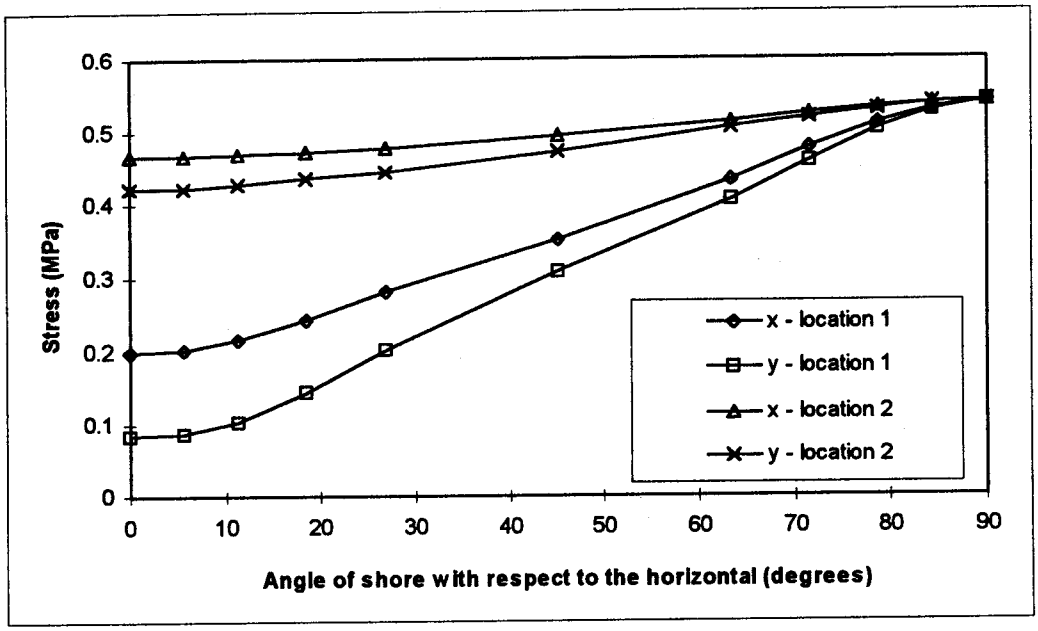

Figure 6.28 - Maximum stress in the top layer versus angle of shore with respect to the horizontal.

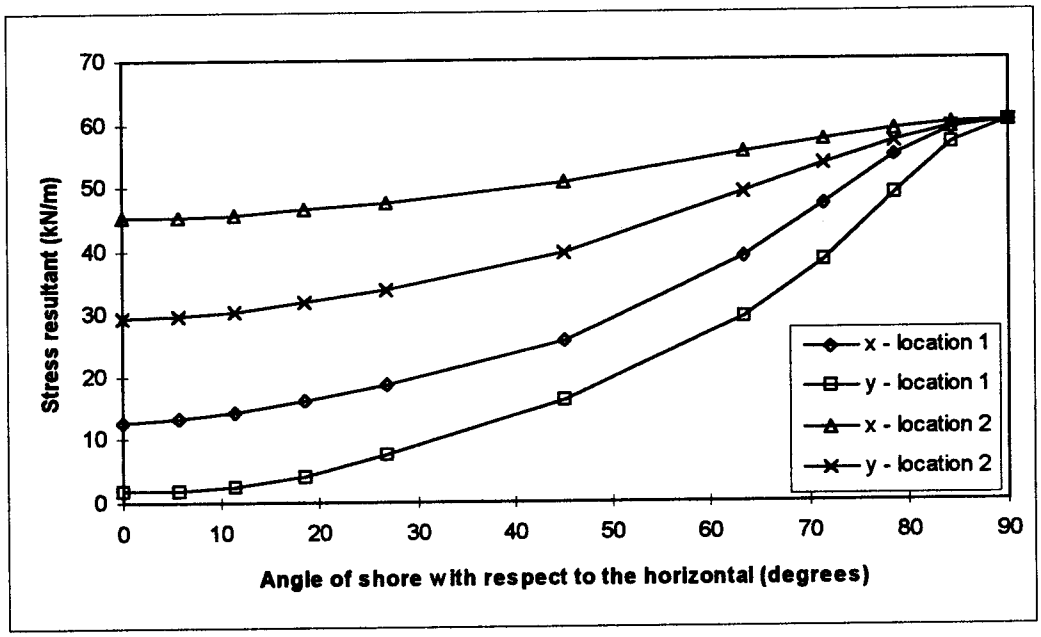

Figure 6.29 - Maximum stress resultant versus angle of shore with respect to the horizontal.

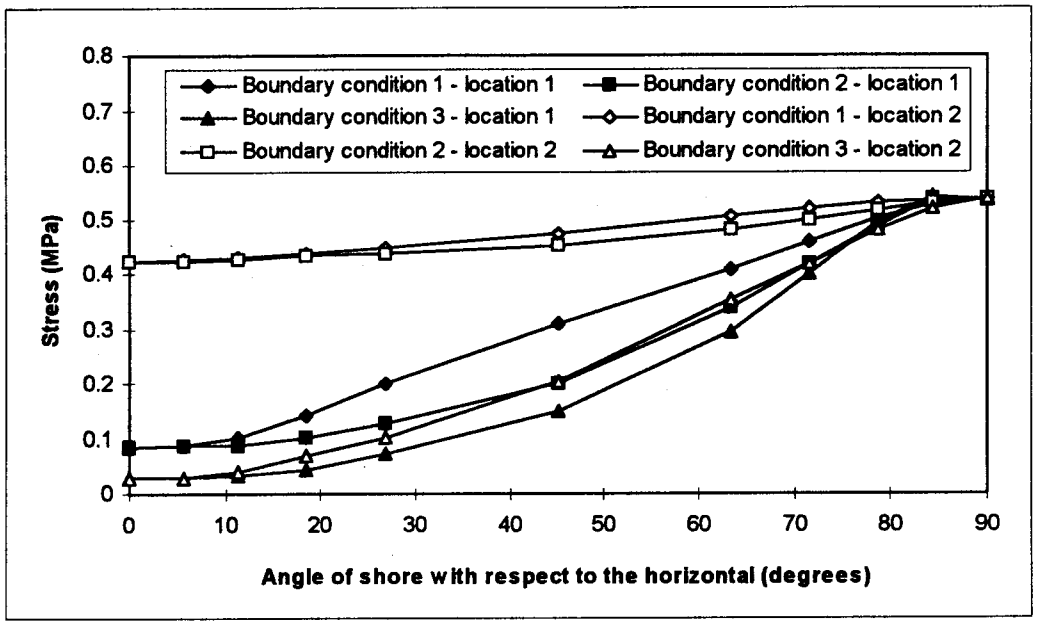

Figure 6.30 - Maximum stress in the top layer for different angles of shore with respect to the horizontal and different boundary conditions.

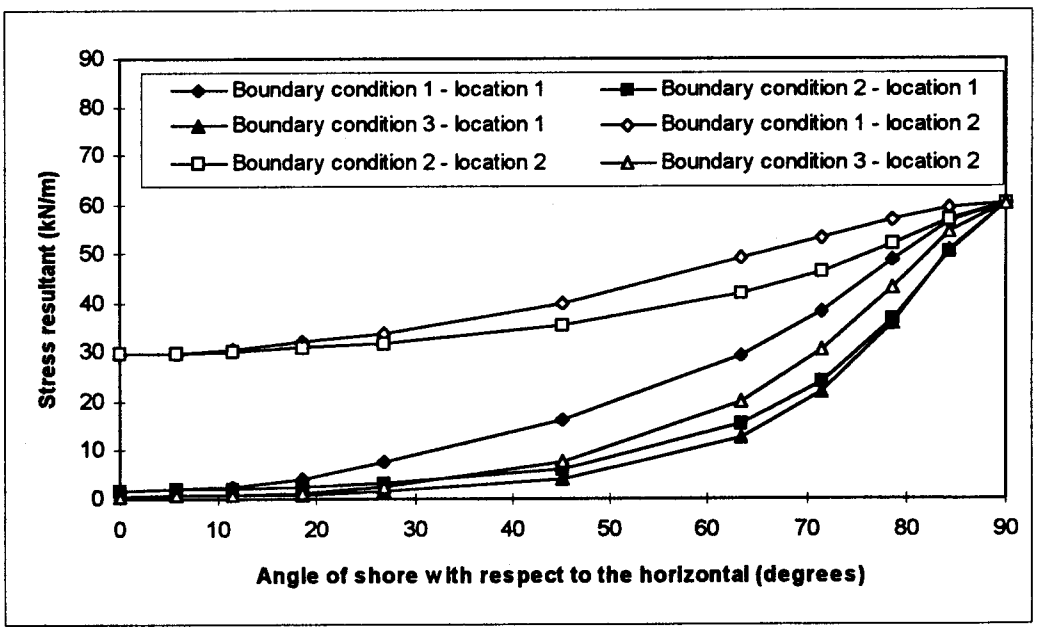

Figure 6.31 - Maximum stress resultant for different angles of shore with respect to the horizontal and different boundary conditions.

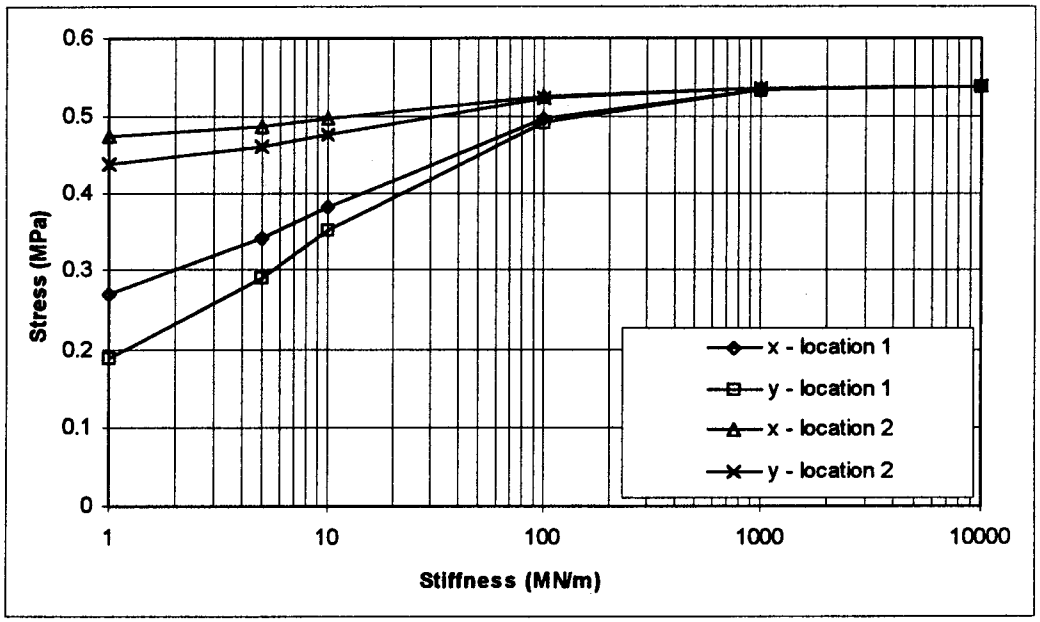

Figure 6.32 - Effect of the stiffness of the resisting structure on the maximum stress in the top layer.

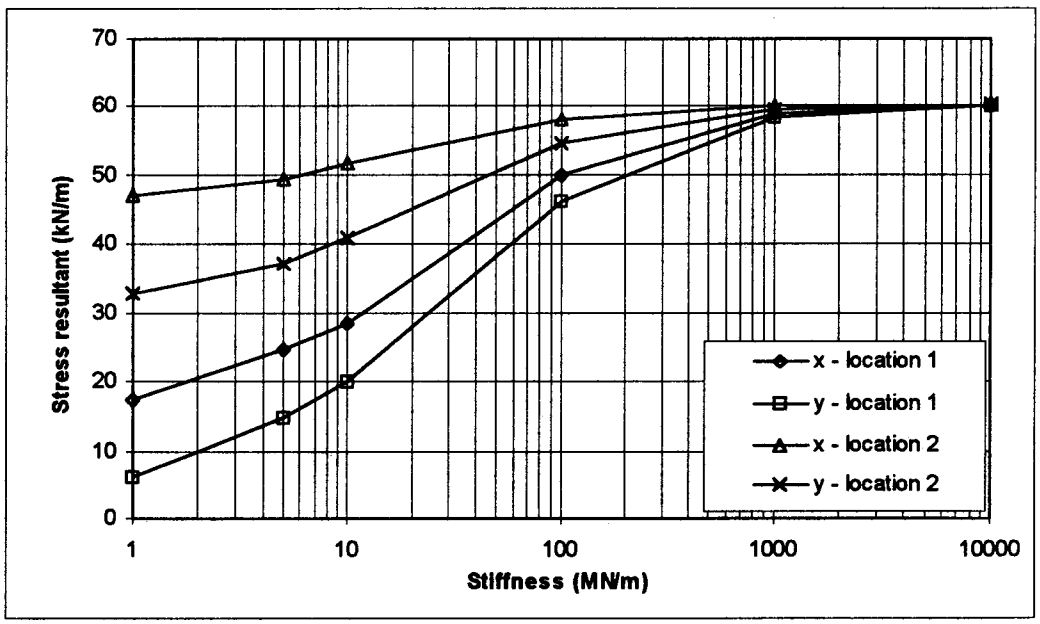

Figure 6.33 - Effect of the stiffness of the resisting structure on the maximum stress resultant.

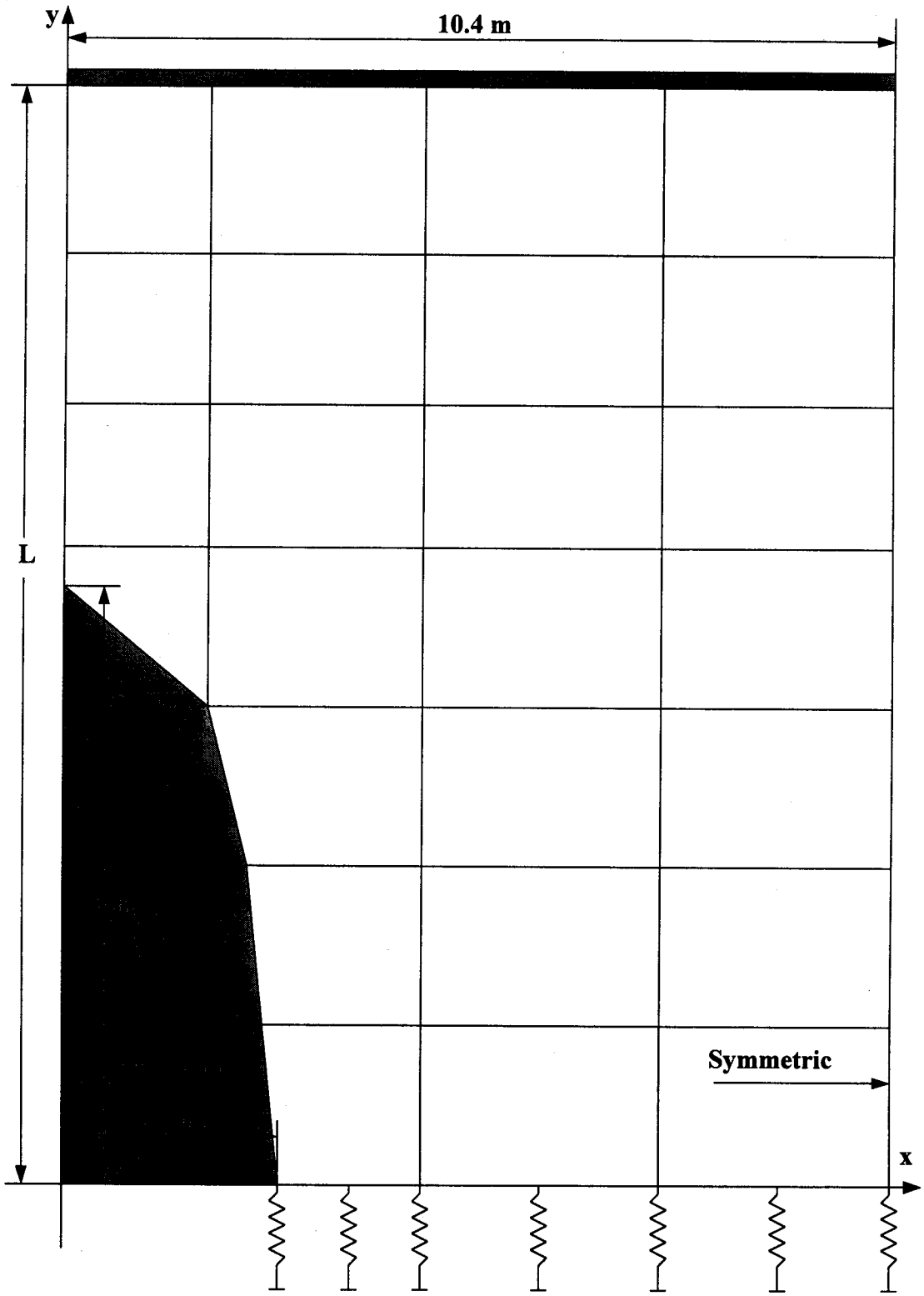

Figure 6.34 - Finite element mesh of the ice cover in the vicinity of the Paugan Dam spillway.

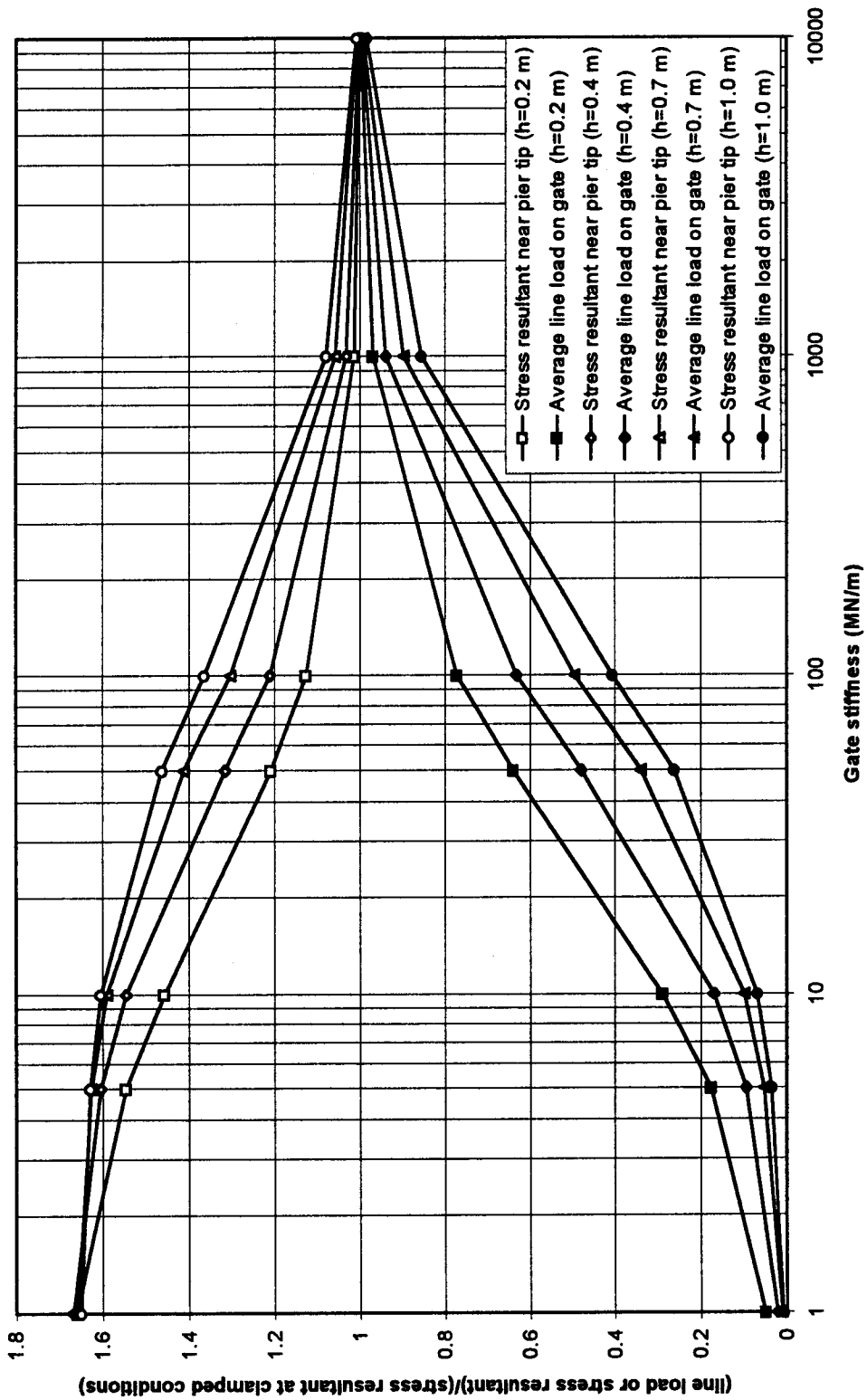

Figure 6.35 - Normalized maximum average line load on the gate and normalized maximum stress resultant near the pier tip for different ice thicknesses (θ_{min} = -10°C).

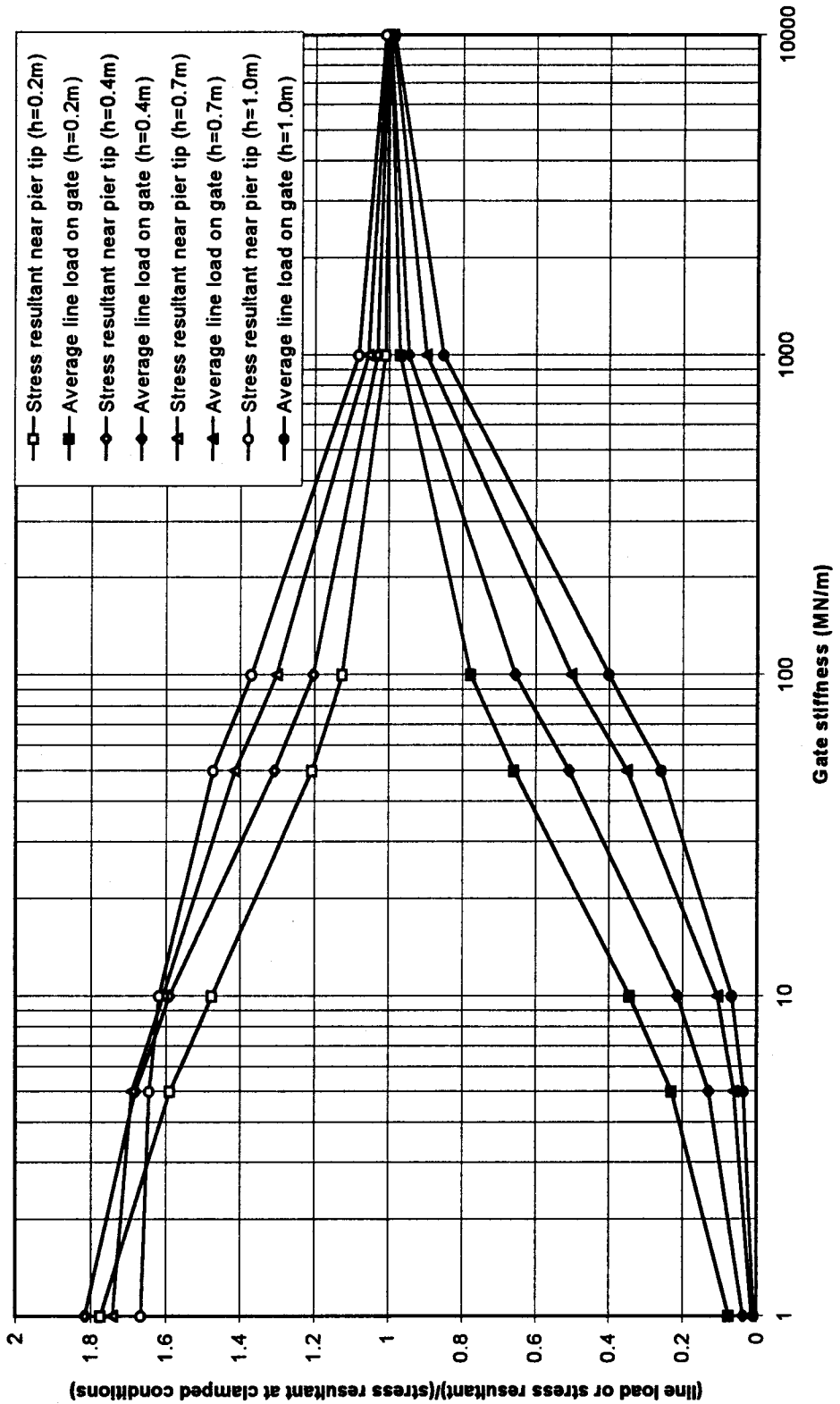

Figure 6.36 - Normalized maximum average line load on the gate and normalized maximum stress resultant near the pier tip for different ice thicknesses (θ_{min} = -20°C).

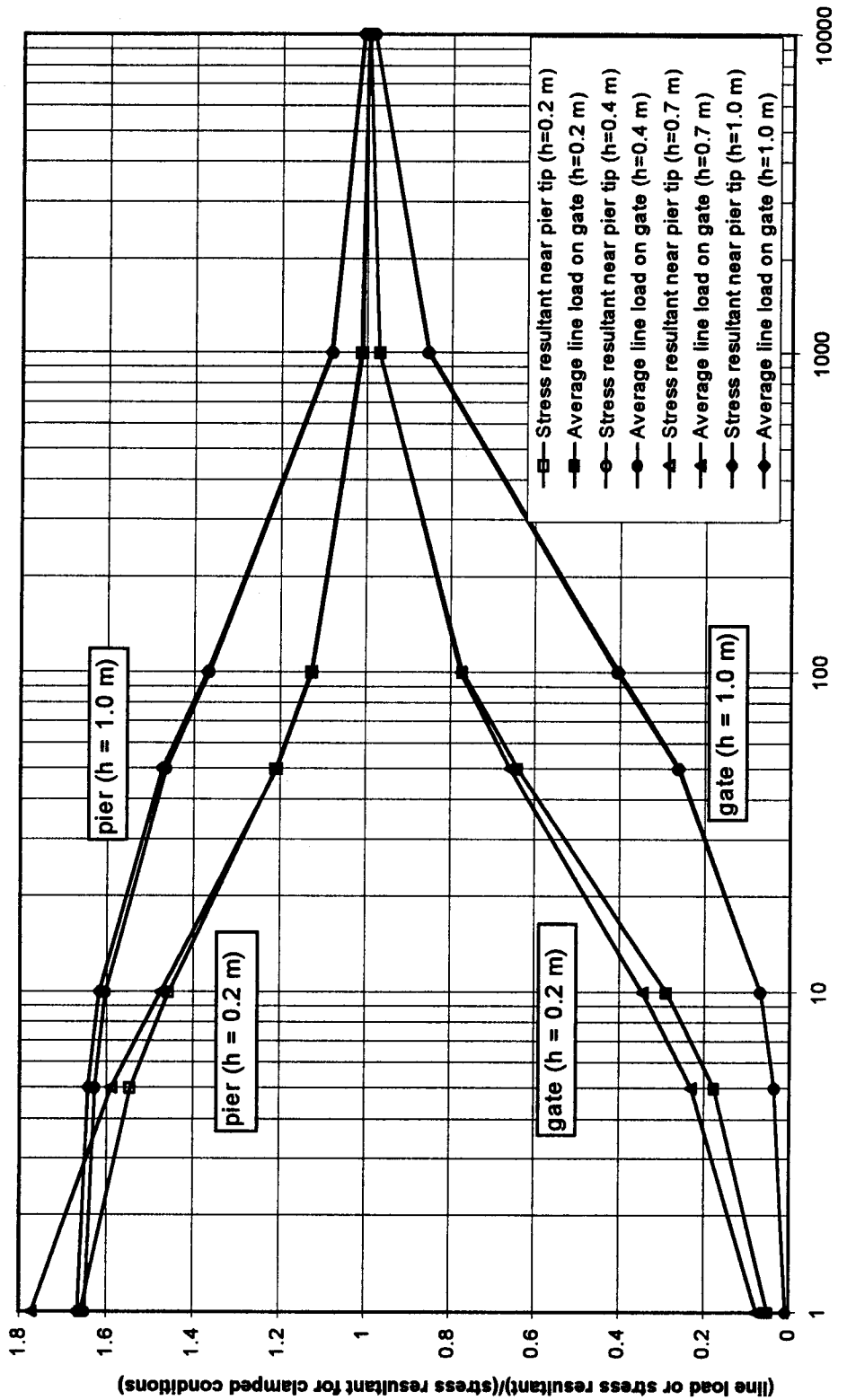

Figure 6.37 - Normalized maximum average line load on the gate and normalized maximum stress resultant near pier tip for different amplitude of temperature increase (θ_{min} = -10 and θ_{min} = -20).

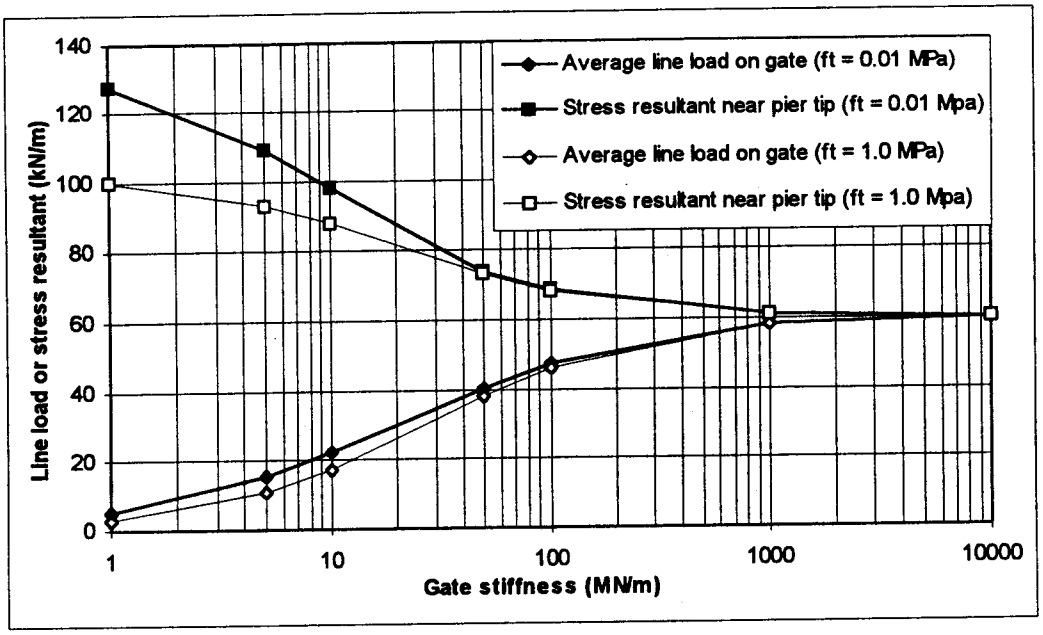

Figure 6.38 - Effect of tensile cracking on maximum average line load on the gate and maximum stress resultant near pier tip.(h = 0.3 m, $\theta_{min\ (air)}$ = -20°C).

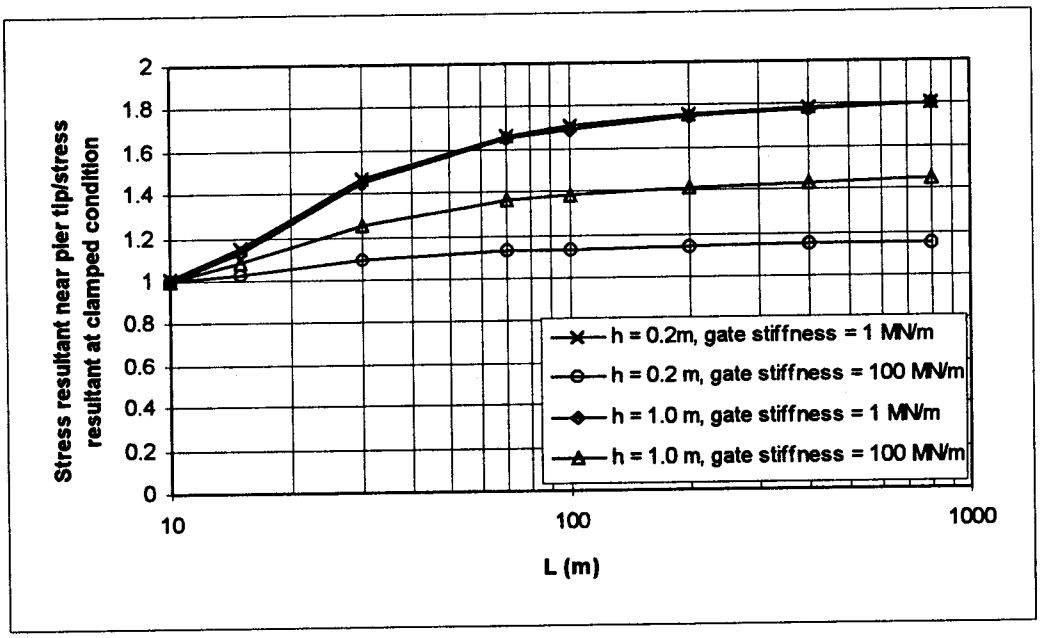

Figure 6.39 - Effect of length (L) in Fig. 6.34, on the maximum normalized stress resultant near pier tip, for different thicknesses and different gate stiffnesses.

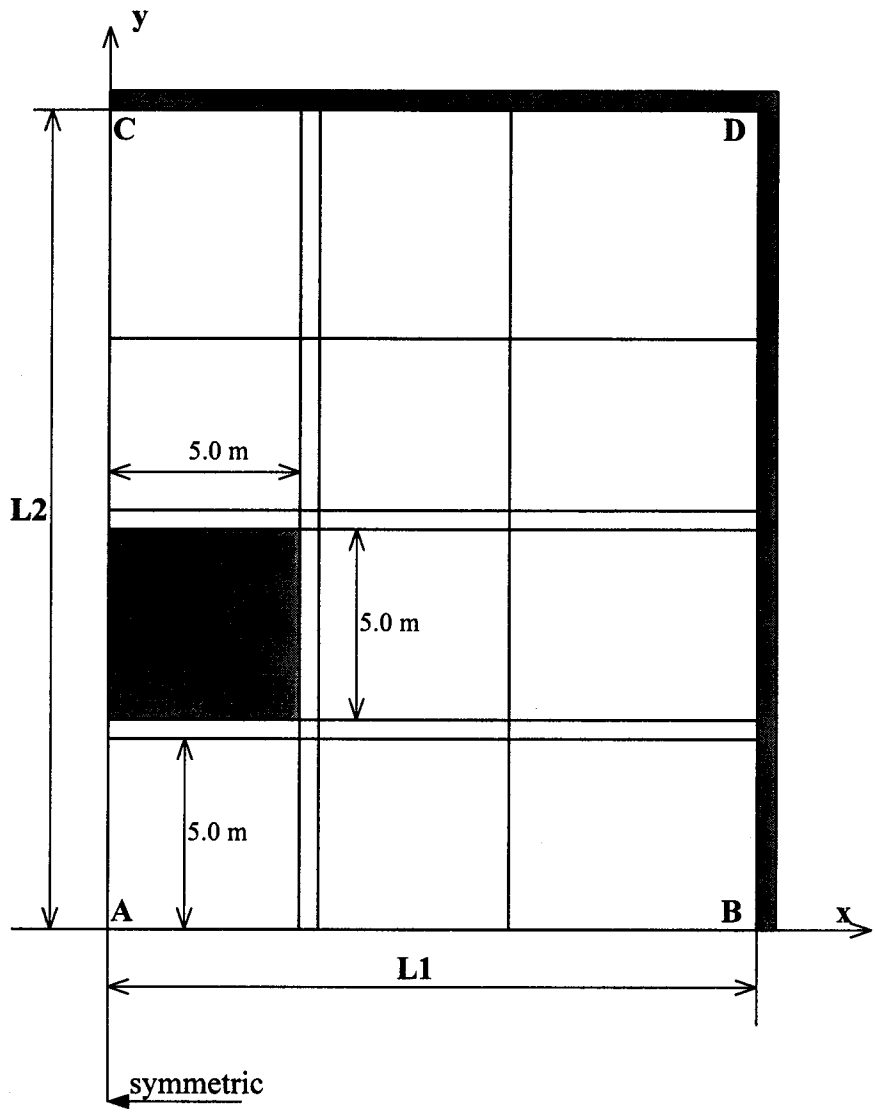

Fig.6.40 - Finite element mesh for analyzing isolated structure.

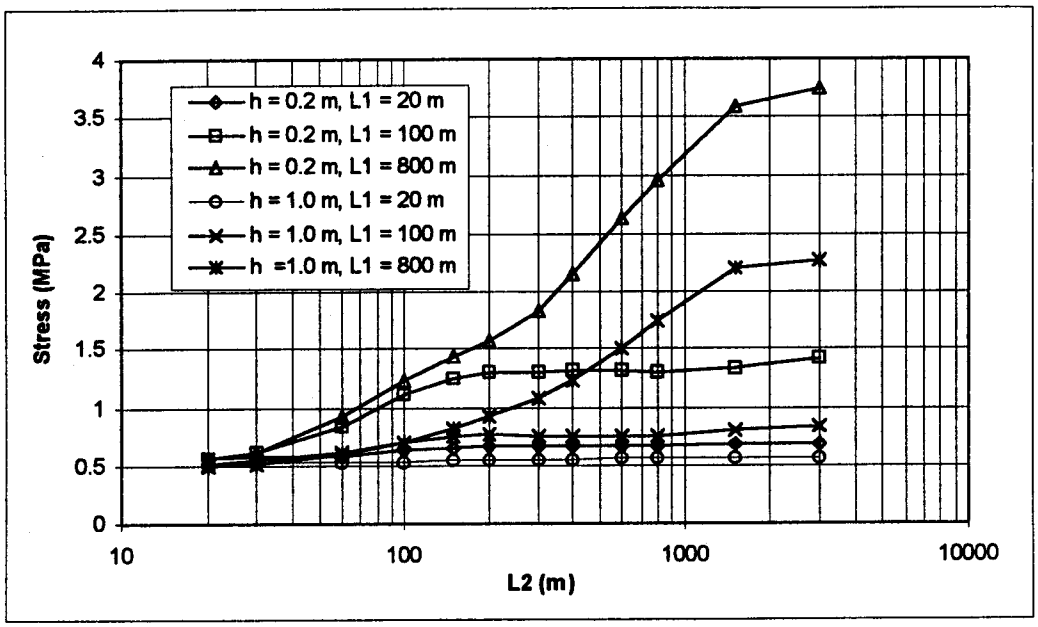

Figure 6.41 - Maximum stress at top layer in front of the isolated structure in Fig. 6.40 for different length of L1 and L2 and different thicknesses.

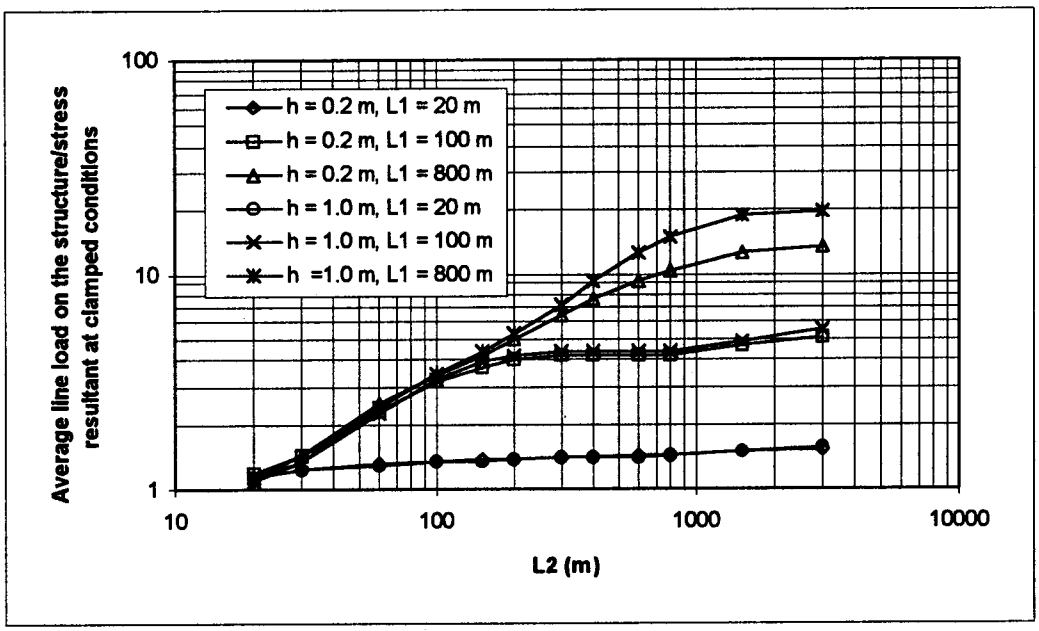

Figure 6.42 - Maximum average normalized line load on the isolated structure in Fig. 6.40, for different lengths of L1 and L2 and different thicknesses.

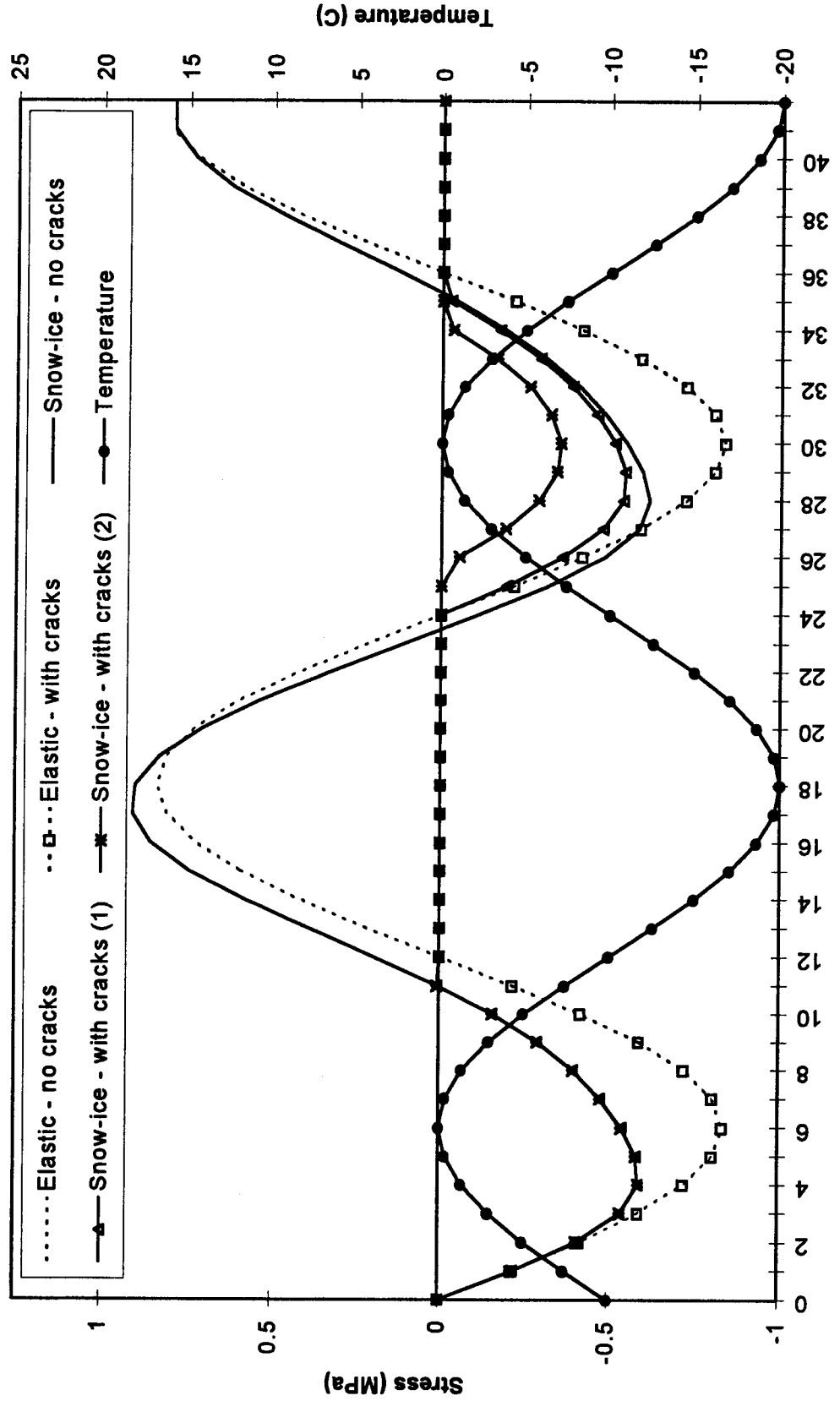

Figure 6.43 - Effect of tensile cracking and crack closing on ice stresses ($\theta_i = -10°C$).

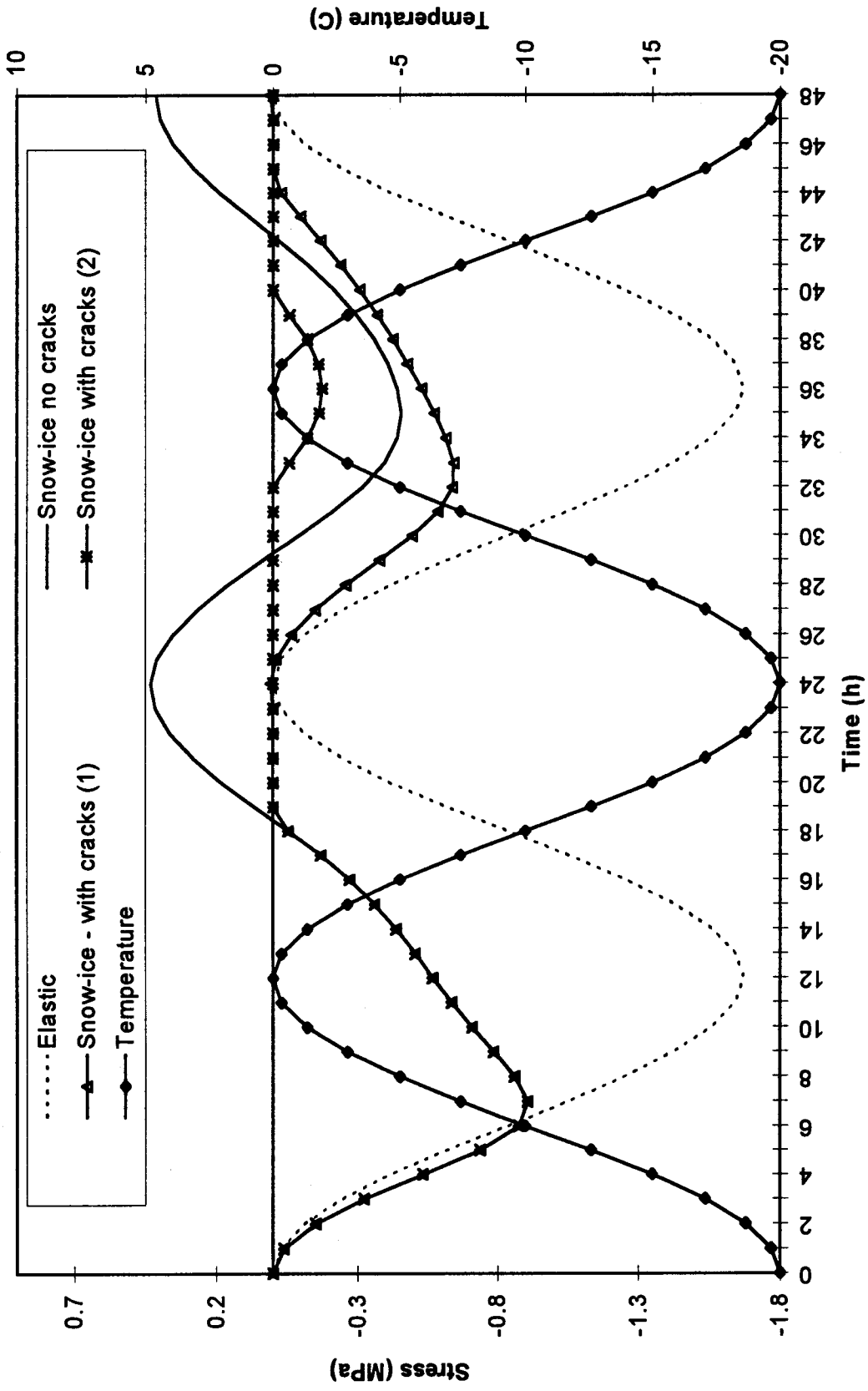

Figure 6.44 - Effect of tensile cracking and crack closing on the stresses (θ_i = -20°C).

7 - CONCLUSIONS AND RECOMMENDATIONS

7.1 - Summary and Conclusions

An analytical capability has been developed in order to investigate the pressure caused from the thermal expansion of a solid ice sheet. The model allows the prediction of the three-dimensional stress field in an ice sheet, as a function of time, under a variety of meteorological input conditions. The analytical model relies on two separate computer programs. One program calculates the temperature distribution through the thickness of the ice cover using the finite difference method. The ice cover is divided into a number of layers which can have different thickness and different material properties. The heat fluxes included in the model are those due to convection, absorbed and emitted long wave radiation, and absorbed short-wave solar radiation. The output of this program is the temperature profile as a function of time. This serves as a part of the input for the second program which uses the finite element method to predict the stress distribution through the ice cover.

In the finite element program, a degenerate shell element is used which is capable of modeling both bending and membrane behavior of the ice cover. Through the thickness the integration is performed by a layered approach. The ice cover is divided into a number of layers. Each layer can have a different thickness, different temperature, and different material properties. The material properties can be defined as a function of temperature of that layer. The layering method avoids the need for more than one element through the thickness direction. Two options are available with regard to the constitutive behavior of the ice. The uniaxial version for the first can be described by a Maxwell unit consisting of a linear temperature dependent spring and a non-linear temperature dependent dashpot. The spring represents the elastic deformation and the dashpot represents the viscous flow. The second constitutive model has an additional Kelvin-Voigt element in series with the

Maxwell unit. The Kelvin-Voigt unit that represents the delayed elastic deformation consists of a dashpot in parallel with a spring. Some of the important features of the finite element program are: elastic foundation for the effect of underlying water, smeared tensile cracking, boundary elements to model the shores with different inclines and non-rigid structures, and loading due to water level changes.

In this formulation it is assumed that the material properties are the same in all directions in the horizontal plane. This is valid for granular ice which is isotropic and columnar ice with optical axis horizontal which is transversely isotropic. The model is designed for low strain rates (less than 10^{-6} s^{-1}) which are typical for naturally occurring thermal loading. Therefore compressive cracking or the softening effect after the peak stress, both of which occur at higher strain rates, are not considered. Buckling of the ice sheets is also not considered.

The thesis contains seven chapters. The problem of the thermal pressure was introduced in Chapter 1 and some background was given. The literature review in Chapter 2 showed that despite recognition of the problem for over a century and the large number of investigations, a complete understanding has not been achieved. The past research was based on one- or at most two-dimensional models which could not consider some important factors such as the three-dimensional stress field in the ice, bending of the ice cover, effect of the underlying water, geometry of the reservoir, different shore types, flexibility of the resisting structure, and tensile cracking. The past research was almost exclusively concerned with fully constrained conditions. Due to the short comings of the models the conditions where the ice cover was free to expand on part of the boundary, was not considered. It was concluded that there was a lack of a three-dimensional model which could consider all of the above mentioned factors and conditions.

In Chapter 3 different aspects of the thermal analysis were explained. After introducing the governing differential equation, the formulations for different components of the heat exchange were given and the finite difference formulation was described. The predicted temperatures were shown to be in good agreement with analytical and other numerical solutions.

Chapter 4 was concerned with the finite element program. The particular finite element used was introduced, the constitutive laws were explained, the important features of the program were described, and the overall formulation and the flowchart were presented. The predictions of the program were shown to be in good agreement with analytical and other numerical solutions.

In Chapter 5 both models were used in simulations of laboratory and field events. The different mechanical properties suggested by previous investigators which were suitable for thermal analysis were presented. These included those suggested by Drouin and Michel (1971), Bergdahl (1978), and Cox (1984). The stresses predicted by the finite element model were compared to the stresses obtained in the uniaxial constant strain rate tests and biaxial constant temperature rates performed by Drouin and Michel (1971). The predictions of both the thermal and mechanical models were also compared to the field data collected by Fleet Technology Ltd. (Comfort et al., 1993, Comfort et al., 1994). The measurements were performed during the 1991-92 and 1992-93 winters at the Paugan dam in Quebec, the Arnprior dam in Ontario, and a large outdoor basin at the National Research Council in Ottawa. The data included the temperature and stress profiles, observations and measurements of ice and snow conditions, and some meteorological data. Some of the conclusions reached in Chapter 5 are:

1) It was observed that good temperature predictions are possible with the thermal program. The accuracy of the results however, depends on the accuracy of the boundary conditions such as air or ice surface temperature and incoming short-wave solar radiation.

2) In the stress simulations, the predicted stresses depended very much on the choice of mechanical properties. The mechanical properties suggested by Drouin and Michel for snow-ice gave the best agreement in most cases. The exception was for one case during the 1991-92 winter at the Paugan Dam site, where the best agreement was achieved using the mechanical properties suggested by Cox.

3) Both constitutive models were used in simulations of laboratory and field data. It was found that the first model, when used with temperature dependent material properties, yielded acceptable predictions of both the experimental and field data. This model had

the advantage of requiring less computing time and fewer material properties. Thus the majority of the simulations were based on this model.

4) The stress history was observed to have a significant effect on the predicted stresses. In order to include the effect of stress history, simulation intervals were selected to be as long as practical, and in some cases simulations were started one or two days in advance of a particular thermal event.
5) It was concluded that cracking of the ice should be considered in the analysis. The tensile strength of ice was set very close to zero (0.01 MPa) in the simulations. This artificially low value accounted for the effect of pre-existing cracks.
6) Where the loading due to water level changes was included, the calculated deflections matched with the prescribed water level changes. The stresses obtained by this method compared very well with the stresses at the NRC Test Basin but did not show the fluctuations that occurred in the stresses at the two dam sites. It was concluded that the fluctuations are due to other mechanisms such as arching action.
7) In the situations where temperatures above freezing were recorded in the ice sheet, some discrepancies were observed between the measured and calculated stresses. Usually during these periods the calculated stresses were higher than the measured stresses and after these periods the measured stresses were higher. In some cases even compressive stresses were recorded during the cooling periods. These discrepancies were attributed to the melting and freezing of the ice cover.

In Chapter 6 a study was performed to investigate the role of different factors that affect the temperature and stress distribution inside the ice cover. Both the thermal the and stress analysis programs were used in the study. The applied temperature variation was a periodical function with prescribed period, amplitude, and initial temperature. For the thermal analysis, the factors studied included: different ice types, wind speed, cloud cover, relative humidity, latitude, time of the year, snow cover, thickness of the ice cover, and different periods and amplitudes of temperature increase. For the stress analysis, factors considered were the number of layers through the thickness, the thickness of the ice cover, period of the temperature increase, initial temperature, amplitude of the temperature increase, underlying water, geometry of the reservoir, boundary conditions,

inclination of the shores, stiffness of the resisting structure, isolated structures, and tensile cracking. The conclusions of this chapter are as follows:

1) Short-wave solar radiation has a significant effect on the maximum temperatures in an ice sheet, especially for snow-ice at lower altitudes and under clear sky conditions.
2) When solar short-wave radiation is not considered, for example when the surface temperature is prescribed, temperatures in the ice are relatively insensitive to the thermal properties of ice.
3) The presence of a snow cover has a significant effect on temperatures in an ice sheet. With 5 and 10 cm of snow, the amplitude of the ice surface temperature was reduced by 66% and 72% respectively from the predictions for clear ice.
4) With increasing period of the air temperature history, the ratio between the amplitudes of the ice surface temperature and the air temperature gets closer to one.
5) With increasing thickness the temperature distribution through an ice cover gets closer to the temperature distribution corresponding to a semi-infinite body. In a thin ice sheet the temperature changes occur through the whole thickness but with increasing thickness only the upper parts undergo temperature changes. The depth of the significant temperature changes depends on the period of temperature increase and is about 0.3 m for daily temperature changes.
6) Depending on the boundary conditions, two different situations exist for stress distributions, fully confined and free expansion conditions.
7) In the fully confined conditions when the displacements and rotations are zero at the boundaries (clamped), there is no bending deformation and no interaction between the different layers. Each layer acts independently under the influence of the temperature changes in the layer.
8) When there is a freedom to expand on part of the boundary, there is interaction between the layers, which affects the stress distribution. In this case tensile stresses can be produced in the bottom layers
9) Under clamped conditions maximum (with respect to time) stress at top layer, does not change very much with thickness. The maximum (with respect to time) stress

resultant, however, depends on the maximum stress and the penetration of temperature variations into the ice sheet. As the thickness increases the stress resultant approaches a constant value.

10) The stresses and the stress resultants both increase if the initial temperature is decreased.

11) Under clamped conditions the effect of reservoir geometry is negligible and it is possible to obtain good estimates of stresses even with a one element finite element analysis. This conclusion was confirmed by comparing single element results with field measurements.

12) Under confined conditions where there is no rotational constraint on the boundary but the displacements are restrained, then near the boundaries some compressive stresses may occur in the lower layers. However the stress resultants do not change very much from those for the corresponding clamped case. Due to resistance of the underlying water against bending of the ice cover, it was found that for large ice covers the stress distribution in regions away from the boundaries gets close to that the clamped case. Therefore in these regions, a one element mesh can still be used to estimate ice loads.

13) When the ice cover is free to expand in some parts of the reservoir, the stresses and the loads decrease in the vicinity of these areas. Examples of this situation are an inclined shore or a flexible structure. The reductions in stress at other locations depend on the boundary conditions and geometry of the reservoir.

14) In the case of free expansion, the in-plane displacements are larger for thin ice sheet where the whole thickness undergoes temperature changes.

15) When a structure is a combination of relatively rigid and flexible parts, the ice load is distributed according to the stiffness each part. In this case the load on the flexible part will be less than the load on a clamped boundary, and the load on the rigid part will be higher than that on a clamped boundary. With decreasing stiffness of the flexible parts, the load on these parts decreases and the load on the rigid parts increases.

16) In the case of free expansion of an ice sheet surrounding a fixed isolated structure, a substantial force can be exerted on that structure. The magnitude of the force depends very much on the geometry and dimensions of the reservoir. In some of the cases studied the forces exerted forces were about 20 times the load for clamped boundary conditions.

7.2 - Recommendations for Future Study

It was observed that the predicted stresses depend very much on the choice of material properties. Most of the material properties suggested in the literature are based on tests performed at high strain rates and cannot be used for thermal stress analysis. Therefore, further study of the thermal load problem would benefit from additional experimental work on the multi-axial behavior of different ice types, especially S2 ice at low strain rates. It is recommended that unloading conditions which occur during cooling periods also be considered in the experimental works.

In most of the comparisons with field measurements the best agreement was achieved when the mechanical properties suggested by Drouin and Michel for snow-ice were used. In one case, however the mechanical properties suggested by Cox gave the best agreement. Since the field data were limited, it was not possible to reach a firm conclusion about the choice of mechanical properties in the analysis. More field measurements are required in order to properly determine the appropriate mechanical properties.

In this study the effect of water level changes was modeled by changing the buoyancy force on the ice cover. Although the vertical displacements matched with the prescribed water level changes, the predicted loads did not show the high fluctuations that occurred in the loads obtained from the measured stresses at dam sites. It is probable that other mechanisms were responsible. Further studies concerning the effect of water level changes is recommended. In particular, the second order geometric effects associated with arching action should be considered.

Most of the effort in this study was concentrated on the development of the analytical models and comparison with field measurements. The available data were mostly for restrained ice sheets and wide structures. The present model can be used to study the ice load on isolated structures as well. It is recommended that the model be used to perform comparative studies between numerical predictions and field measurements of ice loads on isolated structures.

The present model is most suitable for low strain rates (less than $1\times10^{-6}s^{-1}$). In the case of offshore structures, high strain rates and stresses might occur and compressive cracking and buckling which reduce the exerted loads should be considered in the analysis. In these situations the present model will give an upper bound solution. The model could be expanded to include compressive cracking or buckling of the ice sheet.

Cracking of ice and crack closing have a significant affect on the stresses. The tensile strength and closing criteria which are used in this study are based on the field data that correspond to fully confined condition. In this case the tensile stresses occur in the upper layers of the ice sheet during cooling periods. In the case of free expansion however, tensile stresses can occur in the lower layers of an ice sheet during periods of temperature increase. Therefore the tensile strength and closing criteria might be different in these conditions. Further study on this matter is recommended.

REFERENCES

Anderson, E. R. (1954), "Energy Budget Studies", in Water-Loass Investigations, Lake Henfer Studies, Technical Report, USGS Proffesional Paper No. 269.

Angstrom, A. (1915), "The study of Radiation in the Atmosphere", Smithsonian Misc. Coll., Smithsonian Institute, Washington D.C..

Ashton, G. D., editor (1986), "River and Lake Ice Engineering", Book Crafters Inc., Michigan, USA, ISBN, O-918334-59-4.

Assur, A. (1959), "Maximum Lateral Pressure Exerted by Ice Sheets", IAHR VIII Congress, paper 22-SI, Montreal.

Bergdahl, Lars (1977), "Physics of Ice and Snow as Affects Thermal Pressure", Department of Hydraulics, Chalmers University of Technology. Report Series A:1.

Bergdahl, Lars (1978), "Thermal Ice Pressures in Lake Ice Covers", Department of Hydraulics, Chalmers University of Technology, Report Series A:2.

Bergdahl, Lars and Wernersson, Lars (1977), " Calculated and Expected Thermal Ice Pressure in Five Swedish Lakes', Department of Hydraulics, Chalmers University of Technology, Report Series B:7.

Bomeng, Xu (1986), " Design Value of Pressure Due to Expansion of Ice Sheet in Reservoir", Proceedings of IAHR 8th International Symposium on Ice, Iowa city, Iowa, pp. 231-238.

Boucher, R. (1960), "Barrages et Structures Hydrauliques", Ecole Ploytechnique, Montreal, Publ. 53, pp. 28.

Bowen, I. S. (1926), "The Ration of Heat Losses by Conduction and Evaporation from Any Water Surface", Physical Review, series 2, Vol. 27, pp. 779-787.

Brown, E. and Clarke, G. C. (1932), "Ice Thrust in Connection with Hydro-electric Plant Design", The Engineering Journal, Vol. 15, No. 1, January, pp. 18-25, with discussion in Vol. 15 No. 8, August, pp. 393-397.

Brunt, D. (1932), "Notes on Radiation in the Atmosphere", Quarterly Journal of Royal Meteorological Society, London, Vol. 88, 1932.

Carstens, T., Editor(1980), "A State-of-the-Art Report", IAHR Working Group on Ice Forces on Structures, CRREL, Special Report 80-26.

Canadian Dam Safety Association (1995), "Dam Safety Guidelines", P.O. Box 4490, South Edmonton Postal Station, Alberta, Canada T6E 4X7.

Comfort, G., and Abdelnour, R. (1993), "Phase I-Static Ice Loads on Hydro-Electric Structures: Ice Pressures and Conditions at the Paugan Dam During the 1992 Winter", Fleet Technology Ltd., report 3920 submitted to the Canadian Electrical Association.

Comfort, G., Abdelnour, R., and Gong, Y. (1994), "Phase II-Static Ice Loads on Hydro-Electric Structures: Field Measurements and Large Scale Tests Conducted During the 1992-1993 Winter", Fleet Technology Ltd., report 3985 submitted to the Canadian Electrical Association.

Cox Gordon, F.N. (1984), "A Preliminary Investigation of Thermal Ice Pressure", Cold Regions Science and Technology, 9, pp. 221-229.

Cui Wei, (1996), "Modeling Breakup on the Mackenzie River, NWT.", M.Sc. Thesis submitted to the University of Alberta, Edmonton, Alberta.

Drouin, M. and Michel, B. (1971), "Pressure of Thermal Origin Exerted by Ice Sheets on Hydraulic Structures", ("Les poussee d'origin thermique exercees par les couverts de glace sur les structure hydrauliques")(in French), Universite Laval, Quebec, report 5-

23. U.S. Army Cold Regions Research and Engineering Laboratory, Honover, N.H., Draft Translation 427 (1974).

Dumble, J. H., (1891), "Some Observations on the Expansion and Contraction of Ice on Canadian Waters", Transactions, Canadian Society of Civil Engineers, Vol. 5, part 2, pp. 270-308.

Engineering Record (1899), "Failure of a Minneapolis Dam by Ice Pressure", Vol. 39, pp. 542-543.

Frederking, R. (1977), "Plain Strain Compressive Strength of Columnar Grained and Granular Snow-ice", Journal of Glaciology, Vol. 18, No. 80, pp. 505-516.

Gerard, R., (1989), "Thermal Ice Loads on Dams and Ancillary Structures: A Brief Review", Proceedings of Dam Safety Seminar, Edmonton, Alberta, sponsored by CADSO, BiTech Publishers Ltd., pp. 123-137.

Glover, J., and McCulloch J. S. G. (1958), "The Empirical Relation Between Solar Radiation and Hours of Sun-shine", Quarterly Journal of the Royal Meteorological Society of London.

Gray, D. M. and Male, D. H., editors (1981), "Handbook of Snow, Principles, Processes, Management & Use", Pergamon Press.

Haynes, F. D. (1973), "Tensile Strength of Ice Under Triaxial Stresses", U.S. Army Cold Regions Research and Engineering Laboratory, CRREL Report 312.

Hinton, E. and Owen, D. R. J. (1984), "Finite Element Software for Plates and Shells", Pineridge Press, Swansea, U.K.

Hrudey, T. M. (1973), "A Creep Bending Analysis of Plates by the Finite Element Method", International Journal of Solids Structures", 1973, Vol. 9, pp. 291-303.

Hrudey, T. M. (1992), Private communication.

Ivchneko, A. B. (1990), "Investigation of Stress of Ice Cover Under Changes of Temperature", Proceedings of IAHR 10th Symposium on Ice, August 20-24, Espoo, Finland, pp. 149-157.

Jumppanen, Pauli (1973), "Ice Thermal Loads Against Walls of Water Reservoirs", Proceedings POAC Conference Iceland, 2nd International Conference on Port and Ocean Engineering under Arctic Conditions, pp. 679-702.

Kendall, G.R. (1968), "Meteorological Information Relevant to Ice Pressures", Ice Pressure Against Structures, Universite Laval, 1966, Tech. Mem. No. 92, N.R.C. of Canada, pp. 89-94.

Khoo, H. A. (1989), " A Constitutive Model for Ice", M.Sc. thesis presented to the University of Alberta, Edmonton, Alberta.

Klein, W. H. (1948), "Calculation of Solar Radiation and the Solar Heat Load on Man", Journal of Meteorology, US NO. 4.

Lewin, Jack (1995), "Hydraulic Gates and Valves, in Free Surface Flow and Submerged Outlets", Thomas Telford Publications, Thomas Telford Services Ltd., 1 Heron Quay, London E14 4JD.

Li, H.S. , Zhang, X.P., and Shen, W. (1991), "The experimental Study of Ice Expanding Pressure", Proceedings of the 10th International Conference on Offshore Mechanics and Arctic Engineering, Norway, Vol. IV, pp. 187-190.

Lindgren, S. (1970), "Thermal Ice Pressure", IAHR Symposium, Ice and Its Action on Hydraulic Structures, pp. 6.7.1-6.7.40.

Lofquist, Bertil (1954), "Studies of the Effect of Temperature Variation", in Ice Pressure Against Dams: a Symposium, Transactions, American Society of Civil Engineers, Vol. 119, pp. 6-21.

Loset, Sveinung (1992), "Heat Exchange at the Air Exposed Surface of the Icebergs", Proceedings of IAHR 11th International Symposium on Ice, Banff, Alberta, pp. 735-746.

Mellor, M. and Cole, D. M. (1982), "Deformation and Failure of Ice under Constant Stress or Constant Strain Rate", Cold Regions Science and Technology, Vol. 5, pp. 207-230.

Metge, Michel (1976), "Thermal Cracks in Lake Ice", Ph.D. Thesis submitted to Department of Civil Engineering, Queen's University, Kingston, Ontario, Canada.

Michel, Bernard (1978), "Ice Mechanics", Les Presses de L'Universite Laval, Quebec.

Monfore, G. E. (1951), "Laboratory Investigation of Ice Pressure", Structural laboratory report NO. SP-31, USBR, Denver, Colorado.

Monfore, G. E. (1954), "Experimental Investigation by the Bureau of Reclamation", in Ice Pressure Against Dams: a Symposium, Transactions, American Society of Civil Engineers, Vol. 119, pp. 26-42.

Noponen J. and Maattanen M. (1994), "Thermal Ice Load Against Isolated Structures", Proceedings of IAHR 12th International Symposium on Ice, August 23-26, Trondheim, Norway, Vol. 1, pp. 392-400.

Paily, P. P., Macagno, E. O., and Kennedy, J. F. (1974), " Winter Regime Surface Heat Loss from Heated Streams", IAHR Report NO. 155, Institute of Hydraulic Research, University of Iowa, Iowa City, Iowa.

Parmelee, G. V. and Aubelle, W. W. (1952), "Radient Energy Emission of Atmosphere and Ground", ASHVE Transactions, Vol. 58, pp. 85-106.

Patankar, S. V. (1980), "Numerical Heat transfer and Fluid Flow", Hemisphere Publishing Corporation, McGraw-Hill Book Company, Washington, USA.

Peschansky, I. S. (1971), "Static Pressure of Sea Ice", Trans. Arctic and Antarctic Research Institute, Leningrad, Vol. 300, pp. 4-8 (in Russian), Israel Program for Scientific Translation, 1973.

Rimsha, V. A., and Donchenko, R. V. (1958), "The Investigation of Heat Loss from Water Surfaces in Winter Time", (in Russian), Trudy GG1, No. 65.

Rose, E. (1947), "Thrust Exerted by Expanding Ice Sheet" and discussion, Transactions, American Society of Civil Engineers, Vol. 112, pp. 871-900.

Royen, N. (1922), "Ice Pressure With Increasing Temperature", translated from Swedish by W. Nupen, SIPRE bibliography project, Translation 45, 1955, 11 pages.

Sanderson, T. J. O. (1984), "Thermal Ice Force Against Isolated Structures", Proceedings of IAHR 7th International Symposium on Ice, Hamburg pp. 1-11.

Sanderson, T. J. O. (1988), "Ice Mechanics Risks to Offshore Structures", BP Petroleum Development Ltd., London.

Selvadurai, A. P. S. (1992), "Finite Element Modeling of Static Ice Pressure on Hydraulic Structures", contractor report submitted by Selvadurai and Associates Ltd. to Fleet Technology Ltd.

Sinha, N. K. (1982), "Constant Strain and Stress Rate Compressive Strength and Deformation of Columnar Grained Ice" Journal of Materials Science, Vol. 17, No. 3, pp. 785-802.

Smith, C. D. (1985), "Hydraulic Structures", University of Saskatchewan Press, Saskatoon, Saskatchewan, 357 p.

Timoshenko, S. P. and Woinowsky-Kreiger, S. (1959), "Theory of Plates and Shells", McGraw-Hill, New York.

Tunik, A. L. (1988), "Design Ice Forces on Offshore Installations", Proceedings of the Seventh International Conference on Offshore Mechanics and Arctic Engineering, Vol. IV, Houston, Texas, pp. 159-161.

USBR, (1977), "Design of Small Dams", U.S. Bureau of Reclamation, Denver, Colorado.

Wilmot, J. (1952), "Measurements of Ice Thrusts on Dams", Ontario Hydro Research News, No. 3, pp. 23-25.

Woolf, H. M. (1968), " On the Computation of Solar Elevation Angles and the Determination of Sunrise and Sunset Times", NASA Technical Memorandum, NASA TMX-1946, Washington, Sept., 1968.

Xian-Zhi, S. (1988), "Study of Ice Static Pressure on Ice Cover in Reservoir", Proceedings of 9th International Symposium On ice, 1988, Sapporo, Japan, pp. 483-492.

Xu, Bomeng (1986), "Design Value of Pressure Due to Expansion of Ice Sheet in Reservoir, Proceedings of IAHR 8th International Symposium on Ice, Iowa City, Iowa, pp. 231-238.

Yamaoka, I., Fujita, M., and Hasegawa, K. (1988), " Measurement of Thermal Ice Thrust Exerted by an Expanding Ice Cover in Taisetsu Dam Reservoir in Hokkaido, Japan", Proceedings of IAHR 9th International Symposium on Ice, 1988, Sapporo, Japan, pp. 473-482.

Zienkiewicz, O. C. (1977), "The Finite Element Method", McGraw-Hill.

Recent Structural Engineering Reports

Department of Civil and Enviromental Engineering

University of Alberta

183. *Evaluation of Design Procedures for Torsion in Reinforced and Prestressed Concrete* by M.G. Ghoneim and J.G. MacGregor, February 1993.

184. *Distortional Buckling of Steel Beams* by H.S. Essa and D.J.L. Kennedy, April 1993.

185. *Effect of Size on Flexural Behaviour of High-Strength Concrete Beams* by N. Alca and J.G. MacGregor, May 1993.

186. *Shear Lag in Bolted Single and Double Angle Tension Members* by Yue Wu and G.L. Kulak, June 1993.

187. *A Shear-Friction Truss Model for Reinforced Concrete Beams Subjected to Shear* by S.A. Chen and J.G. MacGregor, June 1993.

188. *An Investigation of Hoist-Induced Dynamic Loads* by D.A. Barrett and T.M. Hrudey, July 1993.

189. *Analysis and Design of Fabricated Steel Structures for Fatigue: A Primer for Civil Engineers* by G.L. Kulak and I.F.C. Smith, July 1993.

190. *Cyclic Behavior of Steel Gusset Plate Connections* by J.S. Rabinovitch and J.J.R. Cheng, August 1993.

191. *Bending Strength of Longitudinally Stiffened Steel Cylinders* by Q.Chen, A.E. Elwi and G.L. Kulak, August 1993.

192. *Web Behaviour in Wood Composite Box Beams* by E.T. Lewicke, J.J.R. Cheng and L. Bach, August 1993.

193. *Experimental Investigation of the Compressive Behavior of Gusset Plate Connections* by M.C.H. Yam and J.J.R. Cheng, September 1993.

194. *Some Behavioural Aspects of Composite Trusses* by B. Woldegiorgis and D.J.L. Kennedy, January 1994.

195. *Flexural Behavior of High Strength Concrete Columns* by H.H.H. Ibrahim and J.G. MacGregor, March 1994.

196. *Prediction of Wrinkling Behavior of Girth-Welded Line Pipe* by L.T. Souza, A.E. Elwi and D.W. Murray, April 1994.

197. *Assessment of Concrete Strength in Existing Structures* by F.M. Bartlett and J.G. MacGregor, May 1994.

198. *The Flexural Creep Behavior of OSB Panels Under Various Climatic Conditions* by N. Zhao, J.J.R. Cheng and L. Bach, June 1994.

199. *High Performance Concrete Under High Sustained Compressive Stresses* by S. Iravani and J.G. MacGregor, June 1994.

200. *Strength and Installation Characteristics of Tension - Control Bolts* by S.T. Undershute and G.L. Kulak, August 1994.

201. *Deformational Behavior of Line Pipe* by M. Mohareb, A.E. Elwi, G.L. Kulak and D.W. Murray, September 1994.

202. *Behavior of Girth-Welded Line Pipe*, by N. Yoosef-Ghodsi, G.L. Kulak and D.W. Murray, September 1994.

203. *Numerical Investigation of Eccentrically Loaded Tied High Strength Concrete Columns* by J. Xie, A.E. Elwi and J.G. MacGregor, October 1994.

204. *Shear Strengthening of Concrete Girders Using Carbon Fibre Reinforced Plastic Sheets* by E.H. Drimoussis and J.J.R. Cheng, October 1994.

205. *Shrinkage and Flexural Tests of a Full-Scale Composite Truss* by M.B. Maurer and D.J.L. Kennedy, December 1994.

206. *Analytical Investigation of the Compressive Behavior and Strength of Steel Gusset Plate Connections* by M.C.H. Yam and J.J.R. Cheng, December 1994.

207. *The Effect of Tension Flange Movement of the Strength of Point Loaded I-Beams* by D. Mullin and J.J.R. Cheng, January 1995.

208. *Experimental Study of Transversely Loaded Continuous Steel Plates* by K.P. Ratzlaff and D.J.L. Kennedy, May 1995.

209. *Fatigue Tests of Riveted Bridge Girders* by D. Adamson and G.L. Kulak, July 1995.

210. *Fatigue of Rivet Tension Members* by J. DiBattista and G.L. Kulak, November 1995.

211. *Behaviour of Masonry Cavity Walls Subjected to Vertical Eccentric Loads* by R. Wang, A.E. Elwi, M.A. Hatzinikolas and J. Warwaruk, Feburary 1996.

212. *Transport of High Strength Concrete Column Loads Through Concrete Slabs* by Ospina, C.L. and Alexander, SDB, August 1996.

213. *Thermal Ice Loads on Structures* by Azarnejad, A. and Hrudey, T.M., November 1996.